CRANFIELD UNIVERSITY

VILI PANOV

Modelling of Behaviour of Metals at High Strain Rates

SCHOOL OF ENGINEERING

PhD THESIS

CRANFIELD UNIVERSITY

SCHOOL OF ENGINEERING

PhD THESIS

Academic Year 2005-6

VILI PANOV

Modelling of Behaviour of Metals at High Strain Rates

Supervisor: Prof Rade Vignjevic

This thesis is submitted in partial fulfilement of the requirements for the Degree of PhD

ABSTRACT

The aim of the work presented in this thesis was to produce the improvement of the existing simulation tools used for the analysis of materials and structures, which are dynamically loaded and subjected to the different levels of temperatures and strain rates. The main objective of this work was development of tools for modelling of strain rate and temperature dependant behaviour of aluminium alloys, typical for aerospace structures with pronounced orthotropic properties, and their implementation in computer codes. Explicit finite element code DYNA3D has been chosen as numerical test-bed for implementation of new material models. Constitutive model with an orthotropic yield criterion, damage growth and failure mechanism has been developed and implemented into DYNA3D.

Second important aspect of this work was development of relatively simple experimental methods for characterization of engineering materials, and extensive experimental work has been undertaken. Tensile test has been used for the characterisation of two aluminium alloys, at different levels of the strain rates and temperatures, and for three different orientations of materials. The results from these tests allowed derivation of material constants for constitutive models and lead to a better understanding of aluminium alloy behaviour. Procedures for derivation of parameters for temperature and strain rate dependant strength models were developed and parameters for constitutive relations were derived on the basis of uniaxial tensile tests. Taylor cylinder impact test was used as a validation experiment. This test was used to validate the implementation, and accuracy of material model in computer code. At the end of each incremental development, validation of the constitutive material model has been performed through numerical simulations of Taylor cylinder impact test, where simulation results have been compared with the experimental post-test geometries in terms of major and minor side profiles and impact-interface footprints. Plate impact test has been used to determine the material properties at high strain rate, and to investigate damage evolution in impact-loaded material.

Initially the material model has been designed as a temperature and strain rate dependant strength model in a simple isotopic form, which then has been tested and verified against the experimental results. Coupling of the Hill's orthotropic yield criterion with isotropic, temperature and strain rate dependant, hardening material model, has been chosen to suit the orthotropic behaviour. Method for calibration of orthotropic yield criterion has been developed and parameters have been identified for the orthotropic model under the associated flow rule assumption and in case of plane stress on the basis of tensile and cylinder impact tests. The complexity of the model has been further increased through coupling of hardening model with orthotropic yield criterion including damage evolution and failure criteria. The constitutive model was developed within the general framework of continuum thermodynamics for irreversible processes, and plate impact test and tensile tests have been used for determination of parameters for damage part of the new material model.

ACKNOWLEDGEMENTS

I would like to thank Prof Rade Vignjevic for giving me opportunity to undertake this project and for all help and advice he gave me throughout this work.

The author is grateful to the Airbus UK for sponsoring this research.

The author thanks Prof Neil Bourne and Dr Jeremy Millett, who carried out cylinder and plate impact tests, and Dr Stefan Hiermaier who supported this work with dynamic tensile test at EMI. I also extend my appreciation to Miss Helen Lockett, for measurements on post-test cylinder geometries, and Mr Barry Walker, who made invaluable contributions to the tensile tests.

Thanks to all in Cranfield University who have helped me during my PhD.

Finally, I would like to thank my family for all their support and encouragement.

NOTATION

t	Time
T	Temperature
V	Velocity
ρ	Density
μ	Shear modulus
E	Young modulus
ν	Poisson's ratio
G, U	Activation energy
g, u	Normalized activation energy
S	Engineering stress
σ	Cauchy stress
e	Engineering strain
ε	Strain
$\dot{\varepsilon}$	Strain rate
C_e	Elastic tensor
H	Plastic characteristic tensor
σ_Y	Yield stress
$\overline{\varepsilon}$	Effective strain tensor
$\overline{\sigma}$	Effective stress tensor
$\overline{H}$	Effective plastic characteristic tensor
D	Damage tensor
M	Damage effect tensor
J	Damage characteristic tensor
Y	Damage energy release rate
W	Work
γ	Dissipation rate
ψ	Helmholtz free energy

LIST OF FIGURES

LIST OF TABLES

CONTENTS

1. INTRODUCTION

1.1. Statement of objective

The main objective of this research project is development of constitutive models for modelling of strain rate and temperature dependant behaviour of aluminium alloys, typical for aerospace structures with pronounced orthotropic properties, and their implementation into an explicit nonlinear finite element code. The output of this work is to offer enhanced simulation tools to be used for the analysis of aluminium structures, which are dynamically loaded and subjected to the range of temperatures and strain rates.

The complexity of a constitutive model is generally related to its intended application. Areas of application include metal forming processes, crashworthiness, and high velocity impact problems typical for the aerospace structures. Improvement of the simulation tools in general should result in reduction of the difference between numerical simulations and real mechanical processes.

Computer simulations can replace expensive and time consuming tests, enable designers to validate reliability of structures and manufacturers to check defined manufacturing processes, before the decision is made to start the production. The combination of experiments, numerical solutions and dynamic material characterisation has been shown to be very effective in reducing both manpower requirements and cost.

Goal in material modelling is to develop models, which are widely applicable and reasonable easy to characterise (determine input parameters for the model). Some material models require only a value of dynamic yield stress as input data, while others require a complete description of material behaviour. In the most general case stress depends on strain, strain-rate, damage, temperature and loading history. One model may be applicable for more than one application, but generally it has been found that certain classes of models are used for only certain type of applications.

Generally constitutive models must have following characteristics: capability to describe important aspects of material behaviour, to be mathematically and computationally simple, and to require a reasonable amount of experimental effort to obtain material parameters.

No mater how complex mathematical model is, it is possible to incorporate such model into a computer code. The difficulties in obtaining experimental data and model constants determine the practical value of the model. The second important aspect of this work is the development of relatively simple experimental methods for characterization of engineering materials for the proposed model.

The new material model was implemented into the explicit finite element code DYNA3D. The constitutive model comprises of a strength model, an orthotropic yield criterion, damage initiation, evolution and failure model. Initially the new material model has been designed as a temperature and strain rate dependant strength model in

a simple isotopic form, which then has been tested and verified against the experimental results. The complexity of the model has been increased in the further iterations through coupling of strength model with orthotropic yield criterion including damage evolution and failure criteria.

A schematic representation of the project research methodology is presented in figure Fig. 1.1.1. , and an outline description of the three iterations is given below.

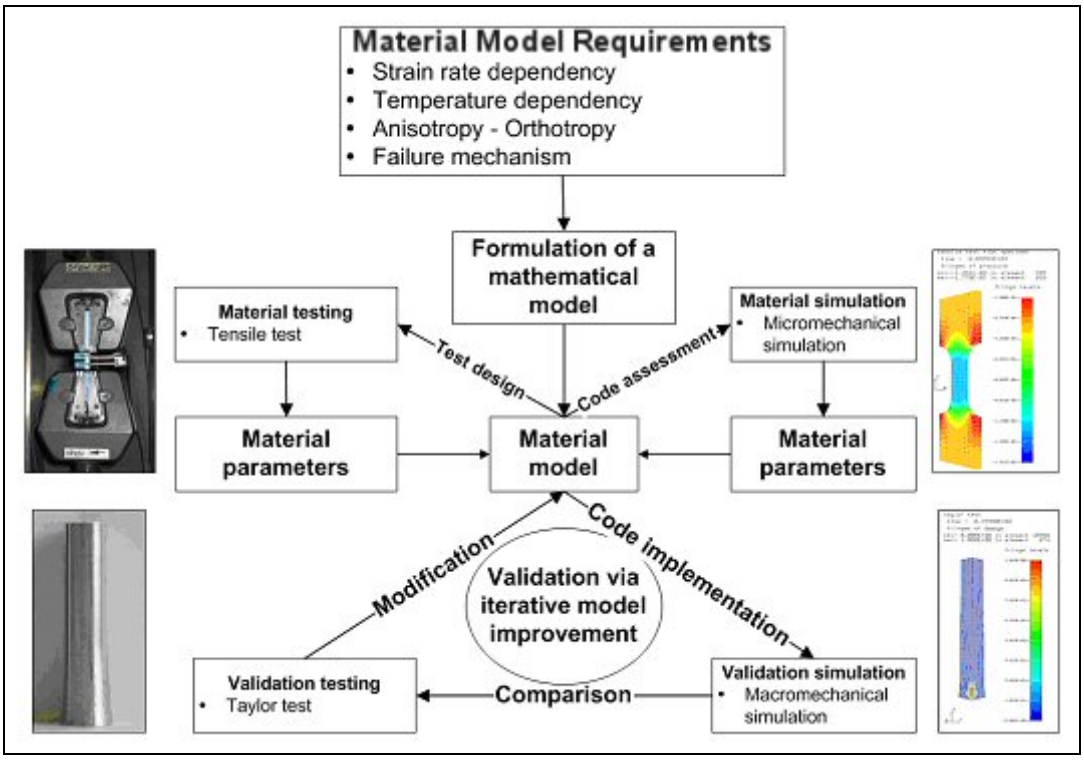

Fig. 1.1.1. Project research methodology

First iteration [1-4] consisted of implementation of the isotropic strength model with strain rate and temperature dependency and determination of parameters for the proposed strength model.

The proposed Mechanical Threshold material model is capable of accurately modelling behaviour of aluminium alloys typical for aerospace structures, which are temperature and strain rate dependent, and as a starting point of this development a number of well established strength models have been considered to suit this behaviour.

Second iteration [5] of the development consisted of coupling orthotropic yield criterion with isotropic, temperature and strain rate dependant, hardening material model, and determination of parameters for orthotropic criterion.

Proposed material model contains an orthotropy definition as a type of anisotropy. This includes the definition of material properties Elastic modulus, Shear modulus, Poisson's ratio for three directions and the anisotropy parameters that define the yield criterion.

Third iteration [6-8] consisted of integration of strength and damage models with orthotropic yield criterion and determination of parameters for damage model.

A number of existing failure material models and approaches to modelling of failure were assessed. For instance, effective surface reduction based models, models based on thermally activated damage and fracture and material instability based damage and failure models. This consideration resulted in the definition of the concept for the new material model.

Tensile tests were used for the characterisation of two aluminium alloys, at different levels of strain rate and temperature, and for different orientations of materials. The results from these tests allowed derivation of material constants for constitutive model and lead to a better understanding of aluminium alloy behaviour. This has been achieved through data processing with final result in the form of input parameters for the material constitutive models.

Taylor cylinder and plate impact test were performed as validation experiments. Depending on the initial impact velocity and sample geometry of the material, a vide range of strains, strain rates and temperatures can be achieved in a single test. These tests provide a clean set of experimental data from which is possible to validate a material model and its implementation into a computer code. Plate impact tests were used to determine the material properties at high strain rate, and to investigate damage evolution in impact-loaded materials.

Implementation of the proposed material model has been followed by validation of the model through the set of simulation tests and comparison with experimental results. On the end of iteration, validation of the constitutive material model has been performed through numerical simulations of Taylor cylinder impact test. The simulations of Taylor impact tests have been done using the public domain version of Lagrangian finite element code DYNA3D, and have been compared with the experimental post-test geometries in terms of major and minor side profiles and impact-interface footprints.

1.2. Structure of the thesis

Chapter 2
Review of relevant experimental and simulation techniques

Literature survey of the most common experimental techniques in the area of material model development and validation was performed. Experimental methods of probing material behaviour at intermediate and high strain of rates are outlined.

Furthermore, the main aspects of computational methods for impacts problems are presented. The review considers a number of hydrocodes, their similarities and differences.

Chapter 3
Experimental work

In order to characterise the materials of interest, i.e. determine material parameters a series of experiments were performed. The materials chosen for this research project AA7010 and AA2024 are commercial aluminium alloys very common in aircraft structures and of high importance to AIRBUS.

Uniaxial tensile test

Uniaxial tensile tests for the two aluminium alloys were performed as a function of temperature at the intermediate strain rate regime using universal hydraulic testing machine fitted with environmental temperature chamber at School of Engineering – Cranfield University. Uniaxial tensile tests for two aluminium alloys were performed in three different material directions, namely 0^o (extrusion), 45^o and 90^o (transversal).

In this work non-standard specimen geometry was used in order to extend the strain rate range of the servo hydraulic machine. To determine specimen geometry a set of simulations has been done and the new specimen geometry was determined.

Since that maximum achievable strain rate was in the intermediate strain-rate regime 10 s^{-1}, temperature chamber provided low temperature tests as alternative for the tests at high strain rates, based on the assumption that that the strain rate and temperature effects are interchangeable.

Results from these tests are presented in this work as stress-strain curves of AA7010 and AA2024 at different strain rates and temperatures, and for different orientations of materials.

Taylor cylinder impact test

Several Taylor impact test, using specimens cut out from a rolled plate of AA7010 aluminium alloy were performed. Geometric profile data for deformed specimens were generated using a 3D scanning machine. The data consist of digitised side profiles for minor and major direction, and digitised footprints that give cross-sectional area at the impact interface.

These digitised shapes show good experimental reproducibility, and represent an excellent data set for direct comparison with numerical simulation results. The specimen heights and radial deformations were used for comparison.

Plate impact test

Plate impact test were performed on OFHC Cu using single-stage gas gun. Plane samples were impacted by plane projectile plates at different velocities.

Using stress gauges, which were supported with PMMA blocks on the back of the target plates, stress-time histories have been recorded.

After testing, micro structural observations of the softly recovered OFHC Cu spalled specimen have been carried out and evolution of damage has been examined.

Chapter 4
Strain rate and temperature dependence

The material models detailed in this chapter are formulated primarily to describe material strength as a function of strain, strain rate and temperature. Significant attention was paid to the temperature and strain rate dependant material models such as Johnson-Cook (JC), Zerilli-Armstrong (ZA) and Mechanical Threshold Stress (MTS), and detailed descriptions of those models are given.

One of the limiting factors in obtaining accurate simulations result is the lack of specific material input parameters for advanced constitutive strength models such as Johnson-Cook, Zerilli-Armstrong and Mechanical Threshold Stress (MTS). Therefore, procedures for determination of the input parameters for the models were developed and presented in detail.

Procedures for derivation of parameters for temperature and strain rate dependant strength models were applied to the aluminium alloy AA7010. Parameters for Johnson-Cook (JC) and Mechanical Threshold Stress (MTS) models were derived on the basis of tensile tests, and used as input parameters for numerical simulation of Taylor impact test.

The numerical simulations of Taylor impact tests were performed using the public domain finite element code DYNA3D, and compared with the experimental post-test geometries. Modified form of MTS material model was implemented in DYNA3D computer code while the JC material model was used as implemented in DYNA3D.

Chapter 5
Anisotropic plasticity

The yield criterion chosen for the orthotropic material is the Hill's yield criterion with isotropic hardening. The MTS model was chosen to represent hardening of material in the referent direction. Rolling direction of plate has been chosen as referent direction.

A modification of Hill's yield criterion was proposed to allow combined isotropic-kinematic hardening, which can be useful for analyses of orthotropic aluminium alloys in sheet or plate form.

Tensile tests in a different material directions resulted in different yield stresses, and those values have been used for calibration of orthotropic yield criterion. Because of the limitations of the uniaxial tests (only longitudinal strain of flat tensile specimen has been measured for all three different directions) results from Taylor tests were used for determination of Lankford coefficients.

A method for calibration of orthotropic yield criterion has been developed and parameters have been identified for Hill's orthotropic model under the associated flow rule assumption.

Using the determined parameters for Hill's criterion, the corresponding temperature and strain rate dependant initial yield loci and yield surfaces were constructed for aluminium alloy AA7010.

Numerical simulations of Taylor test experiments have been done in order to test proposed procedure for calibration of Hill's orthotropic yield criterion and calculated parameters for aluminium alloy AA7010.

Chapter 6
Material failure modelling

This chapter starts with literature survey, which include analysis of the existing work in the field of material failure modelling. Significant attention was paid to the material models, which describe spall phenomenon. A review of exiting dynamic failure criteria is presented in this chapter.

A material failure model based on the assumption that material separation during fracture processes is thermally activated has been adopted for the proposed model. With this basic assumption, the proposed model is compatible with the Mechanical Threshold Stress model and therefore in the first instance it was incorporated into the MTS material model in DYNA3D.

In order to analyse proposed criterion a series of FE simulations have been performed for OFHC Cu. The numerical analysis results clearly demonstrate the ability of the new model to predict the spall process and experimentally observed tensile damage and failure. It allows simulation of high strain rate deformation processes and dynamic failure in tension for wide range of temperatures. Also, the proposed cumulative criterion for fracture enables one to simulate tensile damage including spall over a wide range of impact velocities.

Chapter 7
Coupling of anisotropic elastoplasticity and damage

The coupled anisotropic elastoplastic and damage framework for ductile fracture is presented in this chapter. The yield criterion chosen to suit the orthotropic material is the Hill's yield criterion with isotropic hardening, which was represented with MTS strength model for the material behaviour in the referent direction. To account for the physical mechanisms of failure, the concept that thermal activation of material separation during fracture processes has been adopted as basic mechanism for proposed model.

General coupling of anisotropic elasto-plasticity and damage formulations is demonstrated within a thermodynamically consistent framework. This framework

follows an irreversible thermodynamic approach using internal variables together with their associated generalized forces.

Firstly, the internal variables and thermodynamic potentials used to describe the processes are identified. The concept of transformation or mapping to effective-stress space is introduced. General forms for damage functions and yield functions in the effective-stress space are constructed using homogeneous functions. Finally, the compliance with the first and second thermodynamic laws is enforced.

An anisotropic damage evolution equation and a constitutive equation of plasticity are formulated using a damage effect tensor $M(D)$. Elastic-plastic constitutive and damage evolution equations are formulated by the use of the symmetric tensors H - plastic characteristic tensor and J - damage characteristic tensor, to represent the shapes of the yield and damage surfaces respectively.

Method for calibration of the proposed damage model is presented, and applied on the aluminium alloy AA7010, using experimentally determined stress – strain curves.

Chapter 8
Implementation and Validation

This chapter presents the implementation of proposed strain rate and temperature dependent, anisotropic elasto-plastic-damage model into public domain DYNA3D code. The developed model has been implemented in the code, using proposed elastic predictor/plastic corrector/damage mapping, integration algorithm. Numerical simulations of Taylor impact cylinder have been carried out to validate implemented model and good agreement with experimental results was obtained.

2. EXPERIMENTAL AND SIMULATION TECHNIQUES

2.1. Introduction

It is now well established, that most materials show a significant change in mechanical response under increased rates of straining. Material characterization involves not only the stress-strain response, but also the accumulation of damage and the mode of failure which materials undergoes.

The mathematical description of the relationship between the stresses, strains, their derivatives, temperature and damage is referred to as the constitutive law or relationship.

The basic problem is how to determine the constitutive relationship that best describes a particular material or class of materials. The most general form of a material constitutive equation should cover the description of material behaviour under the widest range of strain rates that may be encountered. However this can be extremely difficult, thus constitutive equations often cover only certain range of strain rates. It has been observed that for a number of materials different physical mechanisms are dominant at different strain rates.

In describing the relationship between stress and strain and their time derivatives for particular material, we have to emphasize that both stress and strain are point tensors functions, so a constitutive law relates stress and strain at a point. In the most general case, the relations between stresses (three normal and three shear stress) and strains (three normal and three shear strains), their time derivates, as well as any other function necessary to describe the material behaviour must be considered. It is obvious that constitutive relationship necessary to completely describe the materials behaviour can be extremely complex, because of the large number of components of stress, strain and their time derivate that may be involved in the formulation.

A several forms of constitutive law are given by following relationship:

$$\sigma = f(\varepsilon, \dot{\varepsilon}, T) \qquad (2.1.1.)$$

Where ε is strain, $\dot{\varepsilon}$ is strain rate and T is temperature. Because plastic deformation is irreversible and path dependant process, the response of the material is dependent on the deformation substructures, thus we can add one more term in the above equation, and we have:

$$\sigma = f(\varepsilon, \dot{\varepsilon}, T, deformation\_history) \qquad (2.1.2.)$$

For simplicity reasons, instead of dealing with tensors, it is much simpler to consider scalar quantities of stress and strains. That is the reason why experimental investigations are focused primarily on one-dimensional states of stress or strain.

In this chapter strain rate effects are discussed, and some of the considerations in dynamic testing of materials are summarized. An overview of major experimental techniques is presented, and details of experimental methods that have been used in this work are given in subsequent chapter.

The second part of this chapter considers computational aspects of development of a material model. Computer programs used to numerically simulate highly dynamic events in solid mechanics are commonly referred to as hydrocodes. One of the reasons for using the hydrocodes is to have a numerical test-bed for developing material models. It is therefore, very important that the code has a flexible material interface subroutine which allows a constitutive model to be added to the code with minimal effort. The availability of the source code provides the most flexible environment for the user.

2. 2. Experimental techniques

2.2.1. Strain-rate regimes

Different mechanisms govern the deformation behaviour of materials within different strain rate regimes, and general classification of strain rate regimes is presented in figure Fig. 2.2.1.1.

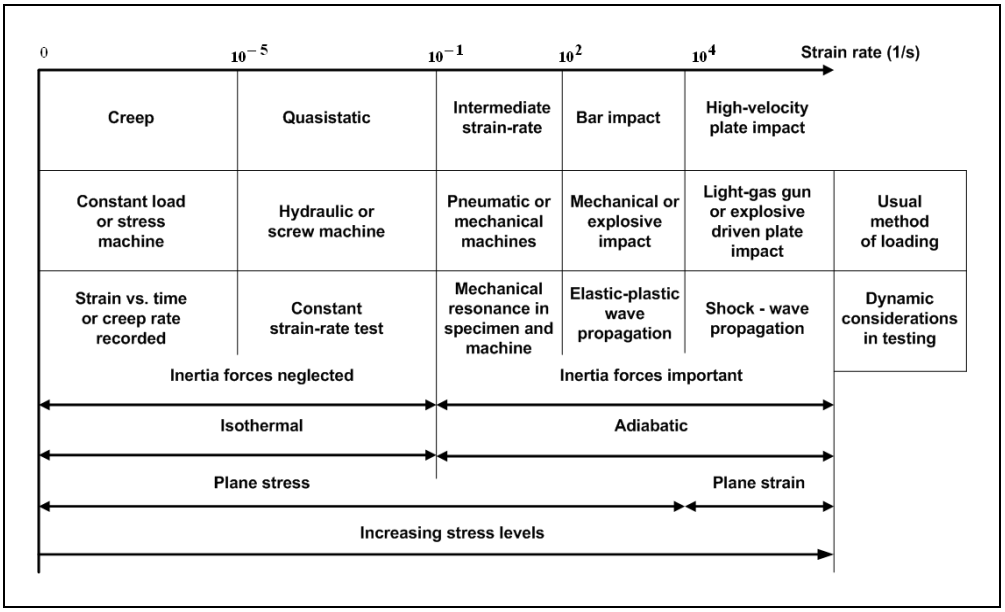

Fig. 2.2.1.1. Dynamic aspects of mechanical testing [35]

The range of strain-rate between 10^{-6} to $10^{-5}\ s^{-1}$ correspond to the ***creep behaviour*** of materials usually observed at elevated temperatures and creep type laws are used to describe the mechanical behaviour.

At strain rates of the order of 10^{-4} to $10^{-3}\ s^{-1}$, ***quasistatic*** stress-strain curve are obtained from constant strain rate tests such as uniaxial tension, compression. Those quasistatic stress-strain curves are often used as an inherent property of

materials. One should be aware that they are valid descriptions of materials only at the strain rate at which test was performed.

At higher strain rates, the stress-strain properties may change and specialized testing techniques have to be applied. The range of strain rates from 10^{-1} to $10^{2}\ s^{-1}$ is known as the ***intermediate*** or ***medium*** strain–rate regime, and within this regime strain-rate effects should be considered in most metals, although the magnitude of such effects may be small in some cases.

Strain rates of $10^{3}\ s^{-1}$ or higher are generally referred as the range of ***high*** strain rate response. Within the high strain-rate regime inertia, thermal and wave-propagation effects become important in material behaviour. At strain rates of $10^{5}\ s^{-1}$ and higher, we are generally dealing with shock waves propagation through material. At these high strain-rates we have to pay attention to thermodynamic effects, because in this region we have transition from nominally isothermal conditions to adiabatic conditions.

2.2.2. Intermediate strain-rate tests

The simplest method for determining strain-rate sensitivity of a material is to increase the speed of a uniaxial tension and compression test. Those tests are ideal, because the state of stress is purely uniaxial. Various types of machines are designed for performing tests at intermediate strain rate, and it is possible to achieve strain rates up to approximately $10^{1}\boldsymbol{s}^{-1}$. Hydraulic or pneumatic devices are utilized to rapidly accelerate a driving ram to a constant speed and then sustain that speed for the duration of test.

Also, different types of machines are utilized for torsion mode of deformation to achieve shear strain rates in the medium strain-rate regime. The torsional mode of deformation allows the achievement of very large strains without geometric instability, which is present during a tension test, and is known as necking.

2.2.3. High strain-rate tests

The Split Hopkinson Pressure Bar (SHPB) or Kolsky apparatus is one of the most widely used experimental configurations for high strain-rate material measurements. The concept of the Hopkinson bar involves the determination of dynamic stresses, strains or displacements occurring at the end of a bar through observation of the effect from some distance away. In addition to the original SHPB developed to measure the compressive response of a material, this technique has been modified for loading samples in uniaxial tension and torsion.

Among the different Hopkinson bar techniques (compression, tension and torsion) the compression bar remains the most readily analysed and least complex method to achieve a uniform high-rate stress state. Compression bar test apparatus consists of: pressure bars - two long symmetric bars, bearing and alignment fixtures to allow the bars and striking projectile to move freely, but in precise axial alignment,

striker bar, a gas gun or on alternate device for accelerating a projectile, strain gauges mounted on both bars to measure the stress wave propagation, instrumentation and data acquisition system to control, record and analyse wave data.

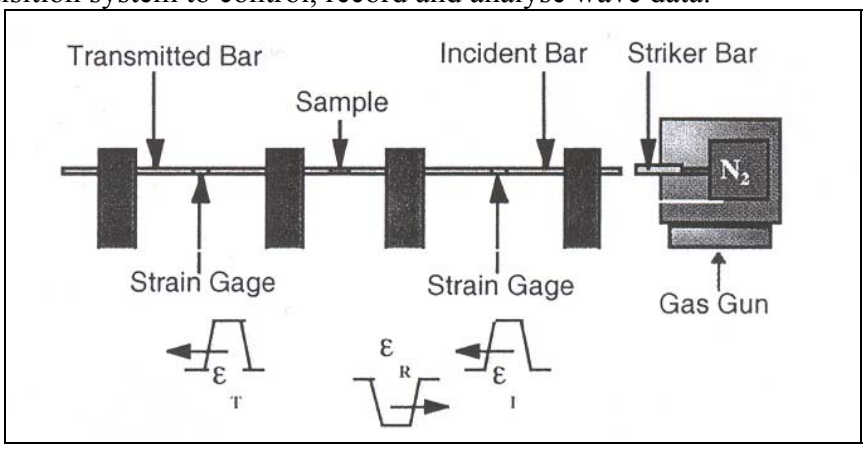

Fig. 2.2.3.1. Schematic of a Split-Hopkinson-Pressure-Bar apparatus [13]

The impact of striker bar with incident bar produces a longitudinal compressive incident wave in the incident bar ε_i. When this wave reaches the bar – specimen interface, a part of pulse is reflected ε_r, while the rest of the stress pulse passes through specimen and the output bar as transmitted wave ε_t. The time of passage and magnitude of these three elastic pulses through the incident and transmitted bars are recorded by strain gages. Forces and velocities at the two interfaces of the specimen can be determined using the wave signals in the function of time from gages. When the specimen is deforming uniformly, the strain rate within specimen is directly proportional to the amplitude of reflected wave. The stress within the sample is directly proportional to the amplitude of transmitted wave. The reflected wave is also integrated to obtain strain and is plotted against stress to produce the dynamic stress strain curve for the specimen.

2.2.4. Taylor impact test

The alternative method of probing the mechanical behaviour of materials at high strain rates is the Taylor rod impact test. This method consists of firing a solid cylinder of the material against a massive and rigid target. The deformation in the rod due to impact shortens the rod as radial flow occurs at the impact end of the bar. The dynamic flow stress of the cylinder material can be estimated by measuring the overall length of the impacted cylinder and the length of the undeformed (rear) section of the cylinder.

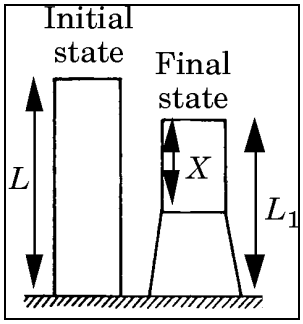

Fig. 2.1.4.1. Schematic of Taylor Impact Cylinder Test [12]

This test has been used mostly as a validation experiment. In this approach, the final length and cylinder profile of the sample are compared with code simulations to validate the material constitutive model implemented in the computer code. Comparisons with the recovered samples provide a check on how accurately the code can calculate the gradient in the deformation stresses, strain rate and thermal effects leading to the final strains of the sample cylinder during the impact.

2.2.5. Plate impact test

Plate impact experiments are used to study dynamic deformation and failure modes of materials at high strain rate. The recovery configurations in these experiments are performed with the objective of examining the microstructural changes in the specimen after it is subjected to loading under a uniaxial strain condition. The experiments are designed to achieve a controlled plane-wave loading of specimens. In practice, this is limited by the finite size of the plates employed, which generates radial release waves.

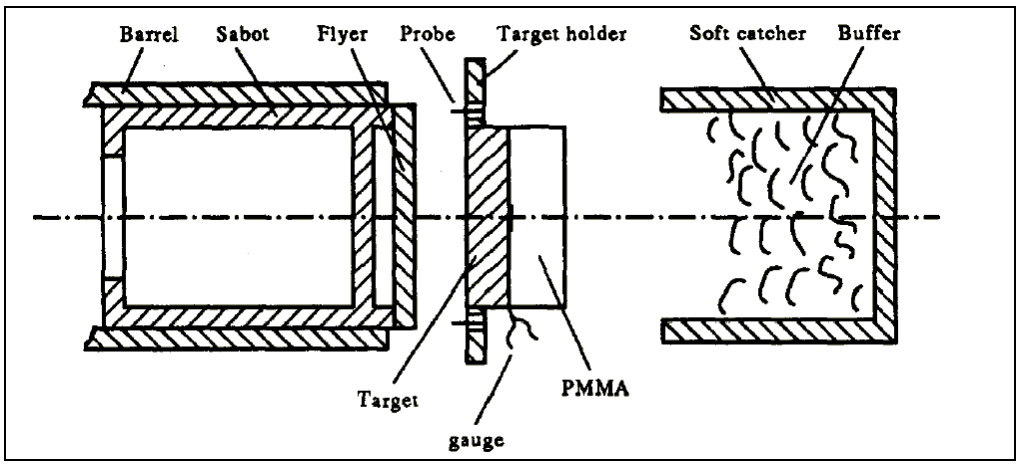

Fig. 2.2.5.1. Schematic of a Plate Impact Test apparatus [31]

A plate impact experiment involves the impact of a moving flat plate, called the flyer, with another stationary plate, called the target, which is usually the specimen. In the normal plate impact experiment, the specimen is subjected to a compression pulse. The test is designed to provide insights into behaviour of materials in presence of shock waves, and thus it is necessary that the material of the specimen is under a uniaxial strain condition. In case where the diameters of both the flyer and the target are much greater then their thicknesses, planar impact generates two one-dimensional shock waves. One propagates into the target and the other into the flyer plate. Those shock waves reflect as rarefaction waves from free surfaces of the flyer and target plates respectively. The experiment can be designed so that these rarefaction waves interact inside the target, producing a state of tension in some region. If this tensile stress level exceeds the dynamic yield strength of the material, fracture takes place, producing a scab from that section of the target. The velocity and the thickness of this scab depend upon the yield strength of the target and impact velocity.

2.3. Numerical analysis

2.3.1. General considerations

The equations governing the impact of solids are, in general, non-linear and cannot be solved analytically, thus, numerical analysis of the equations is used to determine the response. All hydrocodes attempt to solve (numerically) the differential equations that govern the dynamics of a continuous media. These equations are established through the application of conservation laws (energy, momentum, and conservation mass) and compatibility equations (strain, stress, displacement, etc. relations).

All the finite difference and finite element computer program consists of three main logical units: pre-processor, solver and post-processor. A compact description of the computational process is shown in Fig. 2.3.1.1. The three stages listed may be incorporated in a single computer program, or code, or may exist as a three distinct codes, which is more usual case.

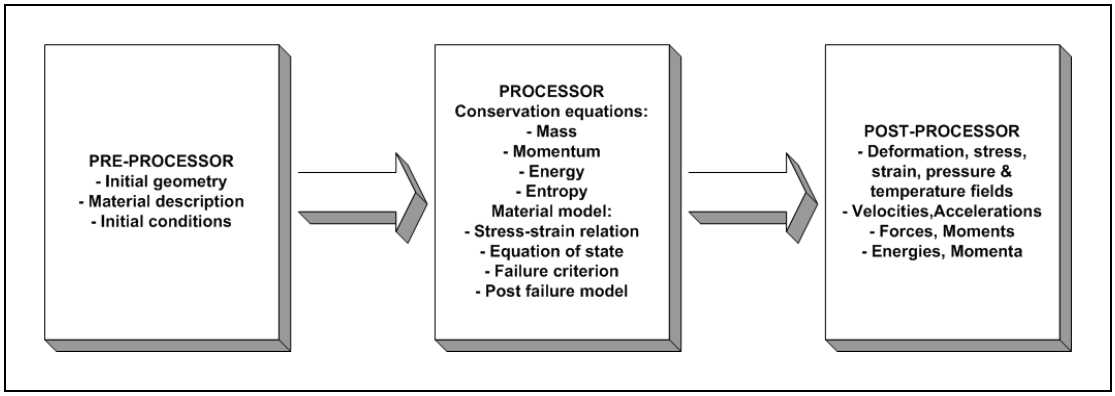

Fig. 2.3.1.1. Schematic representation of the computational process [15]

The pre-processor generally generates a detailed computational mesh for the geometry of interest from an abbreviated description provided by user. This information is coupled to a description of the materials making up the geometric bodies by specifying appropriate parameters for the equation of state, the stress-strain relationship used by the code in both elastic and plastic regimes, and the failure criteria to be used. A description of boundary and initial conditions ends this stage of the process.

The processor, where typically large amounts of computing time are spent, consists of several subroutines, each having a special purpose (calculate element matrix, equation of state, etc). The conservation laws for mass, momentum and energy, coupled to an equation of state for determination of pressures, a constitutive relationship, a failure criterion and post-failure model are cast into finite-difference or finite-element form and integrated in time in this phase, using information generated by the pre-processor.

Output of the computations is generally massive and can run into hundreds of megabytes or even gigabytes, which are difficult to read and interpret. Recourse is therefore made to post-processors, which are essentially computer programs that prepare displays of the items of interest. The graphical representation includes: mesh and contour plots of strain, stress, velocity, strain rate, pressure, temperature, etc. at given time.

2.3.2. Mesh descriptions

Hydrocodes differ in the approach they take to arrive at a solution, and a fundamental difference is in the use of Eulerian or Langrangian spatial discretisation. In Lagrangian coordinates, every point in the deformed body is referred to some reference state, and any discretisation, such as finite element mesh or finite difference zoning used in the analysis, deforms with the material. In Eulerian coordinates, however, the points are fixed in space and discretisation does not move with the material.

Using the Lagrangian method, mass inside the element remains constant and only the volume of the element changes as the material distorts. Because of the fact that the time step is controlled by the size of the smallest element, care should be taken that elements do not become too distorted, otherwise the iterative simulation can diverge. The main advantage of Langrangian approach is that the code is simpler and requires less computational time. Also, the boundary conditions can be more easily specified and history data are easily obtained. Important feature in Langrangian codes is their ability to model the contact interface between different materials.

Eulerian codes enable simulation of large distortions of material and because of that problems with large deformations can be simulated easily. A computational grid is fixed in space and code calculates the quantities that flow into and out of the cells. The main disadvantage of this type of the code compared to the Langrangian codes lies in the fact that it is very difficult to preserve distinct material boundaries.

Langrangian formulation is most appropriate for impact of solide bodies since the surfaces of the bodies will always coincide with discretization and are therefore well defined. The disadvantage is that the numerical mesh can become severely compressed and distorted in many problems [15]. This behaviour has a very adverse effect on the integration time step and accuracy.

2.3.3. Time integrating methods

The time stepping methods are the essence of most structural dynamics problems. There are basically two time integration methods outside of classical closed-form solutions available to analysis: implicit formulation and explicit formulation. The procedure for the discretized equation of motion is called explicit if the solution at some time $t + \Delta t$ in the computational cycle is based on the knowledge of the equilibrium condition at time t, and possibly at previous times. The advantage of using the explicit method is that there is no need to calculate stiffness and mass matrices for the complete system. Thus the solution can be carried out on the element level and relatively little storage is required. The drawback of the method is that it is conditionally stable in time, and the time step must be carefully chosen. The size of the time step must be sufficiently small to accurately treat the high-frequency modes that dominate the response in wave propagation problems.

In an implicit scheme, the solution at any time $t + \Delta t$ is obtained with knowledge of the accelerations at the same time. Implicit methods are unconditionally stable. However, such stability is obtained at the expense of solving a set of simultaneous equations at each time step. Time steps in implicit method can be much lager then in explicit method, but at the expense of progessivly lower time accuracy.

2.3.4. Discretization methods

It is necessary in a computer analysis to replace a continuous physical system by a discretized system. In the discretization process, a computational mesh replaces the continuum. The discretization techniques most commonly used are the finite difference, finite volume, boundary element and finite elements methods. In finite difference techniques, differential equations are approximated directly by replacing the derivatives by difference quotients. In the finite element method, the governing differential equations are first cast in an integral form and then solution is sought in the form of linear combination of algebraic polynomials defined over domain element. A common property of both techniques is the local separation of spatial dependence from time dependence of the dependent variable. This permits separate treatment of the space and time grids. Since there is no basic mathematical difference between the two methods they should have the same accuracy in numerical computation. The main difference lies not in the methods themselves, but in data-management structure of computer programs that implement them.

2.4. Summary

One of the main objectives of this research was development of new material model and implementation in computer code, and hence public domain version of Lagrangian finite element code DYNA3D [14] has been chosen as numerical test-bed. DYNA3D has been used together with TRUEGRID as pre-processor and TAURUS as a post-processor.

TRUEGRID has been used as a pre-processor, and this program tessellates a geometric model into hexahedron brick elements and quadrilateral shell elements. Each block is composed of 3D hexahedral, 2D quadrilateral, and 1D linear or quadratic elements arranged in rows, columns, and layers. It has been optimised to produce high quality, structured, multi-block hex meshes or grids and serves as a pre-processor to most popular analysis codes.

DYNA3D is a Lagrangian, nonlinear, explicit, three-dimensional finite element analysis code for structural/continuum mechanics problems, and it has been used as a platform for new material model development in this research. Due to its explicit nature, DYNA3D uses small time steps to integrate the equations of motion and is especially efficient for the solution of transient dynamic problems. DYNA3D's material library includes isotropic elastic, orthotropic elastic, elastic-plastic, orthotropic elastic-plastic, rate dependent elastic-plastic, and temperature dependent elastic-plastic, concrete, and rubber-like materials. Its element library includes solid, shell, beam, bar, spring and damper elements. DYNA3D also has various contact slideline options for different contact situations between two bodies.

TAURUS has been used as a post-processor, and it reads the binary plot files generated by the DYNA3D three-dimensional finite element analysis code and plots contours, time histories, and deformed shapes. Contours of a large number of quantities may be plotted on meshes consisting of plate, shell, and solid type elements. TAURUS can compute a variety of strain measures, reaction forces along constrained boundaries, and momentum. TAURUS has three phases: initialisation, geometry display with contouring, and time history processing.

Second important aspect of this work was development of relatively simple experimental methods for characterization of engineering materials, and extensive experimental work has been undertaken. Tensile test has been used for the characterisation of two aluminium alloys, at different levels of the strain rates and temperatures, and for three different orientations of materials. Taylor cylinder impact test was used as a validation experiment. Plate impact test has been used to determine the material properties at high strain rate, and to investigate damage evolution in impact-loaded materials. Details of experimental methods that have been used in this work are given in the following chapter.

3. EXPERIMENTAL WORK

3.1. Uniaxial tensile test

3.1.1. Purpose of test

The purpose of the proposed work is to perform a series of tensile tests on two aluminium alloys at varying strain rates and temperatures. The results from these tests will allow derivation of material constants for constitutive models and will lead to a better understanding of aluminium alloy behaviour. This was achieved through the design of experiments and data processing with final result in the form of input parameters for the material constitutive models.

Several tests are proposed in order to investigate different aspects that can influence material properties [20-23]. From material response at different temperatures and strain levels it is possible to identify the mechanism governing the deformation process. This allows the influence of individual mechanisms to be determined; this information is necessary to derive constants for complex models such as the MTS model.

Plastic deformation is controlled by the thermally activated interactions of dislocation with obstacles. In the thermally activated regime, the interaction for short distance obstacles are described by an Arrhenius expression, which relates strain-rate ($\dot{\varepsilon}$) to activation energy (ΔG) and temperature (T), of the form [55]:

$$\dot{\varepsilon} = \dot{\varepsilon}_0 \exp(\frac{-\Delta G}{kT}) \qquad (3.1.1.1.)$$

The strain rate and temperature are therefore interchangeable and different combinations will yield the same thermal activation energies. It was expected that under those circumstances, the overall mechanical response would be very similar as long as thermal-activated processes dominate deformation process.

Based on this idea, ranges of tensile test were performed in this work using Instron servo hydraulic fatigue machine, fitted wit environmental chamber. The tests were performed at temperatures between –50 and $+200^{o}C$ and at strain rates between $10^{-3}s^{-1}$ and $10^{1}s^{-1}$.

3.1.2. Measured variables

A standard tensile test is carried out by moving one end of specimen (via a machine crosshead) at a constant speed, v, while holding other end fixed. The primary variables recorded are *load* and *extension*. Load-extension variables depend on specimen size. Since we want to measure material properties, we normalize the measured variables to account for specimen size. The simplest way to do this is to normalize with respect to the original specimen geometry.

Engineering variables:

Engineering Stress $S = \frac{P}{A_0}$; (3.1.2.1.)

Engineering Strain $e = \frac{\Delta L}{L_0} = \frac{L_f - L_0}{L_0}$; (3.1.2.2.)

where A_0 is initial cross-sectional area, L_0 is gage length and P is measured force.

Engineering strain rate is defined as the rate at which strain increases. This quantity can be simply obtained by noting that all strain takes place in the deforming length, L_d, so that the crosshead speed, v, is the same as the extension rate of L_d:

$$\dot{e} = \frac{de}{dt} = \frac{dL_d / L_{d0}}{dt} = \frac{v}{L_{d0}} = \frac{crosshead\_speed}{defor\_length} \quad (3.1.2.3.)$$

If we normalize measured variables to current configuration we are able to calculate true variables.

We can express the total true strain as a simple integral:

$$\varepsilon = \int_{e_t=0}^{e_t} d\varepsilon = \int_{L_0}^{L_f} \frac{dl}{l} \text{ or } \varepsilon = \ln(L_f / L_0) \quad (3.1.2.4.)$$

Similarly, the real or "true" stress refers to the load divided by the current cross sectional area:

$$\sigma = \frac{P}{A} \quad (3.1.2.5.)$$

Exactly analogously to the definition of engineering strain rate, the true strain rate is defined as de/dt, and this rate is simply related to the crosshead speed:

$$\dot{\varepsilon} = \frac{d\varepsilon}{dt} = \frac{dL_d / L_d}{dt} = \frac{v}{L_d} = \frac{crosshead\_speed}{current\_defor\_length} \quad (3.1.2.6.)$$

If we assume that plastic deformation produces no net change in volume, or that plastic incompressibility can be applied, we can easily find following relationship between true and engineering variables as follows:

Relationship between the two strain measures:

$\varepsilon = \ln(1+e)$ or $e = \exp(\varepsilon) - 1$ (3.1.2.7.)

Relationship between the two stress measures:

$\sigma = S\exp(\varepsilon)$ or $S = \sigma\exp(-\varepsilon)$ (3.1.2.8.)

or, in terms of engineering strains

$\boldsymbol{\sigma} = \boldsymbol{S}(1+\boldsymbol{e})$. (3.1.2.9.)

3.1.3. Test specimen

Materials

Selected materials for this work were commercial aluminium alloys. Materials were supplied by Apollo Metals Corporation, as hot rolled plate form (1475mm x 1200 mm) for AA7010-T7651, and as rolled sheet form (2642 mm X 1270 mm) for AA 2024-T3.

The choice to characterise alloys instead of pure metals has resulted from current lack of available experimental data for anisotropic aluminium alloys loaded at various strain rates and temperatures.

Material AA7010-T7651 was supplied in 6.35 mm thick plate form with following chemical composition (in %): 0.04 Si, 0.08 Fe, 1.66 Cu, 0.01 Mn, 2.26 Mg, 0.78 Cr, 0.81 Ni, 6.08 Zn, 0.11 Zr, 0.03 Ti.

Material AA2024-T3 was supplied in 2.5 mm thick sheet plate form with following chemical composition (in %): 0.09 Si, 0.19 Fe, 4.71 Cu, 0.57 Mn, 1.38 Mg, 0.01 Cr, 0.06 Zn, 0.02 Ti, 0.02 V.

Selection of test specimen

Specimens were selected and prepared taking care not to influence reliable indication of the properties of materials [16-19]. In testing materials from metal plate, regard should be given to the direction of rolling, and for anisotropic characterization, tests were made on specimens which were cut parallel to the direction of rolling, on specimens which were cut perpendicular to the direction of rolling, and on specimens which were cut at the angle of 45^{o} in the respect to the direction of rolling.

For each strain rate, temperature was varied, and five temperature and strain rate levels were proposed. This is related to the analysis of isotropic characterization. For anisotropic case, three direction of anisotropy have been considered.

For each material the number of specimens was related to the number of specified tests and number of necessary repetitions, since each tensile test requires a new specimen, 3 repetitions per test were proposed to ensure accuracy of the experimental data.

Preparation of test specimen

In preparing specimens of plate, we have to satisfy requirement, that finished specimen does not contain any of the damage material.

The finished surface of specimen from shred blanks was at least 3 mm from shred surface and at least 6 mm from flame-cut faces.

Care was taken not to bend the piece, because working of the material tends to change its properties.

The finish cut on mechanical metal specimens was made by turning or milling and a fine enough surfaces were obtained.

Test specimen geometry

Two kinds of tensile specimens are generally used for tensile test [9-11]: a round bar for bulk material, and a flat specimen for sheet products. The **gauge length** of specimen refers to the distance between ends of an extension gage put on the specimen to measure extension between these points. The **deforming length** is the length of the specimen which undergoes plastic deformation during the test and this length may change but should always be significantly longer then the gauge length in order to ensure that deformation is fairly uniform over gage length.

ISO standard proportional flat specimen has geometry as follows: gage length is defined as $L_0 = 5.65 S_0^{1/2}$, where S_0 is the specimen cross-section, and the gauge length may be rounded off to the nearest 5 mm provided that the difference between the computed L_0 and that rounded length is less than 10% of L_0. Deforming length of specimen is defined with following relation $L_d = L_0 + 2S_0^{1/2}$.

As an alternative to the standard specimen geometry mentioned above, in this work non-standard specimen geometry was proposed, because one of the requirements for this test is achieving of intermediate strain rate conditions, using standard servo hydraulic fatigue machine. The dog bone specimen proposed for this work is shown in Fig 3.1.3.1.

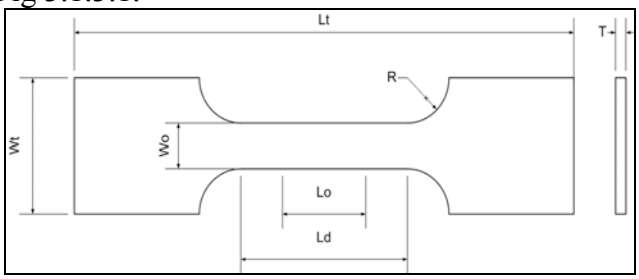

Fig 3.1.3.1. Flat (dog bone) tensile specimen

To determine specimen geometry a set of simulations has been done. A flat specimen subjected to axial loading was studied as a testing model for the initial determination of specimen geometry (Fig 3.1.3.2.).

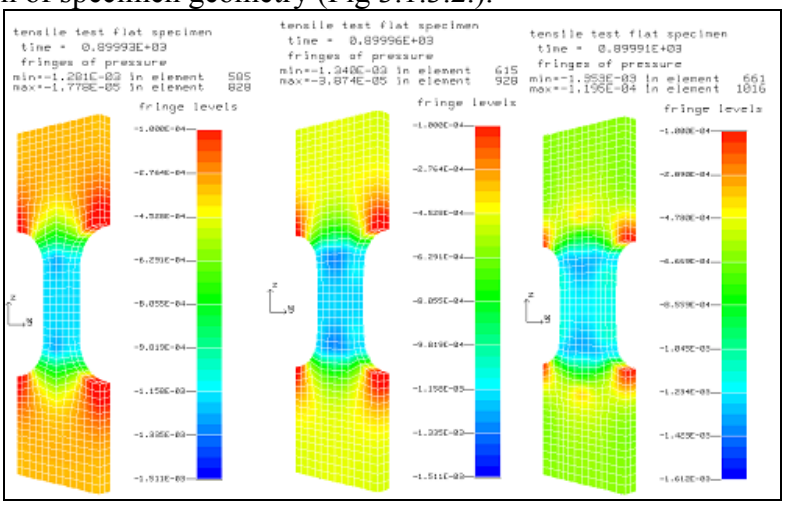

Fig. 3.1.3.2. FE simulation of tensile test for flat specimen

The same boundary conditions as those, which will be used for the experimental test, were imposed on the model, as a prescribed maximal velocity on the one end of specimen of 100 mm/s, and displacement boundary conditions on the

other end were chosen to simulate fixed end of specimen. Boundary conditions were applied on section of specimen, which represented beginig of grep region.

Taking into account limitations of available testing equipment, following geometrical parameters of tensile specimen were chosen for material AA7010: total length $Lt = 150mm$, total width $W_t = 20mm$, thickness $T = 6.35mm$, deforming length $L_d = 20$, gauge length $L_0 = 12.5mm$. Varied parameters for material AA7010 are shown in following table.

Case	I	II	III
R Radius [mm]	5	4	3
W_0 Gage width [mm]	10	12	14

Tab. 3.1.3.1. Varied geometrical parameters of flat test specimen for AA7010

On the basis of simulation, it was concluded that most uniform distribution of stresses corresponds to the specimen with $R = 5mm$ and $W_0 = 10mm$, and this geometry was adopted as an initial geometry for material AA7010.

Similar analysis was performed for the other material AA2024, and on the basis of simulations, geometrical similarity and requirements of existing equipment, same specimen geometry for both materials AA7010 and AA2024, was adopted as follows: total length $Lt = 170mm$, total width $W_t = 25.4mm$, deforming length $L_d = 20$, gauge length $L_0 = 12.5mm$, gage width $W_0 = 10mm$, radius $R = 8mm$, thickness of specimen for AA2024 $T = 2.5mm$ and thickness of specimen for AA7010 $T = 6.35mm$.

3.1.4. Testing apparatus

The selection of apparatus for particular test involves consideration of: the purpose of the test, the accuracy required, availability and economy. On the basis of above criterions following equipment was chosen:

Testing machine:

Instron 8032 Servo hydraulic fatigue machine, supplied with Instron 8500 controlling electronics, and with the following characteristics: 100 kN actuator with 109 kN stall force, 45 litres/minute manifold, 1 litre pressure line accumulator and 40 litres/min servo valve. This test machine can provide a maximum steady-state velocity of 80 mm/s (Fig. 3.1.4.1.).

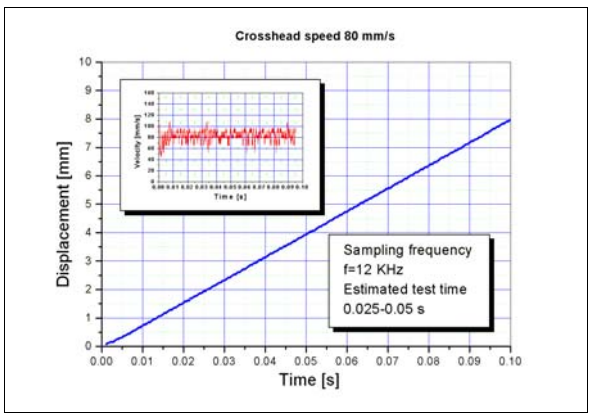

Fig. 3.1.4.1. Characteristic of Instron 8032 Servo hydraulic machine

Environmental chamber:

Instron SFL 3339-406 temperature chamber, supplied with digital control handset Eurotherm 2408, with following characteristics: temperature range: $-70^{o}C$ to $+250^{o}C$, temperature stability $\pm 2^{o}C$.

This temperature chamber can provide a means of carrying out materials test in accurately controlled air temperature environment. Chamber is equipped wit LN2 cooling module, which is required for testing at temperatures below ambient temperature (Fig. 3.1.4.2.).

Fig. 3.1.4.2.100 KN Servo Hydraulic Fatigue Machine with maximal steady-state velocity of 80 mm/s

LN2 supply:

Wessington PV-120 liquid nitrogen storage vessel with following characteristics: capacity: 120 ltr, max working pressure 4.5 bar, static evaporation rate 1.2% per day. Liquid nitrogen is maintained at $-196^{o}C$ in an insulated Dewar flask, which is pressure relived at no more than 1.5 bars.

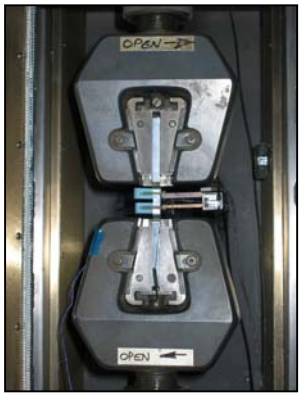

Extensometer:

Instron 2620-602 dynamic strain gauge extensometer, which is designed for use with metals, composites and other materials, exhibiting total strains up to $\pm 20\%$ of the original gauge length. Application of this extensometer include, wide operating temperature range, from $-80^{o}C$ to $+200^{o}C$.

Fig. 3.1.4.3. Dynamic strain gage extensometer mounted on the dog bone specimen

3.1.5. Measurements

For all tests, 3 items are measured and recorded with maximal sampling frequency of 12 kHz, for the calculation of material properties:

- The load that gives access to the stress in the specimen, measured by load cell, which is fitted as a standard to testing machine.
- The position of the crosshead that gives elongation of the free length of the specimen.
- The longitudinal strain measured by mechanical extensometer capable for measurements of strain on the elevated and reduced temperatures.

Fig. 3.1.5.1. Data Logger with maximal sampling frequency of 12 kHz/channel

The temperature is measured with one Inconel sheathed 3 mm diameter type K thermocouple, which is fitted as a standard to temperature chamber, and positioned with its junction at the centre of the return air grid at the centre of the baffle.

3.1.6. Test matrix

Following table (Tab. 3.1.6.1.) represents proposed test matrix with maximal practical achievable ranges for temperature and crosshead speed.

Temperature ---------- Crosshead speed	-50° C	0°C	+70°C	+140°C	+200°C
0.008 mm/s	AA2024 AA7010	AA2024 AA7010	AA2024 AA7010	AA2024 AA7010	AA2024 AA7010
0.08 mm/s	AA2024 AA7010	AA2024 AA7010	AA2024 AA7010	AA2024 AA7010	AA2024 AA7010
0.8 mm/s	AA2024 AA7010	AA2024 AA7010	AA2024 AA7010	AA2024 AA7010	AA2024 AA7010
8 mm/s	AA2024 AA7010	AA2024 AA7010	AA2024 AA7010	AA2024 AA7010	AA2024 AA7010
80 mm/s	AA2024 AA7010	AA2024 AA7010	AA2024 AA7010	AA2024 AA7010	AA2024 AA7010

Tab. 3.1.6.1. Test matrix for tensile test

On the basis of specifications of mechanical properties for AA2024-T3 (Tensile strength R=452-463 MPa, Elongation A=18-20 %) and AA7010-T7651 (Tensile strength R=546-556 MPa, Elongation A=11-12 %), tensile test parameters are adopted and summarized in the following table (Tab. 3.1.6.2.).

Material	Crosshead speed [mm/s]	Engineering strain rate [1/s]	Sampling frequency [Hz]	Estimated test time [s]	Number of samples
AA7010	0.008	6.4×10^{-4}	2	500	1000
AA2024				250	500
AA7010	0.08	6.4×10^{-3}	20	50	1000
AA2024				25	500
AA7010	0.8	6.4×10^{-2}	200	5.0	1000
AA2024				2.5	500
AA7010	8	6.4×10^{-1}	2000	0.50	1000
AA2024				0.25	500
AA7010	80	6.4×10^{0}	12000	0.050	600
AA2024				0.025	300

Tab. 3.1.6.2. Tensile test parameters

Specimens and tests were named with a set of 8 characters/numbers following the hereafter definition:

- ***Character 1*** **:** 2 → Material AA2024
  7 → Material AA7010
- ***Character 2*** **:** L → $\alpha = 45^o$ (L direction)
  T → $\alpha = 45^o$ (LT direction)
  D → $\alpha = 45^o$
- ***Character 3&4&5*** **:** 8M3 → Test speed 0.008 mm/s
  8M2 → Test speed 0.08 mm/s
  8M1 → Test speed 0.8 mm/s
  8P0 → Test speed 8 mm/s
  8P1 → Test speed 80 mm/s
- ***Character 6&7*** **:** M5 → Test temperature -50°C
  00 → Test temperature 0°C
  P7 → Test temperature +70°C
  14 → Test temperature +140°C
  20 → Test temperature +200°C
- ***Character 8*** **:** N → Specimen number

Figures 3.1.6.1. a-c and Fig 3.1.6.2. a-c show photographs of typical tensile specimens used in this project.

Fig. 3.1.6.1. a-c shows AA7010 specimens: a) before, b) after the deformation of $\varepsilon = 20.5$, and c) fractured specimen, tested at 140^0 C and 6.4×10^{-4} s^{-1}.

Examples of the specimens for AA2024 are shown in Fig. 3.1.6.2. : a) before testing, b) deformed with elongation of $\varepsilon = 20.5$, and c) fractured specimen tested at tested at 0^0 C and 6.4×10^{-4} s^{-1}.

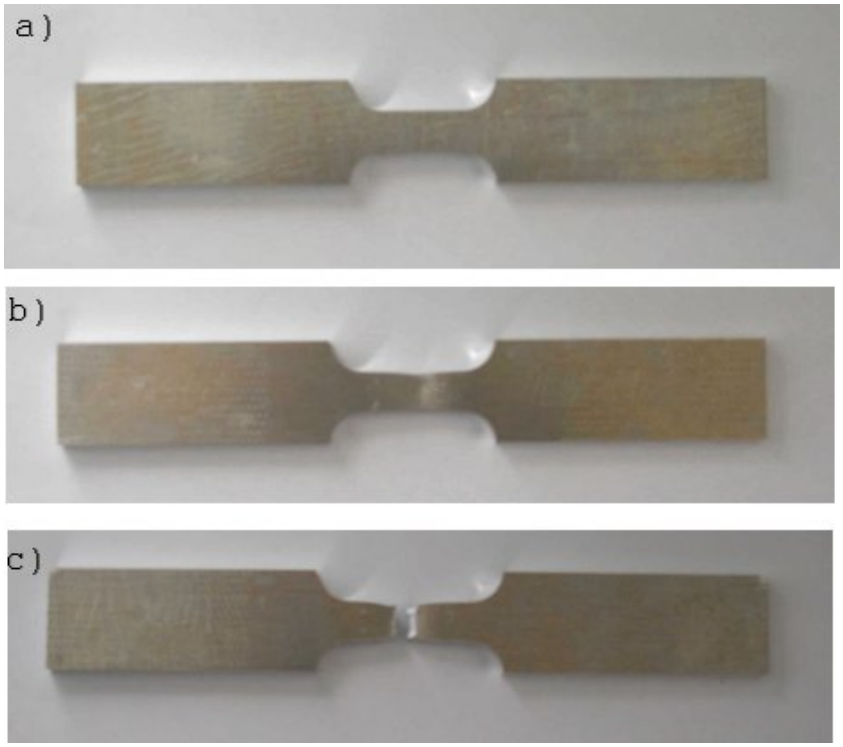

Fig. 3.1.6.1. Tensile specimens for material AA7010: a) Untested flat tensile specimen for material AA7010LT, b) Specimen 7L8M3142 with elongation of $\varepsilon = 20.5$, tested at 140^0 C and 6.4x 10^{-4} s^{-1}, c) Fractured tensile specimen 7L8M3141 tested at 140^0 C and 6.4x 10^{-4} s^{-1}

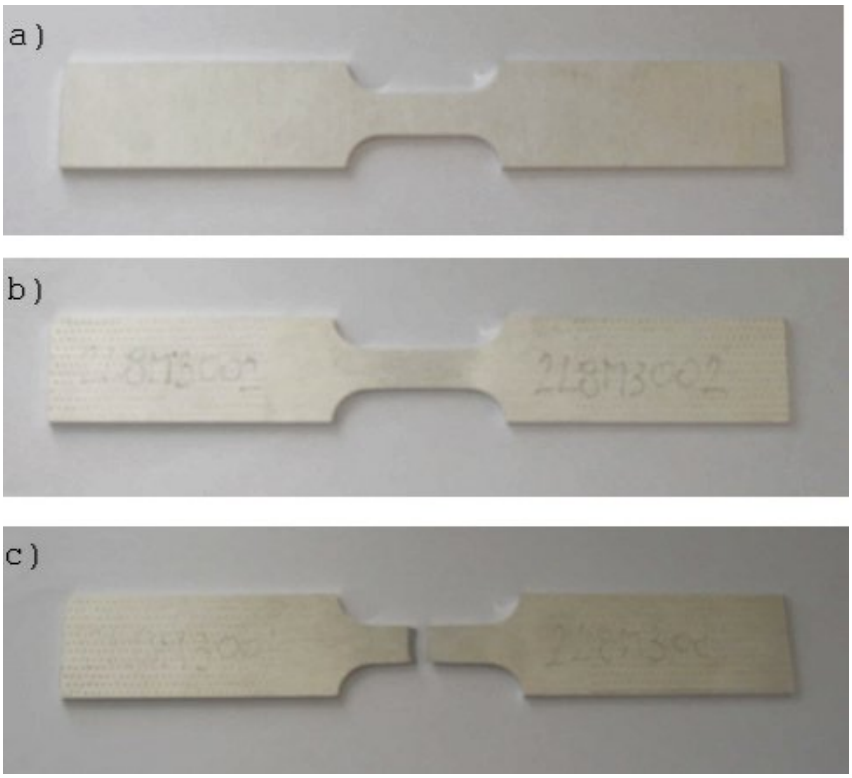

Fig. 3.1.6.2. Tensile specimens for material AA2024: a) Untested flat tensile specimen for material AA2024LT, b) Specimen 2L8M3002 with elongation of $\varepsilon = 20.5$, tested at 0^0 C and 6.4x 10^{-4} s^{-1} , c) Fractured tensile specimen 2L8M3001 tested at 0^0 C and 6.4x 10^{-4} s^{-1}

3.1.7. Tensile test results

Figures Fig. 3.1.7.1. and Fig. 3.1.7.2. show a classical strain rate dependant response for AA7010. The effects of strain rate and temperature are clearly observed since the difference in the flow stress between the different strain rates and temperatures are distinct and significant.

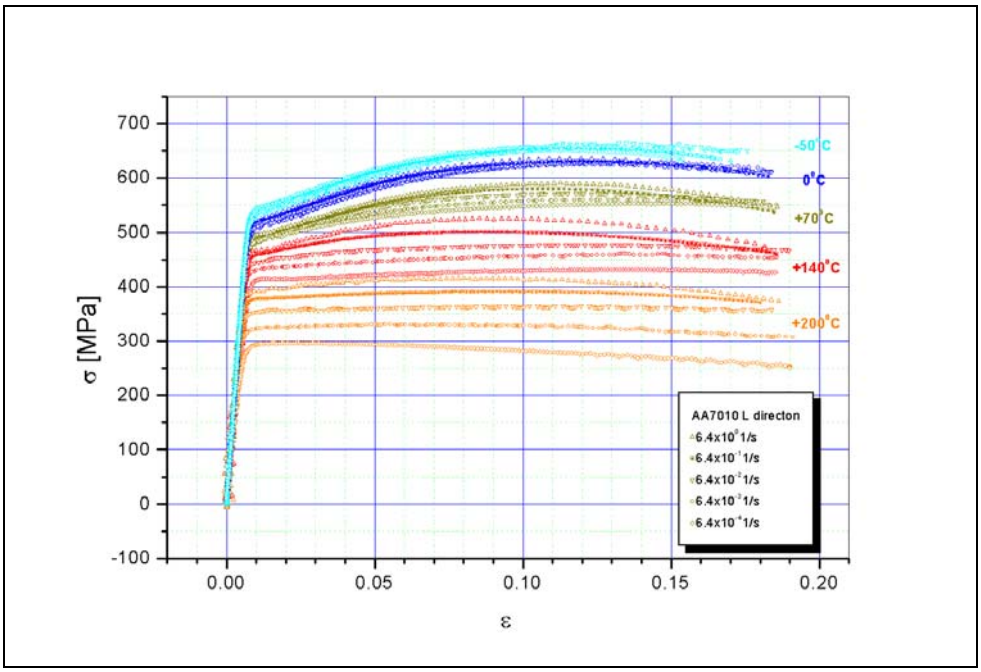

Fig. 3.1.7.1. AA7010 stress-strain curves for L direction at different strain rates and temperatures

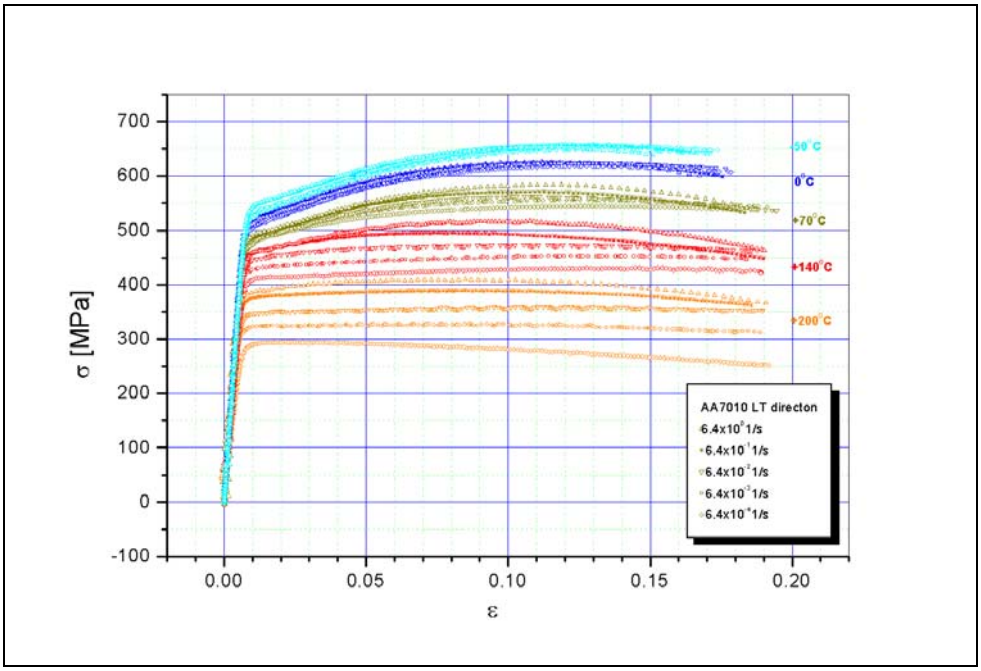

Fig. 3.1.7.2. AA7010 stress-strain curves for LT direction at different strain rates and temperatures

Figures Fig. 3.1.7.3. and Fig. 3.1.7.4. show stress-strain response for AA2024.The AA2024 is not strain rate dependant, but effects of temperature is clearly observed.

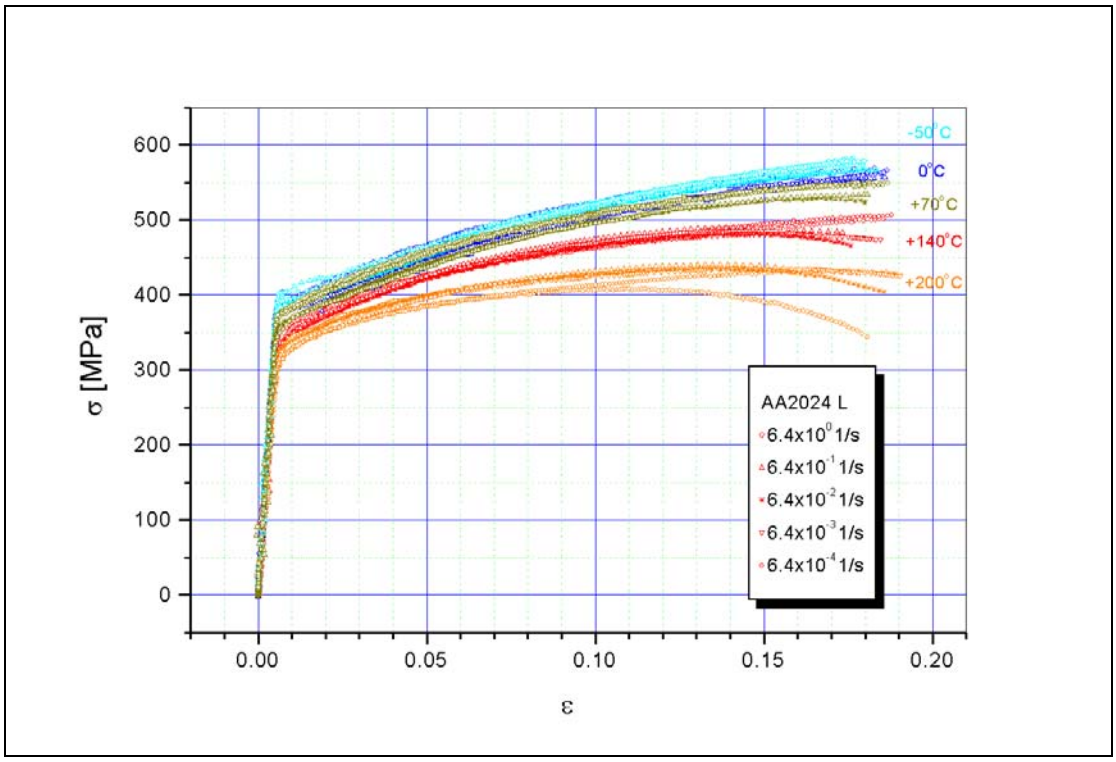

Fig. 3.1.7.3. AA2024 stress-strain curves for L direction at different strain rates and temperatures

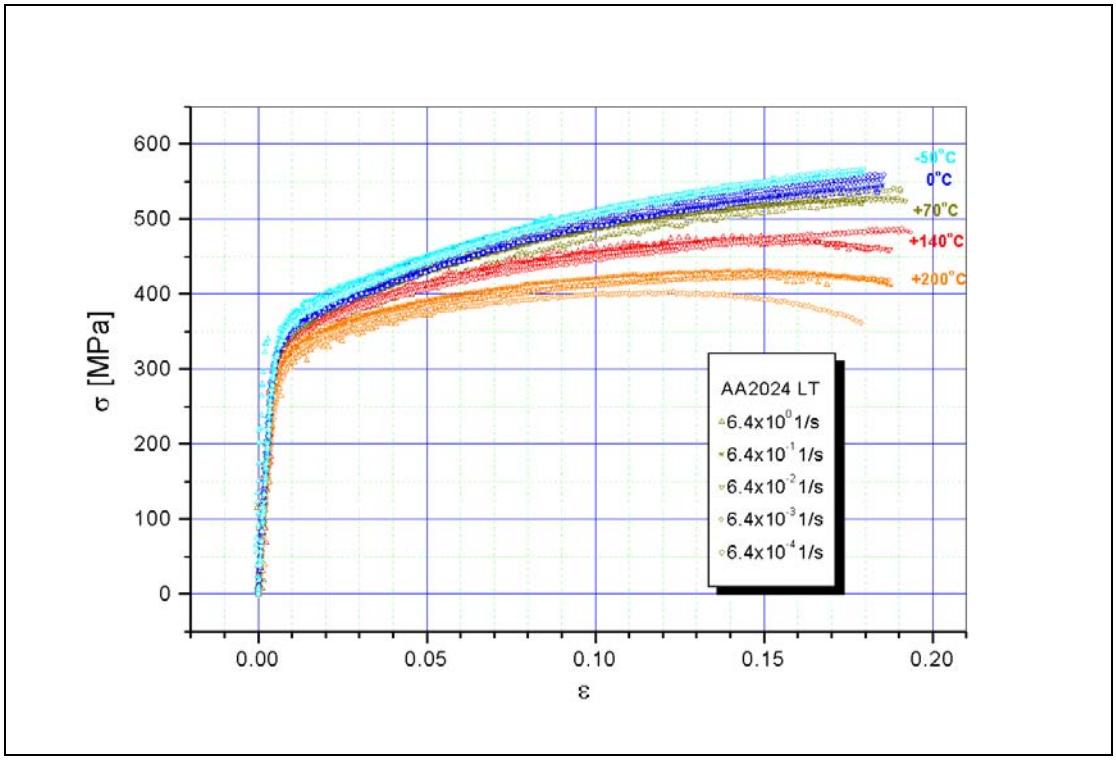

Fig. 3.1.7.4. AA2024 stress-strain curves for LT direction at different strain rates and temperatures

Typical stress-strain plots for aluminium alloy AA2024 and AA7010 from tensile tests performed at $+70^{o}C$ and at the strain rate of $\dot{\varepsilon} = 6.4x10^{-4}s^{-1}$ for three different specimen orientations at 0^{o}, 45^{o} and 90^{o}, are presented in Fig. 3.1.7.5. and Fig. 3.1.7.6.

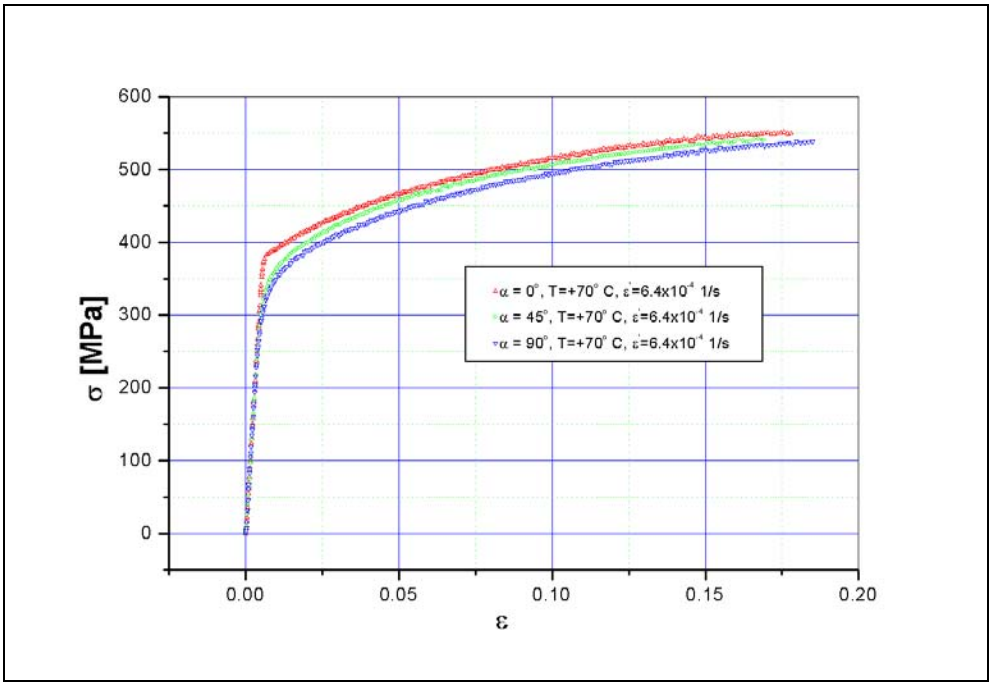

Fig. 3.1.7.5. Stress-strain response for AA2024 at $+70^{0}$ C and $\dot{\varepsilon} = 6.4x10^{-4}s^{-1}$

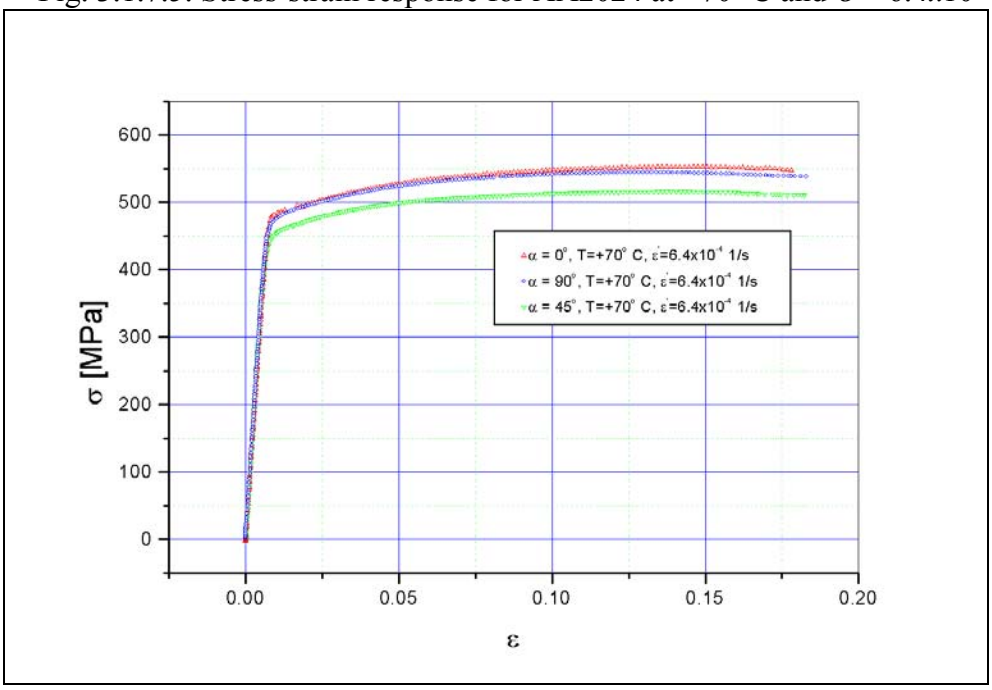

Fig. 3.1.7.6. Stress-strain response for AA7010 at $+70^{0}$ C and $\dot{\varepsilon} = 6.4x10^{-4}s^{-1}$

Stress-strain plots for aluminium alloys AA2024 and AA7010 from tensile tests performed at $+70^{o}C$ in the strain rate range from $\dot{\varepsilon} = 6.4x10^{-4}s^{-1}$ to $\dot{\varepsilon} = 6.4x10^{0}s^{-1}$ for three different specimen orientations at 0^{o}, 45^{o} and 90^{o}, are presented in Appendix A.

3.2. Taylor cylinder impact test

3.2.1. Purpose of test

The Taylor test is a dynamic compression test, which was originally developed to estimate the high strain rate compressive flow stresses of ductile materials and to compare their dynamic compression failure properties. Its main use at present is the validation of high-strain rate constitutive models, by comparing the shapes of recovered cylinders with computer predictions [24-27]. High-speed photography is essential for checking models if viscoelastic materials such as polymers or polymer-bonded explosives are being studied.

G.I. Taylor proposed original cylinder impact test [12]. His method consists of firing a solid cylinder of the material against a massive, rigid target. The dynamic flow stress of the cylinder material can be estimated by measuring the overall length of the impacted cylinder and the length of the undeformed (rear) section of the projectile by means of the following simple formula:

$$\sigma = \frac{\rho V^2 (l - H)}{2(l - l_1)\ln(l / H)} \qquad (3.2.1.1.)$$

where σ is the dynamic yield stress of the material of the projectile, ρ density, V its impact velocity, l initial height and l_1, H are defined in figure Fig. 3.2.1.1.

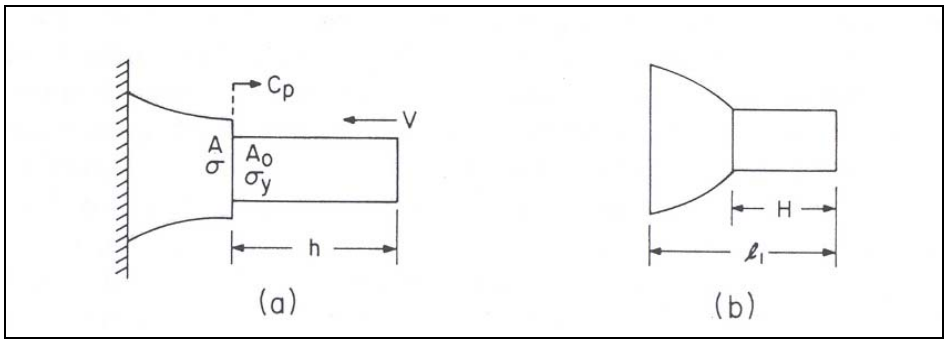

Fig. 3.2.1.1. Schematic diagram of a Taylor impact specimen during deformation and final state

Taylor used a very simple analysis that assumed rigid, perfectly plastic material behaviour and simple one-dimensional wave-propagation concepts. He assumed that deformed region is propagating away from the rigid wall at a velocity C_p, while the undeformed portion of the cylinder whose instantaneous length is h is travelling at a decreasing velocity v. It is assumed that the material behaviour is rate-independent, $\sigma = \sigma(\varepsilon)$, and rigid-plastic, that is elastic strains are negligible.

However, the Taylor test, or variants such as rod-on-rod impact, have been used and developed to the present day. It has not often been used to obtain dynamic yield stresses of materials but for studying (a) the propagation of plastic waves, and (b) for checking constitutive models by comparing the shapes of recovered cylinders

with computer predictions. It has also been used for its original purpose in obtaining the dynamic properties of (a) polymers at room temperature, (b) metals at elevated temperatures and (c) energetic materials.

The most common experimental arrangement for this test consists of firing a cylindrical rod specimen against a rigid target. Very high strain rates (10^3 to 10^5 s^{-1}), with a three-dimensional stress-state, are reached near the impact face. The impacted end deforms plastically into a mushroom-shape, while the other end remains undeformed plastically. The plastically deformed region may reach high levels of strain (exceeding 0.6 for ductile materials). An increasingly widely used variant on this test is the symmetrical Taylor test where a rod of material is fired end-on and coaxially at a rod of identical material and diameter.

High strain rate constitutive models are used in numerical codes for the modelling of dynamic deformation of structures. They are normally derived using data from well-defined constant strain rate techniques such as Hopkinson bars or plate impact. It is important to note that the Taylor test alone cannot be used to derive such constitutive models. However, it is proving to be a sensitive test of their validity.

To conclude, we can recognize two basic types of Taylor test:

- The original configuration, where a single rod is fired against a rigid target. A variant on this is the 'reverse-ballistic' Taylor test where the target is fired at a stationary cylinder. This is particularly useful if it is desired to study the properties of materials at temperatures other than ambient.
- The symmetric test, where a rod is fired end-on and coaxially at a rod of identical material and diameter. This test is more complex to perform, but is recommended for dynamic failure evaluations and for highly rate sensitive materials because of the lack of friction on the impact face.

3.2.2. Material description and experiment

Taylor cylinder specimens were cut out from AA7010 rolled plate. These specimens were 9.30 mm diameter cylinders with length 46.50 mm giving the length-to-diameter ratio L/D=5. A laboratory test frame (X, Y, Z) representing the principal axes of impact test is adopted such that compressive impact loading is always applied along X-axsis. The X direction was the original rolling direction for this plate (Fig 3.2.2.1.).

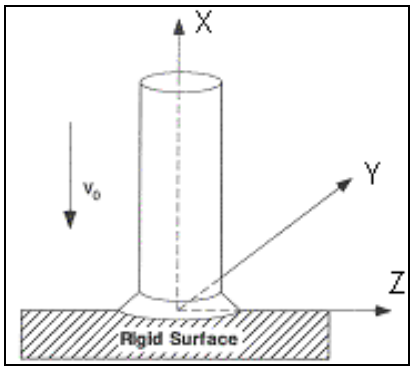

Fig. 3.2.2.1. Principal axes of the Taylor impact test

Several Taylor tests were conducted at Royal Military College of Science Shrivenham, where cylinders were launched at velocities of 200, 214, 244, 400 m/s, using a smooth-bore launch tube (Fig. 3.2.2.2.).

Fig. 3.2.2.2. Gas gun facility at Royal Military College of Science - Shrivenham

Figures, Fig 3.2.2.3. and Fig 3.2.2.4., present photographs of side profiles for the velocities of 200 m/s and 214 m/s, respectively, along with the footprints from a typical post-impact specimen.

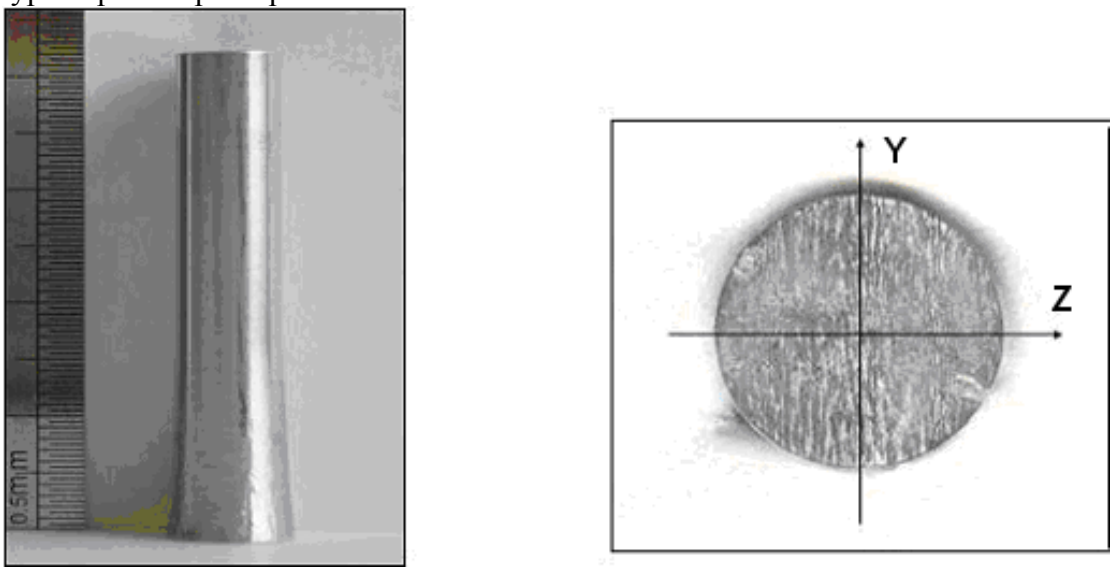

Side Profile Footprint

Fig. 3.2.2.3. Photographs of the post-test geometry for the AA 7010 Taylor specimen V=200 m/s

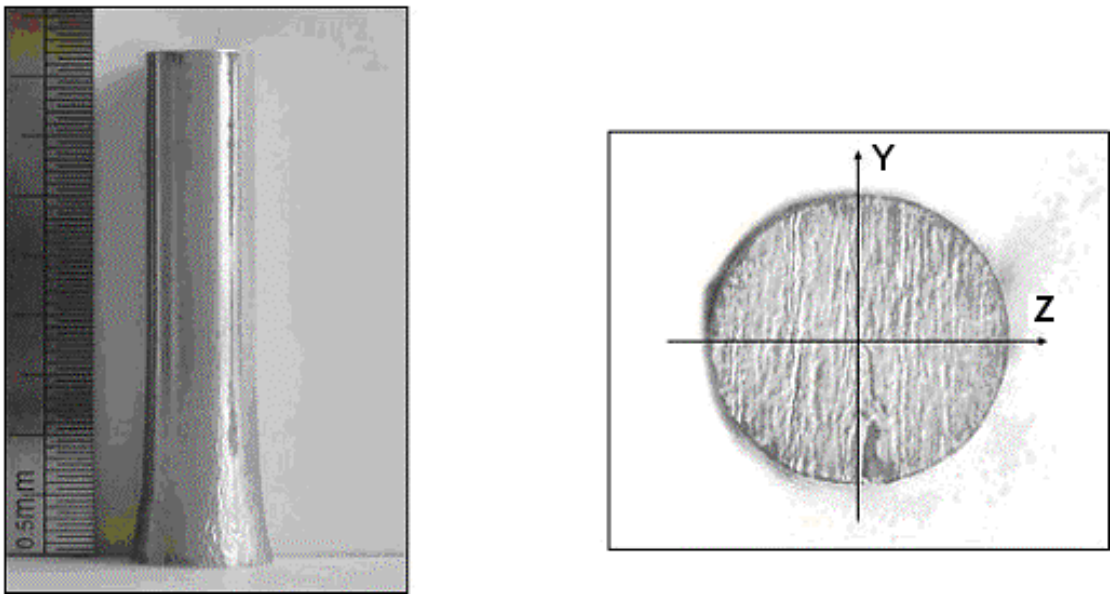

Side Profile Footprint

Fig. 3.2.2.4. Photographs of the post-test geometry for the AA 7010 Taylor specimen V=214 m/s

Photographs show that asymmetric footprints have an eccentricity (ratio of major [0 deg and 180 deg] to minor diameters [90 deg and 270 deg]).

Figure, Fig 3.2.2.5. presents photographs of side profiles for the velocities of 244 m/s and 400 m/s, respectively. These specimens experienced multiple fractures at the impact end, and they have not been used for further analysis.

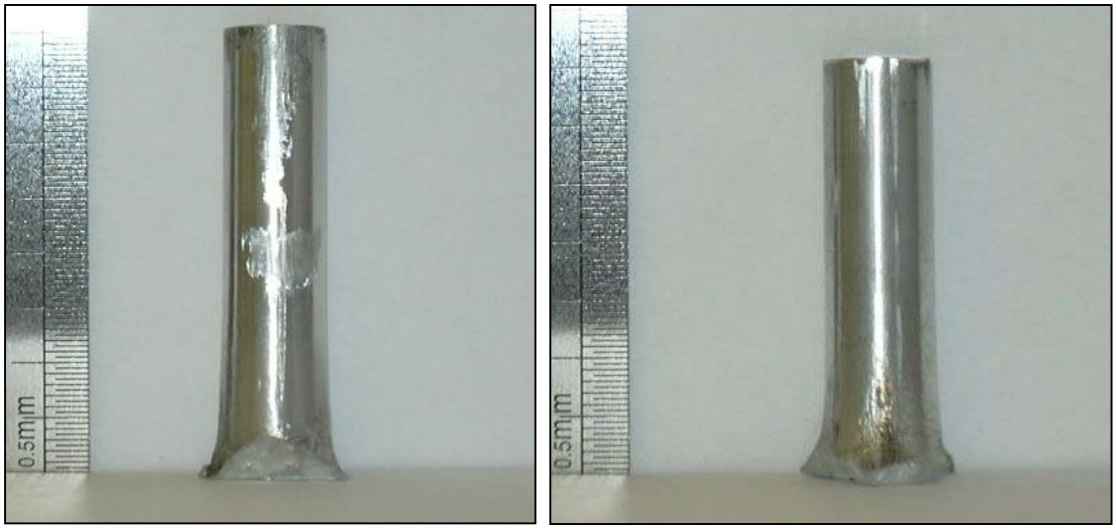

V=244 m/s V=400 m/s

Fig. 3.2.2.5. Photograph of the post-test side profile geometry for the AA 7010 Taylor specimens

3.2.3. Taylor test results

After testing, geometric profile data (Fig. 3.2.3.2.) for deformed specimens were generated using an 3D scanning machine (Fig. 3.2.3.1.). The data consist of digitised side profiles for minor and major dimension, and digitised footprints that give Y-Z cross-sectional area at the impact interface.

Fig. 3.2.3.1. 3D Scanning machine

Final specimen heights are: 42.2 mm for specimen impacted at 200 m/s, and 42.1 mm for specimen impacted at 214 m/s.

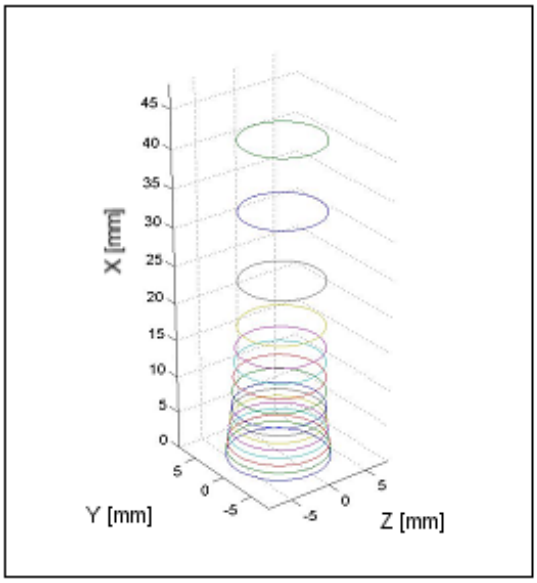

V=200 m/s

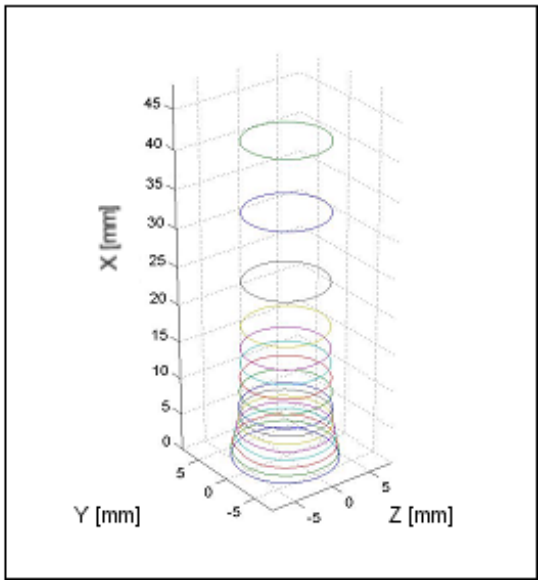

V=214m/s

Fig. 3.2.3.2. 3D Scan of post-test geometry for the AA 7010 Taylor specimen

Figures Fig. 3.2.3.3. and Fig. 3.2.3.4. show Taylor cylinder digitised major and minor side profiles, impacted with velocities of 200 m/s and 214 m/s respectively, and Fig. 18 shows comparison of minor and major side profiles of post-test geometry plotted as radial strain vs. distance.

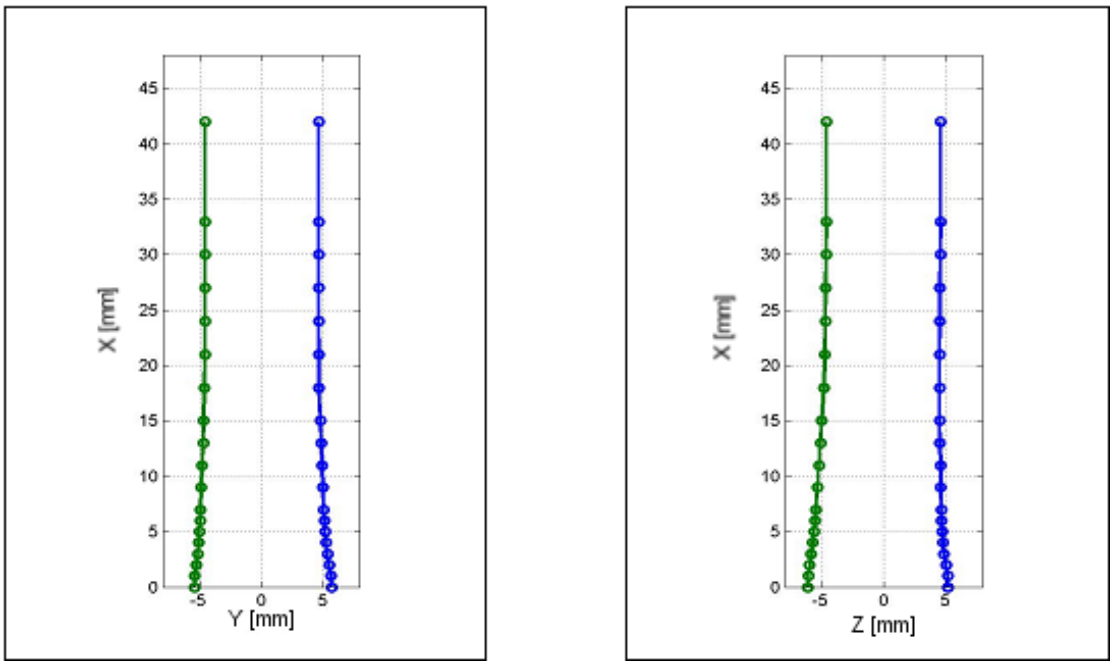

Minor profile Major profile

Fig. 3.2.3.3. Digitised minor and major side profile of post-test geometry for the AA 7010 Taylor specimen (V=200 m/s)

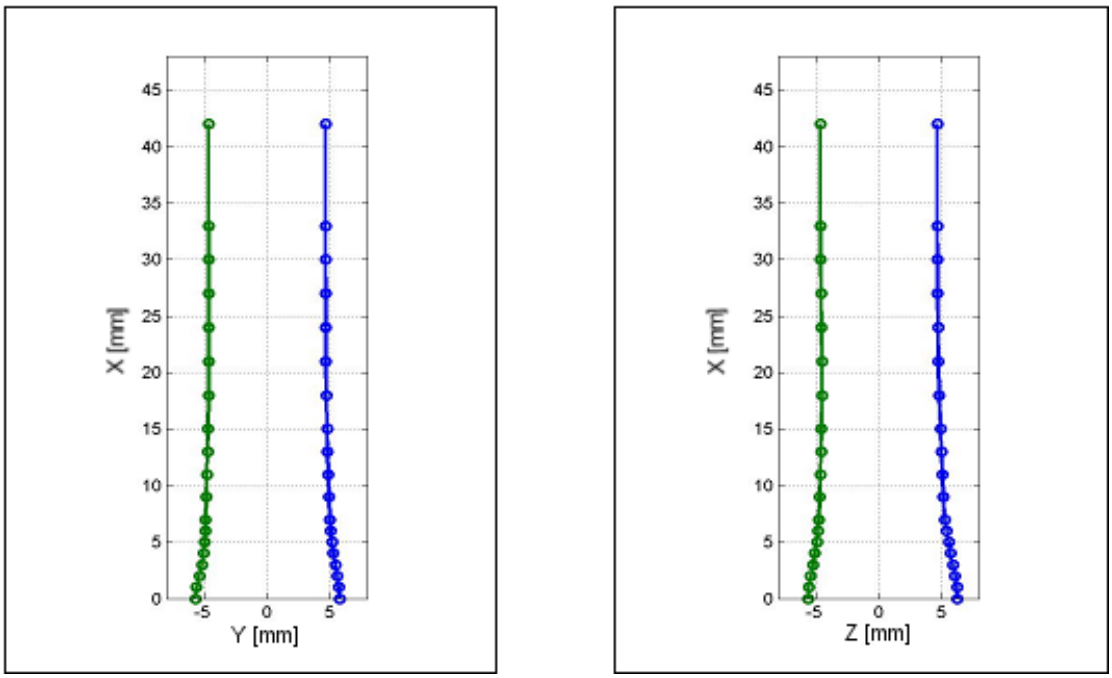

Minor profile Major profile

Fig. 3.2.3.4. Digitised minor and major side profile of post-test geometry for the AA 7010 Taylor specimen (V=214 m/s)

Figure Fig 3.2.3.5. shows digitised footprints of post-test geometries for Taylor specimens. Eccentricity (ratio of major to minor diameters) for the specimen impacted at 200 m/s is 1.04, and eccentricity (ratio of major to minor diameters) for specimen impacted at 214 m/s is 1.06.

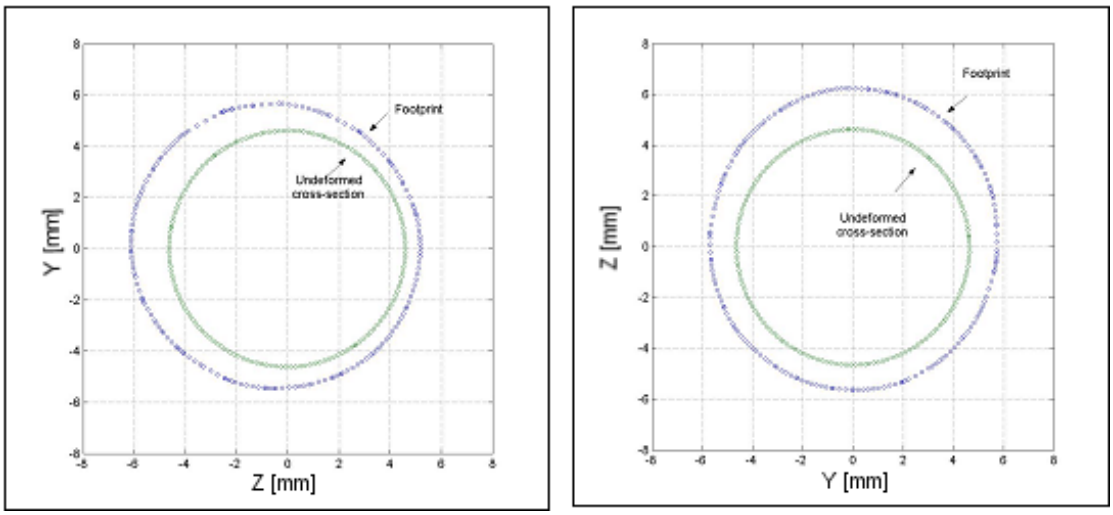

V=200 m/s V=214 m/s

Fig. 3.2.3.5. Digitised footprint of post-test geometry for the AA 7010 Taylor specimen

Figure Fig. 3.2.3.6. shows Taylor cylinders digitised major and minor side profiles, and comparison of minor and major side profiles of post-test geometry for Taylor specimens impacted at 200 m/s and 214 m/s.

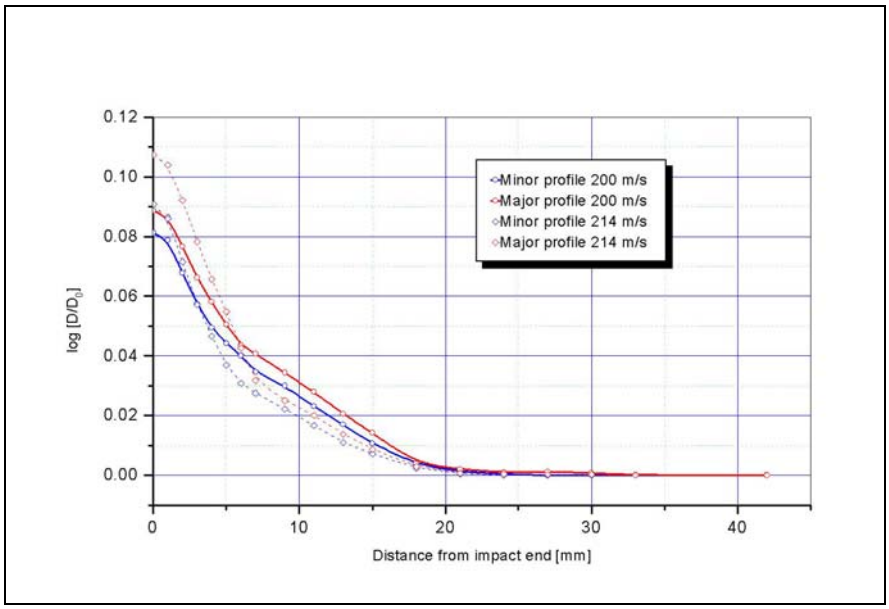

Fig. 3.2.3.6. Comparison of the major and minor side profiles of post-test geometry for the AA 7010 Taylor specimens impacted at 200 and 214 m/s plotted as radial strain vs. distance

3.3. Plate impact test

3.3.1. Purpose of the test

One of the experimental configurations used to study fracturing under dynamic conditions involves impacting a flyer plate against a target specimen of the same or different material. This experiment is known as plate impact test [28-30]. Any impact, at any speed, results in the propagation of stress waves through a solid. Since the stress waves propagate at finite speed, which is a material property, gradients in strain or stress will exist in both space and time. The superposition of two waves in the target plate, incident and reflected, sets material in tension and causes damage leading to spallation.

The incident wave is purely elastic when the stress amplitude is below the Hugoniot Elastic Limit (σ_{HEL}). If the impact velocity, V_0, is high enough, the HEL is exceeded causing the elastic precursor and slower plastic compressive waves to propagate toward the free surface of the target.

Measurement of free surface velocity, V_{fs}^{HEL}, immediately behind the elastic precursor wave front gives us the Hugoniot Elastic Limit as:

$$\sigma_{HEL} = \frac{1}{2}\rho C_l V_{fs}^{HEL} \qquad (3.3.1.1.)$$

The Hugoniot Elastic Limit is related to the dynamic yield strength as;

$$\sigma_{HEL} = \left(\frac{1-2\nu}{1-\nu}\right)\sigma_0 \qquad (3.3.1.2.)$$

where ν is the Poisson's ratio, and σ_0 is the yield limit in uniaxial stress conditions.

Therefore, firstly an elastic precursor propagates with the elastic wave speed:

$$C_1 = \sqrt{\frac{E(1-\nu)}{\rho(1+\nu)(1-2\nu)}}, \qquad (3.3.1.3.)$$

which is followed by a family of plastic waves propagating with different speeds:

$$C_p(\varepsilon_p) = \sqrt{\frac{1}{\rho}\frac{d\sigma}{d\varepsilon_p}}, \qquad (3.3.1.4.)$$

where ε_p is the plastic strain. At the same time, the identical waves propagate in the flyer. The elastic-plastic incident wave is reflected at the target free surface as a tensile wave. After superposition of these waves in the middle of specimen, the material is loaded in tension. The standard phase diagram corresponding to the plate impact experiment is shown in Fig. 3.3.1.1.

A typical experimental configuration consists of a flat flyer plate of thickness $L_i = h$, which is launched at velocity V_0. Flyer strikes a stationary target of thickness larger then Li, typically $L_c = 2h$. For symmetric impact, that is the target and the flyer plates made of the same material, symmetric compressive waves are generated

in the target and in the flayer. Reflection of the compressive incident wave from free surface of the target produces a tensile stress wave. At the distance h from the free surface a high tensile stress occurs before the arrival of release wave from the edges of the plate. The compressive wave in the flayer plate is reflected by the free surface as a tensile wave and returns to the impact surface. The time of contact is $t_c = 2h/C_1$. Consequently, duration of the tensile wave generated in the target is t_c. If the magnitude and duration of this tensile stress wave are high enough, spallation occurs, and a new free surface is created inside the target plate. The stress amplitude of the incident wave can be obtained from relation $\sigma = \rho C_1 V$, where V is the velocity. This is so-called acoustic approximation used frequently to analyse test data near HEL.

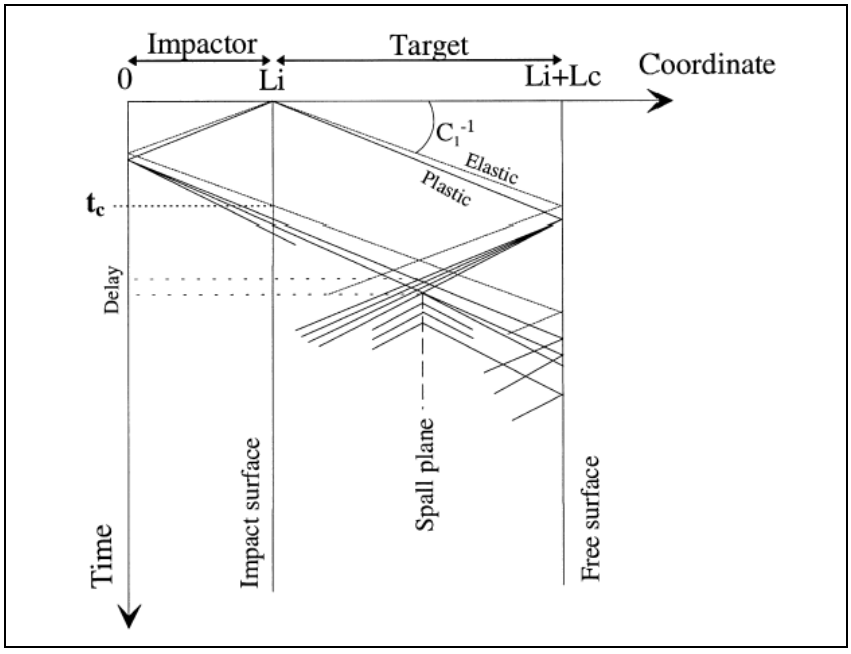

Fig. 3.3.1.1. Characteristics for plate impact experiment

When spalling initiates, the release waves emitted from the newly created free surfaces completely change the pattern of waves inside the target plate. Part of the pressure release wave from the flyer plate back surface, which passed the area where the spallation occurs will reach the target plate's rear surface and reduce the free surface speed. The creation of the spall plane reduces tension stress inside material to zero. This release propagates as a tension stress release wave through the sample and finally also reaches the rear surface. Due to the nature of this wave, it causes a new velocity increase of the material and thus of the rear surface. The pull-out speed or stress measured after spalling at the free surface of the target is frequently used to analyse spall dynamics. From the amount of the speed reduction the spall strength (dynamic tension strength) can be determined.

3.3.2. Experimental

For flyer plate investigations, 10 mm thick OFHC Cu sample was impacted by OFHC Cu flyer plate 5 mm in thickness with the impact velocity of 304 m/s. Target was machined into circular plate 70 mm in diameter, and diameter of flyer was 50mm. Manganin stress gauge was supported on the back of the target with 12 mm block of

polymethylmethacrylate (PMMA). The geometry of the target and the impactor was chosen so that the reflected wave completely released from target and flayer would interact in the centre of the OFHC Cu plate. In such a configuration, the response time of the gauge is approximately 20 ns, due to the close impedance matching of the PMMA, epoxy gauge backing and the epoxy adhesive used to assemble the target assemblies. Thus, the response time of the gauge is minimised and fine detailes in the wave profile can be resolved.

The experiment was performed with a single-stage gas gun at Shrivenham by 3rd party. The specimen was softly recovered with a specially designed catcher to prevent any secondary damage.

This experimental technique is very useful and clean in comparison to explosive loading because the speed and planarity of impact can be precisely controlled to obtain an uniaxial state of deformation inside the target. In addition, an advancement of spalling can be stopped at different levels: incipient, intermediate and complete by using different flayer/target geometries and impact velocities.

The velocity was measured via the shorting of sequentially mounted pairs of pins to an accuracy of approximately 0.1%. Specimen alignment was better then 1 miliradian. The gun is sufficiently accurate that control of the pressure in the breech allowed the speeds to be repeated to $\pm$ 1 m/s.

Measured stress-time history with a gauge in spalled OFHC Cu specimen is shown in Fig. 3.3.2.1. It shows clearly the loading plateau and the signal of spallation. The stress has been measured in PMMA since the gauge was supported on the back of the target with 12 mm block of this material. The stress has been converted to in-material value σ_x using well-known relation [34]:

$$\sigma_x = \frac{Z_x + Z_p}{2Z_p}\sigma_p \qquad (3.3.2.1.)$$

Here σ_p is the stress measured in the PMMA, and Z_x and Z_p are the shock impendances of the specimen and the PMMA, respectively.

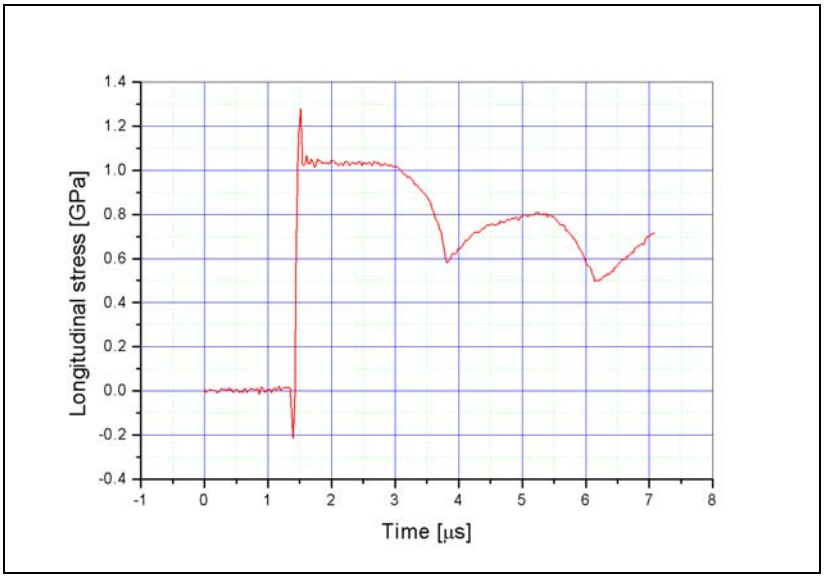

Fig. 3.3.2.1. Stress record from gauge in PMMA behind OFHC Cu specimen for initial impact speed of 304 m/s

3.3.3. Microstructural aspect of spalling

Spallation is one of the dynamic fracture phenomena within a material under intense impulsive loading and is caused by high tensile stresses due to interaction of stress waves. In ductile materials, spallation is consequence of the nucleation, growth and coalescence of voids. Spallation in brittle materials takes place by dynamic crack propagation without large-scale plastic deformation. We will focus our attention only on the former case.

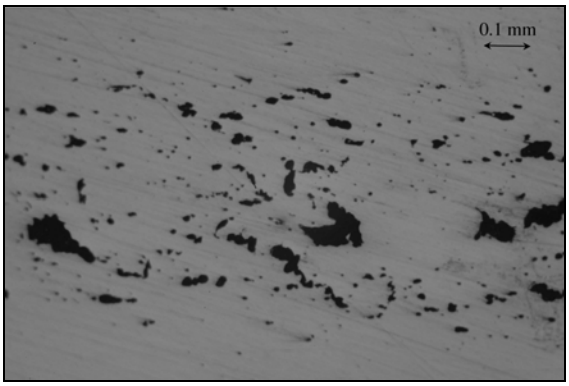

(a)

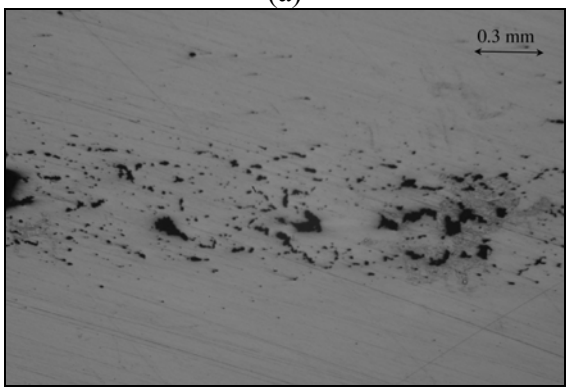

(b)

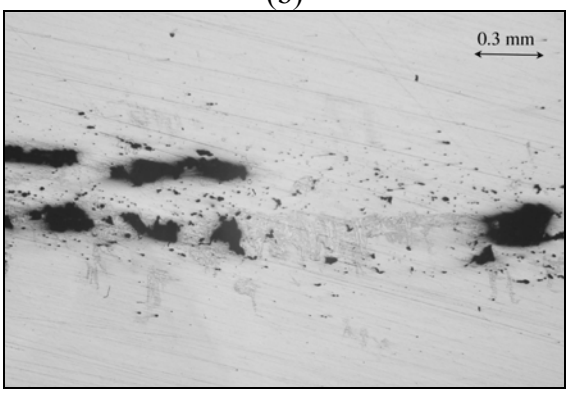

(c)

Fig. 3.3.3.1. Microphotographs of mechanisms of damage and failure due to growth and coalescence of voids in the softly recovered spall specimen from an impact experiment on OFHC Cu target

The process of spallation in ductile materials is a complex phenomenon, due to the number of different physical effects involved. Generally dynamic growth of a void presents some additional complications. Firstly, the heat generated by plastic

deformation cannot dissipate itself due to high rate of deformation. Secondly, the inertial effects associated with the displacement of the material adjoining the voids walls become an important consideration. Thirdly, wave interactions have a bearing on this phenomenon in the final configuration.

The spall strength data [105] clearly indicated the temperature dependency, decreasing as the temperature increases. The yield strength and viscosity also decrease when temperature increases.

In case of ductile separation, voids nucleate through particle-matrix debonding or through particle cracking. Than, they grow by local plastic deformation, and finally coalesce by the onset of local instabilities. The first stage is essentially controlled by the critical stress level which is linked to microstructure, and the two others are controlled by plastic deformation which is linked to temperature and the local strain rate.

Microscopic observations of the OFHC Cu softly recovered spalled specimen have been carried out. Figure 3.3.3.1. shows the photomicrographs of such observation. All micrographs have been taken along central loading axis, and shock direction is vertical. It was found that in the matrix material surrounding large voids, there were many small voids as shown in Fig. 3.3.3.1.(a) Growth of large voids takes place by direct impingement upon near small voids as shown in Fig. 3.3.3.1.(b) Configuration of spall surface, shown in Fig. 3.3.3.1.(c), indicates that spalling is generated by direct link of large voids. In addition, many voids appear near the spall surface.

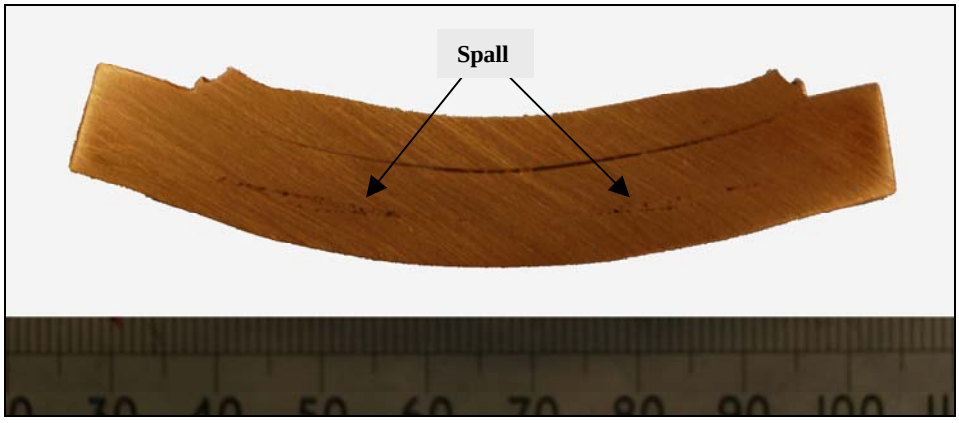

Fig. 3.3.3.2. Cross section of flyer and target impacted at velocity of 304 m/s, OFHC Cu material

Fig. 3.3.3.2. show spallation at the macro-scale for OFHC Cu corresponding to the impact velocity of 304 m/s. At this impact velocity, when spall is initiated, one can also observe plastic bending of the target between the free surface and spall surface.

3.4. Summary

New tensile test procedure has been proposed in this research, and tensile tests that have been carried out in this work are summarized in the table Tab. 3.4.1. Due to limitations of Cranfield University tensile test facility, which are:

- maximal achievable strain rate range up to $10x10^0$ 1/s,

- measurement of only longitudinal strains during tensile tests, due to usage of mechanical extensiometer which was only available measurement technique,

need for the additional tensile tests have been identified. Those additional tests have been carried out at Ernst Mach Institute, and they secured following:

- extended strain rate range up to 10×10^2 1/s

- contact-less optical strain rate measurement technique allowed simultaneous measurement of both longitudinal and transverse strain during tensile tests.

Tab. 3.4.1. Tensile test summary

Tensile Test	
Cranfield University – SoE Facility 5 Strain Rates : 5 Temperatures : 3 Orientations	
AA7010	AA2024
165 Tests	85 Tests
Ernst-Mach-Institute Facility 1 Strain Rate : 1 Temperature : 2 Orientations	
AA7010	AA2024
6 Tests	-

Results from additional tensile tests are presented in Appendix B, and they have been used for validation of constants for constitutive models, which have been initially determined using results form tensile tests which have been carried out at lower strain rate regime, but at different temperatures. In that way hypothesis of interchangeability of strain rate and temperature has been validated.

Tab. 3.4.2. Cylinder impact test summary

Taylor Cylinder Impact Test	
Cranfield University – RMCS Facility Gas Gan Facility 4 Launched Speeds	Cranfield University – SoE Facility 3D Scaning Machine 19 Digitised Cross-Sections per Scan
AA7010	AA7010
4 Tests	2 Scans

Simultaneous measurement of longitudinal and transverse strain of tensile specimen during tensile test, allowed direct measurement of Lankford coefficient, using following relationship:

$$R = \frac{-\varepsilon_w^p}{\varepsilon_l^p + \varepsilon_w^p} \qquad (3.4.1.)$$

and those results are presented and commented in Appendix B. It has been found that value of Lankford coefficient R deduced using impact cylinder test, which is presented in the Chapter 5, corresponds to the maximal value of Lankford coefficient.

Summary of Taylor cylinder and plate impact tests, with corresponding post-test measurements and analysis are presented in tables Tab. 3.4.2. and Tab. 3.4.3.

Tab. 3.4.3. Plate impact test summary

Plate Impact Test
Cranfield University – RMCS Facility Gas Gan Facility 1 Launched Speeds: 1 Orientation
OFHC Cu
1 Test
Post-test Micro-structural Analysis

4. STRAIN RATE AND TEMPERATURE DEPENDENCE

4.1. Introduction

The importance of the effect of strain rate on metal material properties depends on the specific application conditions. In metal processing and crashworthiness problems where strain rate is in the range of 0.01 – 100 1/s, it has been shown that this effect cannot be neglected [35]. Different materials show different degree of strain rate dependency, but if material model is developed for solving dynamic loading structural problems this aspect should be included. Apart from strain rate and strain/work hardening effects the thermal effects typical for deformation processes of metals have to be included into constitutive models.

The most complex rate dependant models define the yield stress as a function of strain, strain rate, and temperature. These models are usually classified as empirical or physically based, depending on their basic assumptions. Today the tendency is to develop more physically based models that will enable application of the model to a broader range of strains, opposite the restriction to a specific strain range when using the less physically sound models.

There are many constitutive equations that have been proposed by different investigators. These equations are very important because they are actually used in computer codes to represent material behaviour.

Steinberg – Guinan [123] proposed a model that gives the definition of the shear stress (G) dependence on the effective plastic strain, pressure and temperature in addition to the definition of the yield strength (Y).

It is assumed that a value of $\dot{\varepsilon}$ exists beyond which strain rate has a minimal effect on Y. The value of strain rate obtained experimentally and used as a limitation value is $\dot{\varepsilon} = 10^5 \, \mathrm{s}^{-1}$. The temperature dependence of Y is assumed to be the same as that of G. The constitutive relations for G and Y as functions of ε, P and T for high $\dot{\varepsilon}$ are

$$G = G_0\left[1+\left(\frac{G_p'}{G_0}\right)\frac{P}{\eta^{1/3}}+\left(\frac{G_T'}{G_0}\right)(T-300)\right], \tag{4.1.1.}$$

$$Y = Y_0\left[1+\beta(\varepsilon+\varepsilon_i)\right]^n\left[1+\left(\frac{Y_p'}{Y_0}\right)\frac{P}{\eta^{1/3}}+\left(\frac{Y_T'}{Y_0}\right)(T-300)\right]. \tag{4.1.2.}$$

subject to the limitation that:

$$Y_{\max} \geq Y_0\left[1+\beta(\varepsilon+\varepsilon_i)\right]^n \tag{4.1.3.}$$

Were η is compression, defined as the initial specific volume v_0 divided by the specific volume v, β and n are work-hardening parameters and ε_i is the initial effective plastic strain, normally equal to zero.

The subscript 0 refers to the reference state (T= 300 K, P= 0, ε = 0). Primed parameters with the subscripts P and T imply derivatives of that parameter with respect to pressure or temperature at the reference state.

Steinberg – Lund [124] proposed an improved version of the Steinberg-Guinan model**.** This model extends its validity to strain rates as low as 10^{-4} s^{-1} should be taken into consideration. The modification of Steinberg-Guinan model for the yield stress has the form

$$\sigma_y = \{Y_T(\dot{\varepsilon}_p, T) + Y_A f(\varepsilon_p)\}\frac{G(p,t)}{G_0} \tag{4.1.4.}$$

Where $Y_T(\dot{\varepsilon}_p, T)$ is the thermally activated part of the yield strength and is a function of $\dot{\varepsilon}_p$ and T and $Y_T \le Y_p$.

The second, athermal, term includes the work hardening term $f(\varepsilon_p)$:

$$Y_A f(\varepsilon_p) = Y_A[1 + \beta(\gamma_i + \varepsilon^p)]^n \le Y_{\max} \tag{4.1.5.}$$

Where Y_p is Peierls stress for rate dependent model and $Y_{\max}$ is work hardening maximum for the rate model.

The last term is the pressure and temperature-dependent shear modulus divided by G_0, the modulus at Standard Temperature and Pressure conditions – reference condirions. The definition of the shear modulus stays the same.

Cowper – Symonds [125] model is based on the assumptions of dynamic, rigid-plastic theory of beams and defines the strain rate dependence of the yield stress. Strain rate law is defined as:

$$\dot{\varepsilon} = D\left(\frac{\sigma_y}{\sigma_0} - 1\right)^p, \tag{4.1.6.}$$

Where σ_0 is the static yield stress, and D, p are empirical constants.

Campbell and Cooper [126] modification suggested for a uniaxial stress and condition $\varepsilon_y \le \varepsilon \le \varepsilon_u$ is defined as:

$$\frac{\sigma}{\sigma_0} = 1 + \left(\frac{(\varepsilon_u - \varepsilon_y)\dot{\varepsilon}}{(\varepsilon - \varepsilon_y)D_u + (\varepsilon_u - \varepsilon)D_y}\right)^{1/q} \tag{4.1.7.}$$

Where ε_y is yield strain, ε_u is ultimate strain, σ is respective dynamic flow stress, σ_0 is respective static flow stress, $\dot{\varepsilon}$ is strain rate, and q parametar independent of strain.

For small strains, $\varepsilon = \varepsilon_y$

$$\frac{\sigma}{\sigma_0} = 1 + \left(\frac{\dot{\varepsilon}}{D_y} \right)^{1/q} \qquad (4.1.8.)$$

For large strains and $\varepsilon = \varepsilon_u$

$$\frac{\sigma}{\sigma_0} = 1 + \left(\frac{\dot{\varepsilon}}{D_u} \right)^{1/q} \qquad (4.1.9.)$$

Coefficient D_y is identified as the usual coefficient for small strains while D_u is evaluated from the strain rate sensitive properties at the ultimate tensile strength of the material.

The most widely used models today, for crashworthiness applications are the **Johnson-Cook**, **Zerilli-Armstrong** and **Mechanical Threshold Stress** models. It should be noted that the validation of these models is mainly done using materials with pronounced strain rate/temperature dependency, usually metals and their alloys. Validation of the rate dependant material models means that those models are used for simulations of the experiments and afterwards for comparison of experimental and numerical simulation results. When it comes to the application of these models to a specific structural material, usually an alloy, the main problem is to define material constants for the strain rate dependant model used.

Detailed descriptions of the Johnson Cook (JC), Zerilli Armstrong (ZA) and Mechanical threshold stress (MTS) material models, are given in this chapter. Novel procedures for calibraton of MTS and JC material models are developed and presented in detail.

While JC and ZA have the simpler definition and require a smaller number of constants, the MTS model is more general and consequently a more complex model. Simpler models, such as ZA and JC models, are more widely used in simulations, as it is easier to obtain the constants required for the models. On the other hand, the MTS model offers better accuracy in predicting the response at higher strains and represents a model of greater importance for the future.

The constitutive equations mentioned above have a number of parameters defining material properties. The Johnson-Cook model has five parameters, the Zerilli-Armstrong has five parameters and the Mechanical Threshold Stress model can be used with two or four parameters. The parameters are experimentally determined in tests performed over a range of strain rates and temperatures. Testing procedures for the Johnson-Cook and Zerilli-Armstrong models do not require low temperature tests and therefore are simpler than required for the MTS model.

The main advantage of the Johnson-Cook model over the Zerilli-Armstrong and MTS models is in the number of materials for which the parameters are known. At the same time the advantage of the Zerilli-Armstrong and MTS models over Johnson-Cook model is in the fact that they are based on physical processes taking

place in the deforming material and therefore can more accurately represent behaviour of the material.

It is generally accepted that at large strains most metallic materials tend to approach a finite “saturation stress” or approach a constant but small hardening rate. Such saturation is lacking in the models like Johnson-Cook and Zerilli-Armstrong. The MTS model contrarily uses a differential form to fit the experimental data.

The lack of saturation stress as an integral part of the models like Johnson-Cook and Zerilli-Armstrong, makes it impossible to create a satisfactory model fit at small strains if these models were previously optimised for large strain applications and vice versa. The MTS model has been shown to fit the experimental results much better [67,68,69].

4.2. Empirical constitutive equations

4.2.1. Johnson – Cook model

The Johnson-Cook [41-43] material model is an empirical model. As most of the models of this type it expresses the equivalent von Mises tensile flow stress as a function of the equivalent plastic strain, strain rate, and temperature. This model is applicable for the range of strain rates from 0.001 to 1000s^{-1}. Typical applications include explosive metal forming, ballistic, and impact.

In the presence of low and constant strain rates conditions, metals work harden along the well-known relationship which is known as parabolic hardening rule:

$$\sigma = \sigma_0 + k\varepsilon^n \qquad (4.2.1.1.)$$

where σ_0 is the yield stress, n is work hardening exponent, and k is the preexponential factor.

Dynamics events often involve increases in temperature due to adiabatic heating, because of this thermal softening must be included in a constitutive model. The effects of temperature on the flow stress can be described with following relation:

$$\sigma = \sigma_r \left[1 - \left(\frac{T - T_r}{T_m - T_r} \right)^m \right] \qquad (4.2.1.2.)$$

Here T_m is the melting point, T_r is a reference temperature at which σ_r reference stress is measured, T is temperature for which σ flow stress is calculated, and *m* is material dependant constant.

The strain rate effect can be simply expressed with following relationship, which is very often observed at strain rates that are not too high.

$$\boldsymbol{\sigma} \propto \ln \dot{\boldsymbol{\varepsilon}} \qquad (4.2.1.3.)$$

Johnson and Cook [41-43] based on the above dependencies, proposed the following equation for **strength model**, where the von Mises flow stress is given as:

$$\sigma = [A + B(\varepsilon)^n][1 + C\ln(\dot{\varepsilon}^*)][1 - (T^*)^m] \qquad (4.2.1.4.)$$

Hhere A, B, C, n and m are material constants which are experimentally determined. The expression in the first set of brackets gives the stress as a function of strain for $\dot{\varepsilon}^* = 1.0$ and $T^* = 0$. The expressions in the second and third sets of brackets represent the effects of strain rate and temperature. This equation describes very well the response of a number of metals.

The term T^*, homologous temperature, is the ratio of the current temperature T to the melting temperature T_m:

$$T^* = \frac{T - T_r}{T_m - T_r} \tag{4.2.1.5.}$$

where T_r is the reference temperature at which σ_0 is measured.

Dimensionless strain rate $\dot{\varepsilon}^*$ is given as

$$\dot{\varepsilon}^* = \frac{\dot{\varepsilon}}{\dot{\varepsilon}_0} \tag{4.2.1.6.}$$

where $\dot{\varepsilon}$ is the effective plastic strain rate, $\dot{\varepsilon}_0$ is the reference strain rate which can for convenience be made equal to 1 ($\dot{\varepsilon}_0 = 1.0s^{-1}$).

One of the problems with this constitutive equation is that strain rate and temperature effects on the flow stress are uncoupled. This implies that the strain rate sensitivity is independent of temperature, which is not generally observed for most metals.

Because the empirical constitutive equations are basically a curve-fitting procedure, they are relatively easy to calibrate with minimum of experimental data in form of few stress-strain curves at several rates and several temperature.

Johnson-Cook model also contains a **damage** model. The strain at fracture is given by:

$$\varepsilon_f = [D_1 + D_2 \exp(D_3 \sigma^*)][1 + D_4 \ln(\dot{\varepsilon}^*)][1 - D_5 T^*] \tag{4.2.1.7.}$$

where:

σ^* is the ratio of pressure divided by effective stress $\sigma^* = \frac{p}{\overline{\sigma}}$,

D_1, D_2, D_3, D_4, D_5 are damage models parameters.

Fracture occurs when damage parameter

$$D = \sum \frac{\Delta \varepsilon}{\varepsilon^f}$$

reaches the value of 1.

Variants of Johnson-Cook model have also been developed with some modification and simplifications.

Simplified Johnson – Cook model

Simplified JC model is used for problems where strain rates vary over a large range and thermal effects are ignored. Flow stress is described as:

$$\sigma = [A + B(\varepsilon)^n][1 + C\ln(\dot{\varepsilon}^*)] \quad (4.2.1.8.)$$

Modified Johnson – Cook model

This model incorporates a simple modification to the JC model to better represent the strain rate effect in a manner of exponential function. There is evidence that strain rate influence on strength of material is not linear function of the natural log, but rather an exponential function. On the basis of this observation [44] flow stress can be expressed as:

$$\sigma = [A + B(\varepsilon)^n][(\dot{\varepsilon}^*)^C][1 - (T^*)^m] \quad (4.2.1.9.)$$

4.2.2. Procedures for obtaining parameters for Johnson-Cook material model

The formulation of the JC model [43-45] is empirically based. The JC model represents the flow stress with an equation of the form:

$$\sigma = [A + B(\varepsilon)^n][1 + C\ln(\dot{\varepsilon}^*)][1 - (T^*)^m] \quad (4.2.2.1.)$$

and the quantity T^* is defined as:

$$T^* = (T - 298)/(T_{melt} - 298) \quad (4.2.2.2.)$$

where T_{melt} is melting temperature and taken as the solidus temperature for an alloy.

The values of A, B, C, n and m are determined from an empirical fit of flow stress data (as a function of strain, strain rate and temperature) to flow stress equation.

The parameters in the JC material model are sensitive to the computational algorithm used to calculate these parameters. In this chapter, procedures to obtain constants for JC model are proposed.

The first step in this process is to determine the constants in the first set of brackets. A is yield stress and B and n represent the effects of strain hardening. At room temperature and for the strain rate of interest, $\dot{\varepsilon}^* = 1$, the JC equation can be written as:

$$\sigma = [A + B(\varepsilon)^n] \quad (4.2.2.3.)$$

It is a straightforward procedure to obtain the appropriate constants for this strain rate. The stress at zero plastic strain $A = \sigma_0$ can be obtained from experimental data, and

quantity $\sigma - \sigma_o$ plotted versus plastic strain on a log-log plot, after applying least squares fit of the data to power law equation, gives us values for B and n constants.

The parameter C can be obtained from $\sigma - \dot{\varepsilon}$ data. At room temperature and for constant strain, constitutive equation can be written as:

$$\sigma = \sigma_a[1 + C\ln(\dot{\varepsilon}^*)] \text{ or } \sigma/\sigma_a - 1 = C\ln(\dot{\varepsilon}^*), \qquad (4.2.2.4.)$$

where σ_a is the stress at strain rate of interest $\dot{\varepsilon}^* = 1$. For constant strain, value of σ_a can be calculated, and $\sigma/\sigma_a - 1$ can be plotted versus $\dot{\varepsilon}$ on a semi-log plot. A least squares fit to the data gives as value of parameter C.

The parameter m can be determined from stress-temperature response of the material. At constant strain rate, constitutive equation can be written as:

$$\sigma = \sigma_b[1 - (T^*)^m] \text{ or } \sigma/\sigma_b = [1 - (T^*)^m] \qquad (4.2.2.5.)$$

where σ_b is the stress at room temperature. For constant strain and constant strain rate, value of σ_b can be calculated, and data plotted as σ/σ_b versus T^*. After applying least squares fit of the data, value of parameter m can be established.

4.3. Physically based constitutive equations

4.3.1. Zerilli-Armstrong model

This model is based on the framework of thermally activated dislocation motion. Zerilli and Armstrong proposed two microstructurally based constitutive equations that show a very good match with experimental results. They analysed the temperature and strain rate response of typical FCC and BCC metals and noticed a difference between these materials. The BCC metals are much higher temperature and strain rate sensitive than FCC metals.

They observed that the activation area A was dependent on strain for FCC metals and independent of strain for BCC metals. The activation area A can be obtained from the activation volume V.

$$V = Ab = l^* \lambda b \qquad (4.3.1.1.)$$

Where b is Burgers vector, λ is the dislocation barrier width, and l^* is the dislocation barrier spacing.

This is area swept by the dislocation in overcoming an obstacle.

The principal thermal activation mechanism for BCC metals is based on overcoming Peierls-Nabarro barriers. The spacing of these obstacles is defined with lattice spacing and thus not affected by plastic strain.

In the case of FCC metals, the activation area decreased with increasing strain. The spacing between dislocations decreases as the forest dislocation density increases, thus spacing among obstacles l^* decrease with plastic strain for FCC metals.

Relation between dislocation density and spacing is expressed with following relationship:

$$\rho \cong \frac{1}{l^{*2}} \text{ or } l^* = \frac{1}{\sqrt{\rho}} \qquad (4.3.1.2.)$$

The movement of arrays of dislocations will produce shear strain γ. It is assumed that the dislocations do not interact. Shear strain can be directly related to the number of dislocation N, per unit area:

$$\gamma = \tan\theta = \frac{Nb}{l} = \frac{Nbl}{l^2} \qquad (4.3.1.3.)$$

where l is a vector parallel to the dislocation line.

If density of dislocation is defined as:

$$\rho = \frac{N}{l^2} \qquad (4.3.1.4.)$$

we have following expression for shear strain:

$$\gamma = \rho bl \qquad (4.3.1.5.)$$

The shear strain can be converted into a longitudinal strain by adding an orientation factor M:

$$\varepsilon = \frac{1}{M}\rho bl \text{ or } \rho = \frac{M\varepsilon}{bl} \qquad (4.3.1.6.)$$

Activation area now can be expressed as:

$$A = \lambda l^* = \lambda \left(\frac{bl}{M} \right)^{1/2} \varepsilon^{-1/2} \qquad (4.3.1.7.)$$

The constitutive relation which describe thermal portion of stress proposed from Zerilli and Armstrog [48] may be expressed as:

$$\sigma_{th} = \frac{M \Delta G_0}{b A_0} e^{-\beta T} \qquad (4.3.1.8.)$$

where

$$\beta = -C_3 + C_4 \ln \dot{\varepsilon} \qquad (4.3.1.9.)$$

β is a parameter dependant on strain rate, ΔG_0 is height of free energy barrier at 0K and A_0 is activation area at 0K.

Since $A = const$ for BCC metals and activation area is proportional to $\varepsilon^{-1/2}$ for FCC metals, we can distinguish two different expressions:

$$\sigma_{th} = C_1 \exp(-C_3 T + C_4 T \ln \dot{\varepsilon}) \text{ BCC} \qquad (4.3.1.10.)$$

$$\sigma_{th} = C_2 \varepsilon^{1/2} \exp(-C_3 T + C_4 T \ln \dot{\varepsilon}) \text{ FCC} \qquad (4.3.1.11.)$$

In addition to this thermal part, athermal component σ_G of flow stress is added and term which describes the flow stress dependant on grain size. Yield stress increases as the grain size decreases, and this dependence can be described by the Hall-Petch equation:

$$\sigma = k d^{-1/2} \qquad (4.3.1.12.)$$

where d is grain diameter and k is constant.

The overall expression now may be written as:

$$\sigma = \sigma_G + \sigma_{th} + k d^{-1/2} \qquad (4.3.1.13.)$$

The separate plastic strain-hardening contribution to the flow stress of BCC metals may be evaluated from an assumed power low dependence on strain given by:

$$\Delta \sigma_G = C_5 \varepsilon^n \qquad (4.3.1.14.)$$

Integral expressions now have following form:

$$\sigma = \sigma_G + C_2 \varepsilon^{1/2} \exp(-C_3 T + C_4 T \ln \dot{\varepsilon}) + k d^{-1/2} \text{ FCC} \qquad (4.3.1.15.)$$

$$\sigma = \sigma_G + C_1 \exp(-C_3 T + C_4 T \ln \dot{\varepsilon}) + C_5 \varepsilon^n + k d^{-1/2} \text{ BCC} \qquad (4.3.1.16.)$$

The main difference between those two equations is that the plastic strain is uncoupled from strain rate and temperature for BCC metals.

Modified Zerilli – Armstrong model

This material model is a rate and temperature sensitive plasticity model [49], which is sometimes preferred in ordnance design calculations. Flow stress is expressed as follows:

FCC metals

$$\sigma = C_1 + \{C_2 (\varepsilon)^{1/2} [\exp((-C_3 + C_4 \ln(\dot{\varepsilon}^*))T)] + C_5\} \left(\frac{\mu(T)}{\mu(293)} \right) \qquad (4.3.1.17.)$$

BCC metals

$$\sigma = C_1 + C_2 [\exp((-C_3 + C_4 \ln(\dot{\varepsilon}^*))T)] + [C_5 (\varepsilon)^n + C_6] \left(\frac{\mu(T)}{\mu(293)} \right) \qquad (4.3.1.18.)$$

where

ε - effective plastic strain

$\dot{\varepsilon}^* = \dot{\varepsilon} / \dot{\varepsilon}_0$ - effective plastic strain rate where $\dot{\varepsilon}_0 = 1, 10^{-3}, 10^{-6}$ for time units of seconds, milliseconds, and microseconds, respectively.

$\left(\frac{\mu(T)}{\mu(293)} \right) = B_1 + B_2 T + B_3 T^2$ and B_1, B_2, B_3 are constants.

Combined Johnson – Cook/ Zerilli – Armstrong model

This material model combines the yield and strain hardening portion of the JC model with temperature and strain portion of ZA model. According to [44] flow stress can be expressed as:

$$\sigma = [A + B(\varepsilon)^n][\exp(-C_3 T + C_4 T \ln \dot{\varepsilon})] \qquad (4.3.1.19.)$$

4.3.2. Procedures for obtaining parameters for Zerilli-Armstrong material model

Integral expressions for ZA constitutive material model [48,50] have following form:

$$\sigma = \sigma_G + k d^{-1/2} + C_1 \exp(-C_3 T + C_4 T \ln \dot{\varepsilon}) + C_5 \varepsilon^n \text{ BCC metals} \qquad (4.3.2.1.)$$

$$\sigma = \sigma_G + k d^{-1/2} + C_2 \varepsilon^{1/2} \exp(-C_3 T + C_4 T \ln \dot{\varepsilon}) \text{ FCC metals} \qquad (4.3.2.2.)$$

One can see that the plastic strain is uncoupled from strain rate and temperature for BCC metals. This is the main difference between constitutive equations for BCC and FCC metals.

The procedure for fitting constants, which are involved in constitutive relation for bcc metals, is described here in brief. The first two terms are independent of temperature, strain rate and strain. The first is attributed to the effect of the initial dislocation density and the second is due to the hardening effect of grain boundaries. In this work they are combined in one athermal material constant, C_0, so that, in total, six material constants need to be determined, C_0, C_1, C_3, C_4, C_5, and n.

By considering the variation of yield stress with strain rate at zero plastic strain the final term in constitutive equation can be omitted, leaving an equation for the yield stress:

$$\sigma_y = C_0 + C_1 \exp(-C_3 T + C_4 T \ln \dot{\varepsilon}), \qquad (4.3.2.3.)$$

involving the four constants, C_0, C_1, C_3, C_4. By fitting the above equation to the experimental data for yield stress over a wide range of strain rate and for different temperatures, optimum values for these constants can be obtained. Ploting value of yield stress versus strain rate on a semi-log plot for different temperatures, one can find values for above constants.

The remaining two material constants C_5 and n, can be derived by assuming isothermal conditions during test at the different strain rates and by fitting the relation:

$$\sigma = \sigma_y + C_5 \varepsilon^n. \qquad (4.3.2.4.)$$

A similar procedure can be applied for determination of constants, which are involved in the constitutive formulation for FCC metals.

4.3.3. Mechanical Threshold Stress Model

Thermally activated dislocation motion as a basic mechanism for MTS model

A dislocation continuously encounters obstacles as it moves though the lattice and these obstacles make the movement of dislocations more difficult. Dislocations themselves can oppose the movement of dislocations.

Peirls-Nabarro forces oppose the movement of dislocation at the atomic level. When a dislocation moves from one equilibrium atomic position to the next it has to overcome an energy barrier, that is force has to be applied to it. The stress required to move the dislocation without any other additional external help is the Pierls-Nabarro stress τ_{PN} .

A moving dislocation encounters periodic barriers of different spacing and different lengths. Temperature and strain rate response of metals are related to the length of these barriers and to the thermal energy of the lattice. The smaller narrower barriers are called short-range obstacles, and the larger, wider barriers are called long-range barriers (Fig. 4.3.3.1.).

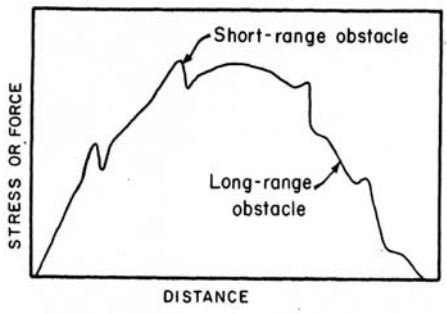

Fig. 4.3.3.1. Schematically display of barrier field [37]

Thermal energy increases the amplitude of vibration of atoms and this energy can help the dislocation to overcome obstacles.

The barrier is shown at four temperatures $T_0 = 0 < T_1 < T_2 < T_3$ (Fig. 4.3.3.2.). The thermal energies $\Delta G_1, \Delta G_2, \Delta G_3$, have been shown by hatching, where area under force-distance curve is an energy term.

The effect of thermal energy is to decrease the height of barrier when the temperature increases, so effective height of the barrier decreases as the temperature rises.

The effect of strain rate is similar, as the strain rate is increased, there is less time available to overcome the barrier and thermal energy is less effective.

Long-range barriers cannot be overcome by thermal energy. The following classification could be noticed: short-range obstacles, which are thermally activate

and long-range obstacles, which are not thermally activated. Based on this, the flow stress of a material can be expressed in a following manner:

$$\sigma = \sigma_G(structure) + \sigma^*(T, \dot{\varepsilon}, structure) \tag{4.3.3.1.}$$

where σ_G term is due to the athermal barriers determined by the structure of material, and σ^* term is due to the thermally activated barriers, the barriers that can be overcome by thermal energy. The principal short-range barrier is the Peierls-Nabarro stress, which is very important for BCC metals and ceramics.

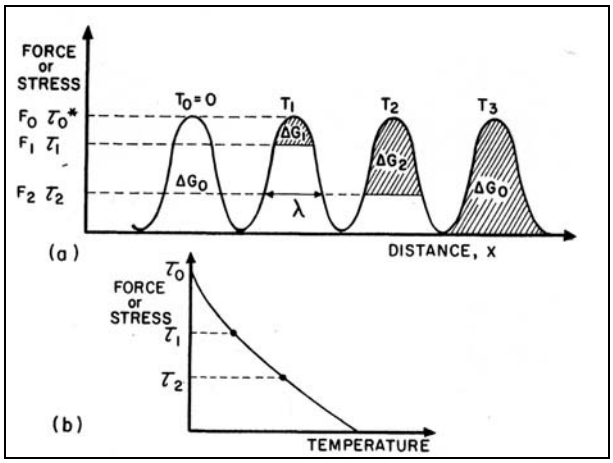

Fig. 4.3.3.2. (a) Thermal energy, (b) Stress or force required to overcome obstacles [37]

The probability of an equilibrium fluctuation in energy greater than a given value ΔG is given by statistical mechanics and is equal to [55]:

$$p_b = \exp\left(-\frac{\Delta G}{kT}\right) \tag{4.3.3.2.}$$

The probability that dislocation will overcome an obstacle can be considered as the ratio of the number of successful jumps over the obstacle divided by the number of attempts. A dislocation will overcome the obstacle if it has energy equal or higher than the energy of barrier. Those values per unit time are frequencies. Based on this definition the probability can be expressed with following relation:

$$p_b = \frac{\upsilon_1}{\upsilon_0} \tag{4.3.3.3.}$$

where υ_1 frequency with which the dislocation overcomes the obstacles and υ_0 vibrational frequency of dislocation. Based on this a relation between this two frequencies can be expressed as:

$$\upsilon_1 = \upsilon_0 \exp(-\frac{\Delta G}{kT}) \tag{4.3.3.4.}$$

In case that spacing between obstacles is l, lower bound of vibrational frequency of dislocations is estimated by Kocks as [55]:

$$\upsilon_0 = \upsilon \frac{b}{4l} \tag{4.3.3.5.}$$

where υ is the vibrational frequency of atoms and this is ground frequency of a dislocation with wavelength 4l.

Time Δt taken by a dislocation to move a distance Δl between two obstacles could be divided into a waiting time in front of obstacles t_w and running time between obstacles t_r:

$$\Delta t = t_w + t_r \tag{4.3.3.6.}$$

The waiting time is governed by the probability that an obstacle will be overcome by an adequately large thermal fluctuation of the free activation energy, so the waiting time is described as:

$$t_w = \frac{1}{\upsilon_1} = \frac{1}{\upsilon_0} \exp\left(\frac{\Delta G}{kT}\right) \tag{4.3.3.7.}$$

In reality the waiting time is much greater then running time $t_w >> t_r$ and it is possible to write:

$$\Delta t = t_w \tag{4.3.3.8.}$$

Strain rate is described with well-known relation as:

$$\dot{\varepsilon} = \frac{d\varepsilon}{dt} = \frac{1}{M} \rho b \nu \tag{4.3.3.9.}$$

where M is the orientation factor, b the dislocation Burger vector, and ν the dislocation velocity.

Using this relation it is possible to write:

$$\frac{\Delta\varepsilon}{\Delta t} = \frac{1}{M} \rho b \frac{\Delta l}{\Delta t} \tag{4.3.3.10.}$$

where Δl is distance between dislocation barriers and is assumed to be l. Thus, using this equation we have:

$$\dot{\varepsilon} = \frac{\upsilon_0 \rho b \Delta l}{M} \exp\left(-\frac{\Delta G}{kT}\right) \tag{4.3.3.11.}$$

Preexponential term can be represented as reference strain-rate:

$$\dot{\varepsilon}_0 = \frac{\upsilon_0 \rho b \Delta l}{M}, \tag{4.3.3.12.}$$

and thus, the final expression can be written as:

$$\dot{\varepsilon} = \dot{\varepsilon}_0 \exp\left(-\frac{\Delta G}{kT}\right) \tag{4.3.3.13.}$$

This expression is known as the Arrhenius expression, which relates strain-rate to activation energy and temperature.

Activation energy ΔG can be calculated from activation barrier:

$$\Delta G = \Delta G_0 - \int_0^{F^*} \lambda(F) dF \tag{4.3.3.14.}$$

where ΔG_0 is activation energy at 0K and $\lambda(F)$ is barrier width. The difference is the effective barrier. The shape of the activation barrier determines the shape of the thermal portion of curve. The athermal portion of the flow curve has a very low temperature dependence, equal to that of the shear modulus. It is easy to rearrange the above equation to obtain the relationship between stress and strain rate in the following manner:

$$kT \ln \frac{\dot{\varepsilon}_0}{\dot{\varepsilon}} = \Delta G_0 - \int_0^{F^*} \lambda(F) dF \tag{4.3.3.15.}$$

This equation is the foundation for constitutive equations, which are based on thermally assisted overcoming of obstacles.

Using this equation, assuming a simple shape for the activation barrier and changing the integration limits from forces to stresses, it is possible to express a constitutive equation in terms of activation volume. Activation volume is defined as:

$$V = l^* \lambda b \tag{4.3.3.16.}$$

where λ is barrier width and l^* barrier spacing (Fig. 4.3.3.3.).

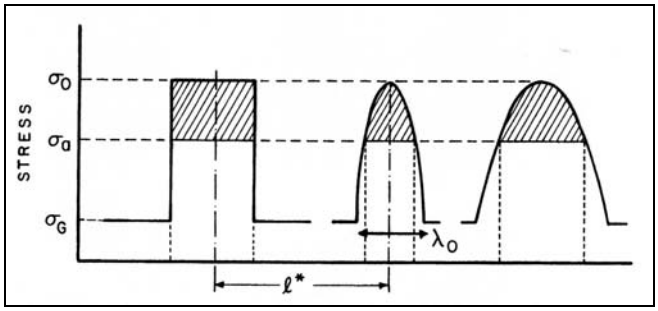

Fig. 4.3.3.3. Three different shapes of barriers [37]

The force on the dislocation per unit length can be expressed as:

$$F = \tau b \tag{4.3.3.17.}$$

where τ is shear stress. Based on this the force per barrier is given by:

$$F = \tau b l^* \tag{4.3.3.18.}$$

According to this we can write:

$$\int_0^{F^*} \lambda(F)dF = \int_0^{\tau^*} \lambda(\tau) b l^* d\tau = b l^* \int_0^{\tau^*} \lambda(\tau) d\tau \tag{4.3.3.19.}$$

If the barrier is rectangular (Fig. 4.3.3.) $\lambda = const$

$$\int_0^{F^*} \lambda(F)dF = b l^* \lambda \int_0^{\tau^*} d\tau = b l^* \lambda(\tau^* - 0) = V\tau^* \tag{4.3.3.20.}$$

The stress τ^* is described as difference between stress σ and base level of stress σ_G and using this formulation we have:

$$\Delta G = kT \ln \frac{\dot{\varepsilon}_0}{\dot{\varepsilon}} = \Delta G_0 - V(\sigma - \sigma_G) \tag{4.3.3.21.}$$

It is obvious that shape of the activation barrier determines the form of the equation. For example if we assume a hyperbolic barrier which is determined with following expression:

$$\sigma = \frac{\sigma_0}{\left[1 + \lambda/\lambda_0\right]^2} \tag{4.3.3.22.}$$

we have following constitutive equation:

$$\Delta G = kT \ln \frac{\dot{\varepsilon}_0}{\dot{\varepsilon}} = \Delta G_0 \left[1 - \left(\frac{\sigma}{\sigma_0} \right)^{1/2} \right]^2 \tag{4.3.3.23.}$$

Based on this Kocks [55] proposed a general expression for the activation energy dependence on σ in the following form:

$$\Delta G = kT \ln \frac{\dot{\varepsilon}_0}{\dot{\varepsilon}} = \Delta G_0 \left[1 - \left(\frac{\sigma}{\sigma_0} \right)^{p} \right]^q \tag{4.3.3.24.}$$

The parameters p and q determine the shape of activation barrier (Fig. 4.3.3.4.)

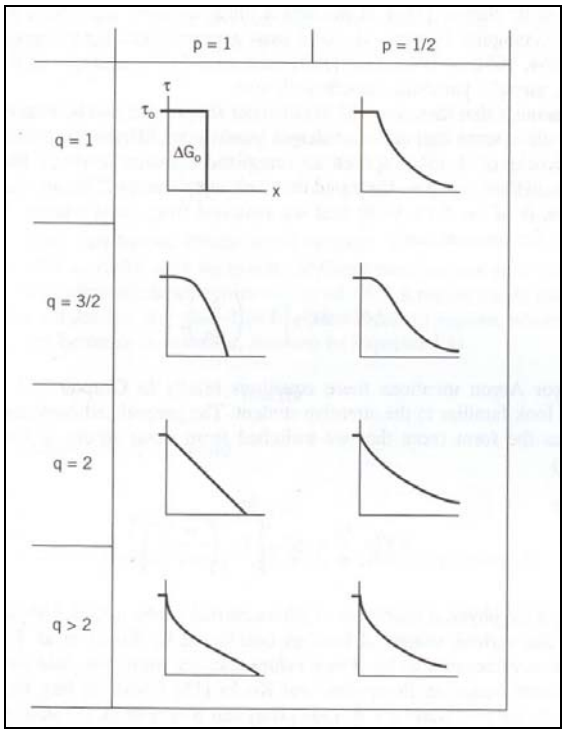

Fig. 4.3.3.4. Obstacles shapes and corresponding values of p and q [55]

The mechanical threshold stress model is based on thermally activated dislocation motion and focuses on the determination of threshold stress $\hat{\sigma}\ (F_0, \tau_0, \sigma_0)$. This threshold stress is defined as the flow stress of a certain structure at 0K. Normalized total activation energy g_0 can be defined in the following manner [59]:

$$\Delta G_0 = \mu(T) b^3 g_0 \tag{4.3.3.25.}$$

where $\mu(T)$ is temperature dependant shear modulus.

Substituting this expression in the above equation yields:

$$\Delta G = kT \ln \frac{\dot{\varepsilon}_0}{\dot{\varepsilon}} = \mu(T) b^3 g_0 \left[1 - \left(\frac{\sigma}{\hat{\sigma}} \right)^p \right]^q \tag{4.3.3.26.}$$

Based on this formulation, the following relation between thermal component of applied stress and the mechanical threshold stress can be found:

$$\sigma = \left[1 - \left(\frac{kT \ln(\dot{\varepsilon}_0 / \dot{\varepsilon})}{\mu(T) b^3 g_0} \right)^{1/q} \right]^{1/p} \hat{\sigma} \tag{4.3.3.27.}$$

where thermal activation function is defined as:

$$S = \left[1 - \left(\frac{kT \ln(\dot{\varepsilon}_0 / \dot{\varepsilon})}{\mu(T) b^3 g_0} \right)^{1/q} \right]^{1/p} \tag{4.3.3.28.}$$

4.3.4. Procedure for determination of the Mechanical Threshold Stress strength model parameters

The current structure of material in the MTS model is represented by an internal state variable, the mechanical threshold $\hat{\sigma}$, which is defined as the flow stress at 0K. The mechanical threshold is separated into athermal and thermal components [66-70]:

$$\hat{\sigma} = \hat{\sigma}_a + \sum \hat{\sigma}_t \ , \tag{4.3.4.1.}$$

where the athermal component characterizes the rate independent interaction with long-range barriers such as grain boundaries, dispersoids or second phases. The thermal component characterizes the rate dependant interactions of dislocations with short-range obstacles such as forest dislocations, interstitial, solutes, Peirls barrier, etc.

The flow stress can be expressed in the terms of the mechanical threshold stress as:

$$\frac{\sigma}{\mu} = \frac{\sigma_a}{\mu} + \sum \frac{\sigma_t}{\mu} \tag{4.3.4.2.}$$

where μ is shear modulus.

Temperature effects in MTS model are represented by a temperature and strain-rate dependant-scaling factor S_j, which specifies the ratio between the applied stress and mechanical threshold stress. This factor is derived from Arrhenius expression relating strain-rate to activation energy and temperature:

$$\dot{\varepsilon} = \dot{\varepsilon}_{0,j} \exp\left(\frac{-\Delta G_j(\sigma_j / \hat{\sigma}_j)}{kT} \right) \tag{4.3.4.3.}$$

where $\dot{\varepsilon}_0$ - reference strain rate, *k* - Boltzmann's constant.

Assuming that stress-dependant activation energy is [55]:

$$\Delta G_j = g_{0,j} \mu b^3 \left[1 - \left(\frac{\sigma_j / \mu}{\hat{\sigma}_j / \mu_0} \right)^{p_j} \right]^{q_j} \tag{4.3.4.4.}$$

where g_0 is normalized activation energy for the dislocations to overcome the obstacles, b is the burgers vector, p and q are empirical constants related to an obstacle profile with ranges $0 < p \le 1$ and $1 \le q \le 2$. It is then possible to write:

$$\frac{\sigma_j}{\mu} = \left[1 - \left(\frac{kT}{g_{0,j} \mu b^3} \ln \frac{\dot{\varepsilon}_{0,j}}{\dot{\varepsilon}} \right)^{1/q_j} \right]^{1/p_j} \frac{\hat{\sigma}_j}{\mu_0} \tag{4.3.4.5.}$$

and the scaling factor can be expressed as:

$$S_j(\dot{\varepsilon},T)=\left[1-\left(\frac{kT}{g_{0,j}\mu b^3}\ln\frac{\dot{\varepsilon}_{0,j}}{\dot{\varepsilon}}\right)^{1/q_j}\right]^{1/p_j} \qquad (4.3.4.6.)$$

The general form of MTS model is then:

$$\frac{\sigma}{\mu}=\frac{\sigma_a}{\mu}+\sum S_j\frac{\hat{\sigma}_j}{\mu_0} \qquad (4.3.4.7.)$$

where μ and μ_0 are the temperature dependent and 0K shear moduli respectively.

Based upon the particular material, the thermal component $\hat{\sigma}_t$ consists of the linear summation of terms. Each of these terms describes particular mechanism: dislocation interactions with long-range barriers, diclocation interactions with interstitial atoms and diclocation interactions with solute atoms.

Shear modulus

The shear modulus can be calculated using following formulations:

for body-centred cubic (bcc) materials:

$$\mu=\frac{(C_{11}-C_{12}-C_{44})}{3} \qquad (4.3.4.8.)$$

for face-centred cubic (fcc) materials:

$$\mu=\sqrt{C_{44}(C_{11}-C_{12})/2} \qquad (4.3.4.9.)$$

where C_{ij} are elastic constants.

An empirical relation for shear modulus [56], could be used for reasons of simplicity:

$$\mu=b_0-\frac{b_1}{\exp(\frac{b_2}{T})-1}, \qquad (4.3.4.10.)$$

where

$b_0=\mu_0$ and b_1, b_2 are fitting constants.

Athermal stress σ_a

Athermal contributions to flow stress can be associated to interactions of dislocations with long-range barriers, i.e. Hall-Petch behavior. The "Hall-Petch" equation has been used to describe a wide range of grain size versus yield or flow stress data:

$$\sigma=M(\sigma_0+k_y d^{-n}) \qquad (4.3.4.11.)$$

where σ flow stress, σ_0 friction stress, d grain diameter, k_y - "unpinning constant",and M the Taylor orientation factor.

Grain size dependency of flow stress is described in the MTS model in the athermal stress component with the following equation:

$$\sigma_a = k_y d^{-n} \tag{4.3.4.12.}$$

where d grain size, n exponent (1/3<n<1) and constant k_y could be determined from Hall-Petch plot [57].

Mechanical threshold stress $\hat{\sigma}_i$ and normalized activation energy g_{oi}

Thermally activated yielding is characterized by the "intrinsic" term $\hat{\sigma}_i$ and describes the rate dependant portion of yield stress mainly due to intrinsic barriers, where thermal portion of yield stress is defined as $\sigma_i = \sigma_y - \sigma_a$.

From the equation which describes relation between applied stress and mechanical threshold stress

$$\frac{\sigma_i}{\mu} = \frac{\sigma_y - \sigma_a}{\mu} = \left[1 - \left(\frac{kT\ln(\dot{\varepsilon}_{0i}/\dot{\varepsilon})}{\mu b^3 g_{0i}}\right)^{1/q_i}\right]^{1/p_i} \frac{\hat{\sigma}_i}{\mu_0} \tag{4.3.4.13.}$$

it is possible to determine g_{oi} and $\hat{\sigma}_i$, when mechanical data is presented in a Fisher plot format [14], with the above equation arranged as:

$$\left(\frac{\sigma_y - \sigma_a}{\mu}\right)^{p_i} = \left(\frac{\hat{\sigma}_i}{\mu_0}\right)^{p_i} - \left(\frac{\hat{\sigma}_i}{\mu_0}\right)^{p_i} \left(\frac{1}{g_{oi}}\right)^{1/q_i} \left[\frac{kT}{\mu b^3}\ln\left(\frac{\dot{\varepsilon}_{oi}}{\dot{\varepsilon}}\right)\right]^{1/q_i} \tag{4.3.4.14.}$$

where reference strain-rate $\dot{\varepsilon}_{0i}$ is an adjustable parameter, p_i and q_i are glide obstacle profile parameters based on empirical observation [55].

Mechanical threshold stress $\hat{\sigma}_\varepsilon$ normalized activation energy $g_{o\varepsilon}$

From the general form of MTS model

$$\frac{\sigma}{\mu} = \frac{\sigma_a}{\mu} + S_i \frac{\hat{\sigma}_i}{\mu_0} + S_\varepsilon \frac{\hat{\sigma}_\varepsilon}{\mu_0}, \tag{4.3.4.15.}$$

when the athermal hardening and intrinsic strengthening are subtracted from overall stress, a value of σ_ε is determined with following relation:

$$\sigma_\varepsilon = \frac{S_\varepsilon}{\mu_0}\hat{\sigma}_\varepsilon(\varepsilon) = \left(\frac{\sigma(\varepsilon)}{\mu} - \frac{\sigma_a}{\mu} - S_i \frac{\hat{\sigma}_i}{\mu_0}\right) \tag{4.3.4.16.}$$

For each curve of $\sigma(\varepsilon)$ the corresponding mechanical threshold stress $\hat{\sigma}_\varepsilon(\varepsilon)$ can be derived from series of tests, where the material is loaded at different

temperatures at a fixed strain rate. Hence stress now can be plotted according to the above equation, which can be rewritten as:

$$\left(\frac{\sigma(\varepsilon)}{\mu}-\frac{\sigma_a}{\mu}-S_i\frac{\hat{\sigma}_i}{\mu_0}\right)^{p_\varepsilon}=\left(\frac{\hat{\sigma}_\varepsilon(\varepsilon)}{\mu_0}\right)^{p_\varepsilon}-\left(\frac{\hat{\sigma}_\varepsilon(\varepsilon)}{\mu_0}\right)^{p_\varepsilon}\left(\frac{1}{g_{0\varepsilon}}\right)^{\frac{1}{q_\varepsilon}}\left[\frac{kT\ln(\dot{\varepsilon}_{0\varepsilon}/\dot{\varepsilon})}{\mu b^3}\right]^{\frac{1}{q_\varepsilon}} \quad (4.3.4.17.)$$

The constant used in the thermal activation function

$$S_\varepsilon=\left[1-\left(\frac{kT\ln(\dot{\varepsilon}_{0\varepsilon}/\dot{\varepsilon}^p)}{\mu b^3 g_{0\varepsilon}}\right)^{1/q_\varepsilon}\right]^{1/p_\varepsilon} \quad (4.3.4.18.)$$

like the reference strain-rate $\dot{\varepsilon}_{0\varepsilon}$, p_ε and q_ε glide obstacle profile parameters are based on empirical observation [55].

In a Fisher plot, data from experiments at constant strain rate but varying temperature should give a strait line. The intercept with zero temperature in this plot gives the mechanical threshold normalized by shear modulus while the slope is inversely related to the normalized activation energy $g_{0\varepsilon}$.

The mechanical threshold stress $\hat{\sigma}_\varepsilon(\varepsilon)$ now can be calculated according to following equation:

$$\hat{\sigma}_\varepsilon(\varepsilon)=\frac{\mu_0}{S_\varepsilon}\left(\frac{\sigma(\varepsilon)}{\mu}-\frac{\sigma_a}{\mu_0}-S_i\frac{\hat{\sigma}_i}{\mu_0}\right) \quad (4.3.4.19.)$$

Saturation stress $\hat{\sigma}_{\varepsilon s}$ and initial hardening rate θ_0

The mechanical threshold stress $\hat{\sigma}_\varepsilon$ evolves with strain due to dislocation accumulation – work hardening and annihilation – recovery [70]. This process can be described as:

$$\frac{d\hat{\sigma}_\varepsilon}{d\varepsilon}=\theta=\theta_0-\theta_r(T,\dot{\varepsilon},\hat{\sigma}_\varepsilon) \quad (4.3.4.20.)$$

where θ_0 is hardening due to dislocation accumulation and θ_r is the dynamic recovery rate.

The hardening rule presumes that material possesses an initial hardening rate, which subsequently decreases with increasing deformation:

$$\frac{d\hat{\sigma}_\varepsilon}{d\varepsilon}=\theta=\theta_0[1-F(\hat{\sigma}_\varepsilon)] \quad (4.3.4.21.)$$

where θ_0 refers to the stage II strain hardening rate or the stage of rapid work hardening, and $F(\hat{\sigma}_\varepsilon)$ is an empirically derived dynamic recovery rate.

For successful application of equation Eq. 4.3.4.21. is correct choice of function F, which describe structure evolution is important. Several functions have been investigated in the past and all of them are based on the simple Voce hardening law [55]. Follansbee and Kocks [59] chose the following form, which is a modified Voce empirical hardening rule – tanh rule:

$$F(\hat{\sigma}_\varepsilon) = \left(\frac{\tanh\left[\alpha \frac{\hat{\sigma}_\varepsilon}{\hat{\sigma}_{\varepsilon s}(\dot{\varepsilon}, T)} \right]}{\tanh(\alpha)} \right) \tag{4.3.4.22.}$$

where α is an empirical best-fit constant which dictates the rate at which saturation is achieved, $\hat{\sigma}_{\varepsilon s}$ is temperature and rate-sensitive saturation stress, $\hat{\sigma}_\varepsilon$ represents the flow stress contribution from dislocation accumulation and annihilation.

Applying fitting process on mechanical threshold stress data at all the strains rates, usingequation Eq. 4.3.4.22., which describes hardening rule, it is possible to determine factors θ_0 and σ_{ε_s} at all strain rates.

After fitting initial hardening rate data θ_0 in the respect to the strain rate data $\dot{\varepsilon}$, stage initial hardening rate θ_0 could be expressed by an empirical relationship:

$$\theta_0 = a_0 + a_1 \ln(\dot{\varepsilon}) + a_2 \dot{\varepsilon}^n \tag{4.3.4.23.}$$

Saturation threshold stress $\hat{\sigma}_{\varepsilon s o}$ (0K) and normalized activation energy $g_{o\varepsilon s}$

Saturation stress $\hat{\sigma}_{\varepsilon s}$ is function of temperature and strain rate [60]:

$$\hat{\sigma}_{\varepsilon s} = \hat{\sigma}_{\varepsilon s 0} \left(\frac{\dot{\varepsilon}}{\dot{\varepsilon}_{\varepsilon s 0}} \right)^{1/n} \tag{4.3.4.24.}$$

where $n = g_{0\varepsilon s} \mu b^3 / kT$

Above equation could be easily rearranged in a following form:

$$\ln(\hat{\sigma}_{\varepsilon s}) = \ln(\hat{\sigma}_{\varepsilon s 0}) - \left(\frac{1}{g_{0\varepsilon s}} \right) \frac{KT}{\mu b^3} \ln\left[\frac{\dot{\varepsilon}_{o\varepsilon s}}{\dot{\varepsilon}} \right] \tag{4.3.4.25.}$$

Normalized activation energy (saturation) $g_{o\varepsilon s}$ and mechanical threshold stress associated with saturation of evolving structure $\hat{\sigma}_{\varepsilon s o}$, now could be calculated using a Fisher-type plot approach [58].

Adiabatic heating effects

The MTS strength model considers the effect of adiabatic heating under dynamic – high strain rate loading conditions, for strain rates above $\dot{\varepsilon} \approx 500 s^{-1}$. Temperature increases due adiabatic heating is given by the relationship:

$$\Delta T = \frac{\psi}{\rho C_p} \int \sigma(\varepsilon) d\varepsilon \qquad (4.3.4.26.)$$

where ψ is percentage of the work of plastic deformation, which is converted into heat, σ and ε are the true stress and true strain, ρ is density, and C_p is the temperature dependent specific heat, that can be written in form of empirical relationship as:

$$C_p = A_0 + A_1 T + A_2 / T^2 . \qquad (4.3.4.27.)$$

4.4. Results and conclusions

4.4.1. Experimental data

Figure Fig. 4.4.1.1. shows a classical strain rate dependant response for AA7010. The effects of strain rate and temperature are clearly observed since the difference in the flow stress between the different strain rates and temperatures are distinct and significant. This set of data has been used for derivation of parameters for temperature and strain rate dependent strength material models. For describing orthotropic properties of materials, it is most convenient to choose a reference direction when using Hill's plastic anisotropy theory. We adopted longitudinal (L) direction as a reference direction and parameters for JC and MTS strength models have been derived for this set of data.

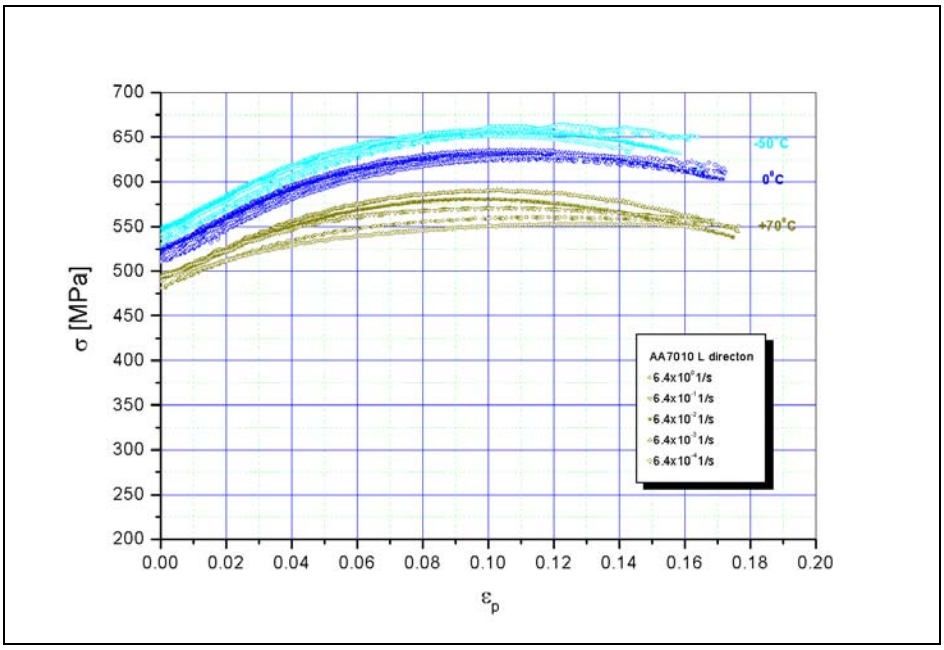

Fig. 4.4.1.1. AA7010 stress-strain curves for L direction at different strain rates and temperatures

4.4.2. Derivation of MTS model parameters for AA7010

On the basis of the procedure described in section 4.3.4. for determination of MTS material model parameters, constants for AA7010 were calculated. The following form of the MTS model is chosen to fit experimental data:

$$\frac{\sigma}{\mu} = \frac{\sigma_a}{\mu} + S_\varepsilon(\dot{\varepsilon}, T)\frac{\hat{\sigma}_\varepsilon}{\mu_0} \qquad (4.4.2.1.)$$

All experimental data used as the input for the calculation of AA7010 constants has been obtained from uniaxial tensile test.

4.4.2.1. Athermal stress

To fit the stress data to the above equation, the athermal stress was estimated as: $\sigma_a = 10MPa$.

No rigorous analysis was performed to calculate this value of σ_a, but athermal stress on the order of 10MPa is not unreasonable [57]. For example Zerili and Armstrong determined for copper a Hall-Petch constant with value of $k_y = 1.58 \times 10^{-4} GPam^{1/2}$. Assuming packet of grain size on the order of $100\mu m$, the Hall-Petch effect is $k_y d^{-1/2} \approx 10MPa$.

4.4.2.2. Shear modulus

The shear modulus for face-centred cubic (fcc) materials can be calculated using following formulations:

$$\mu = \sqrt{C_{44}(C_{11} - C_{12})/2} \qquad (4.4.2.2.1.)$$

where C_{ij} elastic constants are defined with following definition:

$$C_{ij} = a - bT^2/(T + c) \qquad (4.4.2.2.2.)$$

Parameters included in formulation of elastic constants are presented in the following table:

Table 4.4.2.2.1. Elastic constants for AA7010

C_{ij}	C_{11}	C_{12}	C_{44}
$a[10^4 MPa]$	11.44279	6.19963	3.17067
$b[10^1 MPa/K]$	6.16193	1.05999	1.68226
$c[K]$	420.4	445.0	130.0

For reasons of simplicity empirical relation for shear modulus could be used as:

$$\mu = b_0 - \frac{b_1}{\exp(\frac{b_2}{T}) - 1}, \qquad (4.4.2.2.3.)$$

where $b_0 = 28.83GPa$ shear modulus at 0K and $b_1 = 4.45GPa$, $b_2 = 248.5K$ are fitting constants.

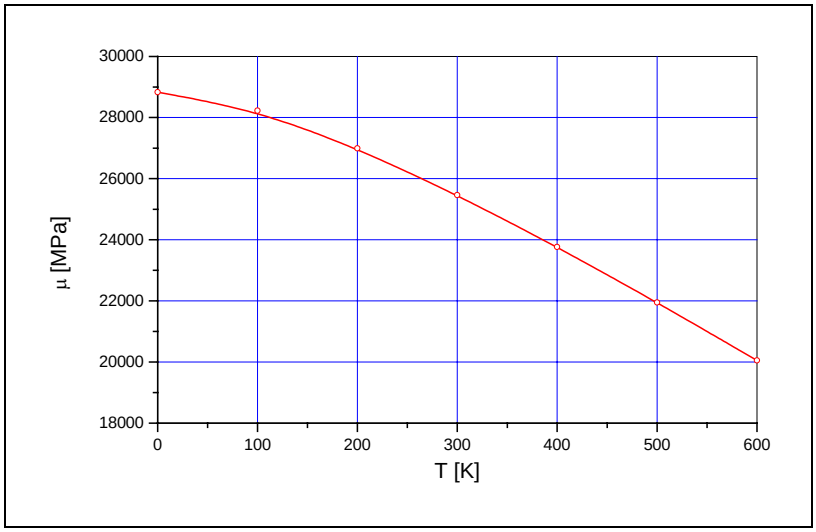

Fig. 4.4.2.2.1. Graf of shear modulus in function of temperature

4.4.2.3. Thermal activation function

Constants used in the thermal activation function

$$S_\varepsilon = \left[1 - \left(\frac{kT\ln(\dot{\varepsilon}_{0\varepsilon}/\dot{\varepsilon}^p)}{\mu b^3 g_{0\varepsilon}}\right)^{1/q_\varepsilon}\right]^{1/p_\varepsilon} \qquad (4.4.2.3.1.)$$

like reference strain-rate $\dot{\varepsilon}_{0\varepsilon}$, p_ε and q_ε glide obstacle profile parameters are based on empirical observation, and they were determined as

$p_\varepsilon = 1$, $q_\varepsilon = 1$ and $\dot{\varepsilon}_{0\varepsilon} = 1X10^7 s^{-1}$.

Influence of p_ε and q_ε glide obstacle profile parameters on the shape of the thermal activation function is presented in the following figure (Fig. 4.4.2.3.1.).

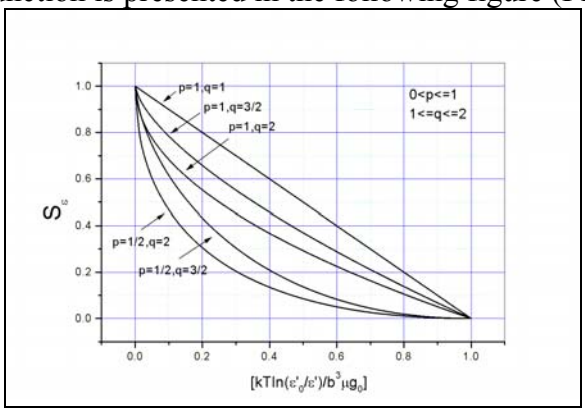

Fig. 4.4.2.3.1.Thermal activation function shapes and corresponding values of p and q

The other parameters included in the definition of thermal activation function were determined as:

$k = 1.38X10^{-23} J/K$ - Boltzman's constant and $b = 0.286X10^{-9} m$ - Burgers vector

where the ratio between Boltzman's constant and Burgers vector has been found as:

$$\frac{k}{b^3} = 0.5899\frac{MPa}{K}$$

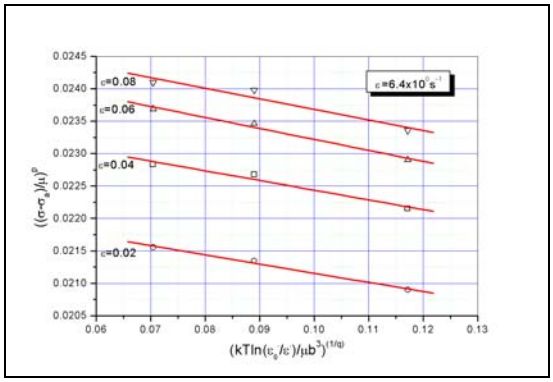

Fig. 4.4.2.3.2. Normalized data for flow stress versus temperature at $\dot{\varepsilon} = 6.4X10^0 s^{-1}$

From equation Eq. 4.3.4.13., which describes relation between applied stress and mechanical threshold stress, it is possible to determine $g_{0\varepsilon}$. After rearranging equation Eq. 4.3.4.13. in the form of the fitting equation,

$$\left(\frac{\sigma-\sigma_a}{\mu}\right)^{p_\varepsilon} = \left(\frac{\hat{\sigma}_\varepsilon}{\mu_0}\right)^{p_\varepsilon} - \left(\frac{\hat{\sigma}_\varepsilon}{\mu_0}\right)^{p_\varepsilon}\left(\frac{1}{g_{o\varepsilon}}\right)^{1/q_\varepsilon}\left[\frac{kT}{\mu b^3}\ln\left(\frac{\dot{\varepsilon}_{oi}}{\dot{\varepsilon}}\right)\right]^{1/q_\varepsilon} \qquad (4.4.2.3.2.)$$

and presenting mechanical data in a Fisher plot format (Fig. 4.4.2.3.3.– Fig. 4.4.2.3.6.), average value of normalized activation energy has been found as $g_{0\varepsilon} = 1.6$.

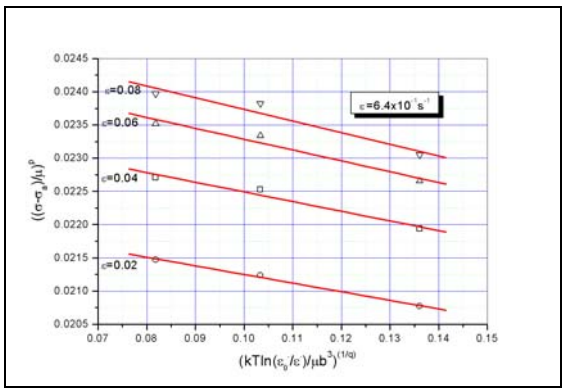

Fig. 4.4.2.3.3. Normalized data for flow stress versus temperature at $\dot{\varepsilon} = 6.4X10^{-1}\,s^{-1}$

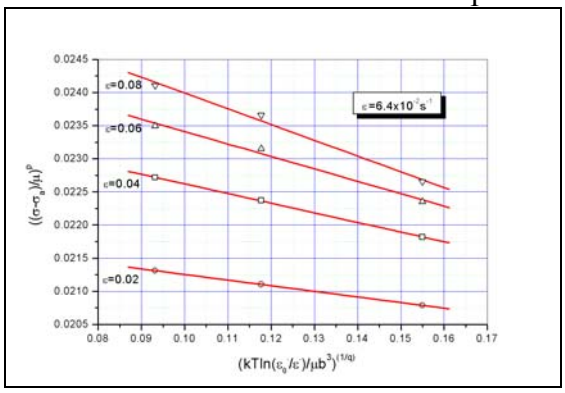

Fig. 4.4.2.3.4. Normalized data for flow stress versus temperature at $\dot{\varepsilon} = 6.4X10^{-2}\,s^{-1}$

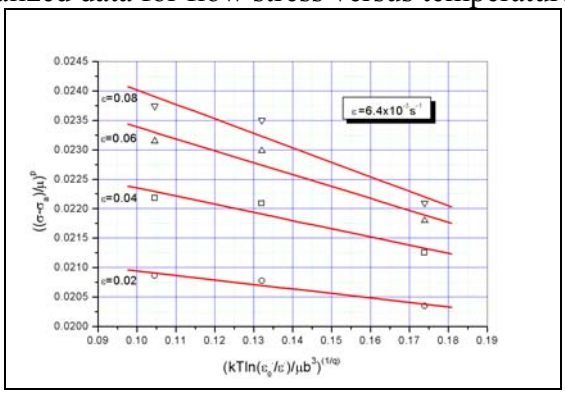

Fig. 4.4.2.3.5. Normalized data for flow stress versus temperature at $\dot{\varepsilon} = 6.4X10^{-3}\,s^{-1}$

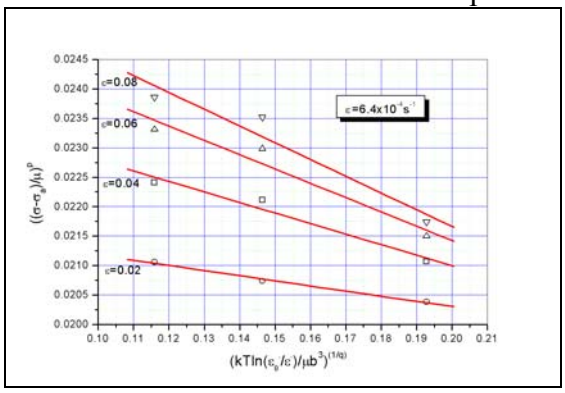

Fig. 4.4.2.3.6. Normalized data for flow stress versus temperature at $\dot{\varepsilon} = 6.4X10^{-4}\,s^{-1}$

4.4.2.4. Mechanical threshold stress $\hat{\sigma}_{\varepsilon}(\varepsilon)$

From the general form of MTS model when athermal hardening is subtracted from overall stress, value of $\hat{\sigma}_{\varepsilon}$ is determined with following relation:

$$\hat{\sigma}_{\varepsilon}(\varepsilon) = \frac{\mu_0}{S_{\varepsilon}}\left(\frac{\sigma(\varepsilon)}{\mu} - \frac{\sigma_a}{\mu_0}\right) \qquad (4.4.2.4.1.)$$

For each curve of $\sigma(\varepsilon)$ corresponding mechanical threshold stress $\hat{\sigma}_{\varepsilon}(\varepsilon)$ could be derived from series of tests, where material is loaded at different temperatures at a fixed strain rate (Fig. 4.4.2.4.1 – Fig. 4.4.2.4.3).

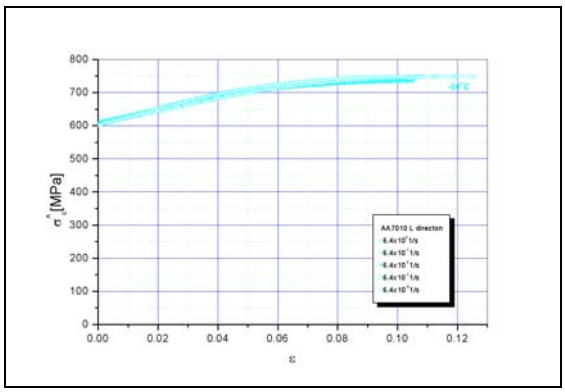

Fig. 4.4.2.4.1 Mechanical threshold data at T=223.15 K.

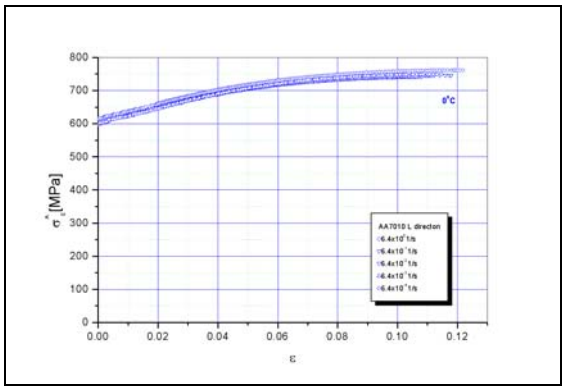

Fig. 4.4.2.4.2. Mechanical threshold data at T=273.15 K.

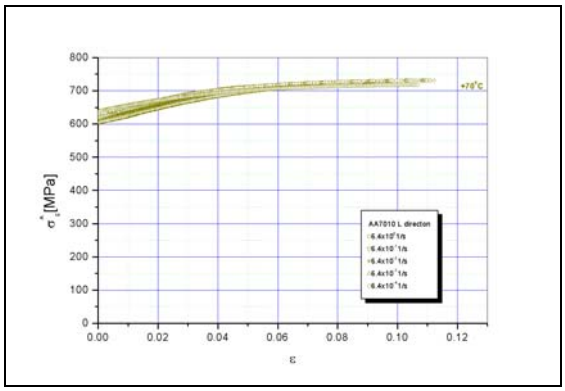

Fig. 4.4.2.4.3. Mechanical threshold data at T=343.15 K.

4.4.2.5. Hardening rule

Mechanical threshold stress $\hat{\sigma}_{\varepsilon}$ evolves with strain and this process can be described with modified Voce empirical hardening rule – tanh rule [59]:

$$\frac{d\hat{\sigma}_{\varepsilon}}{d\varepsilon} = \theta_0 \left[1 - \left(\frac{\tanh\left[\alpha \frac{\hat{\sigma}_{\varepsilon}}{\hat{\sigma}_{\varepsilon s}(\dot{\varepsilon}, T)} \right]}{\tanh(\alpha)} \right) \right] \qquad (4.4.2.5.1.)$$

where θ_0 is initial hardening rate, which subsequently decreases with increasing deformation, $\alpha = 2$ is an empirical best-fit constant which dictates the rate at which saturation is achieved and $\hat{\sigma}_{\varepsilon s}$ is temperature and rate-sensitive saturation stress.

Applying fitting process on the above equation, which describes the hardening rule with mechanical threshold stress data at all the strains rates, it is possible to determine factors θ_0 and σ_{ε_s} at all strain rates (Fig. 4.4.2.5.1. - Fig. 4.4.2.5.5.).

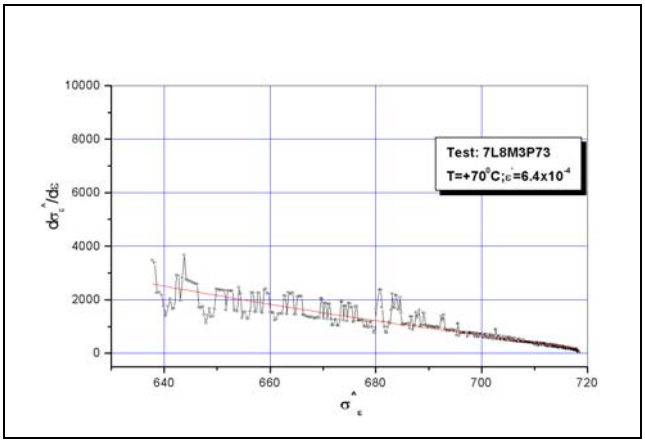

Fig. 4.4.2.5.1. Variation of the strain hardening rate versus threshold stress. Hardening curve used in MTS model at T= 343.15 K and 6.4 x 10^{-4} 1/s.

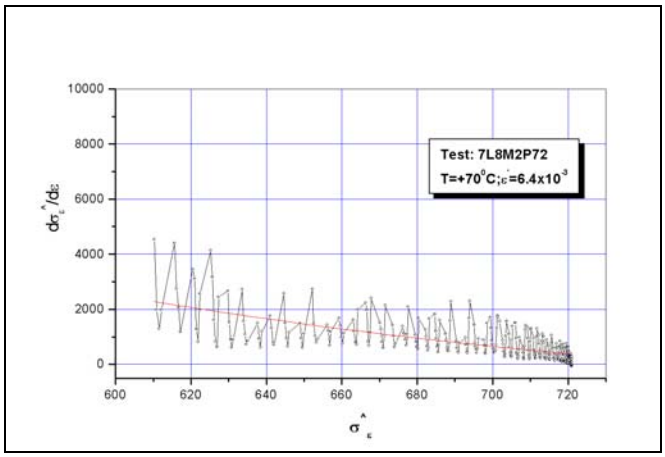

Fig. 4.4.2.5.2. Variation of the strain hardening rate versus threshold stress. Hardening curve used in MTS model at T= 343.15 K and 6.4 x 10^{-3} 1/s.

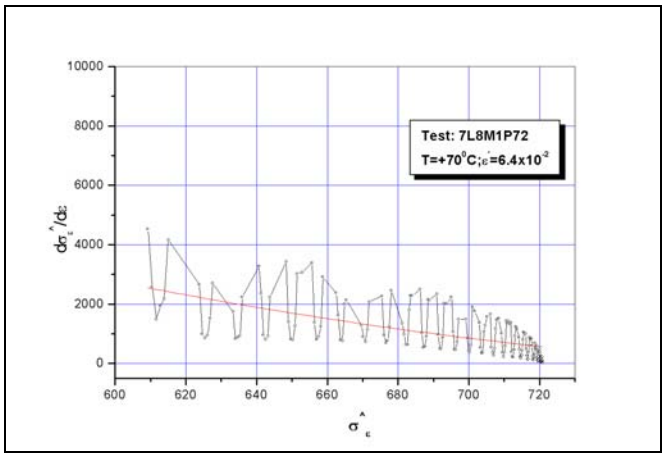

Fig. 4.4.2.5.3. Variation of the strain hardening rate versus threshold stress. Hardening curve used in MTS model at T= 343.15 K and 6.4 x 10^{-2} 1/s.

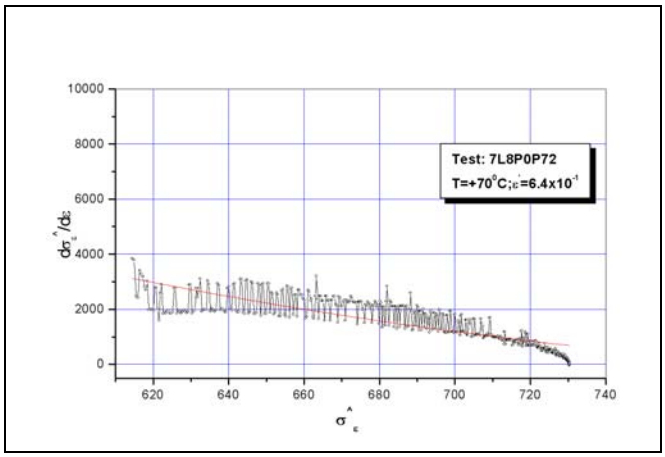

Fig. 4.4.2.5.4. Variation of the strain hardening rate versus threshold stress. Hardening curve used in MTS model at T= 343.15 K and 6.4 x 10^{-1} 1/s.

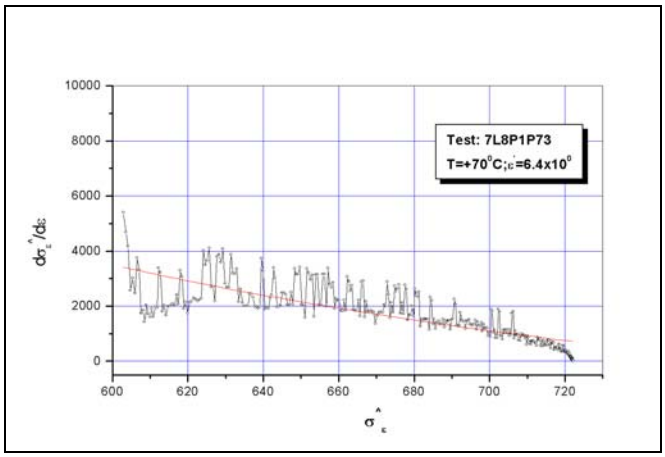

Fig. 4.4.2.5.5. Variation of the strain hardening rate versus threshold stress. Hardening curve used in MTS model at T= 343.15 K and 6.4 x 10^{0} 1/s.

4.4.2.6. Initial hardening rate θ_0

It has been observed that initial hardening rate data are strongly dependant on the strain rate, which is similar to the behaviour of OHFC Cu [59]. After fitting initial hardening rate data θ_0 in the respect to the strain rate $\dot{\varepsilon}$, it has been found that initial hardening rate θ_0 could be expressed by an empirical relationship (Fig. 4.4.2.6.1.):

$$\theta_0 = a_0 + a_1 \ln(\dot{\varepsilon}) + a_2 \dot{\varepsilon}^n \qquad (4.4.2.6.1.)$$

and following parameters were determined as: $a_0 = 67604.6MPa$, $a_1 = 1816.9MPa$, $a_2 = 202.3MPa$ and .

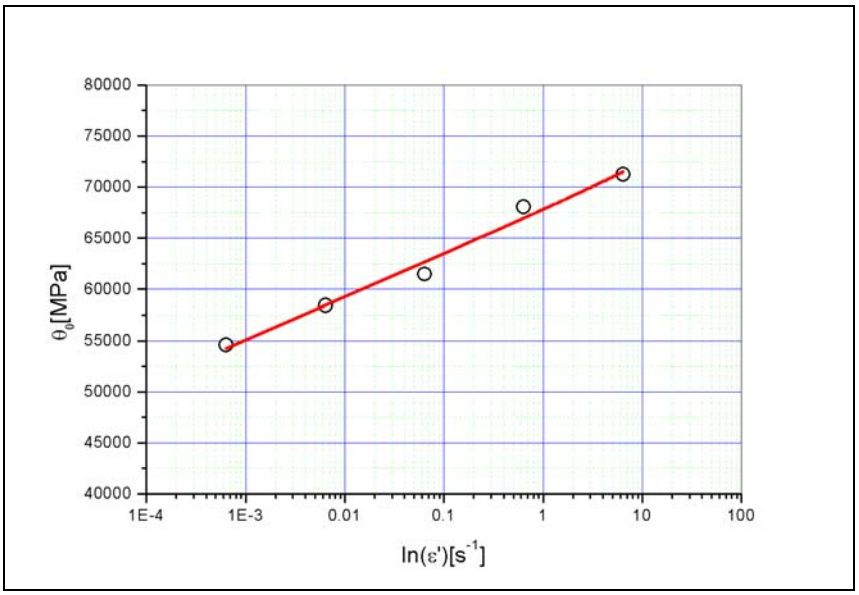

Fig. 4.4.2.6.1. Variation of θ_0 with strain rate

4.4.2.7. Saturation threshold stress $\hat{\sigma}_{\varepsilon s o}$ (0K)

Saturation stress $\hat{\sigma}_{\varepsilon s}$ is function of temperature and strain rate:

$$\hat{\sigma}_{\varepsilon s} = \hat{\sigma}_{\varepsilon s 0} \left(\frac{\dot{\varepsilon}}{\dot{\varepsilon}_{\varepsilon s 0}} \right)^{\frac{kT}{g_{0\varepsilon s} \mu b^3}} \qquad (4.4.2.7.1.)$$

After rearranging above equation in a form of fitting equation:

$$\ln(\hat{\sigma}_{\varepsilon s}) = \ln(\hat{\sigma}_{\varepsilon s 0}) - \left(\frac{1}{g_{0\varepsilon s}} \right) \frac{KT}{\mu b^3} \ln\left[\frac{\dot{\varepsilon}_{o\varepsilon s}}{\dot{\varepsilon}} \right], \qquad (4.4.2.7.2.)$$

and plotting experimental data in a Fisher-type plot format (Fig. 4.4.2.7.1.), following data were determined: normalized activation energy (saturation) $g_{0\varepsilon s} = 5.54$ and mechanical threshold stress associated with saturation of evolving structure $\hat{\sigma}_{\varepsilon s 0} = 801.01MPa$.

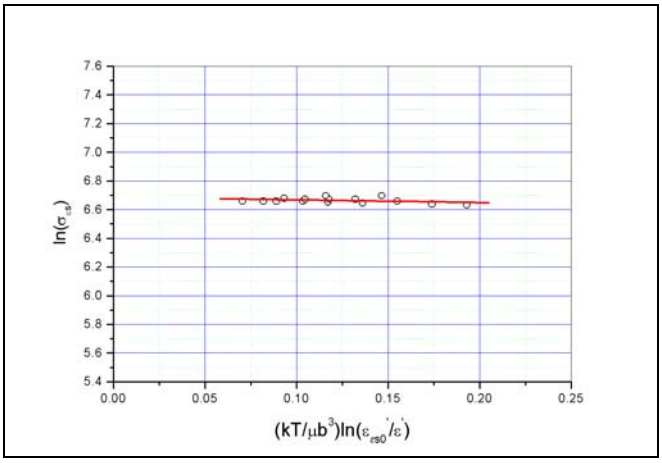

Fig. 4.4.2.7.1. Arrhenius plot of the temperature and strain-rat sensitivity of saturation stress for AA7010

4.4.2.8. Adiabatic heating effects

The MTS strength model considers the effect of adiabatic heating under dynamic – high strain rate loading conditions, for strain rates above $\dot{\varepsilon} \approx 500 s^{-1}$. Temperature increases due adiabatic heating is given by the relationship:

$$\Delta T = \frac{\psi}{\rho C_p} \int \sigma(\varepsilon) d\varepsilon \qquad (4.4.2.8.1.)$$

where $\psi = 0.95$ is percentage of the work of plastic deformation, which is converted into heat, σ and ε are the true stress and true strain, $\rho = 2.810 \frac{Mg}{m^3}$ is density, and C_p is the temperature dependent specific heat, that can be written in form of empirical relationship as (Fig. 4.4.2.8.1.):

$C_p = A_0 + A_1 T + A_2 / T^2$

with following parameters $A_0 = 0.7995$, $A_1 = 0.00039$ and $A_2 = -2775.2755$, for this material.

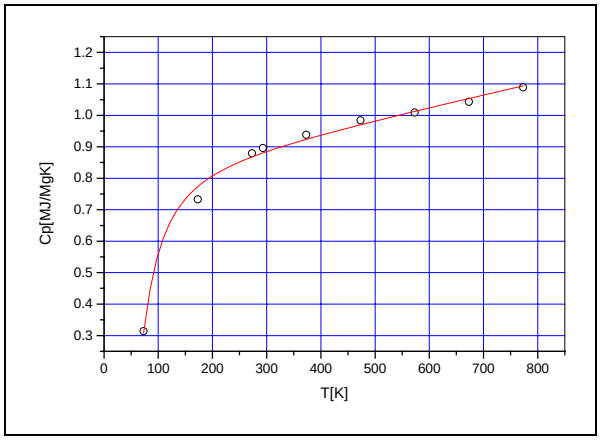

Fig. 4.4.2.8.1. Dependence of specific heat on temperature

Comparisons of experimental stress-strain curves and Mechanical Threshold Stress model fit are given on the following graphs (Fig. 4.4.2.8.2. - Fig. 4.4.2.8.6.).

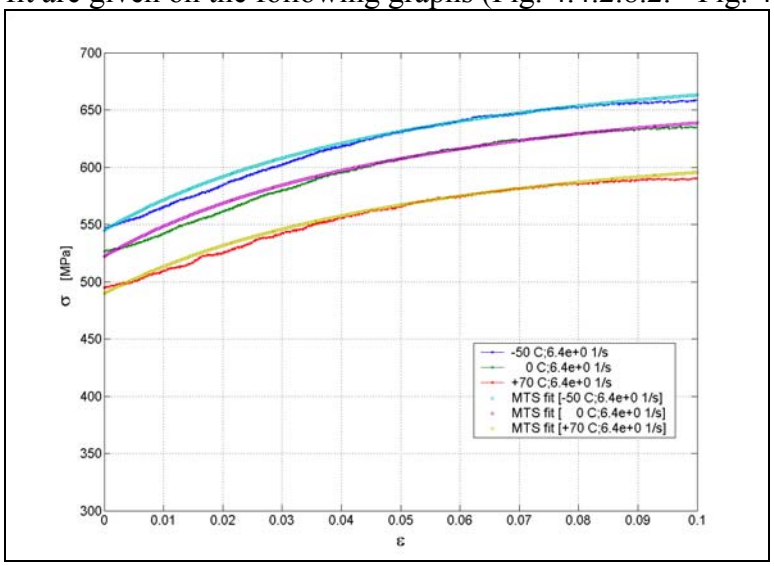

Fig. 4.4.2.8.2. Stress-strain response of AA7010 at $\varepsilon = 6.4x10^{0} s^{-1}$

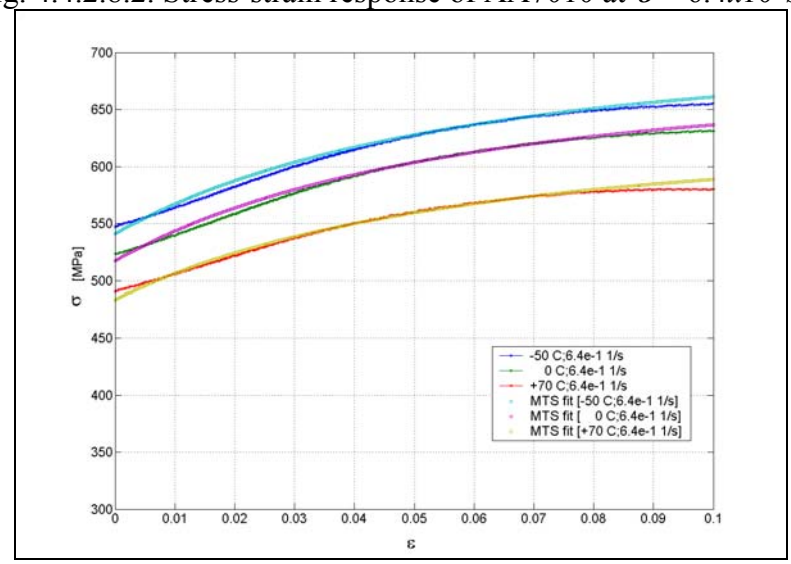

Fig. 4.4.2.8.3. Stress-strain response of AA7010 at $\boldsymbol{\varepsilon} = 6.4\boldsymbol{x}10^{-1}\boldsymbol{s}^{-1}$

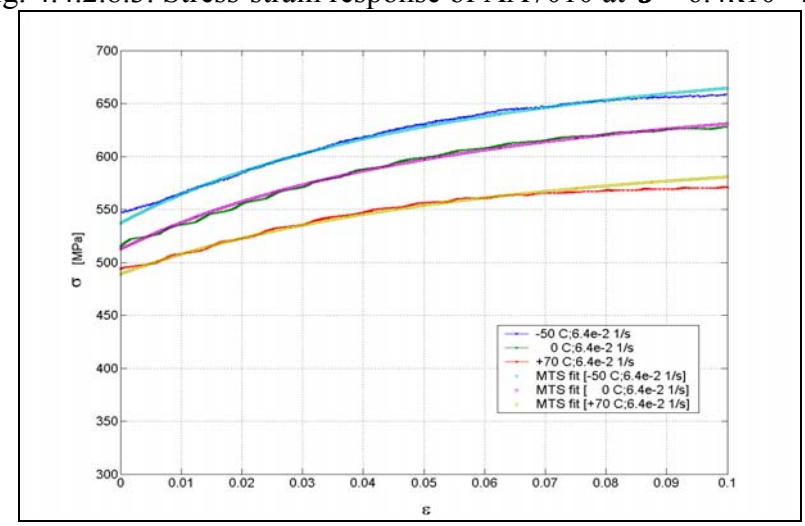

Fig. 4.4.2.8.4. Stress-strain response of AA7010 at $\boldsymbol{\varepsilon} = 6.4\boldsymbol{x}10^{-2}\boldsymbol{s}^{-1}$

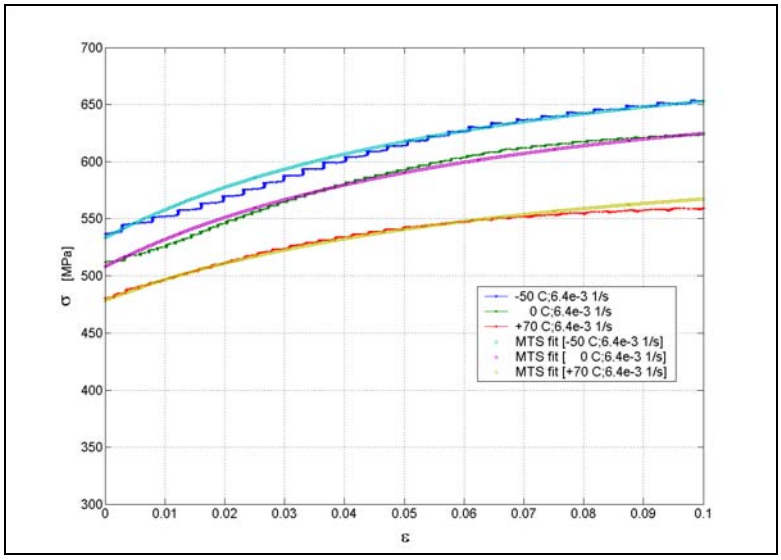

Fig. 4.4.2.8.5. Stress-strain response of AA7010 at $\dot{\varepsilon} = 6.4x10^{-3}\, s^{-1}$

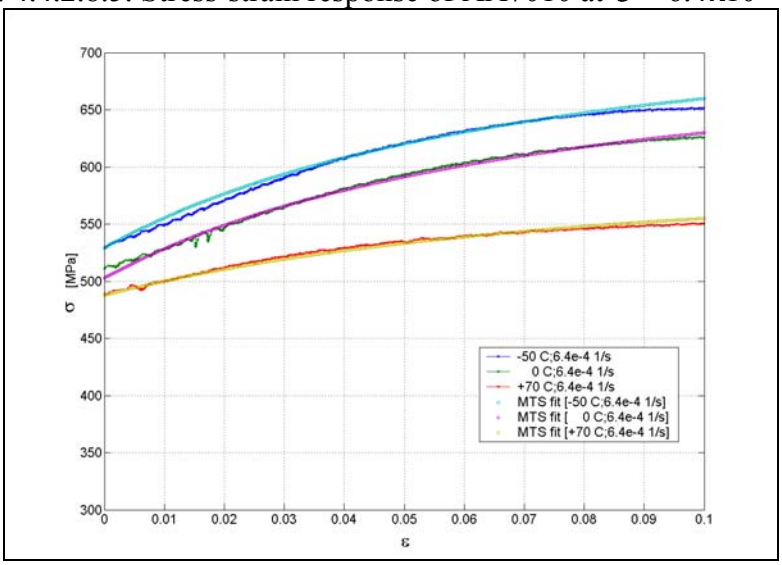

Fig. 4.4.2.8.6. Stress-strain response of AA7010 at $\dot{\varepsilon} = 6.4x10^{-4}\, s^{-1}$

Comparison of the predictions of the model with experimental results showed good agreement and the following conclusions can be made:

A two-term MTS strength model can describe very well behaviour of AA7010 in strain rate regimes from 10^{-4} to 10^{1} s^{-1}.

The MTS model can provide robust fitting results for large strain response, as function of temperature, strain rate and grain size.

The high strain rate and temperature sensitivity of the flow stress indicate that the rate controlling mechanism for deformation of AA7010 at intermediate strain rate regime [10^{-4} - 10^{1} s^{-1}] and at intermediate temperature regime [-50^{o} C - +70^{o} C] is thermal activation, which is basic mechanism for MTS model.

4.4.3. Derivation of JC model parameters for AA7010

On the basis of procedure described in Section 4.2.2. for determination of JC material model parameters, the following form of the JC model wass chosen to fit experimental data for AA7010:

$$\sigma = [A + B(\varepsilon)^n][1 + C\ln(\dot{\varepsilon}^*)][1 - (T^*)^m] \qquad (4.4.3.1.)$$

where σ is the effective plastic strain, $\dot{\varepsilon}^* = \dot{\varepsilon} / \dot{\varepsilon}_{ref}$ is normalized effective plastic strain rate, n is the work hardening exponent and A, B, C and m are constants. The quantity T^* is defined as:

$$T^* = (T_{ref} - 298)/(T_{melt} - 298) \qquad (4.4.3.2.)$$

where T_{melt} is melting temperature and taken as the solidus temperature for an alloy.

At the reference temperature $T_{ref} = 223.15K$ and for the strain rate of interest $\varepsilon_{ref} = 6.4x10^0 s^{-1}$, above equation can be written as:

$$\sigma = [A + B(\varepsilon)^n] \qquad (4.4.3.3.)$$

The stress at zero plastic strain was obtained from current data and found to be $\sigma_0 = 547.03\,\text{MPa}$. The quantity $\sigma - \sigma_0$ was calculated and plotted versus plastic strain (Fig. 4.4.3.1.). The quantities B and n were obtained from a least squares fit of the data to a power low equation as B=601.58 MPa and n=0.65.

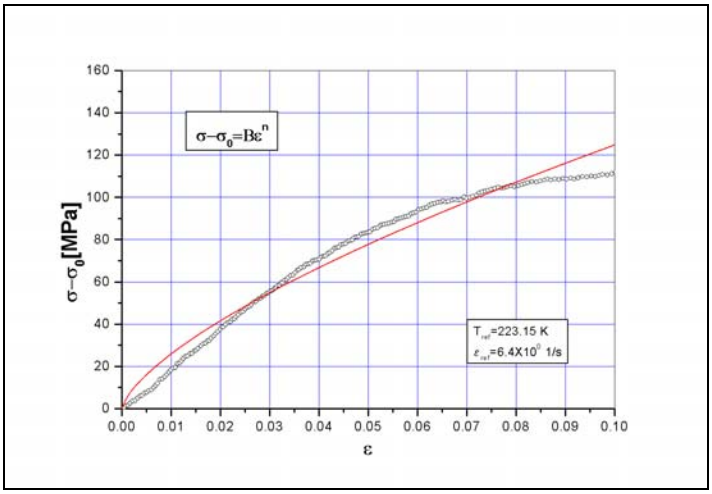

Fig. 4.4.3.1. $\sigma - \sigma_0$ versus plastic strain at $T_{ref} = 223.15K$ and $\varepsilon_{ref} = 6.4x10^0 s^{-1}$

The parameter C was obtained from $\sigma - \dot{\varepsilon}$ data. At reference temperature and for constant strain, constitutive equation can be written as:

$$\sigma = \sigma_a[1 + C\ln(\dot{\varepsilon}^*)] \text{ or } \sigma/\sigma_a - 1 = C\ln(\dot{\varepsilon}^*), \qquad (4.4.3.4.)$$

where σ_a is the stress at strain rate of interest $\dot{\varepsilon}^* = 1$. For constant strain, value of σ_a can be calculated, and $\sigma/\sigma_a - 1$ can be plotted versus $\dot{\varepsilon}$ on a semi-log plot (Fig. 4.4.3.2.). A least squares fit to the data gives, as an average value, C=0.0022.

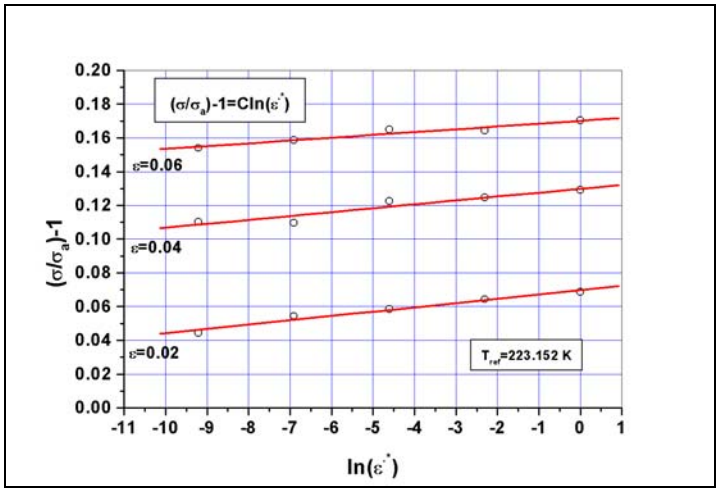

Fig. 4.4.3.2. σ/σ_a versus strain rate at $T_{ref} = 223.15K$

The parameter m was determined from the stress-temperature response of the alloy. At constant strain and strain rate, constitutive equation can be written as:

$$\sigma = \sigma_b[1 - (T^*)^m] \text{ or } \sigma/\sigma_b = [1 - (T^*)^m] \qquad (4.4.3.5.)$$

where σ_b is the stress at reference temperature. For constant strain and constant strain rate, value of σ_b can be calculated, and data plotted as σ/σ_b versus T^* (Fig. 4.4.3.2.). After applying least squares fit of the data, average value of parameter m was found as m=1.3.

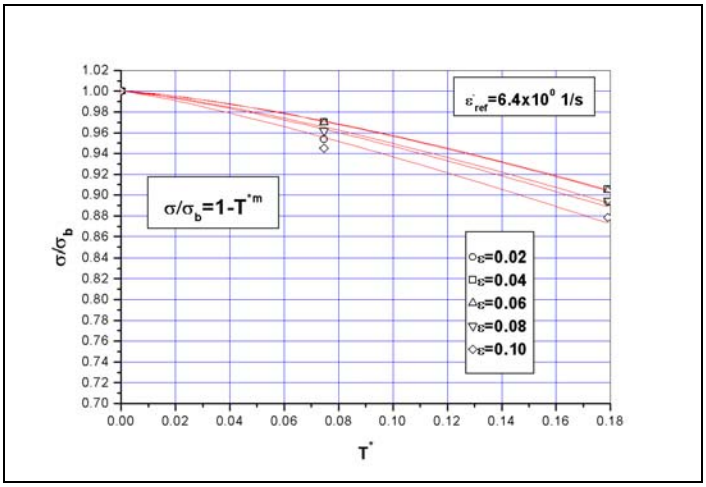

Fig. 4.4.3.2. σ/σ_b versus homologous temperature

Comparisons of experimental stress-strain curves and Johnson-Cook model fit are given on the following graphs (Fig. 4.4.3.3. – Fig. 4.4.3.7.).

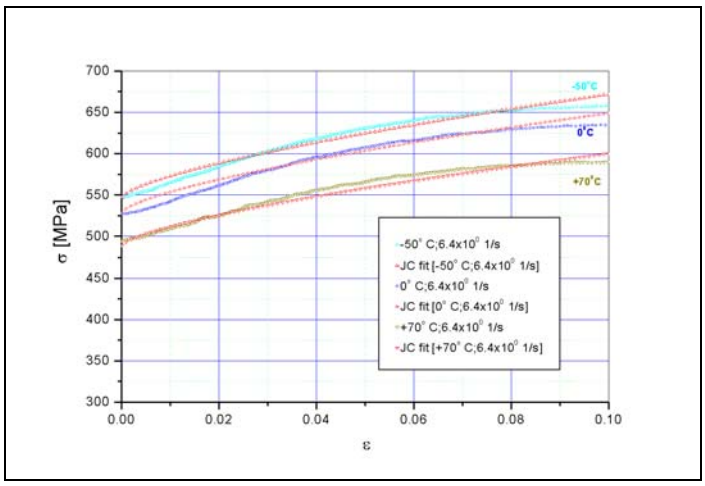

Fig. 4.4.3.3. Stress-strain response of AA7010 at $\varepsilon = 6.4x10^{0}s^{-1}$

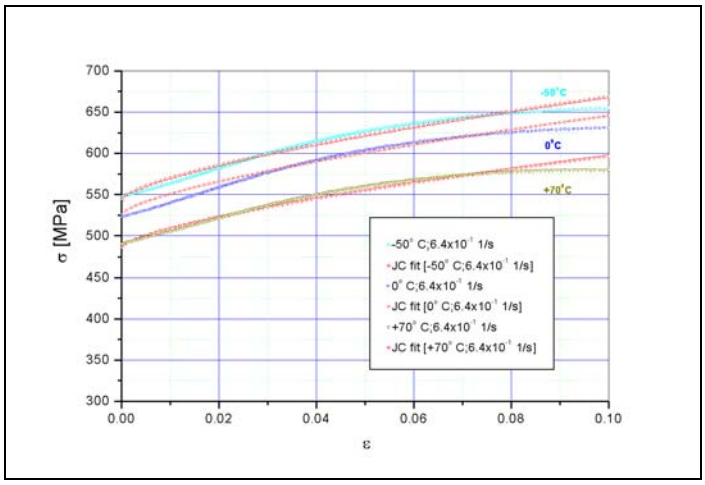

Fig. 4.4.3.4. Stress-strain response of AA7010 at $\varepsilon = 6.4x10^{-1}s^{-1}$

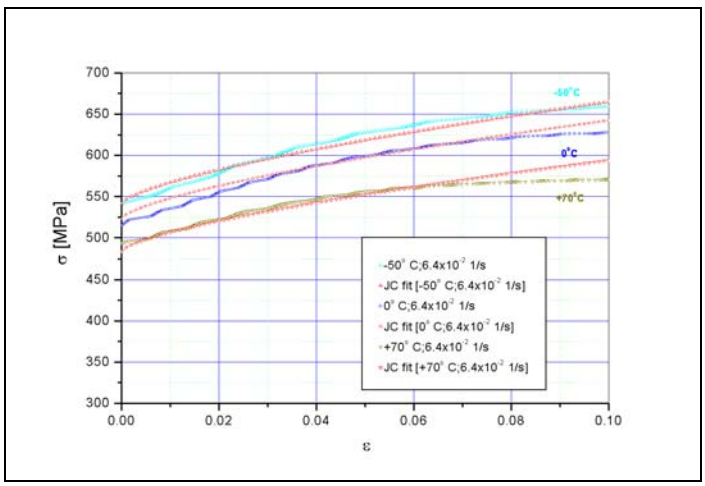

Fig. 4.4.3.5. Stress-strain response of AA7010 at $\varepsilon = 6.4x10^{-2}s^{-1}$

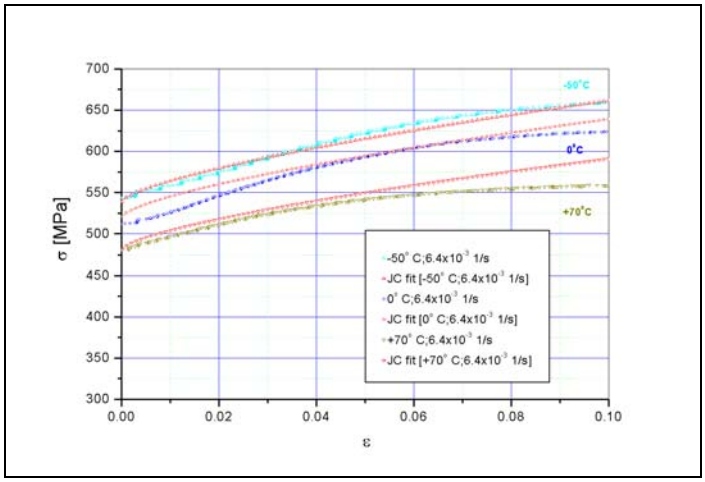

Fig. 4.4.3.6. Stress-strain response of AA7010 at $\varepsilon = 6.4x10^{-3}s^{-1}$

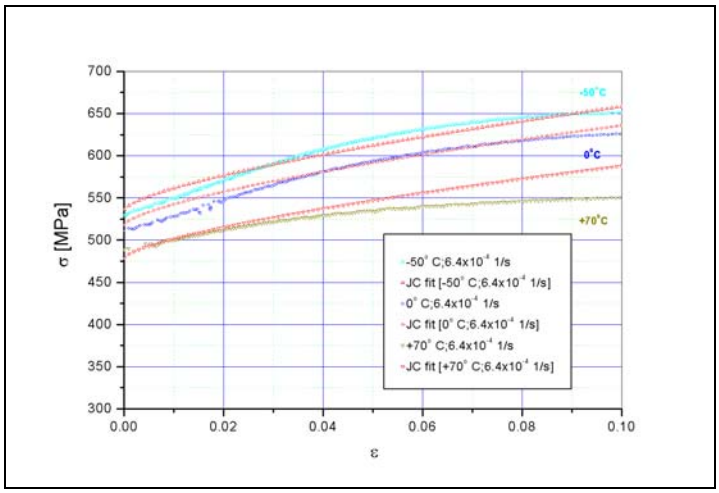

Fig. 4.4.3.7. Stress-strain response of AA7010 at $\varepsilon = 6.4x10^{-4}s^{-1}$

The main advantage of the Johnson-Cook model over MTS model is in the number of materials for which the parameters are known. At the same time the advantage of MTS model over Johnson-Cook model is in the fact that MTS is based on physical processes taking place in deforming material and therefore can more accurately represent the behaviour of the material.

It is generally accepted that at large strains most metallic materials tend to approach a finite "saturation stress" or approach a constant but small hardening rate at large strains, and we can observe that such saturation is lacking in the model like Johnson-Cook. The MTS model contrarily uses a differential form to fit the experimental data and it has been shown that modified form of the MTS model can fit the experimental result much better.

The lack of saturation stress as an integral part of the models like Johnson-Cook, makes it impossible to create a satisfactory model fit at small strains if these models were previously optimised for large strain applications and vice versa.

4.4.4. Taylor impact test simulation

In order to test the MTS and JC models and the calculated constants for AA7010, a Taylor impact test simulation has been done.

Parameters for the constitutive relations were derived on the basis of tensile tests, and used as input parameters for the numerical simulation of Taylor impact test. The simulations were performed with DYNA3D computer code and compared with experimental results for two different impact velocities 200 m/s and 214 m/s.

From AA7010 plate, several Taylor cylinder specimens were machined, tested using a gas gun, and their final deformed shapes were digitised. Taylor cylinder specimens were 9.30 mm initial diameter cylinders with initial length 46.50 mm giving the length-to-diameter ratio L/D=5. Test cylinders have been machined and tested by Royal Military College of Science at Shrivenem.

Definition of material model MTS in DYNA3D computer code was modified with definition of Mechanical Threshold Stress material model in the manner, which is previously described, and material model JC was used as implemented in DYNA3D.

In the simulations the $cm-g-\mu s$ systems of units was used. MTS and JC material models were used in the combination with a Gruneisen Equation of State.

In order to reduce the number of elements in the simulations model, and the overall time of simulations, only quarter of Taylor cylinder was modelled with a uniform solid butterfly mesh (Fig. 4.4.4.1.). The material parameters that were used in the analyses are summarized in the following tables (Table 4.4.4.1. – Table 4.4.4.3.).

Table 4.4.4.1. JC model constants for AA7010

Parameter	Description	Nominal value
G	Shear modulus	26.0 GPa
A	Yield stress constant	547.03 MPa
B	Strain hardening coefficient	601.58 Mpa
n	Strain hardening exponent	0.65
C	Strain rate dependence coefficient	0.0022
m	Temperature dependence coefficient	1.30
T_m	Melt temperature	893.15 K
T_r	Reference temperature	293.15 K
$\dot{\varepsilon}_0$	Reference strain rate	$6.4x10^{0}1/s$
C_p	Specific heat	896 J/kgK
$p_{cut}(\sigma_m)$	Pressure cutoff (Failure stress)	1.3 GPa

Table 4.4.4.2. MTS model constants for AA7010

Parameter	Description	Nominal value
σ_a	Athermal rate independent threshold stress	10.0 MPa
σ_0	Initial threshold stress at zero plastic strain	600.0 MPa
$g_{0\varepsilon}$	Normalized activation energy	1.606
$\dot{\varepsilon}_{0\varepsilon}$	Reference strain rate	$1x10^7$ s^{-1}
B	Magnitude of Burgers vector	$0.286x10^{-9}$m
K	Boltzmann's constant	$1.38x10^{-23}$ J/K
p_ε	Free energy equation exponent	1
q_ε	Free energy equation exponent	1
A	Saturation stress equation material constant	5.542
$\hat{\sigma}_{s0}$	Saturation stress at zero degrees K	801.01 MPa
$\dot{\varepsilon}_{s0}$	Saturation stress reference strain rate	$1x10^7$ s^{-1}
a_0	Hardening function constant	67604.6 MPa
a_1	Hardening function constant	1816.9 MPa
a_2	Hardening function constant	202.3 MPa
b_0	Shear modulus at zero degrees K	28.83 GPa
b_1	Shear modulus constant	4.45 GPa
b_2	Shear modulus constant	248.5 K
T_r	Reference temperature	293.15 K
ρ	Density	2810 kg/m^3
C_p	Heat capacity	896 J/kgK

Table 4.4.4.3. Grunisen EOS constants for AA7010

Parameter	Description	Nominal value
C_0	Bulk sound speed	0.52 $cm/\mu s$
S_1	First Hugoniot slope coefficient	1.36
S_2	Second Hugoniot slope coefficient	0
S_3	Third Hugoniot slope coefficient	0
γ_0	Gruneisen coefficient	2.20
B	First order volume correction coefficient	0.48
E_0	Initial internal energy	0.0
V_0	Initial relative volume	1.0

The simulations clearly show that the JC and MTS strength models can simulate high strain rate deformation processes for wide range of temperatures.

Comparing the experimental shapes of the impact-interface footprints with DYNA3D code results (Fig. 4.4.4.2. – 4.4.4.3.), we can observe that the modified MTS material model can capture more accurately impact-interface footprint then JC model.

The MTS flow stress model needs to be carefully characterized for the material of interest within the strain, strain rate and temperature regime to obtain accurate calculation results, in this case capturing the cylinder specimen heights, and axial major and minor distributions of plastic strain. The MTS model should be

coupled with orthotropic yield surface criterion in order to capture orthotropic behaviour of AA7010.

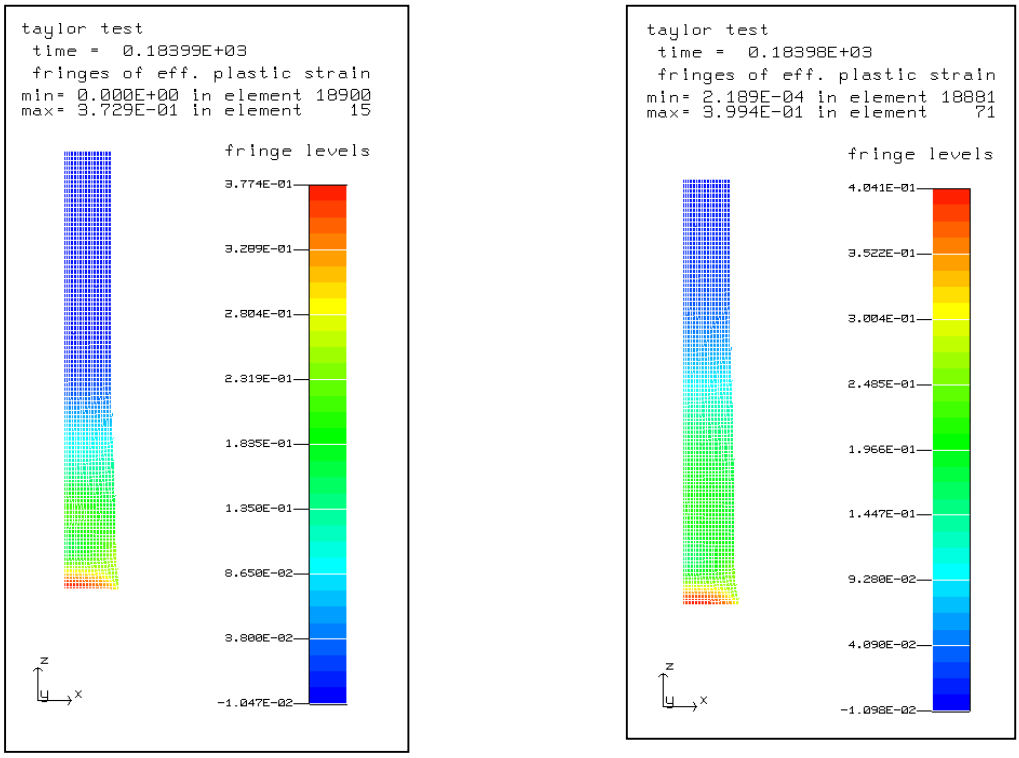

JC model MTS model

Fig. 4.4.4.1. Deformed quarter of cylinder outline and contours of effective plastic strain of the Taylor cylinder launched with initial velocity of 200 m/s

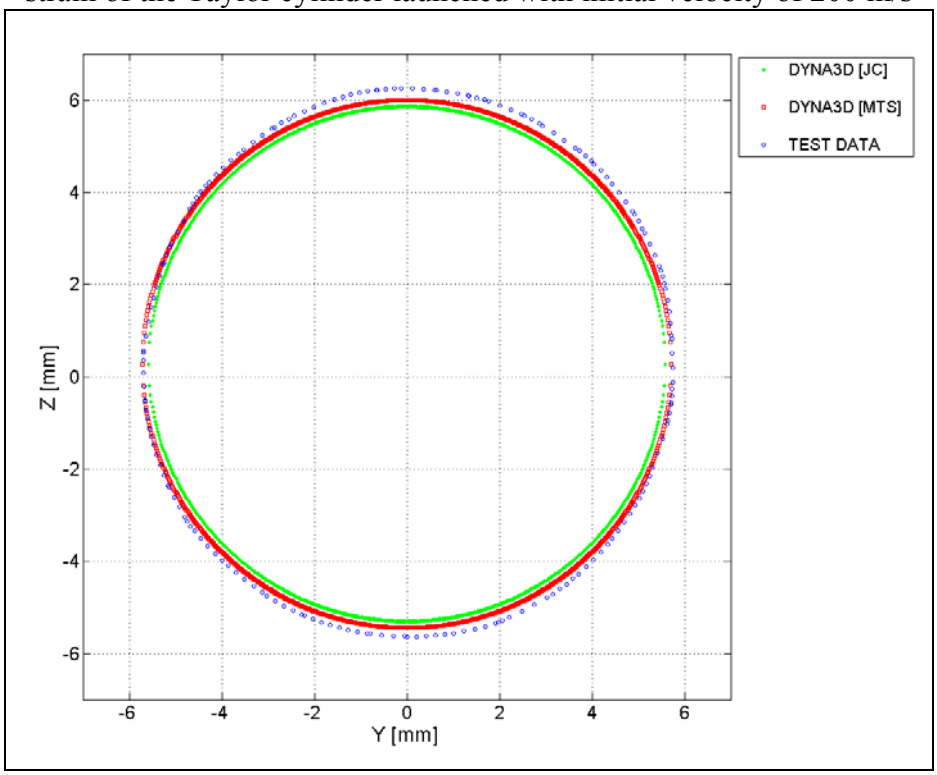

Fig. 4.4.4.2. Comparison of footprints of the Taylor cylinder launched with initial velocity of 214 m/s

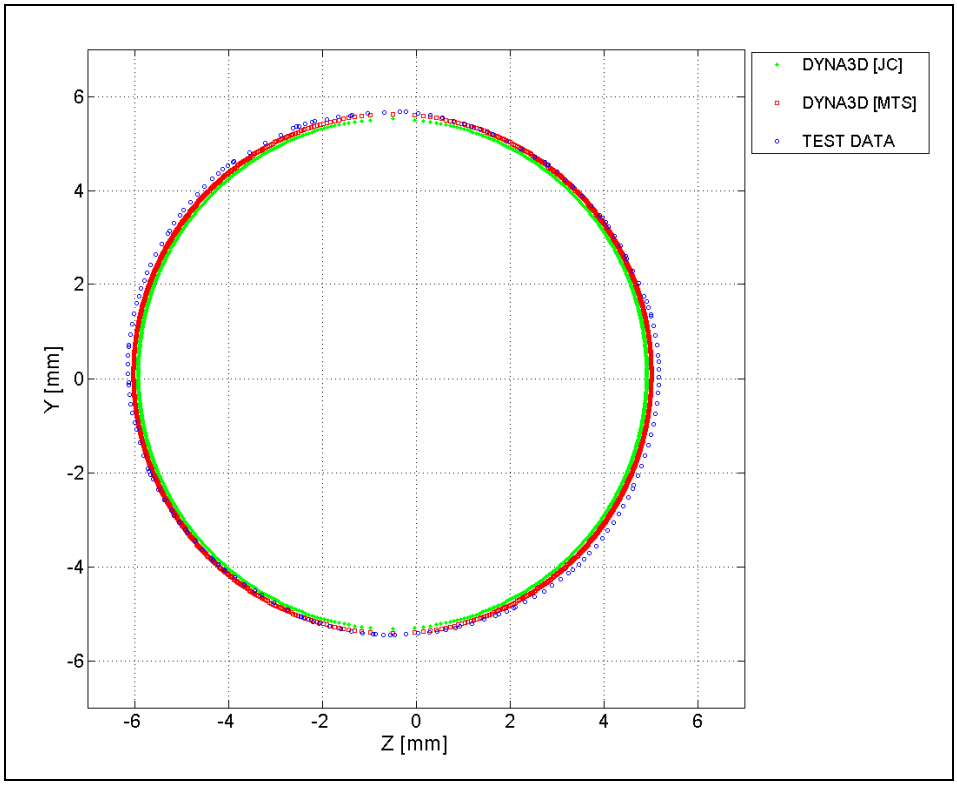

Fig. 4.4.4.3. Comparison of footprints of the Taylor cylinder launched with initial velocity of 200 m/s

5. ANISOTROPIC METAL PLASTICITY MODEL

5.1. Introduction

There are several requirements that we have to satisfy in order to be able to describe the state of the material during plastic deformation. First of all, it is essential to be able to define the point at which the material will start to yield. In a one dimensional stress state, this is straightforward, as one just has to define a value of stress that will mark the start of yielding. This point can be determined by performing a uniaxial tensile test. Even in this simple case this approach is limited as not all materials exhibit a clearly defined yield point. In the case of a complex stress state yielding is defined by a yield condition which, in general is of the form:

$$\begin{aligned} &\boldsymbol{F}\left(\boldsymbol{\sigma_{ij}},\boldsymbol{\alpha}\right)=0 \;\; \left(\boldsymbol{Yielding}\right) \\ &\boldsymbol{F}\left(\boldsymbol{\sigma_{ij}},\boldsymbol{\alpha}\right)<0 \;\; \left(\boldsymbol{No\ Yielding}\right) \end{aligned} \qquad (5.1.1.)$$

So the yield function is dependent on the stress tensor and an initial yield stress value σ_Y. If the material is yielding then F= 0, and hence:

$$dF = 0 \qquad (5.1.2.)$$

This expression is called the consistency condition, and can be interpreted as the condition that ensures that during a plastic deformation the corresponding stress-state stays on the yield surface.

A second characteristic of plasticity model is that once yielding occurrs, the yield surface has to be changed in some way. If the hardening is described using only one material constant, it implies that the hardening behaviour is assumed to be independent of the stress state. So the assumption is that the material hardens in the same way regardless of direction of loading.

The equation that describes the change in yield surface is called a Hardening Rule. The two most commonly used hardening rules are isotropic hardening and kinematic hardening. Hardening is a function either of the effective plastic strain

$$\boldsymbol{\alpha} = \bar{\boldsymbol{\varepsilon}}^{\boldsymbol{pl}} = \int_0^{\boldsymbol{\varepsilon}} \boldsymbol{d\varepsilon}^{\boldsymbol{pl}} \qquad (5.1.3.)$$

or the plastic work

$$\boldsymbol{\alpha} = \boldsymbol{W_p} = \int \boldsymbol{\sigma_{ij}} \boldsymbol{d\varepsilon_{ij}^{pl}} \; . \qquad (5.1.4.)$$

The case where the effective plastic strain is used to calculate the increase in radius of the yield surface r is called ***Strain Hardenin***g. If the plastic work is used the term ***Work Hardening*** is used.

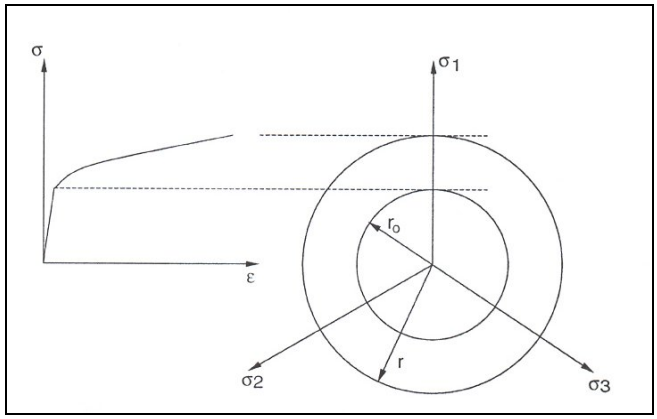

Fig. 5.1.1. Isotropic hardening

Isotropic Hardening is a uniform expansion of the initial yield surface due to plastic deformation [Fig. 5.1.1.], and hence the isotropic response of the material to yielding does not change during plastic deformation. The evolution of the radius of the yield surface is then assumed to be proportional to the measure for the plastic deformation:

$$\dot{r} = C_i \dot{\bar{\varepsilon}}^{pl} \qquad (5.1.5.)$$

Another hardening model known as the ***Kinematic hardening*** model or Prager's model is also widely used. This model assumes that yield surface translates as a rigid surface in stress space during the plastic deformation. Therefore the shape of the subsequent yield surface [Fig. 5.1.2.], does not change during plastic deformation - the shape and size of the initial yield surface is maintained.

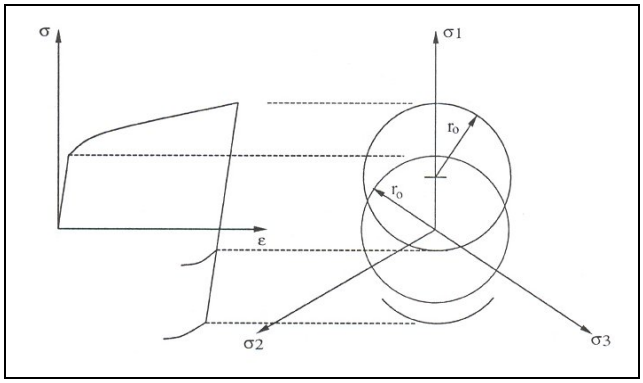

Fig. 5.1.2. Kinematic hardening

This is achieved by introducing a so-called back stress α_{ij}, which defines the position of the centre of the yield surface in the stress space. The evolution of α_{ij} is assumed to be in the direction of the plastic strain rate:

$$\dot{\boldsymbol{\alpha}}_{ij} = \boldsymbol{C}_k \dot{\boldsymbol{\varepsilon}}_{ij}^{pl} \qquad (5.1.6.)$$

The last issue to be addressed is the evolution of the plastic strain. In the current context the assumption will be made that the total strain can be decomposed (additive decomposition) into elastic and plastic parts:

$$\varepsilon_{ij} = \varepsilon_{ij}^{el} + \varepsilon_{ij}^{pl} \tag{5.1.7.}$$

The evolution of the plastic strain is, in general, done through use of a plastic potential Q, which is a function of the stress and hardening variables. The evolution of the plastic strain is assumed to be proportional to the gradient of Q:

$$d\varepsilon_{ij}^{pl} = d\lambda \frac{\partial Q}{\partial \sigma_{ij}} \tag{5.1.8.}$$

A special case of this theory is the associative plasticity where, plastic potential is the same as the yield function, or Q = F.

Equation (Eq. 5.1.8.) can then be rewritten as:

$$\boldsymbol{d\varepsilon_{ij}^{pl}} = \boldsymbol{d\lambda} \frac{\partial \boldsymbol{F}}{\partial \boldsymbol{\sigma_{ij}}} \tag{5.1.9.}$$

where the plastic strain rate is normal to the yield surface. On the other hand, if $\boldsymbol{Q} \neq \boldsymbol{F}$, the flow rule is called nonassociated.

Several plasticity models, which are formulated for orthotropic materials and plane stress case, have been considered in this research.. ***Hill*** [76] proposed a quadratic yield criterion for orthotropic materials, which is an extension of the von Mises criterion for isotropic plasticity. Hill's yield function reads:

$$f^2 = F\sigma_y{}^2 + G\sigma_x{}^2 + H(\sigma_x - \sigma_y)^2 + 2N\sigma_{xy}{}^2 \tag{5.1.10.}$$

in which σ_x , σ_y and σ_{xy} are non-zero stress components in plane stress.

Barlat and Lian and further developments [83] utilize non-quadratic three-component yield criterion for rolled sheets. This criterion introduces a coupling between normal and shear stress components, which is in agreement with findings based on polycrystalline plasticity theory. The Barlat and Lian yield criterion, which is considered to be suitable for aluminium alloys, is expressed in the following equation:

$$f^{2k} = a\left(K_1 + H_2\right)^{2k} + a\left(K_1 - K_2\right)^{2k} + \left(2 - a\right)\left(2K_2\right)^{2k} \tag{5.1.11.}$$

where

$$K_1 = \frac{\sigma_x + h\sigma_y}{2};\ K_2 = \sqrt{\left(\frac{\sigma_x - h\sigma_y}{2}\right)^2 + \left(p\sigma_{xy}\right)^2} \tag{5.1.12.}$$

The constants a, h and p are fitted to experimental result. The exponent 2k is an even number that can be determined from the crystal structure of the material, or it is calibrated to the available experimental data.

Hill also proposed also proposed a non-quadratic yield function for planar isotropic sheets, but later modified this to incorporate in-plane anisotropy. This criterion is given by the following function:

$$f^m = \left|\sigma_x + \sigma_y\right|^m + \left[\frac{\sigma_b}{\tau_y}\right]^m \left|\left(\sigma_x - \sigma_y\right)^2 + 4\tau_{xy}^2\right|^m + \left|\sigma_x^2 + \sigma_y^2 + 2\tau_{xy}^2\right|^{\frac{m}{2}-1}\left[-2a\left(\sigma_x^2 - \sigma_y^2\right) + b\left(\sigma_x - \sigma_y\right)^2\right] \tag{5.1.13.}$$

Here σ_b is the yield stress in balanced biaxial tension, τ_y is the yield stress in simple shear, and a and b are anisotropic parameters.

The yield criterion of ***Logan-Hosford*** [90], which is considered to be suitable for fcc metals comparatively, is as follows:

$$f^M = \frac{1}{1+R}\left(\sigma_x^M + \sigma_y^M\right) + \frac{R}{1+R}\left(\sigma_x - \sigma_y\right)^M \qquad \bar{\varepsilon} = \frac{\left(\sigma_x \varepsilon_x + \sigma_y \varepsilon_y\right)}{\bar{\sigma}} \tag{5.1.14.}$$

where R is average r-value or Lankford coefficient and M is the material constant, which is suggested as 8 for fcc materials.

Karafillis and Boyce [87] proposed a yield criterion based on the linear combination of two convex functions

$$\boldsymbol{f}^{2\boldsymbol{k}} = \left((1-\boldsymbol{c})\boldsymbol{g}_1 + \boldsymbol{c}\boldsymbol{g}_2\right) \tag{5.1.15}$$

where

$$g_1 = (\tilde{S}_1 - \tilde{S}_2)^{2k} + \left(\tilde{S}_2 - \tilde{S}_3\right)^{2k} + \left(\tilde{S}_3 - \tilde{S}_1\right)^{2k} \qquad g_2 = \frac{3^{2k}}{2^{2k-1}+1}\left(\tilde{S}_1^{2k} + \tilde{S}_2^{2k} + \tilde{S}_3^{2k}\right) \tag{5.1.16.}$$

In above equations $\tilde{S}_1$, $\tilde{S}_2$ and $\tilde{S}_3$ are the principal values of the so-called isotropic plasticity equivalent stress components.

$$\tilde{S}_{1,2} = \frac{\tilde{S}_x + \tilde{S}_y}{2} \pm \sqrt{\left(\frac{\tilde{S}_x - \tilde{S}_y}{2}\right)^2 + \tilde{S}_{xy}^2} \; ; \; \tilde{S}_3 = \tilde{S}_z \tag{5.1.17.}$$

where

$$\begin{bmatrix} \tilde{S}_x \\ \tilde{S}_y \\ \tilde{S}_z \\ \tilde{S}_{xy} \end{bmatrix} = C \begin{bmatrix} 1 & \beta_1 & \beta_2 & 0 \\ \beta_1 & \alpha_1 & \beta_3 & 0 \\ \beta_2 & \beta_3 & \alpha_2 & 0 \\ 0 & 0 & 0 & \gamma_3 \end{bmatrix} \begin{bmatrix} \sigma_x \\ \sigma_y \\ \sigma_z \\ \sigma_{xy} \end{bmatrix} \tag{5.1.18.}$$

$$\beta_1 = \frac{\alpha_2 - \alpha_1 - 1}{2}; \; \beta_2 = \frac{\alpha_1 - \alpha_2 - 1}{2}; \; \beta_3 = \frac{1 - \alpha_1 - \alpha_2}{2} \tag{5.1.19.}$$

The constants c, C, α_1, α_2 and γ_3 are calibrated with experimental results, while the exponent $2k$ is given a high value, e.g. $k = 15$. Note that $\sigma_z \equiv 0$ in plane stress states.

Although all discussed criteria can predict very reasonably the yield stress variation with orientation for aluminium alloys, the yield criterion chosen for this material model development was the Hill's yield criterion with isotropic hardening, because of its mathematical simplicity. For aluminium alloys of interest the "strength" aspects (yield surface shape) are much more important then the "kinematic" aspects of plastic yielding, and assumption of isotropic hardening has been adopted.

5.2. Orthotropic yield criterion

The proposed othotropic model is based on the following assumptions:

$$\boldsymbol{F}(\overline{\boldsymbol{\sigma}}, \boldsymbol{\sigma_Y}) = 0, \tag{5.2.1.}$$

where $\overline{\sigma}$ is the equivalent stress and σ_Y is isotropic strain hardening yield stress. Model considers case of associative plasticity with the Hill's orthotropic plastic potential.

Hill's theory describes the yielding and plastic flow of an anisotropic metal on a macroscopic scale. The type of anisotropy considered is that resulting from preferred orientation. A yield criterion is similar in form to the Mises criterion for isotropic metals, but contains six parameters specifying the state of anisotropy.

With increasing strain, a preferred orientation of crystal planes and directions gradually develops, and the individual crystals become elongated to form a characteristic fibrous texture in the direction of the most severe tensile strain. In this way an originally isotropic metal becomes anisotropic in respect of many physical properties. It is well known that fibre texture produced in the technological forming processes, rolling, drawing, and extrusion, is sometimes the cause of undesirable properties in the final product. Such anisotropy can be removed with difficulty by careful heat treatment. Preferred orientation of crystal planes is not the only cause of anisotropic plastic properties: laminar inclusions and cavities occasionally produce similar effects. Residual or internal stresses are another cause of the anisotropy. The present theory is, however, valid only when the anisotropy is mainly due to preferred orientation of crystal planes. Whenever the anisotropy is present the theories of plastic flow for isotropic metals are only valid to a first approximation.

If the criterion of yielding under combined stresses is:

$$f(\sigma_{ij}) = constatnt \tag{5.2.2.}$$

then in the case of an anisotropic metal the form of f depends on the choice of axes of reference. Function f is regarded as a function of the components of the stress tensor, and involves certain parameters characterising the current state of the material.

It is assumed that the anisotropy has three mutually orthogonal directions which may be called the principal axes of anisotropy. These axes can, and frequently will, vary in direction at any moment form point to point within the bulk metal.

If we fix our attention on a given element in certain state of anisotropy and choose the principal axes of anisotropy as Cartesian axes of reference, then by analogy with the Von Mises yield criterion for isotropic metal it is natural to select some homogeneous function quadratic in the stresses to represent the plastic potential f. In view of the symmetry assumption terms in which any one shear stress occurs

linearly must be rejected. It is also assumed that the hydrostatic pressure does not influence yielding.

Hill [76] proposed a quadratic yield criterion for anisotropic materials and this criterion carries on to be interesting for the behaviour modelling of several metallic materials. Hill's criterion is an extension of the von Mises criterion for isotropic plasticity, and this criterion is given as follows:

$$f^2 = F(\sigma_y - \sigma_z)^2 + G(\sigma_z - \sigma_x)^2 + H(\sigma_x - \sigma_y)^2 + 2L\sigma_{yz}^2 + 2M\sigma_{zx}^2 + 2N\sigma_{xy}^2 \quad (5.2.3.)$$

where F, G, H, L, M, N are parameters characteristic of the current state of anisotropy.

In the plane stress case with in-plane anisotropy this criterion reduces to:

$$f^2 = F\sigma_y^2 + G\sigma_x^2 + H(\sigma_x - \sigma_y)^2 + 2N\sigma_{xy}^2 \quad (5.2.4.)$$

which can be rearranged as:

$$f^2 = (G + H)\sigma^2{}_x - 2H\sigma_x\sigma_y + (F + H)\sigma^2{}_y + 2N\sigma^2{}_{xy} \quad (5.2.5.)$$

where σ_x, σ_y and σ_{xy} are components of the stress tensor, F, G, H and N are material constants.

In case of plane stress state Hill's orthotropic model requires the following data:

- Strain hardening curve σ_Y
- Anisotropic coefficients (F, G, H and N)

Hill's orthotropic yield criterion with isotropic hardening can be extended to include the concept of combined isotropic-kinematic hardening [82], and yield function in this case is:

$$\begin{aligned} f^2 &= (G + H)(\sigma_x - r_x)^2 - 2H(\sigma_x - r_x)(\sigma_y - r_y) \\ &+ (H + F)(\sigma_y - r_y)^2 + 2N(\sigma_{xy} - r_{xy})^2 \end{aligned} \quad (5.2.16.)$$

where the material parameters F, G, H and N are determined by the initial state of anisotropy of the material. The components of the back stress, r_x, r_y and r_{xy}, specify the centre of the yield surface and are directly related to the kinematic hardening of the material. The function f specifies the size of the yield surface, and it is an expression of isotropic hardening. The function f increases with accumulated plastic strain.

When there is significant presence of anisotropy in the material initial values of r_x, r_y and r_{xy}, are not zero. In this situation, it is then desirable to fit the yield

criterion to the experimental yield surface through an optimisation procedure. In this way it is possible to determine the values of coefficients (F, G, H and N), and initial back stress components.

As in classical plasticity theory, the plastic strain increments were derived from a plastic potential which was assumed to be the yield surface, and a yield function $f(\sigma_{ij})$ is required to match the trends observed when used in conjunction with normality rule - the plastic strain increments are normal to the yield locus:

$$d\varepsilon_{ij}^{p} = d\lambda \frac{\partial f}{\partial \sigma_{ij}} \tag{5.2.7.}$$

where $d\lambda$ is scalar depending on material hardening and σ_{ij} are the components of the Cauchy stress tensor

In the above equation the yield function f is differentiated partially with respect to the components of the stress tensor σ_{ij}. The product of each differential and scalar multiplier $d\lambda$ (an incremental plastic modulus) gives the components of the plastic strain increment tensor $d\varepsilon_{ij}^{p}$.

Using the extended Hill's yield criterion and normality rule, yields:

$$D_x^p = d\varepsilon_x^p / dt = \dot{\lambda}\left[(G+H)\alpha_x - H\alpha_y\right]$$

$$D_y^p = d\varepsilon_y^p / dt = \dot{\lambda}\left[-H\alpha_x + (H+F)\alpha_y\right] \tag{5.2.8.}$$

$$D_{xy}^p = d\varepsilon_z^p / dt = \dot{\lambda} N \alpha_{xy}$$

where components of the "effective stress vector" are

$$\alpha_x = \sigma_x - r_x \;\; \alpha_y = \sigma_y - r_y \;\; \alpha_{xy} = \sigma_{xy} - r_{xy} \tag{5.2.9.}$$

the plastic multiplier $\dot{\lambda}$ is a positive scalar that may vary during the straining process, and D_x^p, D_y^p and D_{xy}^p are the plastic parts of the rate of deformation, such that:

$$D_x = D_x^e + D_x^p \;\; D_y = D_y^e + D_y^p \;\; D_{xy} = D_{xy}^e + D_{xy}^p \tag{5.2.10.}$$

In the case of uniaxial tension test using a specimen cut out from a sheet at angle α, measured counter-clockwise from the rolling direction, the stress components are:

$$\sigma_x = \sigma \cos^2 \alpha \;\; ; \;\; \sigma_y = \sigma \sin^2 \alpha \;\; ; \;\; \sigma_{xy} = \sigma \sin\alpha \cos\alpha \tag{5.2.11.}$$

where σ is the stress along the axial direction x' of the specimen. Let y' be along the width direction of the specimen, the $x'-y'-z'$ axes thus for a rectangular specimen coordinate system with x' and y' lying in the $x-y$ plane and $z'=z$.

In this case, the rate of plastic deformation in the specimen coordinate system is:

$$D^p_{x'} = D^p_x \cos^2\alpha + D^p_y \sin^2\alpha + 2D^p_{xy}\sin\alpha\cos\alpha$$

$$D^p_{y'} = D^p_x \sin^2\alpha + D^p_y \cos^2\alpha - 2D^p_{xy}\sin\alpha\cos\alpha \qquad (5.2.12.)$$

$$D^p_{xy'} = -\frac{1}{2}(D^p_x - D^p_y)\sin^2(2\alpha) + D^p_{xy}\cos(2\alpha)$$

Using Pragers's kinematic hardening rule, according to which the rate of translation of the centre of the yield surface is proportional to the plastic strain rate, the deviatoric part of back stress rates can be found as:

$$\dot{r}^D_x = CD^p_x = C\dot{\lambda}[(G+H)\alpha_x - H\alpha_y]$$

$$\dot{r}^D_y = CD^p_y = C\dot{\lambda}[-H\alpha_x + (H+F)\alpha_y] \qquad (5.2.13.)$$

$$\dot{r}^D_{xy} = CD^p_{xy} = C\dot{\lambda}N\alpha_{xy}$$

and

$$\dot{r}^D_x + \dot{r}^D_y + r^D_z = 0 \qquad (5.2.14.)$$

Knowing that $\dot{r}_z = 0$ for plane stress, it may be shown that

$$\dot{r}_x = 2\dot{r}^D_x + \dot{r}^D_y \text{ and } \dot{r}_y = \dot{r}^D_x + 2\dot{r}^D_y \qquad (5.2.15.)$$

The scalar parameter C characterizes the material behaviour, and if it is assumed to be a constant, this leads to a linear-kinematic strain hardening.

The plastic strain ratio, R_α for a test coupon cut at an angle α from the rolling direction, is defined by:

$$R_\alpha = \frac{D^p_{y'}}{D^p_{z'}} = -\left(\frac{D^p_{y'}}{D^p_{x'} + D^p_{y'}}\right) \qquad (5.2.16.)$$

where the plastic incompressibility of the material is assumed. From this equation, the following expressions can be found:

$$R_0 = \frac{\sigma_0 H - Hr_x + (H+F)r_y}{\sigma_0 G - Gr_x - Fr_y}$$

$$R_{45} = \frac{1}{2}\left[\frac{2N(\sigma_{45} - 2r_x)}{\sigma_{45}(G+F) - 2Gr_x - 2Fr_y} - 1\right] \qquad (5.2.17.)$$

$$R_{90} = \frac{\sigma_{90} H + (G+H)r_x - Hr_y}{\sigma_{90} F - Gr_x - Fr_y}$$

where σ_0, σ_{45}, σ_{90}, R_0, R_{45}, and R_{90} represent the yield stress and plastic strain ratio at orientations 0, 45 and 90 degrees from the rolling direction, respectively. In the case of $r_x = r_y = r_{xy} = 0$, above equations reduce to original Hill's definition of plastic strain ratios given by:

$$R_0 = \frac{H}{G};\ R_{90} = \frac{H}{F} \text{ and } R_{45} = \frac{2N - (F+G)}{2(F+G)} \qquad (5.2.18.)$$

5.3. Procedures for calibration of the orthotropic yield criterion

The determination of the material constants for an anisotropic material is more complex then for an isotropic material. Several types of tests can be performed. Hill [76] proposes a series of simple tensile tests. If one determines the yield stress of the material in the three principal axes of anisotropy then it is clear that:

$$\frac{1}{\sigma_{Y,xx}} = G + H \,,$$

$$\frac{1}{\sigma_{Y,yy}} = H + F \,, \qquad (5.3.1.)$$

$$\frac{1}{\sigma_{Y,zz}} = F + G \,,$$

from which one could determine F, G and H as follows:

$$2F = \frac{1}{\sigma_{Y,yy}} + \frac{1}{\sigma_{Y,zz}} - \frac{1}{\sigma_{Y,xx}}$$

$$2G = \frac{1}{\sigma_{Y,zz}} + \frac{1}{\sigma_{Y,xx}} - \frac{1}{\sigma_{Y,yy}} \qquad (5.3.2.)$$

$$2H = \frac{1}{\sigma_{Y,xx}} + \frac{1}{\sigma_{Y,yy}} - \frac{1}{\sigma_{Y,zz}}$$

The other three material constants for Hill's yield criterion can be determined from the yield stresses in shear with respect to the principal axes of anisotropy.

$$2L = \frac{1}{\sigma_{Y,yz}}$$

$$2M = \frac{1}{\sigma_{Y,zx}} \qquad (5.3.3.)$$

$$2N = \frac{1}{\sigma_{Y,xy}}$$

However instead of this direct method of determining the anisotropy parameters, it is better to measure the incremental strains in all three directions during a tensile test. For example for a tensile test in the X-direction these strains would be in the ratios:

$$d\varepsilon_x : d\varepsilon_y : d\varepsilon_z = (G+H) : (-H) : (-G) \qquad (5.3.4.)$$

Similarly tensile tests in Y and Z directions will provide the ratios between F and H, and G and F:

$$d\varepsilon_x : d\varepsilon_y : d\varepsilon_z = (-H) : (F+H) : (-F) \tag{5.3.5.}$$

$$d\varepsilon_x : d\varepsilon_y : d\varepsilon_z = (-G) : (-F) : (F+G) \tag{5.3.6.}$$

This then allows a test of the accuracy of the measurements and the theory, as the following identity should be satisfied:

$$\left(\frac{H}{G}\right)\left(\frac{G}{F}\right)\left(\frac{F}{H}\right) = 1 \tag{5.3.7.}$$

This method is preferable to the direct (stress based method) method if the yield stress is not very well defined. Or it can be used as a way to determine the through thickness yield stress when the material is in the form of a thin sheet.

For a material with anisotropic yield properties, tensile tests using a specimen cut out from a sheet or a plate in different material directions, result in different yield stresses, σ_α, where the index α denotes the specimen's direction relative to the extrusion direction. Considering the tensile yield stresses in the principal directions of anisotropy one can see that the parameters in Hill's criterion should satisfy following relations:

$$\begin{aligned} \frac{1}{\sigma_0{}^2} &= G + H \\ \frac{1}{\sigma_{90}{}^2} &= H + F \end{aligned} \tag{5.3.8.}$$

The plastic anisotropy is also characterized by a difference in plastic flow relative to the principal anisotropy direction, and as a measure of the flow properties of the material, the specimen's R_α ratio or Lankford coefficient is defined as the ratio between the plastic strains in its width and thickness directions:

$$R_\alpha = \left.\frac{\dot{\varepsilon}_w{}^p}{\dot{\varepsilon}_t{}^p}\right|_\alpha \tag{5.3.9.}$$

where α is the angle from the extrusion direction, and $\dot{\varepsilon}_w{}^p$, $\dot{\varepsilon}_t{}^p$ are true, plastic strain increments in the width and thickness directions of the specimen, respectively. Often these increments are assumed to have the same ratio for increasing strains, enabling the R ratio to be written as:

$$R_\alpha = \left.\frac{\varepsilon_w{}^p}{\varepsilon_t{}^p}\right|_\alpha \tag{5.3.10.}$$

or in terms of Hill's orthotropic parameters as:

$$R_\alpha = \frac{H + (2N - F - G - 4H)\sin^2\alpha\cos^2\alpha}{F\sin^2\alpha + G\cos^2\alpha} \qquad (5.3.11.)$$

The above equation then yields:

$$R_0 = \frac{H}{G};$$

$$R_{90} = \frac{H}{F}; \qquad (5.3.12.)$$

$$R_{45} = \frac{2N - (F+G)}{2(F+G)}$$

For a material exhibiting isotropic flow properties the strains in the width and thickness direction of the specimen are known to be equal for all directions in the material and for an isotropic material the Lankford coefficients reduces to $R_\alpha = 1$ for all directions α.

The R_α values can be determined with uniaxial tensile tests of specimens, which are cut out at the angle α from the rolling direction. The Lankford coefficient thus describes the ability of the material to resist thinning, i.e. a large value implies that the material is has high resistance to thickness changes while a low value means that the material is has high resistance to straining in the width direction.

Measuring stress and strains in the width and length direction, true stress σ, true longitudinal strain ε_l and true strain in width direction ε_w can be calculated by use of formulas:

$$\sigma = S(1 + e_l);\ \varepsilon_l = \ln(1 + e_l);\ \varepsilon_w = \ln(1 + e_w) \qquad (5.3.13.)$$

where S, e_l, e_w are the respective engineering values. Subsequently, true plastic strains could be calculated from these values as:

$$\varepsilon^p{}_l = \varepsilon_l - \frac{\sigma}{E};\ \varepsilon^p{}_w = \varepsilon_w - \frac{\sigma}{E}\upsilon_w \qquad (5.3.14.)$$

where E is Young's modulus and υ_w is Poisson's ratio for the width direction.

Utilising the incompressibility condition the true plastic strain in the thickness direction of the specimen can be found as:

$$\varepsilon^p{}_t = -(\varepsilon^p{}_l + \varepsilon^p{}_w) \qquad (5.3.15.)$$

The Hill's yield criterion in the plane stress case contains four material coefficients, which need to be determined. This can bee done with data from uniaxial tensile tests and biaxial tensile test [86]. However, since four material coefficients are needed, only four properties from the tests can be considered.

For the identification of the parameters of Hill's yield criterion the procedure based on the experimental values of the tensile uniaxial yield stresses in 0^o, 45^o, 90^o directions and the balanced yield stress σ_b from biaxial test, give the following set of equations [84]:

$$F = \frac{1}{2}\left(\frac{1}{\sigma_{90}{}^2} - \frac{1}{\sigma_0{}^2} + \frac{1}{\sigma_b{}^2}\right)$$

$$G = \frac{1}{2}\left(\frac{1}{\sigma_0{}^2} - \frac{1}{\sigma_{90}{}^2} + \frac{1}{\sigma_b{}^2}\right) \qquad (5.13.16.)$$

$$H = \frac{1}{2}\left(\frac{1}{\sigma_0{}^2} + \frac{1}{\sigma_{90}{}^2} - \frac{1}{\sigma_b{}^2}\right)$$

$$N = \frac{1}{2}\left(\frac{1}{\sigma_{45}{}^2} - \frac{1}{\sigma_b{}^2}\right)$$

It is possible to rearrange this set of equations in the following from:

$$F = \frac{1}{\sigma^2{}_{90}(1+R_{90})}$$

$$G = \frac{1}{\sigma_{90}{}^2} - \frac{R_{90}}{\sigma^2{}_{90}(1+R_{90})} \qquad (5.13.17.)$$

$$H = \frac{R_{90}}{\sigma_{90}{}^2(1+R_{90})}$$

$$N = \frac{1}{2}\left(\frac{4}{\sigma^2{}_{45}} - \frac{1}{\sigma^2{}_0} + \frac{R_{90}-1}{\sigma_{90}{}^2(1+R_{90})}\right)$$

In this case parameters included in Hill' yield criterion can be determined using the measured uniaxial yield stress in 0^o, 45^o, 90^o directions and R_{90} strain rate ratio at $\alpha = 90^o$

We can also calculate the parameters for the Hill's criterion using the measured uniaxial yield stress in 0^o, 45^o, 90^o directions and Lankford coefficient R_0 strain rate ratio at $\alpha = 0^o$ utilizing following explicit solution:

$$F = \frac{1}{{\sigma_{90}}^2} - \frac{R_0}{{\sigma_{90}}^2(1+R_0)}$$

$$G = \frac{1}{{\sigma_0}^2(1+R_0)} \qquad (5.13.18.)$$

$$H = \frac{R_0}{{\sigma_0}^2(1+R_0)}$$

$$N = \frac{1}{2}\left(\frac{4}{\sigma^2{}_{45}} - \frac{1}{\sigma^2{}_{90}} + \frac{R_0 - 1}{{\sigma_0}^2(1+R_0)}\right)$$

Both yield stresses σ_α and Lankford coefficients R_α may be employed for the calibration of the yield criterion, where R_α-ratio represents the gradient of the yield surface [89]. We can choose any combination of those parameters and apply different identification procedures as long as the points are not lying in a plane, since this will not give solution for the constants.

5.4. Experiments

5.4.1. Tensile test

Uniaxial tensile tests for two aluminium alloys AA2024 and AA7010 have been performed in three different directions, namely 0^o (extrusion), 45^o and 90^o (transversal). Because only the longitudinal strain of flat tensile specimen has been measured for all three different directions, Taylor test data has been used for determination of Lankford coefficient R_α for AA7010.

A plane stress state is defined in an orthogonal system (θ, ϕ), rotated in the plane of the sheet or plate with an angle α. The angle α is the angle between the θ - axis and the x – axis in the orthogonal material system (x, y), where the x – axis is chosen in the direction of rolling. The angle α is defined positive counter clockwise. The plane stress state may be transformed to material axes by the relation:

$$\begin{bmatrix} \sigma_x \\ \sigma_y \\ \sigma_{xy} \end{bmatrix} = \begin{bmatrix} \cos^2\alpha & \sin^2\alpha & -2\sin\alpha\cos\alpha \\ \sin^2\alpha & \cos^2\alpha & 2\sin\alpha\cos\alpha \\ \sin\alpha\cos\alpha & -\sin\alpha\cos\alpha & \cos^2\alpha - \sin^2\alpha \end{bmatrix} x \begin{bmatrix} \sigma_\theta \\ \sigma_\phi \\ \sigma_{\theta\varphi} \end{bmatrix} \qquad (5.4.1.1.)$$

In a uniaxial tensile test performed in the direction α, the stress state is defined as $\sigma_\theta = \sigma$ and $\sigma_\phi = \sigma_{\theta\varphi} = 0$. Choosing directions 0, 45, 90° and using above relation, following table defines stress states referred to the material axes:

Tab. 5.4.1.1. Stress states referred to the material axes

α	σ_x	σ_y	σ_{xy}
0°	σ	0	0
45°	$\sigma/2$	$\sigma/2$	$\sigma/2$
90°	0	σ	0

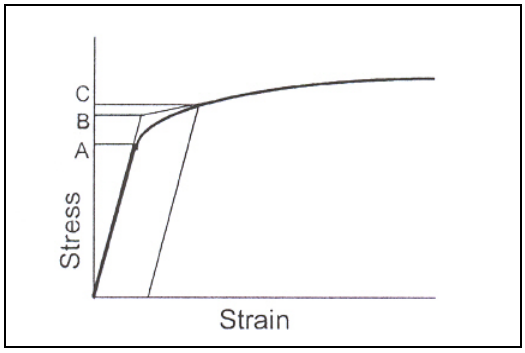

Fig. 5.4.1.1. Definition of yield point

For higher temperatures, the apparent yield point disappears and determination of the yield stress becomes difficult. There are three types of methods [81], for determination of the yield point in a stress-strain curve as shown in Fig. 5.4.1.1.:

A - The point where the proportional relation between stress and strain disappears

B - The point, which is determined by the extrapolation

C – The point determined by certain off-set strain as the stress at a certain plastic strain.

In this work, the stress at the C point was defined as the yield stress. Permanent deformation may be detrimental, and the industry adopted 0.002 plastic strain as an arbitrary limit that is considered acceptable by all regulatory agencies. For tension and compression, the corresponding stress at this offset strain is defined as the yield stress. For practical purposes, yield stress can be determined from a stress-strain diagram by extending a line parallel to the elastic modulus line and offset from the origin by an amount of 0.002. The yield stress is determined as the intersection of the offset with the stress-strain curve.

5.4.2. Taylor test

Taylor test data has been used for determination of the Lankford coefficient R_α for AA7010. Taylor cylinder specimens were cut from rolled plate. The specimens were 9.30 mm in diameter with length 46.50 mm and the length-to-diameter ratio L/D=5.

A laboratory test frame (X, Y, Z) representing the principal axes of impact test is adopted such that compressive impact loading is always applied along X-axsis. The X direction was the original rolling direction for this plate.

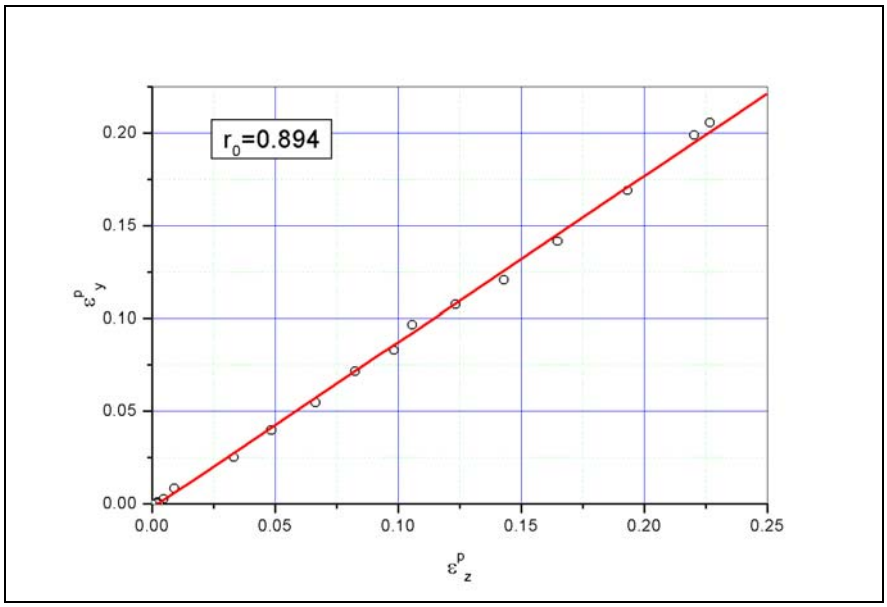

Fig. 5.4.2.1. R-ratio deduced using Taylor test with initial velocity V=200 m/s

It has been found that the Lankford coefficient for AA7010 has value of $R_0 = 0.894$ for the specimen, which was launched with initial velocity of 200 m/s and value of $R_0 = 0.778$ for the specimen, which was launched with initial velocity of 214 m/s, and average value is adopted for Lankford coefficient of $R_0 = 0.836$.

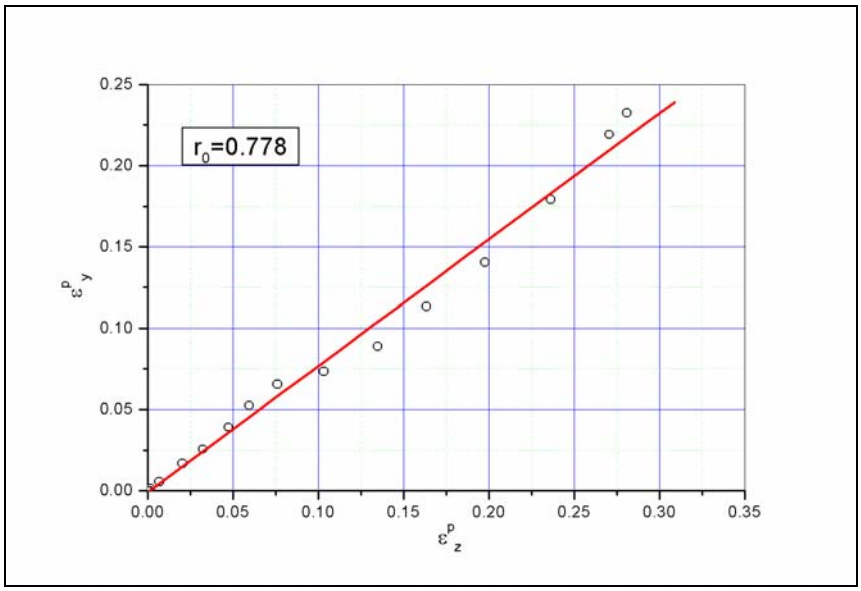

Fig. 5.4.2.2. R-ratio deduced using Taylor test with initial velocity V=214 m/s

5.4.3. Yield locus

Using above described procedure for identification of parameters for the Hill's criterion, using measured uniaxial yield stresses in 0^o, 45^o, 90^o directions and Lankford coefficient R_0, the following values have been calculated: F=0.5524; G=0.5447; H=0.4553 and N= 1.6870. The corresponding yield loci are plotted in Fig. 5.4.3.1 – Fig. 5.4.3.5.

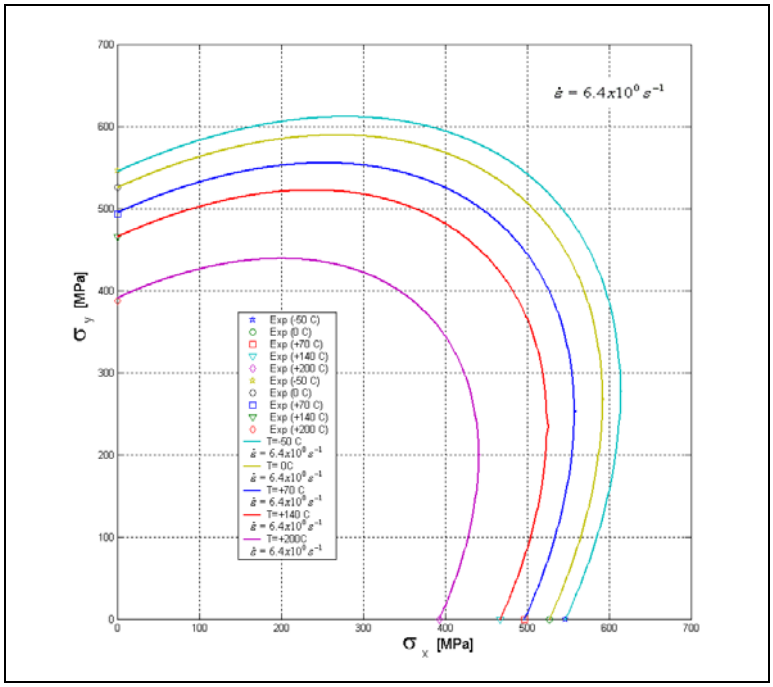

Fig. 5.4.3.1. Yield loci for AA7010 alloy plate as predicted by Hill's criterion at $\dot{\varepsilon} = 6.4X10^0\,s^{-1}$

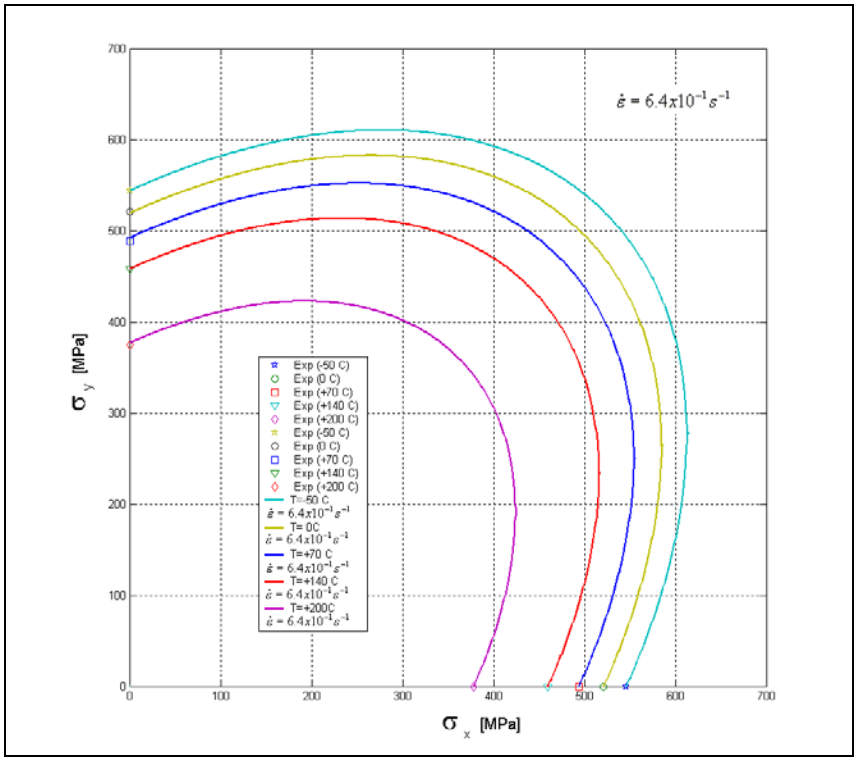

Fig. 5.4.3.2. Yield loci for AA7010 alloy plate as predicted by Hill's criterion at $\dot{\varepsilon} = 6.4X10^{-1}\,s^{-1}$

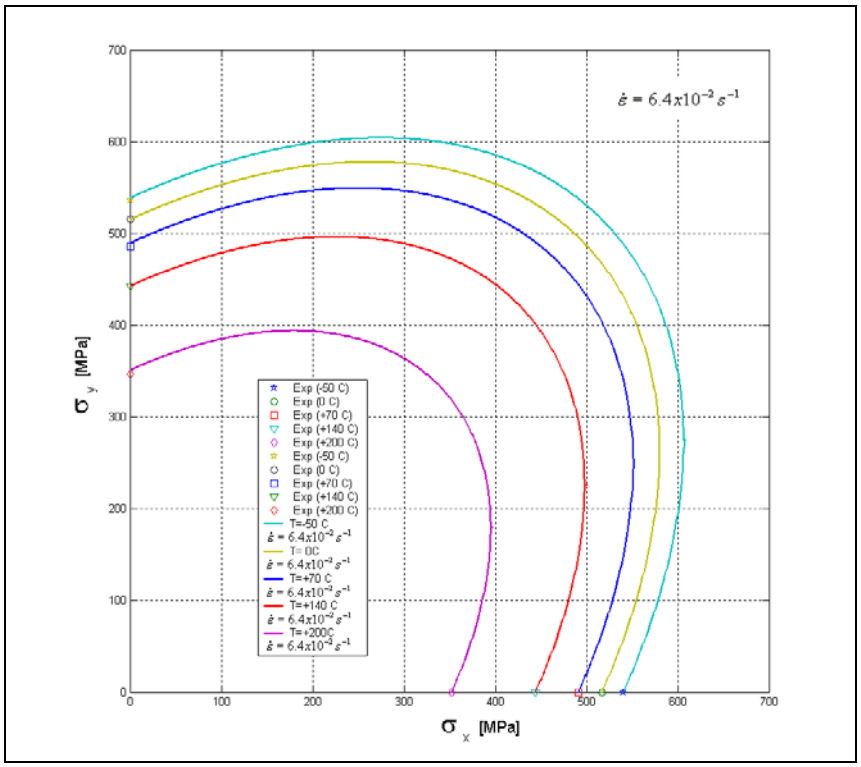

Fig. 5.4.3.3. Yield loci for AA7010 alloy plate as predicted by Hill's criterion at $\dot{\varepsilon} = 6.4X10^{-2}\,s^{-1}$

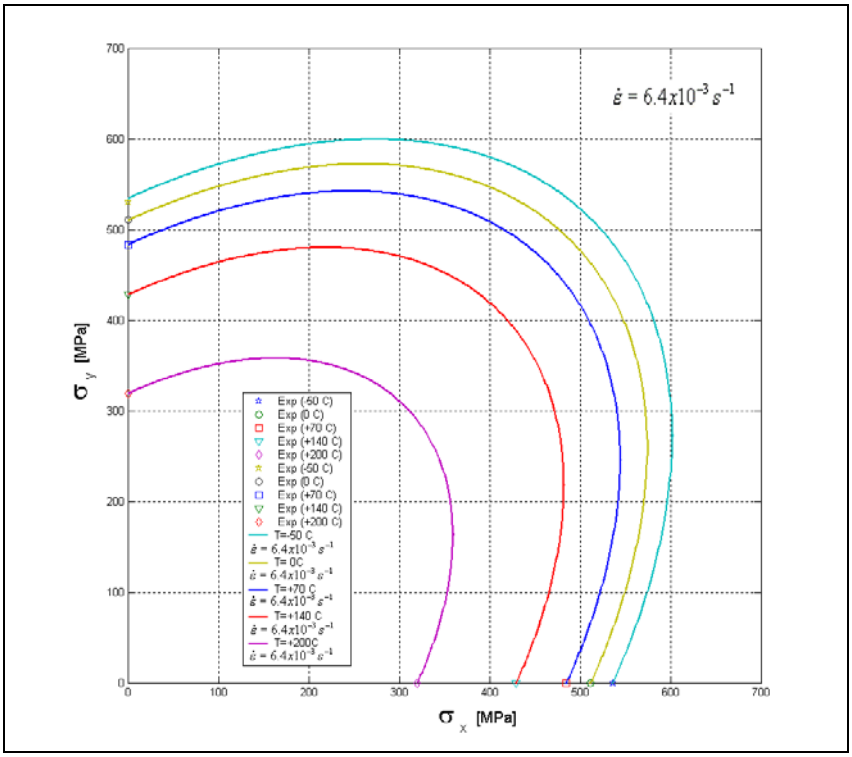

Fig. 5.4.3.4. Yield loci for AA7010 alloy plate as predicted by Hill's criterion at $\dot{\varepsilon} = 6.4X10^{-3}\,s^{-1}$

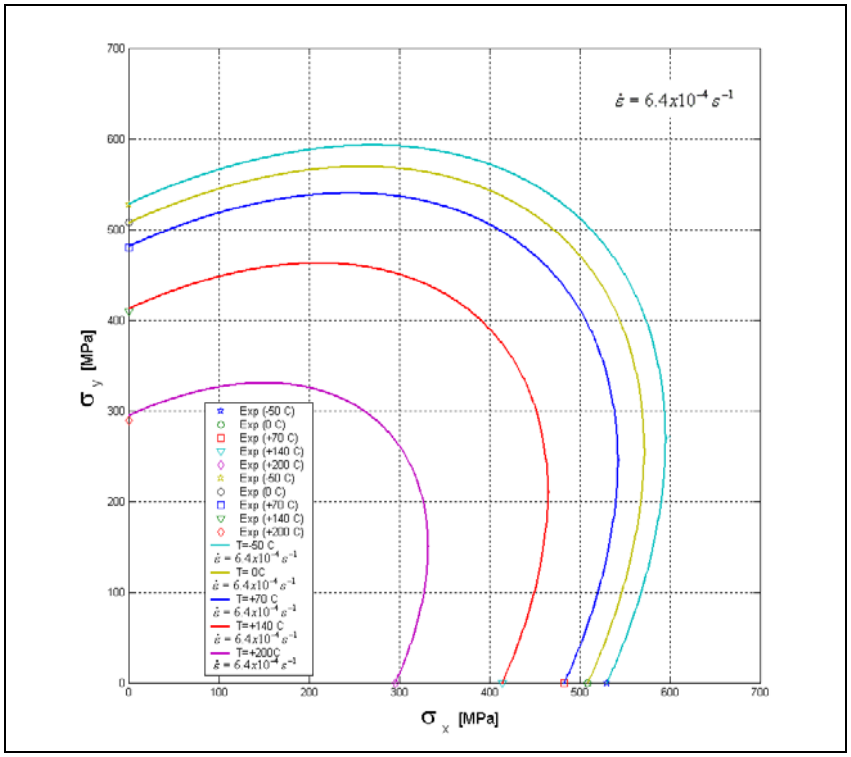

Fig. 5.4.3.5. Yield loci for AA7010 alloy plate as predicted by Hill's criterion at $\dot{\varepsilon} = 6.4X10^{-4}\,s^{-1}$

Above figures show the experimental data and predicted yield loci by Hill's orthotropic yield criterion at –50°, 0°, +70°, +140° and +200° C. The yield loci show remarkable temperature dependence.

5.4.4. Yield surface

The yield stress determined from each tensile specimen is transformed into a set of stress components σ_x, σ_y and σ_{xy}. These sets of stress components can then be plotted as a yield surface in a three-dimensional stress space, with σ_x and σ_y forming two perpendicular axes on the horizontal plane, and σ_{xy} the vertical axis normal to horizontal plane [80].

The Hill's yield condition for plane stress state

$$\bar{\sigma}^2 = (G+H)\sigma^2{}_x - 2H\sigma_x\sigma_y + (F+H)\sigma^2{}_y + 2N\sigma^2{}_{xy} \qquad (5.4.4.1.)$$

is for fixed x and y directions geometrically represented in the stress space $(\sigma_x, \sigma_y, \sigma_{xy})$ by an ellipsoid. The different loading conditions can be represented by ellipses lying on the surface of the ellipsoid.

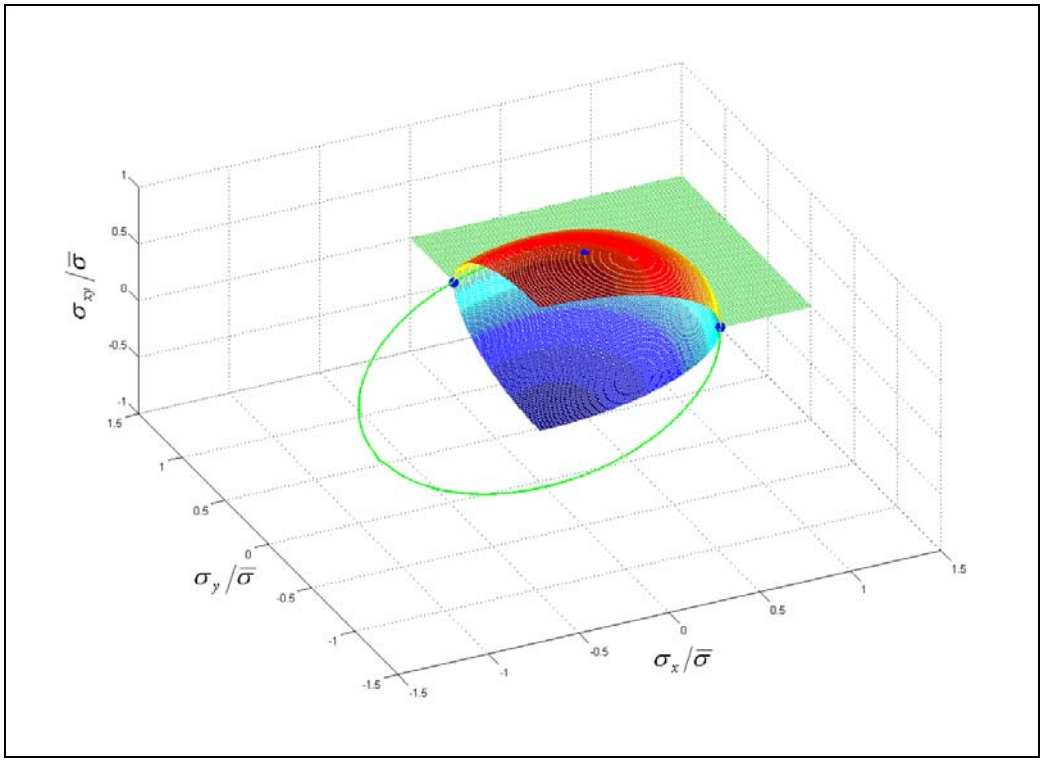

Fig. 5.4.4.1. Predicted initial yield surface for AA7010 alloy plate

Fig. 5.4.4.1. shows the yield surface which was computed with identified anisotropic coefficient of Hill's yield function for the AA7010 , where rolling direction was chosen as the reference direction.

Corresponding initial yield surfaces for AA7010 alloy plate predicted by Hill's criterion at $T = +70^o C$, and in the strain rate range from $\dot{\varepsilon} = 6.4X10^{-4} s^{-1}$ to $\dot{\varepsilon} = 6.4X10^{0} s^{-1}$, are presented in Fig. 5.4.4.2. – Fig. 5.4.4.6.

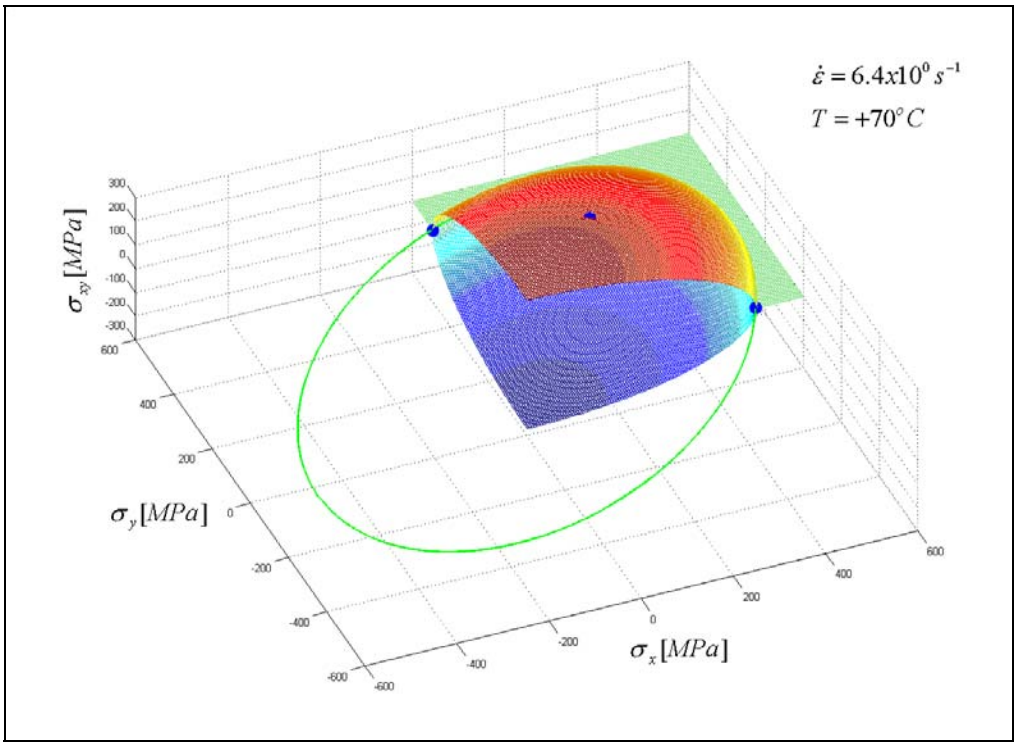

Fig. 5.4.4.2. Yield surface for AA7010 alloy plate as predicted by Hill's criterion at $\dot{\varepsilon} = 6.4X10^{0}\, s^{-1}$ and $T = +70^{o}\, C$

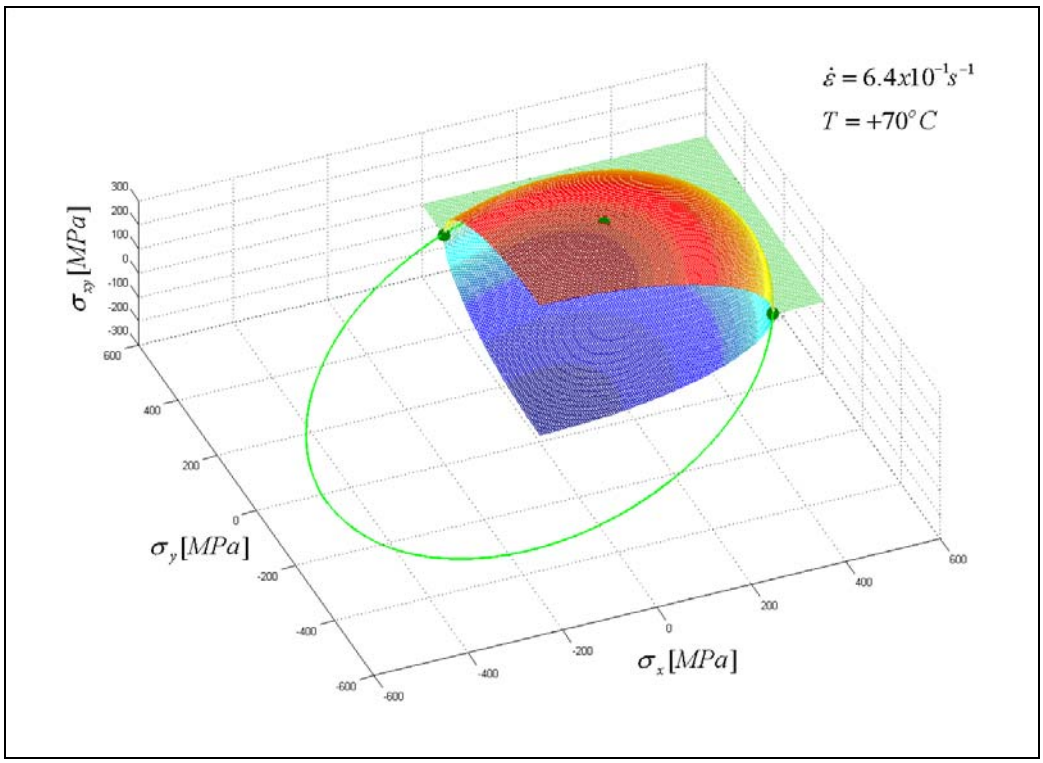

Fig. 5.4.4.3. Yield surface for AA7010 alloy plate as predicted by Hill's criterion at $\dot{\varepsilon} = 6.4X10^{-1}\, s^{-1}$ and $T = +70^{o}\, C$

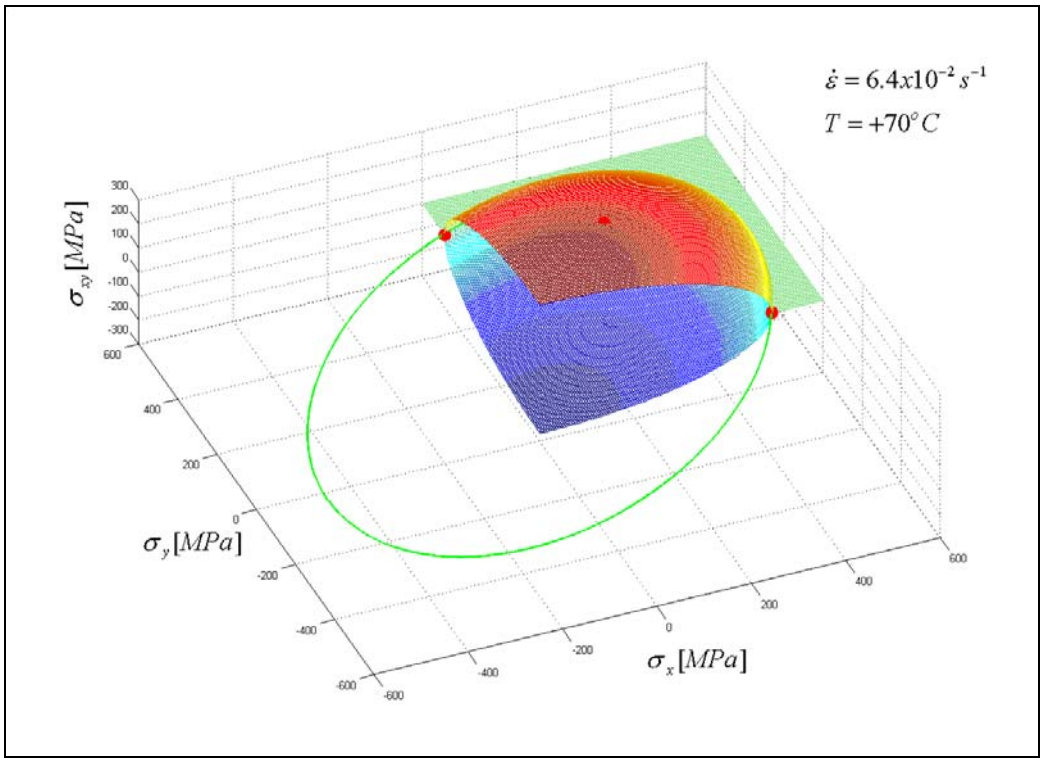

Fig. 5.4.4.4. Yield surface for AA7010 alloy plate as predicted by Hill's criterion at $\dot{\varepsilon} = 6.4X10^{-2}\,s^{-1}$ and $T = +70^{o}\,C$

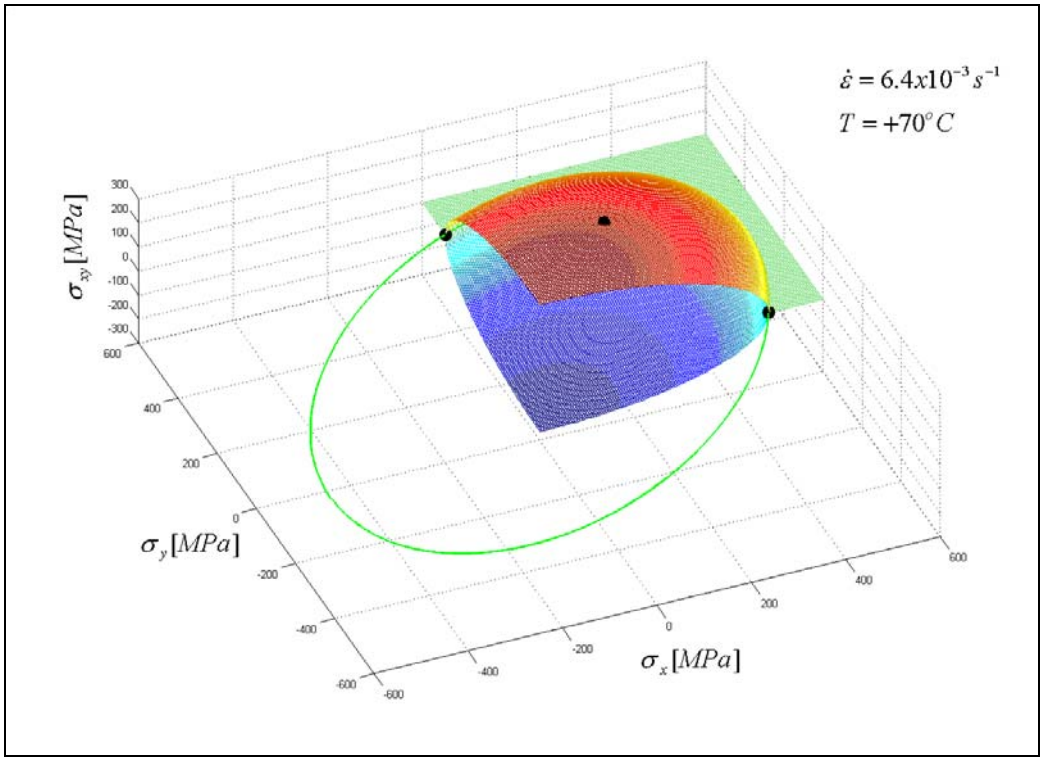

Fig. 5.4.4.5. Yield surface for AA7010 alloy plate as predicted by Hill's criterion at $\dot{\varepsilon} = 6.4X10^{-3}\,s^{-1}$ and $T = +70^{o}\,C$

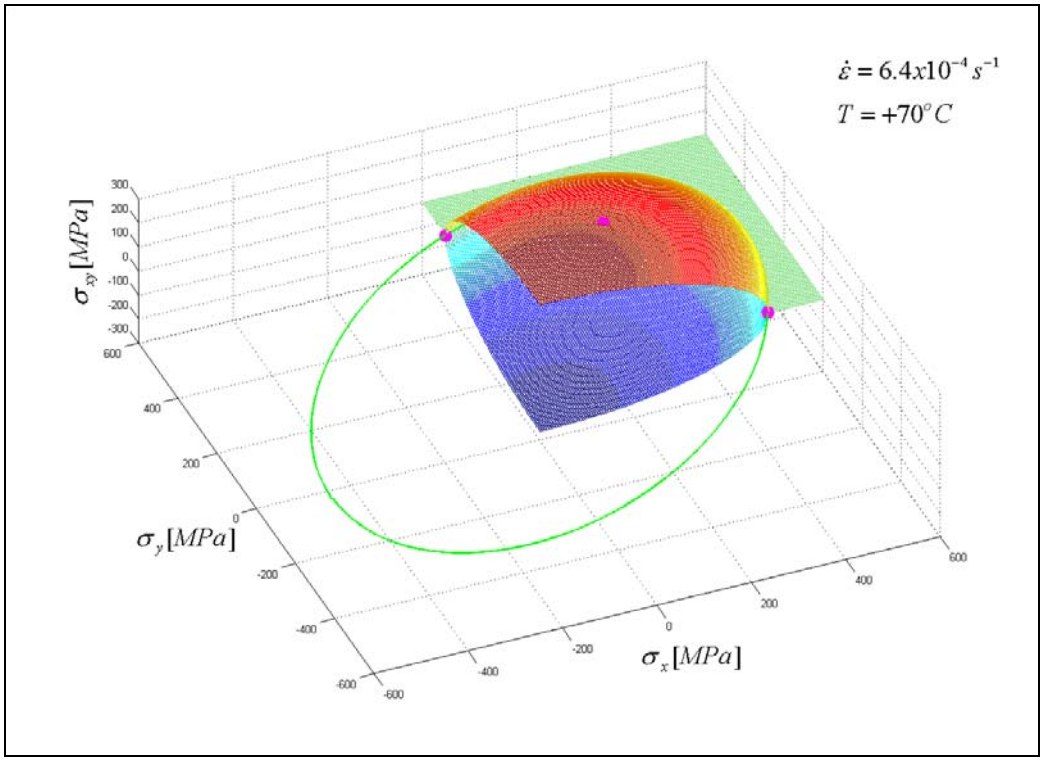

Fig. 5.4.4.6. Yield surface for AA7010 alloy plate as predicted by Hill's criterion at $\dot{\varepsilon} = 6.4X10^{-4}\,s^{-1}$ and $T = +70^{o}C$

5.5. Validation

5.5.1. Implementation in DYNA3D

A general Anisotropic Elastic-Plastic material model is already implemented in DYNA3D, and this material model has been chosen as the starting point for the further development of new orthotropic material model.

The implemented model combines the orthotropic elasticity of the Orthotropic elastic model with the Hill's orthotropic plasticity model.

The constitutive matrix C that relates increments in global components of stress to increments in global components of strain is defined as:

$$C = T^T C_L T\,, \tag{5.5.1.1.}$$

where T is the transformation matrix between the local material coordinate system and the global coordinate system, and C_L is the constitutive matrix defined in terms of the material constants of the local orthogonal material axes.

$$\boldsymbol{C_L^{-1}} = \begin{bmatrix} \frac{1}{\boldsymbol{E_a}} & -\frac{\boldsymbol{\nu_{ba}}}{\boldsymbol{E_b}} & -\frac{\boldsymbol{\nu_{ca}}}{\boldsymbol{E_c}} & 0 & 0 & 0 \\ -\frac{\boldsymbol{\nu_{ab}}}{\boldsymbol{E_a}} & \frac{1}{\boldsymbol{E_b}} & -\frac{\boldsymbol{\nu_{cb}}}{\boldsymbol{E_c}} & 0 & 0 & 0 \\ -\frac{\boldsymbol{\nu_{ac}}}{\boldsymbol{E_a}} & -\frac{\boldsymbol{\nu_{bc}}}{\boldsymbol{E_b}} & \frac{1}{\boldsymbol{E_c}} & 0 & 0 & 0 \\ 0 & 0 & 0 & \frac{1}{\boldsymbol{G_{ab}}} & 0 & 0 \\ 0 & 0 & 0 & 0 & \frac{1}{\boldsymbol{G_{bc}}} & 0 \\ 0 & 0 & 0 & 0 & 0 & \frac{1}{\boldsymbol{G_{ca}}} \end{bmatrix} \tag{5.5.1.2.}$$

Symmetry of the elastic compliance $\boldsymbol{C_L^{-1}}$ implies

$$\frac{\nu_{ab}}{E_a} = \frac{\nu_{ba}}{E_b}\,,\ \frac{\nu_{ca}}{E_c} = \frac{\nu_{ac}}{E_a}\,,\ \text{and}\ \frac{\nu_{cb}}{E_c} = \frac{\nu_{bc}}{E_b} \tag{5.5.1.3.}$$

Positive definiteness of C_L yields the following restriction on the elastic constants:

$$\nu_{ba} < \left[\frac{E_b}{E_a}\right]^{1/2},\ \nu_{ca} < \left[\frac{E_c}{Ea}\right]^{1/2},\ \text{and}\ \nu_{cb} < \left[\frac{E_c}{E_b}\right]^{1/2} \tag{5.5.1.4.}$$

Values of the Poisson's ratio are defined as

$$\nu_{ij} = \frac{-\varepsilon_j}{\varepsilon_i} \tag{5.5.1.5.}$$

where ε_j is the strain in the j^{th} direction and ε_i is the strain in the i^{th} direction in a uniaxial stress test in the i^{th} direction.

In the present model, only isotropic strain hardening is included in the form of the linear strain hardening. The linear strain hardening law has the form:

$$\sigma_y = \sigma_0 + E_p \bar{\varepsilon}^p \tag{5.5.1.6.}$$

where the effective plastic strain $\bar{\varepsilon}^p$ is given by

$$\bar{\varepsilon}^p = \int_0^t d\bar{\varepsilon}^p \,. \tag{5.5.1.7.}$$

It is most convenient to choose a reference direction when using the Hill's theory, and in the implemented model the a-direction is chosen as a reference direction.

The a-direction hardening modulus E_p^a, can be written in terms of the a-direction tangent modulus E_T^a as

$$E_p^a = \frac{E_a E_T^a}{E_a - E_T^a}, \tag{5.5.1.8.}$$

where E_a is the elastic modulus in the a-direction. The plastic hardening modulus E_p^a is the slope of the stress vs. plastic strain curve in a uniaxial stress test, and the tangent modulus E_T^a is the slope of the inelastic portion of a uniaxial stress vs. strain curve.

Tangent modulus is defined as the slope of a line tangent to the stress-strain curve at a point of interest. The tangent modulus can have different values depending on the point at which it is determined.

For the a-direction as reference direction Hill's criterion may be written as:

$$\bar{\boldsymbol{\sigma}}^2 = \frac{1}{\boldsymbol{R}+1}\begin{bmatrix} \boldsymbol{F}'(\boldsymbol{\sigma_c} - \boldsymbol{\sigma_b})^2 + \boldsymbol{G}'(\boldsymbol{\sigma_b} - \boldsymbol{\sigma_a})^2 + \boldsymbol{H}'(\boldsymbol{\sigma_a} - \boldsymbol{\sigma_c})^2 \\ + 2\boldsymbol{L}'\boldsymbol{\sigma}_{\boldsymbol{bc}}^2 + 2\boldsymbol{M}'\boldsymbol{\sigma}_{\boldsymbol{ab}}^2 + 2\boldsymbol{N}'\boldsymbol{\sigma}_{\boldsymbol{ca}}^2 \end{bmatrix} \tag{5.5.1.9.}$$

where F', G' and H' are found in terms of the anisotropy parameters R and P as:

$$F' = \frac{R}{P} = \frac{F}{G}$$

$$G' = 1 = \frac{G}{G} \qquad (5.5.1.10.)$$

$$H' = R = \frac{H}{G}$$

The shear terms L, M and N are found using:

$$L' = \left(Q_{bc} + \frac{1}{2}\right)(R+Z) = \frac{L}{G}$$

$$M' = \left(Q_{ba} + \frac{1}{2}\right)(R+Z) = \frac{M}{G} \qquad (5.5.1.11.)$$

$$N' = \left(Q_{ca} + \frac{1}{2}\right)(Z+1) = \frac{L}{G}$$

where Z is defined as:

$$Z = \frac{R}{P} = \frac{F}{G} \qquad (5.5.1.12.)$$

The anisotropy parameters R, P, Q_{bc}, Q_{ba}, and Q_{ca} can be determined from simple uniaxial material tension test in orthogonal directions.

In the plane stress case with in-plane anisotropy, the anisotropy parameters are defined in terms of Lankford and Hill's coefficients as:

$$R = R_0 = \frac{H}{G};$$

$$P = R_{90} = \frac{H}{F}; \qquad (5.5.1.13.)$$

$$Q_{ca} = R_{45} = \frac{2N - (F+G)}{2(F+G)}$$

and Hill's criterion reduces to:

$$\bar{\sigma}^2 = \boldsymbol{F}\sigma_c^{\,2} + \boldsymbol{G}\sigma_a^{\,2} + \boldsymbol{H}(\sigma_a - \sigma_c)^2 + 2\boldsymbol{N}\sigma_{ca}^{\,2}. \qquad (5.5.1.14.)$$

5.5.2. Numerical simulation

Numerical simulations of Taylor test experiments have been done in order to test proposed procedure for calibration of Hill's orthotropic yield criterion and calculated parameters for aluminium alloy AA7010.

The material parameters that were used in the analyses are summarized in the following table (Table 5.5.2.1.).

Table 5.5.2.1. Constants for AA7010 in the Hill's General Anisotropic Model

Parameter	Description	Nominal value
E_a	Elastic modulus	70.326 GPa
E_b	Elastic modulus	70.326 GPa
E_c	Elastic modulus	70.326 GPa
R	Anisotropy coefficient	0.836
P	Anisotropy coefficient	0.824
Q_{bc}	Anisotropy coefficient	1
Q_{ab}	Anisotropy coefficient	1
Q_{ac}	Anisotropy coefficient	1.0377
υ_{ba}	Poisson's ratio	0.33
υ_{ca}	Poisson's ratio	0.33
υ_{cb}	Poisson's ratio	0.33
AOPT	Material axes option	2
σ_{ya}	Yield stress in a-direction	504 MPa
β	Material angle	0
a_x	X component of vector a	0
a_y	Y component of vector a	0
a_z	Z component of vector a	1
d_x	X component of vector d	0
d_y	Y component of vector d	1
d_z	Z component of vector d	0
E_p^a	Hardening modulus in a-direction	0.65 GPa
G_{bc}	Shear modulus	26.889 GPa
G_{ab}	Shear modulus	26.889 GPa
G_{ac}	Shear modulus	26.889 GPa

Definition for globally orthotropic material (Fig. 7.1.) has been used in the simulation with material axes determined by vectors defined as: c=a X d; b= c X a, and following vector orientations:

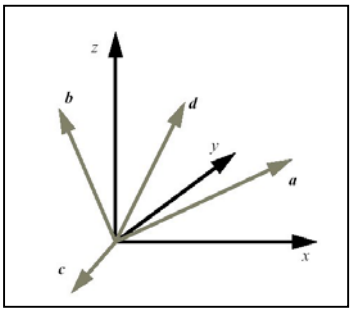

a = x (Z axis - DYNA model); $\vec{a} = 0\vec{i} + 0\vec{j} + 1\vec{k}$

b = z (Y axis - DYNA model); $\vec{b} = \vec{d} = 0\vec{i} + 1\vec{j} + 0\vec{k}$

c = y (X axis - DYNA model); $\vec{c} = 1\vec{i} + 0\vec{j} + 0\vec{k}$

Fig. 5.5.2.1. Definition of orthotropic material axes

Comparisons of simulated Taylor cylinder profiles with minor and major side profiles of post-test geometry for Taylor specimens impacted at 200 m/s and 214 m/s are presented in Fig. 5.5.2.2. and Fig 5.5.2.3.

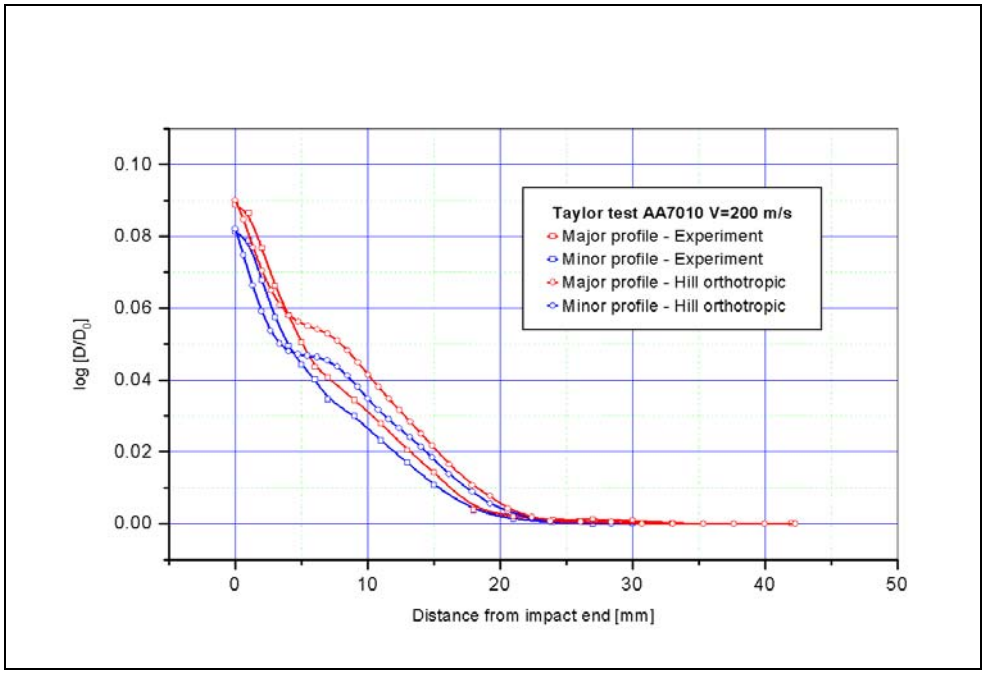

Fig. 5.5.2.2. Major and minor side profile of post-test geometry and simulation results for the AA7010 Taylor specimen impacted at 200 m/s plotted as radial strain vs. distance

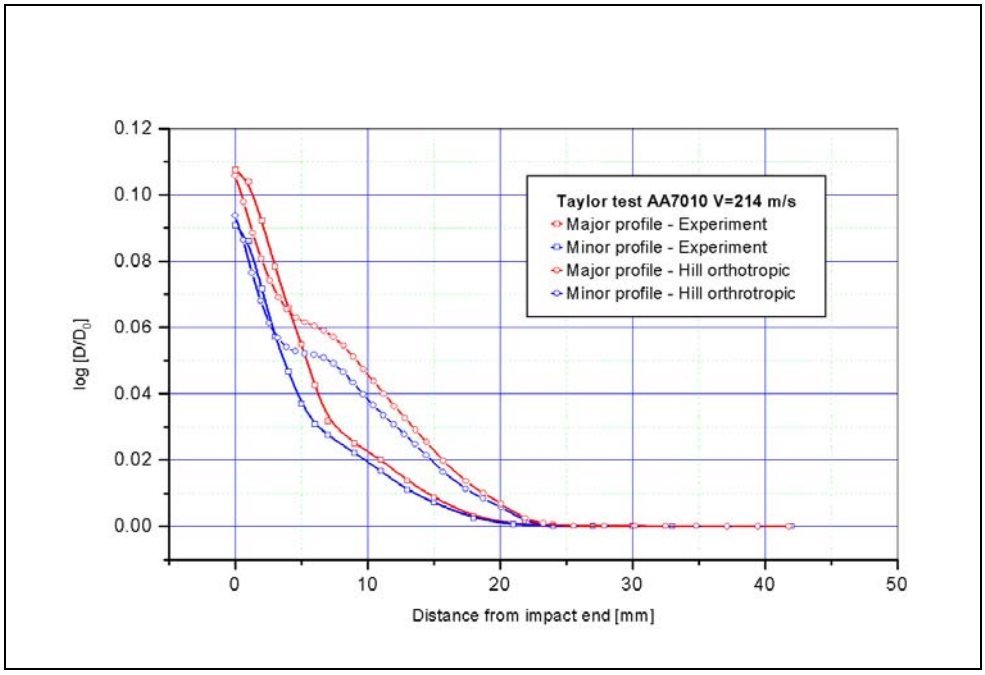

Fig. 5.5.2.3. Major and minor side profile of post-test geometry and simulation results for the AA7010 Taylor specimen impacted at 214 m/s plotted as radial strain vs. distance

Comparing the experimental shapes of the impact-interface footprints with DYNA3D code results (Fig. 5.5.2.4. – Fig 5.5.2.5.), we can observe that Hill's orthotropic yield criterion can capture orthotropic behaviour for aluminium alloy AA7010.

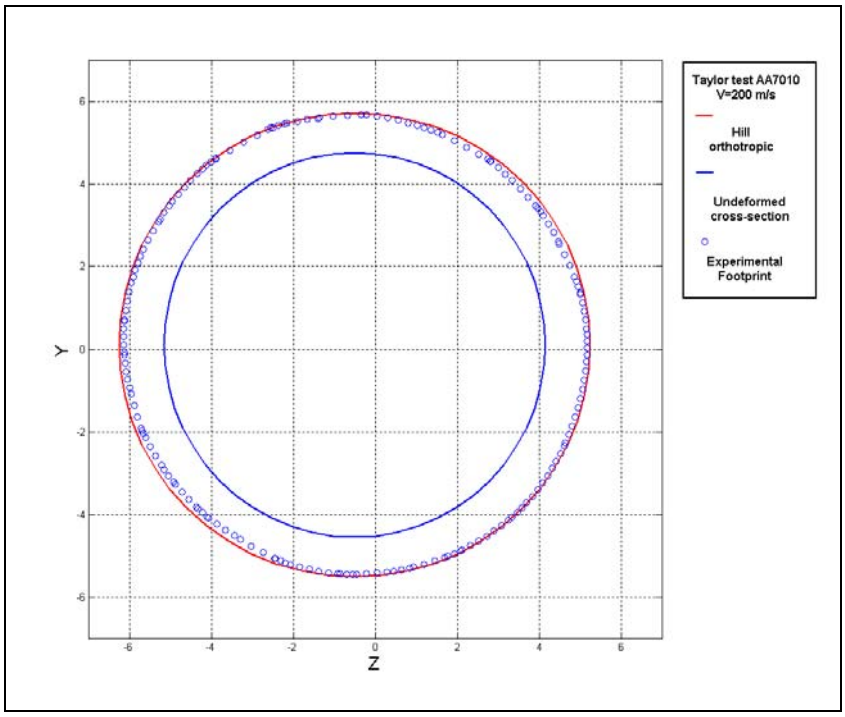

Fig. 5.5.2.4. Comparison of footprints of the Taylor cylinder launched with initial velocity of 200 m/s

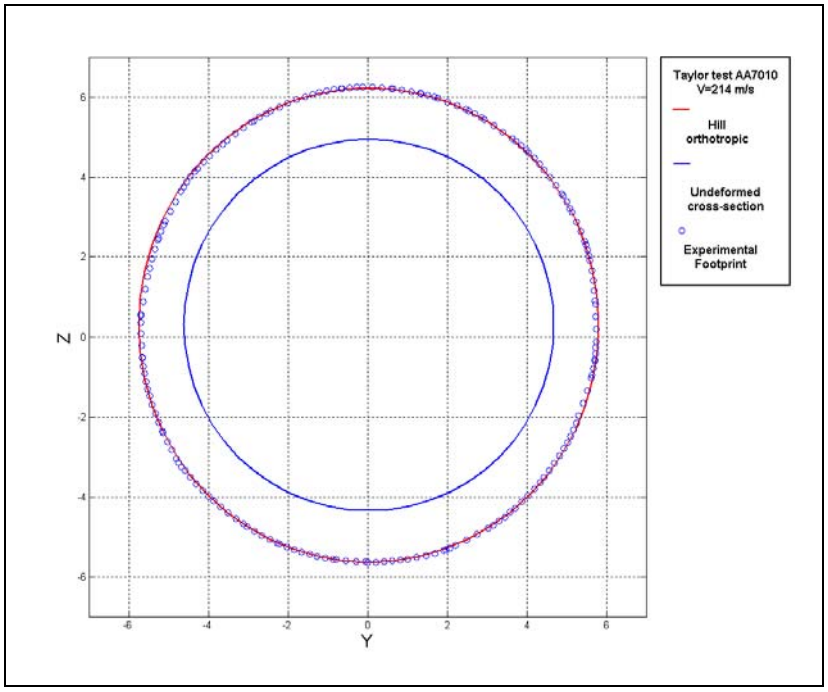

Fig. 5.5.2.5. Comparison of footprints of the Taylor cylinder launched with initial velocity of 214 m/s

5.6. Conclusions

It has been shown that the anisotropic behaviour of the aluminium alloy AA7010 can be correctly described by Hill criteria in combination with a sound parameter estimation procedure, and that accurate description of material behaviour can be achieved. Simple assumption of isotropic hardening has been proven to be sufficient to obtain good agreement with experimental data.

A novel method for calibration of orthotropic yield criterion has been developed in this work. Parameters for the Hill's orthotropic model under the associated flow rule assumption have been identified using uniaxial tensile and Taylor impact tests.

The uniaxial tensile test, used for material model calibration is cheap, simple and robust. Tensile tests in a different material directions resulted in different yield stresses, and those values have been used for calibration of orthotropic yield criterion. Because of the limitations of the uniaxial tests (only longitudinal strain of flat tensile specimen has been measured for all three different directions) results from Taylor tests were proposed for determination of Lankford coefficients.

Numerical simulations of Taylor test experiments have been done, and results from the simulations of the cylinder impact test (major and minor side profiles, and impact-interface footprints) showed a good correlation to experimental results.

6. MATERIAL FAILURE MODELLING

6.1. Introduction

Today it is very well known that material fracture depends on numerous factors like loading time, local stress, initial temperature and microstructure. Several formulae exist to predict material fracture, and those formulations represent three different approaches, physical, microstatistical and phenomenological.

We may distinguish two different phenomena:

- Brittle fracture phenomena
- Phenomena associated with ductile fracture

Brittle fracture is characterised by the propagation of a crack with a sharp front. Usually, this crack follows crystallographic orientation of the material. In some cases crack may propagate between the individual material grains (inter-granular mode).

Ductile fracture is a second common cause of failure in engineering structures. A damaged ductile material consists of two parts: matrix medium and damage, e.g. voids. Ductile failure is characterised by significant plastic deformation prior to material failure. As a consequence the propagation of the crack requires more energy and the crack tip becomes blunted. Ahead of the crack tip voids develop in the material undergoing plastic deformation. The crack extends by linking with voids. In contrast to quasi-static fracture, dynamic fracture is usually nucleated independently at many locations.

The mode of failure that is representative for aluminium alloys is ductile failure. From experimental studies, ductile fracture is dominated by the accumulation of localised large strain and damage in the forms of void nucleation, growth and coalescence.

The starting point for this work is to discuss simple criteria with the lowest number of constants but with some physical meaning. A review of exiting dynamic failure criteria is presented in the following chapter. These criteria are mainly used to simulate spall failure for the planar impact test. For a cylindrical target, the stress controlling damage formation (spall) is the stress $\sigma(t)$ in the loading direction, which is also the maximum normal stress. Therefore, a one-dimensional analysis can be used in spall criteria. This can be extended to the three-dimensional analysis, by using for the instance the mean stress or a combination of mean and equivalent stress.

6.2. Dynamic failure criteria

The most commonly used failure criteria are based on the assumption that time and stress, are the important variables in predicting both microfracture and structural failure under dynamic loading conditions. A general method presented by **Tuler and**

Butcher [96] and by **Gilman and Tuler** [97] suggests the use of a damage function ϕ as a function of the entire stress history $\sigma(t)$:

$$\phi = \int_0^t f[\sigma(t)]dt \qquad (6.2.1.)$$

where ϕ is selected to be any convenient function of damage and t is time. When ϕ reaches a critical value, t becomes the failure time or lifetime t_c. For example ϕ could be total number or volume of microcracks formed.

Tuler and Butcher suggested a general criterion based on the concept of cumulative damage and they found that function ϕ can be expressed in powers of $\sigma - \sigma_0$, where σ_0 is threshold stress below which no damage occurs regardless of the stress duration. It was further suggested that one term might be expected to be dominant. They proposed a relation between various loading conditions and spall fracture, including time dependence of spalling in the form of generalized criterion, where the spall stress depends on the stress pulse duration:

$$\int_0^{t_c} (\sigma(t) - \sigma_0)^{\lambda} dt = \phi \qquad (6.2.2.)$$

where λ and ϕ are material constants determined experimentally, σ_0 is threshold stress and t_c is time to failure.

Freund suggested that Tuler's and Butcher's model could be rewritten in the following manner:

$$\int_0^{t_c} \left[\frac{\sigma(t)}{\sigma_0} - 1 \right]^{\lambda} dt = t_{c0} \text{ with } t_{c0} = \phi / \sigma_0^{\lambda} \qquad (6.2.3.)$$

where σ_0 is threshold stress for the accumulated damage, λ is a positive constant and t_{c0} is the characteristic time, which is different for different materials. This criterion is based on the overstress concept and in the limit $\sigma(t) \to \sigma_0$, $t_c \to \infty$. This is not true since the longest critical times observed experimentally are finite and relatively short, and they are about several microseconds. For longest intervals of loading near the threshold stress σ_0, only the initial damage is usually found.

A number of criteria have been derived from the following form of the Tuler and Butcher failure criterion:

$$1 = \int_0^{t_c} \left(\frac{\sigma - \sigma_0}{\sigma_r} \right)^{\lambda} dt \qquad (6.2.4.)$$

by introducing a damage parameter D as an internal variable, where in the original Tuler and Butcher failure criterion σ_r is reference stress and t_c is the time to failure.

For example the modified Tuler-Butcher criterion proposed by **Cagnoux** is given by:

$$1 = \int_0^{t_c} \left(\left(\frac{1}{\sigma_r} \right) \left(\frac{\sigma - \sigma_0}{1 - D} \right) \right)^{\lambda} (1 - D)^{\lambda - b\sigma} \, dt \tag{6.2.5.}$$

where b and λ are material parameters.

In the work of **Wanjia** the modified Tuler-Butcher criterion is proposed in the following form:

$$1 = \int_0^{t_c} \left(\left(\frac{1}{\sigma_r} \right) \left(\frac{\sigma - \sigma_0}{1 - D} \right) \right)^{\lambda} dt \tag{6.2.6.}$$

Davison and Stevens introduced a continuous measure of damage D, and proposed a theory of compound-damage accumulation. Their function D can be assumed to be the degree of separation along the spall interface and varies from 0 (which represents state of no incipient spall) to 1 (which represent state of complete splall).

If a time τ_0 at the stress σ produces a damage D_0, then an increment in time of Δt at the same stress level, will produce an increment in damage ΔD:

$$\frac{\Delta D}{\Delta t} = \frac{D_0}{\tau_0} \tag{6.2.7.}$$

where τ_0 decreases with increasing tensile stress σ

$$\tau_0 = \hat{\tau}(\sigma) . \tag{6.2.8.}$$

For two or more load applications, we can write:

$$\Delta D_i = \Delta t_i \frac{D_0}{\hat{\tau}(\sigma)} . \tag{6.2.9.}$$

The sequence of load applications produces the following damage:

$$D = \sum_i D_i = \sum \left[\frac{\Delta t_i}{\hat{\tau}(\sigma)} \right] D_0 \tag{6.2.10.}$$

and this discretized form after integrating can be represented as a continuous function of time as:

$$\boldsymbol{D}(\boldsymbol{x}, \boldsymbol{t}_f) = \boldsymbol{D}_0 \int_{-\infty}^{\boldsymbol{t}_f} \left[\frac{\boldsymbol{dt}}{\hat{\boldsymbol{\tau}}[\boldsymbol{\sigma}(\boldsymbol{x}, \boldsymbol{t})]} \right] . \tag{6.2.11.}$$

Now we can use relationship between σ and $\hat{\tau}(\sigma)$, which is proposed by Tuler and Butcher:

$$\hat{\boldsymbol{\tau}}(\boldsymbol{\sigma}) = \boldsymbol{\tau} \left[\frac{(\boldsymbol{\sigma} - \boldsymbol{\sigma}_0) + |\boldsymbol{\sigma} - \boldsymbol{\sigma}_0|}{2\boldsymbol{\sigma}_0} \right]^{-\boldsymbol{\lambda}} \tag{6.2.12.}$$

where σ_0 is a critical stress below which there is no damage, and we can rearrange above equation as:

$$\boldsymbol{D}(\boldsymbol{x},\boldsymbol{t}_f) = \frac{\boldsymbol{D}_0}{\boldsymbol{\tau}} \int_{-\infty}^{t_f} \left[\frac{(\boldsymbol{\sigma}(\boldsymbol{x},\boldsymbol{t}) - \boldsymbol{\sigma}_0) + |\boldsymbol{\sigma}(\boldsymbol{x},\boldsymbol{t}) - \boldsymbol{\sigma}_0|}{2\boldsymbol{\sigma}_0} \right]^{\lambda} \boldsymbol{dt} \,. \qquad (6.2.13.)$$

All of the above mentioned criteria, where time and stress history are the important variables, are ***phenomenologically*** based. To account for the ***physical mechanisms*** of failure, **Zhurkov** [98] introduced, the concept based on the assumption that thermal activation is involved in material separation during fracture processes. It is generally accepted that rate and temperature effects are related to the thermally activated micromechanical processes of plasticity and fracturing. The creation of free surfaces in a stressed body occurs with assistance of thermal activation processes, or in other words, thermal vibration of the crystalline lattice reduces the energy threshold, which has to be exceeded for fracture to occur.

The kinetic concept of the mechanism of fracture is understood as time dependant process for which the rate is determined by stress and temperature. Systematic studies of the relationship between the lifetime of solids under load and the magnitude of the tensile tress and temperature have been carried out by Zhurkov. The relationship observed between the lifetime t_c, the critical stress σ and absolute temperature T could be written in the form of the kinetic equation:

$$t_c = t_{c0} \exp\left(\frac{U_0 - \gamma\sigma}{kT} \right) \qquad (6.2.14.)$$

where k is Boltzman's constant, whils t_{c0}, U_0 and γ represent material constants. The physical sense of the kinetic equation is defined by the three parameters: t_{c0}, U_0 and γ. They are as follows: t_{c0} coincides with the period of the natural oscillation of atoms for the material under consideration, U_0 can be interpreted as the magnitude of the energy barrier related to the probability of breaking the bonds defining strength, and γ called the activation volume, is linked to the microstructure. This constant may be interpreted as a coefficient which takes into account the overstress on a bond as compared to the average stress in a solid. The dependence of effective barrier energy $\Delta U = U_0 - \gamma\sigma$ on the stress results in sharp acceleration of the fracture process in a stressed body, and in a decrease of its lifetime under load.

Another approach to incorporate ***physical mechanisms*** of failure is based on the rate theory of fracture. The rate theory of thermally activated fracture was developed by considering the bond-breaking and establishing processes as fundamental mechanism of fracture initiation. In this approach a fracture forms and propagates because the rate of bond breaking is greater then the rate of bond re-establishment. **Tobolsky and Eyring** [93] originally developed this theory for polymeric threads. It has been shown by the other investigators, that theory is equally valid for crystalline and amorphous materials.

In this approach we can observe constant stress σ, which acts on N bonds per unit area. The work done by the force acting on a bond during its breaking is

$$W = \sigma / N \lambda \tag{6.2.15.}$$

where λ is the average distance over which the force acts during bond breaking process. The net rate of bond breaking is approximated as:

$$-\frac{dN}{dt} = N\frac{kT}{h}\exp\left(-\frac{U}{kT}\right)2\sin\frac{\lambda\sigma}{NkT} \tag{6.2.16.}$$

where k is Boltzmann's constant, T is absolute temperature, h is Planck's constant and U is free energy of activation.

At large stresses and low temperature when the bond healing process does not take place, the equation for net bond breaking can be written as:

$$-\frac{dN}{dt} \approx N\frac{kT}{h}\exp\left(-\frac{U}{kT}\right)\exp\left(\frac{\lambda\sigma}{NkT}\right) \tag{6.2.17.}$$

Above equation can be integrated as:

$$-\int_{N_0}^{0}\frac{1}{N}\exp\left(-\frac{\lambda\sigma}{NkT}\right)dN = t_c\frac{kT}{h}\exp\left(-\frac{U}{kT}\right), \tag{6.2.18.}$$

where t_c is the lifetime of specimen subjected to constant stress. If the following substitution is made, $\chi = \frac{\lambda\sigma}{NkT}$, we can write:

$$-\int_{\lambda\sigma/N_0kT}^{\infty}\frac{1}{\chi}\exp(-\chi)d\chi = t_c\frac{kT}{h}\exp\left(-\frac{U}{kT}\right) \tag{6.2.19.}$$

The exponential integral on the left-hand side of this equation for large values of χ reduces to:

$$-\int_{\lambda\sigma/N_0kT}^{\infty}\frac{1}{\chi}\exp(-\chi)d\chi \approx \frac{\exp(-\chi)}{\chi}, \tag{6.2.20.}$$

Therefore, at constant load the lifetime can be expressed as:

$$\ln t_c = \ln\frac{hN_0}{\lambda\sigma} + \frac{U}{kT} - \frac{\lambda\sigma}{N_0kT} \tag{6.2.21.}$$

One can rearrange this equation in the form, which was used by Zhurkov:

$$t_c = \frac{hN_0}{\lambda\sigma}\exp\left(\frac{U - \lambda\sigma / N_0}{kT}\right) = t_{co}\exp\left(\frac{U-\gamma\sigma}{kT}\right) \qquad (6.2.22.)$$

Dremin and Molodets [100], have proposed a modification of the Zhurkov criterion, to be applied in spall mechanics. They proposed modification, which takes into account the local parameters of the fracture process. This is because the barriers are overcome inhomogeneously at different macroscopic stress levels. The overcoming takes place only in some microvolumes. It means that the activation energy has to be a function of the local stress and the local activation volume. They used the fact that during plastic deformation, failure does not occur instantaneously, but rather after a certain cumulative time. That introduced the damage accumulation rate function $\dot{\phi}$ that characterizes thermally activated damage evolution:

$$\dot{\phi} = \dot{\phi}_0 \exp\left(\frac{-\Delta U}{kT}\right),\ 1 = \int_0^{t_f} \dot{\phi} dt \ \text{ and } \ \Delta \boldsymbol{U} = \boldsymbol{U}_0 - \boldsymbol{\beta\sigma} \qquad (6.2.23.)$$

Their assumption is that parameters $\dot{\phi}_0 = 1/t_0$, U_0 and β do not depend on temperature, and that $\Delta U(\sigma)$ is the stress-dependent free energy of damage activation. It is also assumed that time interval of the micro crack growth is very short (typically few nanoseconds in hard materials) in comparison to the critical time to spalling.

Klepaczko [101], following Zhurkov's approach, proposed cumulative criterion for short and very short loading times. It should be noted that this criterion has physical motivation based on thermally activated rate processes, and it can predict very well the critical time for failure t_c as a function of the spall stress σ for different materials.

The proposed model introduces a temperature factor that depends on the activation energy ΔU_0. To derive this criterion, he used the stress dependent activation energy given by **Yokobori** [104]:

$$\Delta U(\sigma) = \Delta U_0 \ln\left(\frac{\sigma_0}{\sigma}\right) \qquad (6.2.24.)$$

where σ is the local stress, σ_0 is threshold stress, ΔU_0 is the barrier energy for non-stressed body or its activation energy.

Substituing the expression for Yokobori's activation energy, Eq. (6.2.24.), into cumulative damage criterion, Eq. (6.2.23.), which was proposed by Dremin and Molodets, Klepaczko's cumulative failure criterion in the integral form becomes:

$$\int_0^{t_c}\left(\frac{\sigma(t)}{\sigma_0}\right)^{\alpha(T)} dt = t_{c0}\ ;\ t_c \le t_{c0}\ ;\ \sigma \ge \sigma_0 \qquad (6.2.25.)$$

where:

- t_c is the time to failure and $\sigma_0, t_{c0}, \alpha(T)$ are three material constants at constant temperature T
- σ_0 is threshold stress which corresponds to the characteristic time t_{c0}
- t_{c0} is the longest critical time when $\sigma(t_{c0}) = \sigma_0$, for $t_c \geq t_{c0}$, $\sigma = \sigma_0$ and $\sigma_0 = const$
- $\alpha(T) = {\Delta U_0}/{kT}$, where T is absolute temperature, ΔU_0 is activation energy, and k is Boltzmann's constant.

When the process is non-isothermal, as it is in the case of spalling, the exponent $\alpha(T)$ is time dependent due to changes of temperature during loading or unloading $\alpha(T,t)$. In such a case the proposed cumulative criterion must be integrated accordingly, including the temperature history T(t).

Since this spall criterion is general, it includes both the brittle and ductile micromechanisms of separation. Those two modes are combined in different proportions determined by the value of exponent α. The criterion universality lies in the fact that it has a cumulative character and the exponent α is temperature dependent. When temperature increases more ductile micromechanisms are activated and threshold stress for spalling increases up to a high level of ductility.

Recently, **Hanim and Klepaczko** [104], have introduced another effect of temperature in this criterion by expressing the threshold stress σ_0 as a function of temperature:

$$\sigma_0(T) = \sigma^o{}_0 \frac{\mu(T)}{\mu_0} \tag{6.2.26.}$$

where $\sigma^o{}_0$ is the threshold stress at absolute temperature near 0K, $\mu(T)$ is shear modulus as a function of temperature T, and μ_0 is shear modulus near 0 K.

Following the work of Kocks [55], normalized activation energy u_0 can be defined in the following manner:

$$\Delta U_0 = \mu(T) b^3 u_0 \tag{6.2.27.}$$

where b is Burgers vector, and $\mu(T)$ is temperature dependent shear modulus. We can assume that stress dependent activation energy given by Yokobori can be written in the following form:

$$\Delta U(\sigma) = \mu(T) b^3 u_0 \ln\left(\frac{{\sigma_0}/{\mu_0}}{{\sigma}/{\mu(T)}} \right) \tag{6.2.28.}$$

Substituing the above expression for activation energy into cumulative damage criterion Eq. (6.2.23.), which was proposed by Dremin and Molodets, a modified Klepaczko's cumulative failure criterion in the integral form can be written as:

$$\int_0^{t_c} \left(\frac{\sigma(t)/\mu(T)}{\sigma_0/\mu_0} \right)^{\left(\frac{\mu(T)b^3u_0}{kT}\right)} dt = t_{c0} \qquad (6.2.29.)$$

To determine the parameters t_{c0}, σ_0 and u_0, modified Klepaczko's failure criterion, could be integrated [106] and defined as a fitting equation in the following form:

$$\frac{\sigma}{\mu(T)} = \frac{\sigma_0}{\mu_0}\left[\left(\frac{u_0 b^3 \mu(T)}{kT}+1\right)\frac{t_{c0}}{t_c}\right]^{\left(\frac{kT}{u_0 b^3 \mu(T)}\right)} \qquad (6.2.30.)$$

Using this fitting equation and plotting normalized critical spall stress data $\boldsymbol{\sigma/\mu(T)}$ versus critical time of loading data $\boldsymbol{t_c}$, from series of plate impact tests, parameters t_{c0}, σ_0 and u_0 could be easily determined. Plate impact tests are carried out at different impact speeds resulting in different stress levels, and with different plates thicknesses, resulting in different loading times.

Besides those criteria, which can be generalized as *Tuler-Butcher type criteria*, we can recognize second type of dynamic failure criteria and those are based on *nucleation and growth of cracks or voids*. First type of these criteria are based only on one evolution equation of damage and do not specify the mechanisms of nucleation, growth and coalescence.

Microdamage nucleates at heterogeneities in the material such as inclusions, grain boundaries, etc. Nucleation occurs in two stages. First, a threshold condition must be exceeded before nucleation can begin. Second, once the threshold is met, nucleation will occur over a size range of heterogeneities and at a material specific rate. Growth, by definition, is the increase in size of the microscopic cracks or voids. And finally, after the microcraks or voids have grown by an amount comparable to the average void spacing, coalescence must begin.

Curran et al. [107] developed a physically based model involving the nucleation, growth and coalescence of voids in a region undergoing tensile stresses. Their approach involves expressions for the rate of nucleation N and the rate of growth R.

In this criterion, the form of the equation for nucleation rate function is consistent with experimental results of Zhurkov, and is expressed as:

$$\dot{N} = \dot{N}_0 \exp\left(\frac{\sigma - \sigma_{n0}}{\sigma_r}\right) \qquad (6.2.31.)$$

where $\dot{N}_0$ is the threshold nucleation rate, σ_{n0} is nucleation tensile threshold stress, and σ_r is reference stress or stress sensitivity for nucleation.

This equation expresses the fact that below σ_{n0}, no nucleation is observed, and above threshold stress the nucleation rate increases exponentially with tensile stress σ.

The growth rate is given by:

$$\dot{R} = \left(\frac{\sigma - \sigma_{g0}}{4\eta} \right) R \tag{6.2.32.}$$

where R is void radius, σ_{g0} is the growth threshold stress, and η is material viscosity. This equation states that the growth rate $\dot{R}$ is proportional to the radius of void.

The total relative void volume Vv associated with nucleation and growth at the end of loading time interval Δt consists of the void nucleation volume and the void growth volume and is given by:

$$V_v = 8\pi \dot{N} \Delta t R_0^3 + V_{v0} \exp\left(3 \frac{\sigma - \sigma_{g0}}{4\eta} \Delta t \right) \tag{6.2.33.}$$

where $V_{v0} = 8\pi \dot{N} \Delta t R_0^3$ is relative void volume at the beginning of the time interval, and R_0 is the radius at the beginning of the time interval.

To describe void nucleation and growth in ductile metals, a dynamic model has been proposed by **Rajendran** at al [107]. In this criterion, the void nucleation proess was modelled through a Gaussian distribution. This model is based on pressure dependent yield criterion for compressible plastic flow and is strain rate and loading history dependent. If we denote by f the volume fraction of voids, the evolution rate of this fraction is given by:

$$\dot{f} = F_\sigma \dot{\sigma} + F_\varepsilon \dot{\varepsilon} + \dot{f}_g \tag{6.2.34.}$$

The first term in this equation represents the stress-controlled evolution where $\dot{\sigma}$ is the stress rate. The second term represents the strain-controlled evolution where $\dot{\varepsilon}^p$ is the plastic strain rate and the last term represents the rate of growth. Functions F_σ and F_ε are given by the following Gaussian distributions as initially proposed by **Chu and Needleman** [105]**:**

$$F_\sigma = \frac{f_1}{s_1 \sqrt{2\pi}} \exp\left(-\frac{1}{2} \left(\frac{\sigma - \sigma_n}{s_1} \right)^2 \right)$$

$$F_\varepsilon = \frac{f_2}{s_2 \sqrt{2\pi}} \exp\left(-\frac{1}{2} \left(\frac{\varepsilon^p - \varepsilon_n}{s_2} \right)^2 \right) \tag{6.2.35.}$$

Here, σ_n and ε_n are the mean equivalent threshold stress and strain, respectively, around which the nucleation stress and strain are distributed in a Gaussian manner, respectively. The terms s_1 and s_2 are the standard deviations of these distributions. The terms f_1 and f_2 define the maximum allowable void volume fraction due to stress and strain nucleation, respectively. In this model, the rate of growth of voids is given by the classical relationship:

$$\dot{f}_g = (1-f)\dot{\varepsilon}_{ii}^p \qquad (6.2.36.)$$

where $\dot{\varepsilon}_{ii}^p$ is the trace of the plastic strain rate tensor which represents the volumetric inelastic strain rate.

The **Cochran-Banner** model [108] is another representative of this group of damage models. This model was originally developed and tested for solid elements as a part of the 1D code. The Cochran-Banner damage model has a simple and efficient theoretical definition, and input constants can be obtained from the uniaxial tensile test. These arguments ensure that the model can be useful for the crashworthiness simulations.

It is assumed that the level of resulting tensile stress controls the damage initialisation in material. Once the certain level of tensile stress is reached, this triggers the nucleation and growth of microscopic voids. In the final stages the micro-voids will coalesce to form the macroscopic void. The formation of macroscopic void represents the stage of material separation, or material failure.

The main idea behind this model is to describe the transition from undamaged ductile material to ductile failure, i.e., to formulate the weakening process in material influenced by the damage growth.

This model is based on two parameters, σ^{fail} (tensile strength) and D_0 (critical length, corresponds to total fracture):

- σ^{fail} is defined as the largest tensile stress that the material can withstand before any damage in material occurs. This value can be approximated quite well from the experimental tensile data for the material of interest.
- D_0 is defined as a material constant which corresponds to total fracture. D_0 is proportional to the size of voids when they coalesce, and it may be related to the grain size.

The method of statistical averaging of microscopic processes into a continuum description of material fracture is applied in the Cochran-Banner model. Variable D(x,t) is defined as the volume of the microcracks at a given location and time.

$$D(x,t) = \int_0^t dV / A, \qquad \text{dV>0} \qquad (6.2.37.)$$

where A is the current element cross-section normal to the loading direction.

In one dimensional finite difference calculation, the damage will be the volume of microcracks (actual volume, not the relative value) per unit area normal to

the strain in a given mass zone. In a general 3D case, the damage is defined by the volume of microcracks (actual volume, not the relative value) per average element cross-section area.

In order to calculate the damage a simplification can be made that all expansion that occurs after the tensile strength σ^{fail} has been exceeded could be recognised as the microcrack volume growth. This definition allows damage to be related directly to the other dynamic variables.

Following from theory of microvoids growth, the strength function is defined as:

$$F_{dam} = 1 - \left(\frac{D}{D_0} \right)^{2/3} \qquad (6.2.38.)$$

The value of F_{dam} can be interpreted as a factor that reduces the cross sectional area over which the stress acts. During the phase of damage growth material properties are degraded. This is described by scaling of the yield strength, Young's modulus and shear modulus by the value of F_{dam}, with the global effect in the decrease in stress and flow stress increments.

The power of 2/3 comes from the cross sectional area of spherical voids being proportional to the two-thirds power of the void volume. In this case it is assumed that microvoids have spherical shape. This is an isotropic damage model, which can be used for both isotropic and orthotropic materials.

To account for the physical mechanisms of failure, the concept of thermal activation of damage and failure has been adopted as basis for this material model development and Klepaczko's failure criteria has been used as a starting point. This basic assumption makes the proposed approach compatible with the Mechanical Threshold Stress model, which was used as the strength part of the proposed constitutive model. The developments were incorporated into public domain DYNA3D.

6.3. Model validation

6.3.1. Plate impact test experiment - analysis of pullback speed

Plate impact experiments are used to study dynamic deformation and failure modes of materials at high strain of rates. Variations of the free surface speed in the planar impact test can be directly related to the spall strength. The analysis of these profiles provides us with the values of spall stress and time to failure. Unloading starts at point of first maximum and continues until point of first minimum, where the new compressive wave arrives. This wave is created by the formation of spall surface inside the target. The amplitude of spall is signalled with second maximum (Fig. 6.3.1.1.). Four different approaches [104] for determination of spall strength and critical time of spalling are summarized.

1) The difference of free surface speeds between the first maximum (impact speed) and the first minimum called pull-back speedvelocity, can be directly related to the spall strength σ_{Fi} by the following equation:

$$\sigma_{Fi} = \frac{1}{2}\rho C_{1R}\Delta V_{fs} \tag{6.3.1.1}$$

where C_{1R} is the speed of the rarefaction wave emitted by the spall surface. It is assumed in this calculation that the rarefaction wave is purely elastic $C_{1R} \approx C_1$. This speed can be found from the distance of the spall surface Zc to the free surface and the travel time Δt_R of rarefaction wave:

$$C_{1R} = \frac{Zc}{\Delta t_R}. \tag{6.3.1.2}$$

The critical time of spalling t_c can be found from the following expression:

$$t_c = t_B - t_A. \tag{6.3.1.3}$$

2) The second approach is based on propagation of elasto-plastic wave with the bilinear material behaviour, and consequently with two wave speeds, elastic $\boldsymbol{C}_1$ and plastic $\boldsymbol{C}_2$. Therefore, following formula was derived:

$$\sigma_{Fi} = \rho C_1 \Delta V_{fs}\left(1 + \frac{C_1}{C_p}\right)^{-1}. \tag{6.3.1.4}$$

The critical time can be calculated using the elastic and plastic slownesses $S_1 = 1/C_1$ and $S_p = 1/C_p$:

$$\Delta t_c = Z_c(S_p - S_1) \tag{6.3.1.5}$$

where ΔZ_c is distance between the spall surface and free surface of the target where ΔV_{fs} is measured.

3) The third is a slightly different approach for determining the critical conditions of spalling and is based on the increment of the free surface speed δV_{fs} and the formula used is:

$$\sigma_{Fi} = \rho C_1 (\Delta V_{fs} + \delta V_{fs}) \qquad (6.3.1.6)$$

where δV_{fs} is the speed correction caused by plastic waves. When acceleration or deceleration of the free surface speed $\dot{V}_{fs}$ is determined, the final formula for the speed correction takes the form:

$$\delta V_{fs} = \Delta Z_c (S_1 - S_p) \frac{\left|\dot{V}_1 \dot{V}_2\right|}{\left|\dot{V}_1\right| + \left|\dot{V}_2\right|} \qquad (6.3.1.7)$$

where $\dot{V}_1$ and $\dot{V}_2$ are accelerations of mass at the wave front before and after spalling.

4) A direct application of the acoustic approach can be used to estimate the critical conditions of spalling. The critical time t_c after which spall occurs can be determined using acoustic approximation:

$$t_c = \frac{2L_i}{C_1} \qquad (6.3.1.8)$$

where $\boldsymbol{L_i}$ is thickness of flyer and $\boldsymbol{C_1}$ is speed of elastic wave. This is the time interval from beginning of tensile loading in the middle of target to the final spall. During this interval the stress plateau is σ_F and applied stress can be represented with following formula:

$$\sigma_F = \rho C_1 \frac{V_0}{2} \qquad (6.3.1.9)$$

Thus, with the input data L_i and V_0, two parameters can be determined after each experiment. It means that for the given stress level σ_F the spall occurs at t_c.

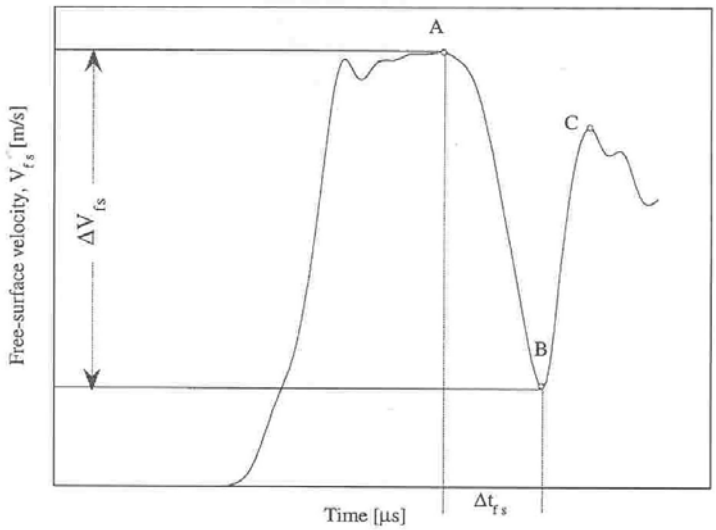

Fig. 6.3.1.1. The characteristic points during variations of the free surface velocity

6.3.2. Plate impact test simulation

In order to analyse proposed criterion for spall phenomenon, proposed criterion was implemented in DYNA3D code and incorporated into the MTS material model. A series of FE simulations have been performed for OFHC Cu with a circular target plate d=70.0 mm, impacted with flayer plate with diameter of 50 mm and with the impact speed of 304 m/s. The thickness of flyer plate was 5.0 mm, and the thickness of the target plate was 10.0 mm. Target was supported on the back with 12 mm block of polymethylmethacrylate (PMMA). Due to radial symmetry only quarter of the flyer and the target supported with PMMA backing have been modelled with a uniform solid butterfly mesh (Fig. 6.3.2.1.).

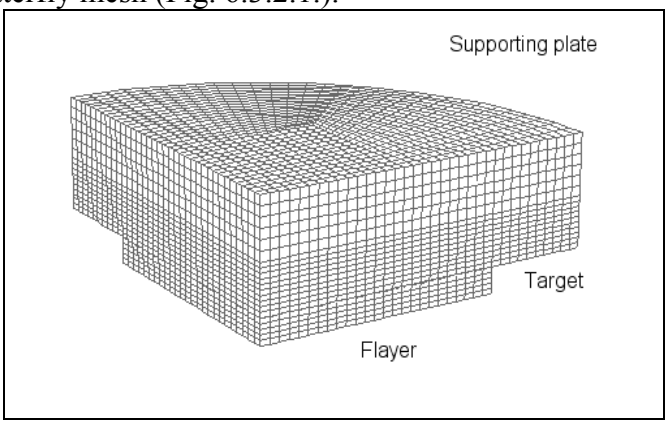

Fig. 6.3.2.1. FE model of the plate impact test

On the basis of published data [33] for spall strength for OFHC Cu (Fig. 6.3.2.2.), parameters, which are included in proposed failure criterion Eq. (6.2.29.) were determined as: threshold stress $\sigma_0 = 0.95GPa$, normalized activation energy related to the damage bond breaking $u_0 = 0.0508$ and critical time $t_{c0} = 1.4\mu s$.

Values of the other parameters, which are included in the proposed criterion are: Boltzmann's constant $k = 1.38X10^{-23}\,{}^{J}\!/_{K}$, Burgers vector $b = 0.255X10^{-9}\,m$, and shear modulus $\mu = b_0 - b_1 / \left(\exp(\frac{b_2}{T}) - 1 \right)$, where $b_0 = 47.3GPa$ is shear modulus at 0K, $b_1 = 2.40GPa$ and $b_2 = 130K$. Parameters $\boldsymbol{b}_0$, $\boldsymbol{b}_1$ and $\boldsymbol{b}_2$ are fittting constants.

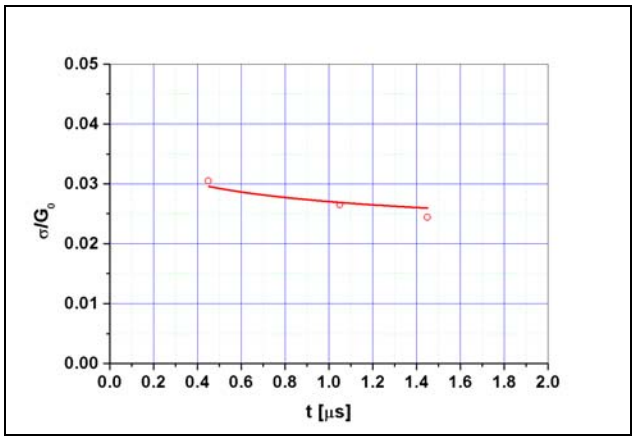

Fig. 6.3.2.2. Normalized critical spall stress versus critical time of lading for OFHC Cu

The flyer plate was modeled with Isotropic-Elastic-Plastic-Hydrodynamic model with Grunisen Equation of State. The material constants of the OFHC Cu and PMMA are listed in following tables.

Tab. 6.3.2.1. Material parameters for OFHC Cu used in the numerical simulation

Parameter	Description	Nominal value
G	Shear modulus	48.4 Gpa
σ_0	Yield stress	150 MPa
ρ	Density	8924 kg/m^3

Tab. 6.3.2.2. Grunisen Equation of State constants for OFHC Cu

Parameter	Description	Nominal value
C	Bulk sound speed	0.394 $cm/\mu s$
S_1	First Hugoniot slope coefficient	1.489 (1.51)
S_2	Second Hugoniot slope coefficient	0
S_3	Third Hugoniot slope coefficient	0
γ_0	Gruneisen coefficient	2.02
a	First order volume correction coefficient	0.47

Target plate was modelled with Mechanical Threshold Stress model in the combination with Grunisen Equation of State. (Tab. 6.3.2.3.)

Tab. 6.3.2.3. Mechanical Threshold Stress model parameters for OFHC Cu [26, 59]

Parameter	Description	Nominal value
$\hat{\sigma}_a$	Athermal rate independent threshold stress	40.0 MPa
$\hat{\sigma}_0$	Initial threshold stress at zero plastic strain	46.0 MPa
g_0	Normalized activation energy	1.6
$\dot{\varepsilon}_0$	Reference strain rate	10^7 s^{-1}
b	Magnitude of Burgers vector	0.255x10^{-9}m
k	Boltzmann's constant	1.38x10^{-23} J/K
p	Free energy equation exponent	2/3
q	Free energy equation exponent	1
A	Saturation stress equation material constant	0.312
$\hat{\sigma}_{s0}$	Saturation stress at zero degrees K	900.0 MPa
$\dot{\varepsilon}_{s0}$	Saturation stress reference strain rate	6.2x10^{10} s^{-1}
a_0	Hardening function constant	2371 MPa
a_1	Hardening function constant	8.295 MPa
a_2	Hardening function constant	3.506 MPa
b_0	Shear modulus at zero degrees K	47.3 GPa
b_1	Shear modulus constant	2.40 GPa
b_2	Shear modulus constant	130 K
T_r	Reference temperature	300 K
ρ	Density	8924 kg/m^3
C_p	Heat capacity	385 J/kgK

PMMA backing was modeled with isotropic–elastic–plastic-hydrodynamics material model with Mie-Grunisen equation of state, and value of 350 MPa was used for dynamic yield stress.

Tab. 6.3.2.4. Material parameters for PMMA used in the numerical simulation

Parameter	Description	Nominal value
G	Shear modulus	2.32 GPa
σ_0	Dynamic yield stress	350 MPa
ρ	Density	1182 kg/m^3

Tab. 6.3.2.5. Grunisen Equation of State constants for PMMA

Parameter	Description	Nominal value
C	Bulk sound speed	0.218 $cm/\mu s$
S_1	First Hugoniot slope coefficient	2.088
S_2	Second Hugoniot slope coefficient	-1.124
S_3	Third Hugoniot slope coefficient	0
γ_0	Gruneisen coefficient	0.85
a	First order volume correction coefficient	0

A uniform solid butterfly mesh was created for the parts, flyer and target plate having identical mesh density. A sensitivity analysis used to define an appropriate mesh density is presented in Appendix D. The density of the mesh of the PMMA backing was twice as coarse than the backing plate mesh in the thickness direction. Ten elements were defined through the thickness of the model of the target, and the same ratio was applied to the model of the flayer. A fine mesh was required in order to capture the continuous propagation of shock wave through the thickness of the plates. A sliding contact interface was defined between the flyer and target. This type of contact allows the surfaces to separate and move relative to each other in a completely arbitrary fashion.

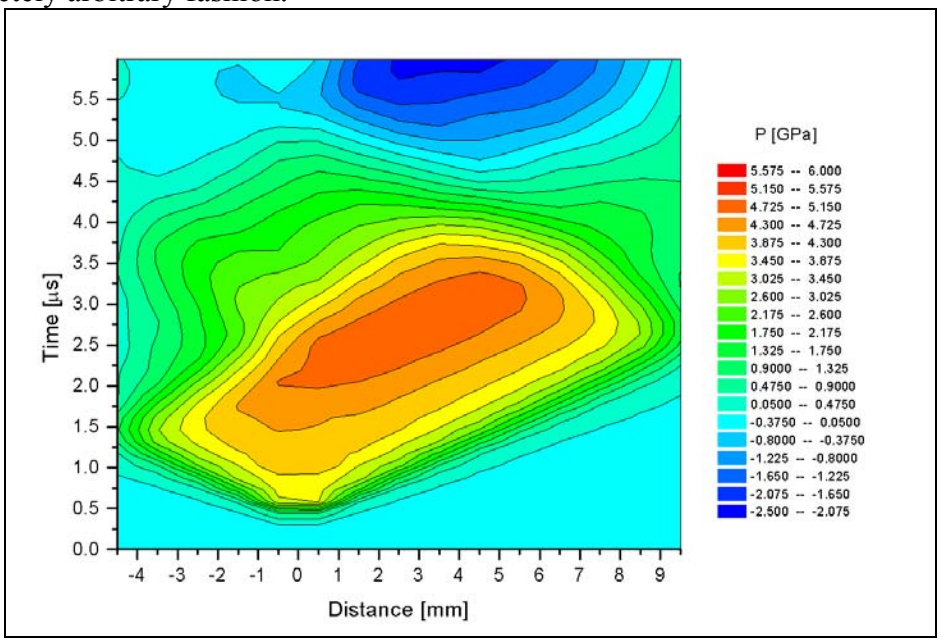

Fig. 6.3.2.3. Time-distance diagram for OFHC Cu plate impact test simulation without failure criterion for the 6 μs response time.

In order to analyse implemented failure criterion, Langrangian time-distance diagrams were used, and the results from numerical simulations with and without implemented criterion were compared. Diagrams were created for the sets of the elements through thickness of the flayer and the target. Points whose coordinates are calculated for the centroids of the elements represent each element.

The time-distance diagrams were constructed from pressure-time data for each of the elements, which are positioned on the axis of the symmetry. For the elements, the coordinate through the thickness of the material represents distance in the time-distance diagram. The figures Fig. 6.3.2.3. and Fig. 6.3.2.4. show the time-distance diagrams for 6 μs response time.

One can observe that release waves propagating into the material from both sides superpose inside the target plate and cause high-tension stress. When this tension stress exceeds the dynamic tension strength of the material, the material fails and new free surface is created inside the target plate. The creation of the spall plane – free surface, reduces the tension stress inside the material to zero, and results in the reflection of the reminder of the release wave as a compressive wave.

The implemented damage model detects incipient spall if the mean stress exceeds the spall threshold stress. Once incipient spall is detected, model calculates evaluation of damage using proposed cumulative criterion. When an element fails due to accumulated damage, it is removed from calculation.

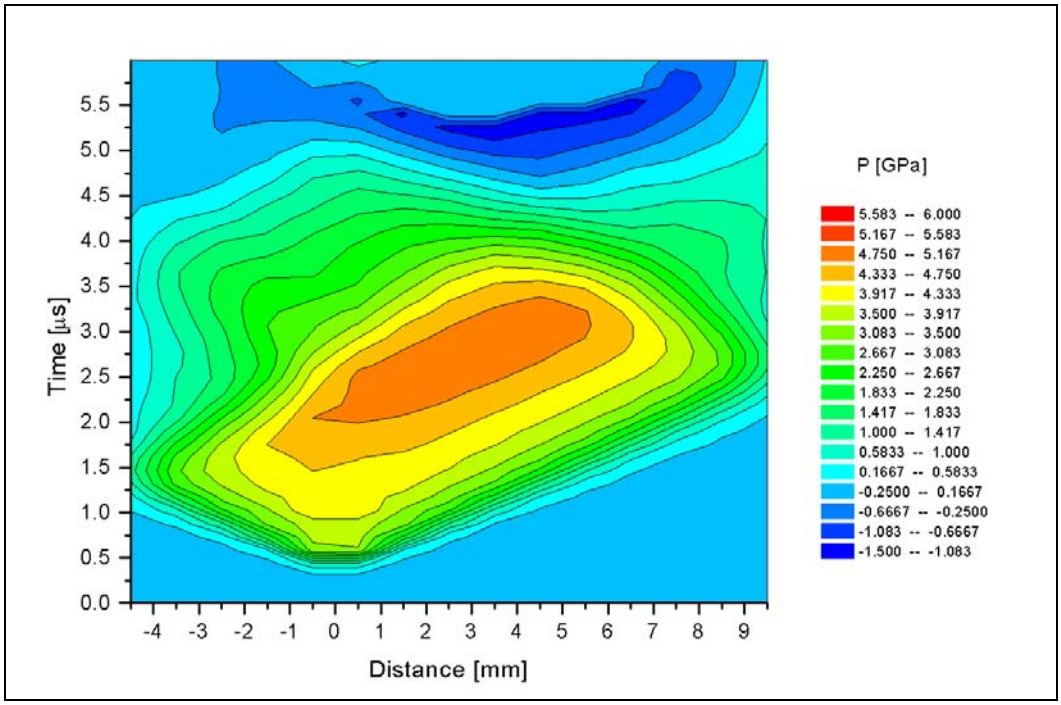

Fig. 6.3.2.4. Time distance diagram for OFHC Cu plate impact test simulation with implemented failure criterion 6 μs response time.

Contour plots of pressure at different stages of spalling for impact speed of 304 m/s are presented in Fig. 6.3.2.5. Spall starts near external diameter where the lateral release wave superimposes with the longitudinal release waves. However, the spall propagates almost instantaneously, and the free surface is created.

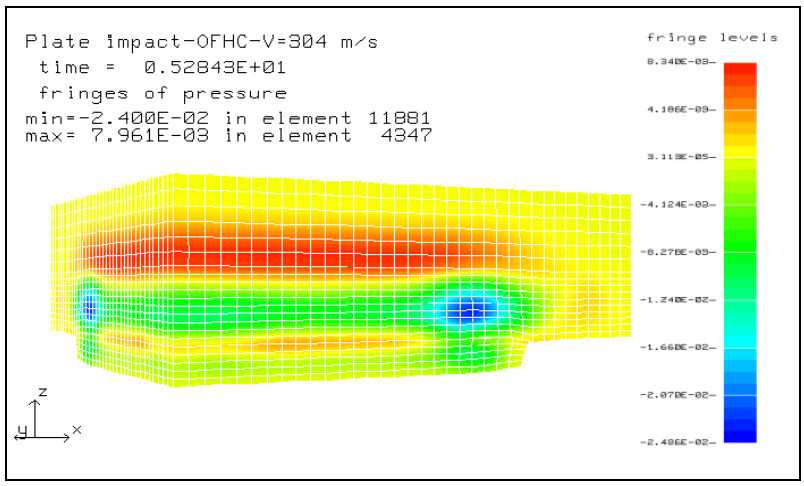

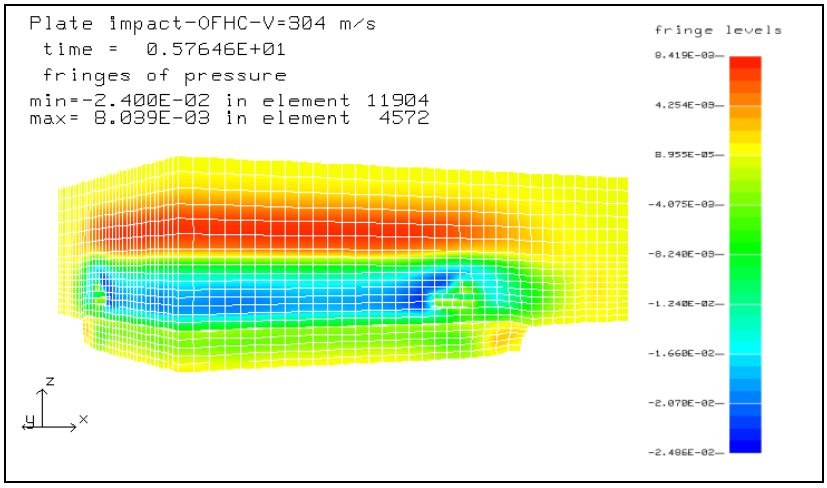

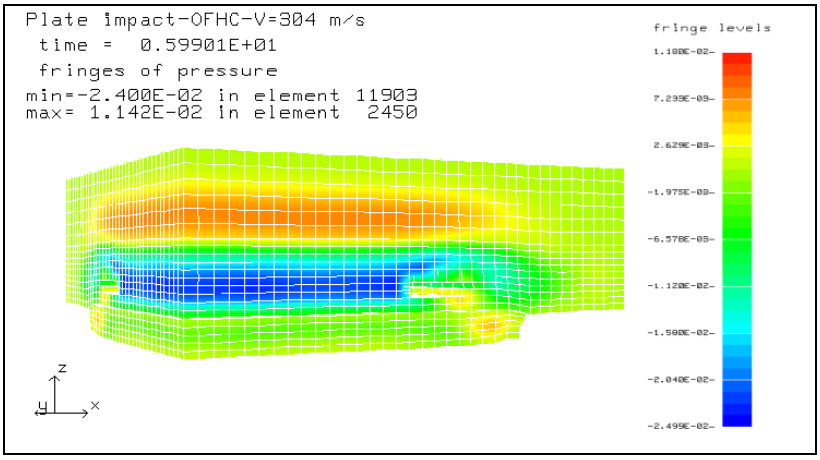

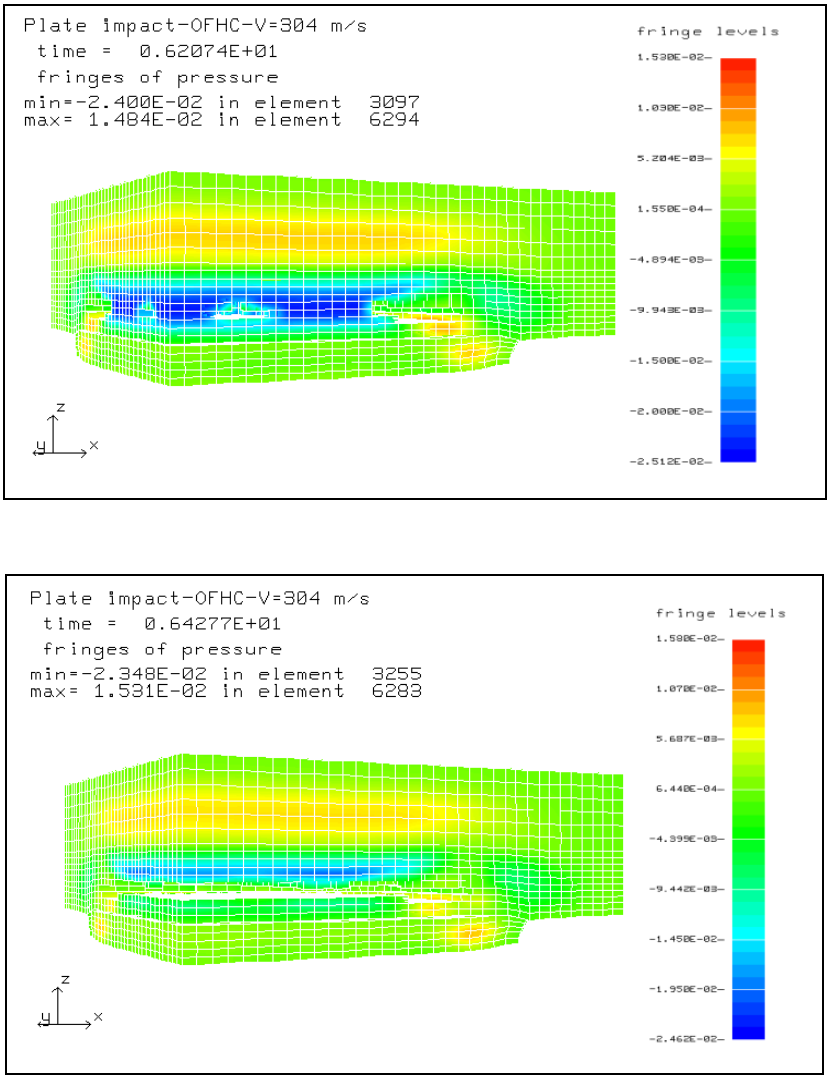

Fig. 6.3.2.5. The pressure plots at different stages of spalling of OFHC Cu for incident speed 304 m/s

The characteristic of the plate impact problem is that it can be reduced to a 1D wave propagation, and building an FE model in this case is greatly simplified.

In the model that was used for the simulation the three parts were modelled as rectangular bars (Fig. 6.3.2.6.) of 4x4 elements, and symmetry planes were applied on all the sides. This resulted in a 1D strain state along the length of the bar. A non-reflecting boundary condition was applied at the back of the PMMA block, and this condition ensures that no release wave travels back through the PMMA in to the OFHC Cu target block.

The impactor is modelled with 25 elements along the axis of impact, the test specimen and the PMMA block are modelled with 50 and 60 elements along the axis of impact, respectively. A contact interface was specified between the impactor and the test specimen. This mesh is sufficient to allow the resolution of all the relevant elastic and plastic waves in the target and the flyer.

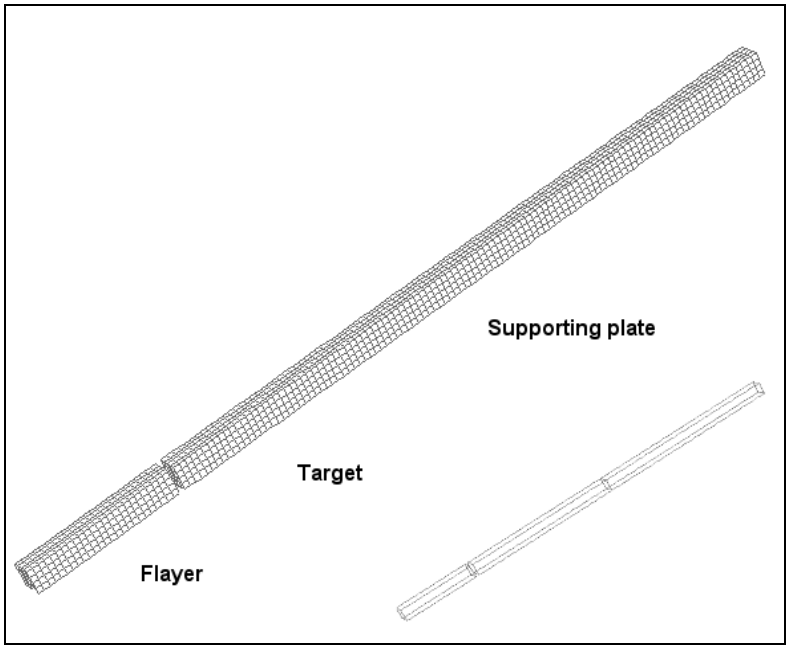

Fig. 6.3.2.6. FE model of the plate impact test – 1D case

The stress time history was recorded in the elements at the back of the test specimen. In the figure Fig. 6.3.2.7. the simulated stress trace at the interface between the target material and PMMA block, for the plate impact at 304 m/s, is presented.

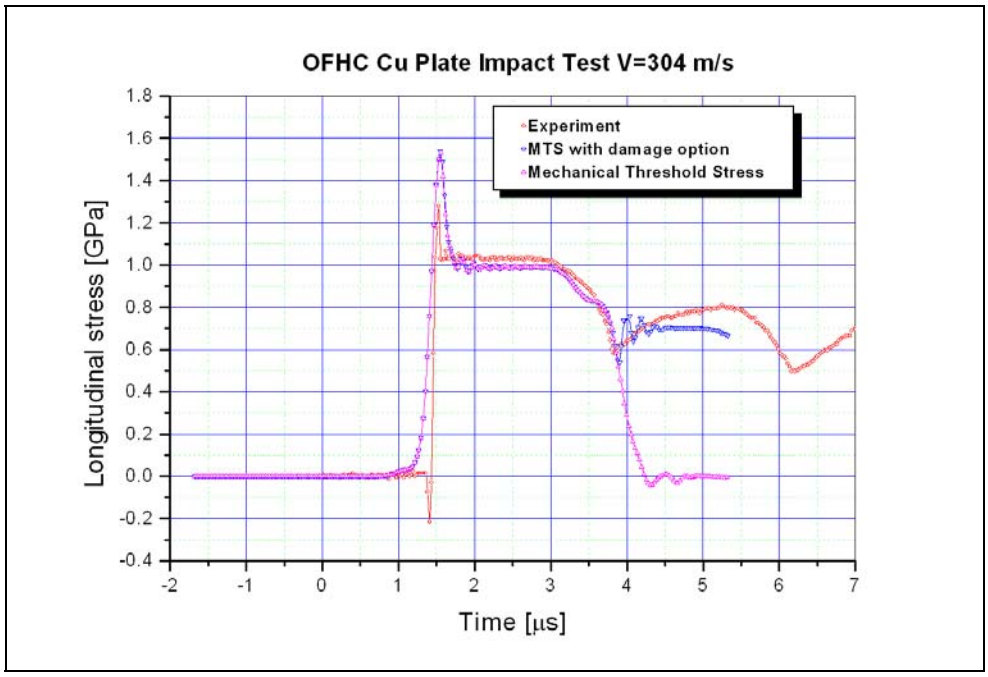

Fig. 6.3.2.7. Simulation results of 304 m/s OFHC Cu plate impact test

6.3.3. Taylor cylinder impact test simulation

Another validation, using Taylor cylinder impact test, of the proposed criterion for tensile failure was performed after implementation of material model into computer code and determination of material constants for AA7010. In order to analyse proposed criterion for tensile failure, as previously stated, proposed criterion was implemented in DYNA3D code and incorporated into MTS material model.

A series of FE simulations of Taylor cylinder impact test have been performed for AA7010. In the simulations the $cm-g-\mu s$ system of units was used. MTS material model was used in the combination with a Gruneisen Equation of State, and they have been presented in tables Table 4.4.3. and Table 4.4.4. The material parameters of the failure criteria determined on the basis of published data [103], and used in numerical simulation of Taylor impact test are summarized in the following table (Table 6.3.3.1.).

Table 6.3.3.1. Failure criteria material parameters for AA7010

Parameter	Description	Nominal value
σ_0	Threshold stress	$1.05\,GPa$
u_0	Normalized activation energy	0.0087
t_{c0}	Critical time	$2\ \mu s$
B	Magnitude of Burgers vector	$0.286\text{x}10^{-9}$m
K	Boltzmann's constant	$1.38\text{x}10^{-23}$ J/K
b_0	Shear modulus at zero degrees K	28.83 GPa
b_1	Shear modulus constant	4.45 GPa
b_2	Shear modulus constant	248.5 K

Depending on the initial impact velocity and the material strength a very vide range of strain rates, temperatures due to adiabatic heating, and strains can be achieved from single test. This test provides a clean set of experimental data from which is possible to validate the implementation, and accuracy of material model in computer code.

Loading situations in Taylor test can obviously (Fig. 6.3.3.1.), generate internal tensile stresses in materials, leading to internal fracture, if the amplitude and duration are sufficient. This computer simulation shows how reflected compressive and lateral release waves interact in a cylindrical Taylor specimen subjected to normal impact, generating tensile stresses. Tension generated by lateral release is shown and those tensile stresses can lead to fracturing.

Time sequence of stress fields and damage fields generated in Taylor specimen, impacting target with velocity of 214 m/s is shown in figure Fig. 6.3.3.1., and damage parameter in this simulation is defined as:

$$D=\frac{\int_0^{t_c}\left(\frac{\sigma(t)/\mu(T)}{\sigma_0/\mu_0}\right)^{\left(\frac{\mu(T)b^3u_0}{kT}\right)}dt}{t_{c0}} \qquad (6.3.3.1.)$$

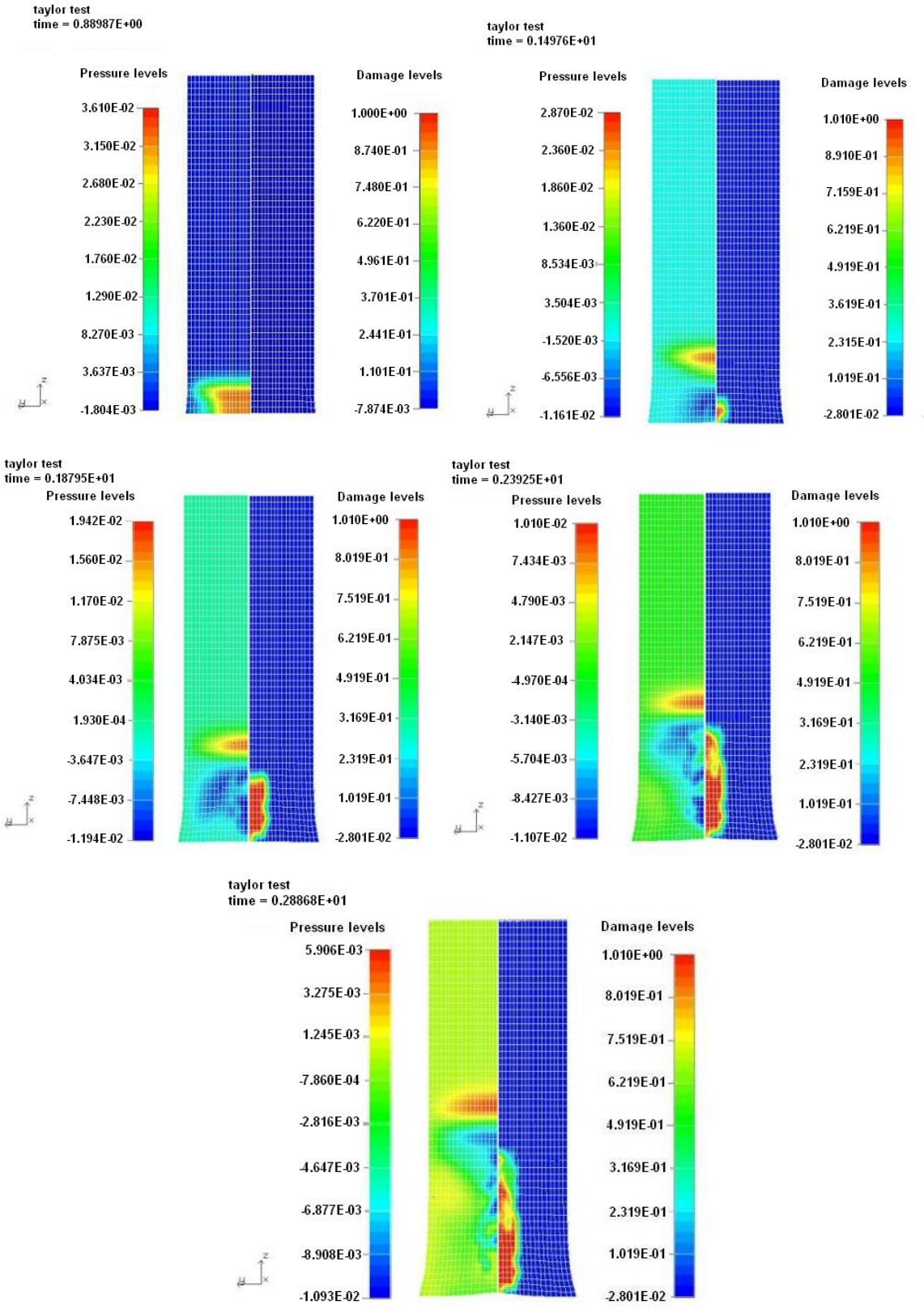

Fig. 6.3.3.1. Time sequences of stress fields and damage fields generated in Taylor specimen impacted at 214 m/s

In order to reduce the number of elements in the simulations model, and the overall time of simulations, only quarter of Taylor cylinder was modelled with a uniform solid butterfly mesh. Final damage fields generated in Taylor specimen, impacting target with velocity of 200 m/s and 214 m/s are shown in figure Fig. 6.3.3.2.

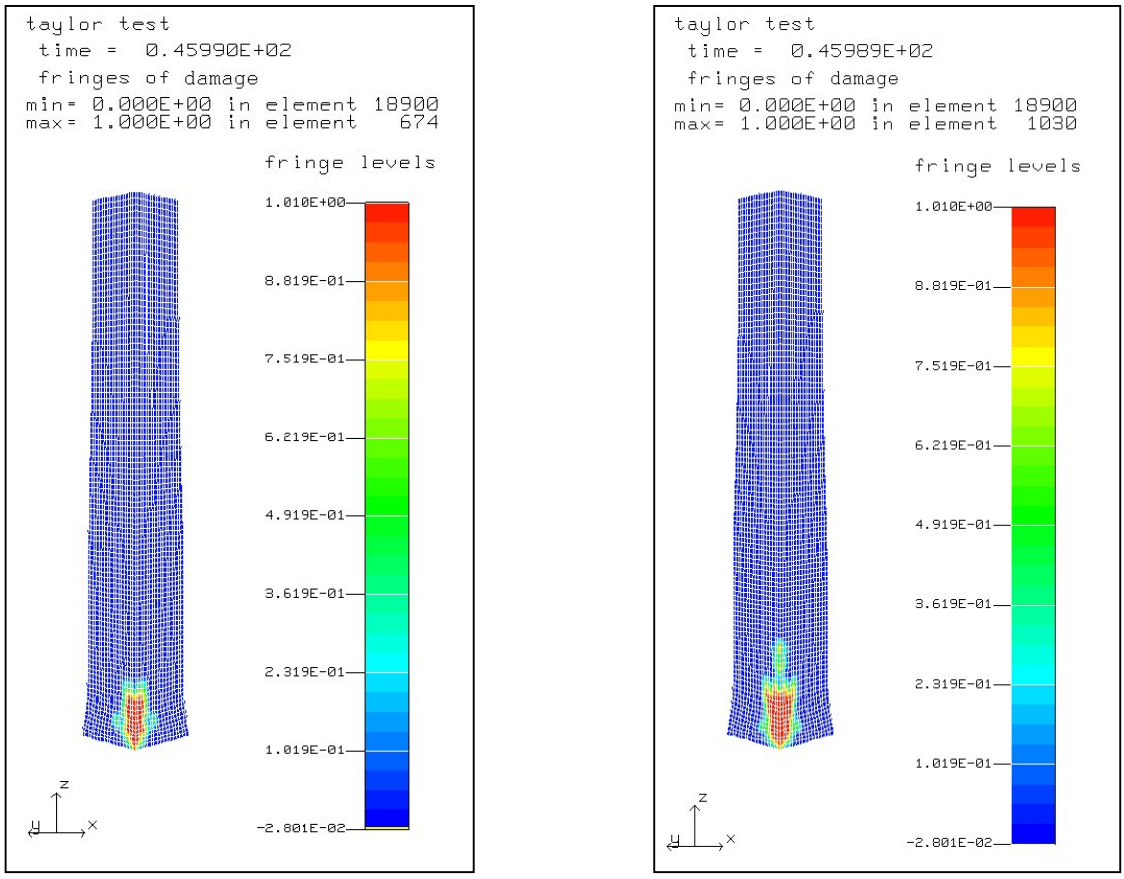

V=200 m/s V=214 m/s

Fig. 6.3.3.2. Damage fields generated in AA7010 Taylor specimen

6.4. Conclusions

The presented results demonstrate that the proposed cumulative damage and failure model based on the assumption that damage and fracture processes occur with the assistance of thermal activation can simulate high strain rate deformation processes and dynamic tension failure.

This basic concept of thermal activation of damage and material separation during fracture process has been adopted as basis for this material model development. Klepaczko failure criterion, has been modified and used as a starting point in this research. The assumption is that creation of free surfaces in a stressed body occurs with assistance of thermal activation processes makes the proposed approach compatible with the Mechanical Threshold Stress model, which was used as the strength part of the proposed constitutive model, and those developments were incorporated into public domain DYNA3D.

The damage model, combined with the MTS strength part of the constitutive relation and Grunisen equation of state, can simulate high strain rate shock induced deformation processes. Numerical analysis predicted the occurrence of spall, including the location of initiation of spall zone and evolution of the free surface in the interior of target for the plate impact test considered. Proposed cumulative criterion is able to reproduce the "pull-back" stresses of the free surface caused by creation of the internal spalling.

Numerical simulation clearly demonstrates the ability to predict the damage process in Taylor impact test simulation and proposed material model enables one to analyse numerically the damage over a wide range of impact speeds and temperatures.

Proposed material model has to be coupled with orthotropic yield criterion in order to capture orthotropic behaviour of material of interest, and proposed thermodynamic framework for coupling elasto-plasticity and damage is presented in the following chapter.

7. COUPLING OF ANISOTROPIC ELASTOPLASTICITY AND DAMAGE

7.1. Introduction

The nonlinear material behaviour may be attributed to two distinct mechanical processes: plasticity and damage mechanics. The two phenomena can be described at the continuum level by the theories of plasticity and continuum damage mechanics. Thus, a multi-dissipative model is necessary, and this can be accomplished by adopting two loading surfaces and two potential functions, one for plasticity and the other for damage [120].

Ductile materials usually fail as the result of nucleation of microscopic voids, growth of the microvoids by means of deviatoric and volumetric strain, and coalescence of microvoids linking the growing microvoids with adjacent ones, thus leading to complete reduction or loss of load carrying capacity of the material, as the damage density approaches unity. Experimental observations show that the accumulation of microdamage has a tendency to be localized. This progressive physical process of degradation of the material mechanical properties up to complete failure is commonly referred to as the damage process. This work is concerned with anisotropic ductile damage.

Many models for estimation of microdamage accumulation in ductile materials have been proposed. Some of them are based on damage micromechanics – micromechanical damage models, while others are based on the continuum damage theory – phenomenological damage models.

Gurson [127]**,** formulated a model of the first type where he obtained, based on an approximation analysis of spherical voids, a yield function for porous ductile materials with perfectly plastic matrix. Several authors have proposed modification of the Gurson's model, e.g., Tvergaard and Needleman. **Tvergaard** [128] modified Gurson's model to improve the predictions at low void volume fractions. **Needleman** modified Gurson's yield function in order to account for rate sensitivity and necking instabilities in plastically deforming solids and to provide better representation of final void coalescence. In this way, micromechanical models are based on physical principles and various applications have modelled microdamage growth and ductile failure [129].

Phenomenological models are based on the concept of **Kachanov** [94], who was the first to introduce for the isotropic case a scalar variable, which may be interpreted as the effective surface density per unit volume. Kachanov pioneered the subject of continuum damage mechanics by introducing the concept of effective stress. This concept is based on considering a fictious undamaged configuration of a body and comparing it with the actual damage configuration. He originally formulated his theory using simple uniaxial tension. Following Kachanov's work researchers in different fields applied continuum damage mechanics to their fields, e.g., **Krajcinovic** [94] for brittle materials and **Lemaitre** [122] for ductile materials.

Ductile materials undergo a strong plastic deformation, which has a major influence on the damage evolution. There are many models with coupling between plasticity and damage. The models that adopt two separate damage and plasticity

loading surfaces with two independent associated flow rules present a way for coupling between plasticity and damage. Those models have been extensively used by many authors, e.g., **Chow and Wang** [113,114], **Simo and Ju** [117,118], **Zhu and Cescetto** [111], etc. This approach has also been used in this development.

Second approach for coupling between plasticity and damage can be achieved by using one single smooth generalized yield surface and an associated flow rule for the plasticity and damage evolutions, e.g., **Gurson, Tvergaard, Needleman, etc.** Those models obviously cannot describe all loadings correctly since a hydrostatic stress will certainly cause damage before any plastic deformation can be noticed. In addition, most of those models are restricted to low damage levels or dilute distribution of defects and therefore they fail to account for the interaction of the defects adequately.

Another approach to achieve this coupling is by using separate plasticity and damage surfaces with separate non-associated flow rules in such a way that both damage and plasticity flow rules are dependent on both the plastic and damage potentials. This approach has been used by **Voyiadjis** [120].

7.2. Continuum thermodynamics

The thermodynamic relations proposed in this development follow the widely accepted approach based on internal variable representations. This work is limited for pure mechanical adiabatic (no internal heat generation sources and heat fluxes) and infinitesimal deformations. This assumption allows for an additive decomposition of the strain tensor, ε into elastic and plastic components, that is:

$$\varepsilon = \varepsilon^e + \varepsilon^p \tag{7.2.1}$$

The internal energy per unit mass, u, at a continuum point x, depends on a set of internal thermodynamic state variables. In functional form, the internal energy potential is:

$$u = u\left[x, s(x), \varepsilon(x), \nu_i(x)\right] \tag{7.2.2}$$

where s is the entropy per unit mass and ν_i is a set of mechanical variables or sub-states used to model the irreversible or dissipative processes.

The ***second law of thermodynamics*** expressed in the form of the Clausius-Duhem inequality:

$$\rho\theta\dot{s} \geq \rho\dot{u}(s, \varepsilon, \nu_i) - \sigma : \dot{\varepsilon} \tag{7.2.3}$$

where ρ is the density, θ is the absolute temperature, and σ is the Cauchy stress tensor. The substitution of the internal energy into above equation yields:

$$\boldsymbol{\rho}\left(\boldsymbol{\theta} - \frac{\partial \boldsymbol{u}}{\partial \boldsymbol{s}}\right)\dot{\boldsymbol{s}} + \left(\boldsymbol{\sigma} - \boldsymbol{\rho}\frac{\partial \boldsymbol{u}}{\partial \boldsymbol{\varepsilon}}\right) : \dot{\boldsymbol{\varepsilon}} - \boldsymbol{\rho}\frac{\partial \boldsymbol{u}}{\partial \boldsymbol{\nu_i}}\dot{\boldsymbol{\nu}}_{\boldsymbol{i}} \geq 0 \tag{7.2.4}$$

This inequality must hold for all admissible processes. Since $\dot{s}$ and $\dot{\varepsilon}$ are arbitrary, their coefficient must vanish, resulting in two consequences. The absolute temperature, θ, is the thermodynamic variable or force conjugate to the entropy and the stress tensor, σ, is the thermodynamic force conjugate to the strain tensor, that is:

$$\theta = \frac{\partial u}{\partial s} \qquad (7.2.5) \qquad\qquad \sigma = \rho \frac{\partial u}{\partial \varepsilon} \qquad (7.2.6)$$

A thermodynamic variable conjugate to an extensive parameter, such as strain, is often called a thermodynamic force and the time rate of change of the extensive parameter (strain rate) is termed a flux. The final term is often defined as the dissipation rate, due to the association with the dissipative variables, ν_i. The dissipation rate is defined to be the following:

$$\gamma \equiv -\rho \frac{\partial u}{\partial \nu_i} \dot{\nu}_i \qquad (7.2.7)$$

Then the second law reduces to:

$$\gamma \geq 0 . \qquad (7.2.8)$$

The Helmholtz free energy is thermodynamic potential given by a "contact" or Legendre transformation of the internal energy using conjugate pair (s, θ). The Helmholtz function is:

$$\psi = u(s, \varepsilon, \nu_i) - \theta s . \qquad (7.2.9)$$

By taking the total derivative, the following functional dependency is obtained:

$$d\psi = du - d(\theta s) = \frac{\partial u}{\partial s} ds + \frac{\partial u}{\partial \varepsilon} d\varepsilon + \frac{\partial u}{\partial \nu_i} d\nu_i - \theta ds - \theta ds = \frac{\partial u}{\partial \varepsilon} d\varepsilon + \frac{\partial u}{\partial \nu_i} d\nu_i - s d\theta \qquad (7.2.10)$$

therefore,

$$\psi = \psi(\theta, \varepsilon, \nu_i) \qquad (7.2.11)$$

Hence, the internal energy is thermodynamic potential for entropy and the mechanical variables and the Helmholtz function is a potential for temperature and mechanical variables. The natural choice for isentropic and isothermal processes are the internal and the Helmholtz potentials, respectively.

For purely mechanical theories ***the first law of thermodynamics*** or balance of energy yields:

$$\rho \dot{u} = \sigma : \dot{\varepsilon} \qquad (7.2.12)$$

$$\rho \theta \dot{s} = \gamma \qquad (7.2.13)$$

This concludes the overview of the thermodynamic equations proposed in this development of general thermodynamic framework for coupled elasto-plasticity and damage.

7.3. General thermodynamic framework for coupled elasto-plasticity and damage

7.3.1. Thermodynamic variables and potentials

Since the plasticity and the damage processes are irreversible, they are by definition dissipative, and the excess energy is dissipated in the form of heat. The local generation of heat, which for heterogeneous deformation fields results in a flow of heat, is not considered, because of isothermal assumption. The isothermal assumption is a reasonable approximation when the amount of heat generated is relatively small, or when a process occurs rapidly and the material parameters are relatively insensitive to changes in temperature.

To describe the irreversibility associated with the plastic deformation and damage evolution processes, a set of variables is introduced.

For plasticity, let ε^p be the plastic-strain tensor and introduce two second-order tensor variables in strain space that will be used to describe the plastic hardening phenomena. Let α'' be the hardening variable that describes the shift in the centre of the yield surface (kinematic hardening) and α' be hardening variable that describes the shape and size of the yield surface (isotropic hardening).

To describe the damage process, a generalized damage tensor, D, is introduced as a measure of degradation of the material integrity. Let β'' be the damage variable, which describes the shift in the centre of the damage, surface and which is a tensor of the same order as D. Furthermore, let β' be damage variable which describes the shape and size of the damage surface. With this definitions and assumptions, the functional form of the Helmholtz free energy is:

$$\psi = \psi(\varepsilon, \varepsilon^p, \alpha', \alpha'', D, \beta', \beta'') . \tag{7.3.1.1}$$

The conjugate thermodynamic forces are defined by:

$$\sigma^p \equiv -\rho \frac{\partial \psi}{\partial \varepsilon^p} \qquad Y \equiv -\rho \frac{\partial \psi}{\partial D}$$

$$\sigma' \equiv -\rho \frac{\partial \psi}{\partial \alpha'} \qquad Y' \equiv -\rho \frac{\partial \psi}{\partial \beta'} \tag{7.3.1.2}$$

$$\sigma'' \equiv -\rho \frac{\partial \psi}{\partial \alpha''} \qquad Y'' \equiv -\rho \frac{\partial \psi}{\partial \beta''}$$

The internal energy now takes following form:

$$\rho u(s, \varepsilon, \varepsilon^p, \alpha', \alpha'', D, \beta', \beta'') = \rho \psi(\varepsilon, \varepsilon^p, \alpha', \alpha'', D, \beta', \beta'') + \rho \theta s \tag{7.3.1.3}$$

Based on the assumptions given above the Helmholtz free energy can be divided as follows:

$$\rho \psi(\varepsilon, \varepsilon^p, \alpha', \alpha'', D, \beta', \beta'') = W_e(\varepsilon, \varepsilon^p, D) + H(\alpha', \alpha'', \beta', \beta'') \tag{7.3.1.4}$$

where the stored or elastic energy function is defined to be:

$$W_e(\varepsilon,\varepsilon^p,D) \equiv \frac{1}{2}(\varepsilon-\varepsilon^p):\overline{C}_e(D):(\varepsilon-\varepsilon^p) \qquad (7.3.1.5)$$

The exact form of the damage stiffness tensor, $\overline{C}_e$, depends on the specific damage representation theory employed, where corresponding fourth-order stiffness tensor in undamaged state is denoted by C_e. The second term in equation for Helmholtz free energy, $H(\alpha',\alpha'',\beta',\beta'')$, defines contribution of the hardening and damag variables to the Helmholtz potential - dissipated energy.

This form of the Helmholtz function assumes an additive decomposition into a stored elastic energy term and additional term related to the hardening and damaging processes. The proposed approach may be too restrictive but it is used by others authors [109] because the formulation is still fairly general but no so abstract that the derivations become overly complicated.

Assuming that elastic properties of the material depend only on the accumulated damage D, and the energies involved in the plastic flow and damaging processes, dissipated by heat or stored in the material due hardening, are independent, in the proposed model, the Helmholtz free energy takes following form:

$$\rho\psi(\varepsilon,\varepsilon^p,\alpha',\alpha'',D,\beta',\beta'') = W(\varepsilon,\varepsilon^p,D) + H_p(\alpha',\alpha'') + H_d(\beta',\beta'') \qquad (7.3.1.6)$$

where $H_p(\alpha',\alpha'')$ is the free energy related to plastic hardening, and $H_d(\beta',\beta'')$ is the free energy related to damage hardening.

Using choice of the variables associated with the irreversible processes as:

$$\nu_i = \left\{\varepsilon^p,\alpha',\alpha'',D,\beta',\beta''\right\} \qquad (7.3.1.7)$$

and according to the second law of thermodynamics, the total dissipation rate is defined as:

$$\gamma = -\rho\left(\frac{\partial\psi}{\partial\varepsilon^p}:\dot{\varepsilon}^p + \frac{\partial\psi}{\partial\alpha'}:\dot{\alpha}' + \frac{\partial\psi}{\partial\alpha''}:\dot{\alpha}'' + \frac{\partial\psi}{\partial D}:\dot{D} + \frac{\partial\psi}{\partial\beta'}:\dot{\beta}' + \frac{\partial\psi}{\partial\beta''}:\dot{\beta}''\right) \qquad (7.3.1.8)$$

or using the conjugate force relations the dissipation rate can be rewritten as:

$$\gamma = \sigma^p:\dot{\varepsilon}^p + \sigma':\dot{\alpha}' + \sigma'':\dot{\alpha}'' + Y:\dot{D} + Y':\dot{\beta}' + Y'':\dot{\beta}'' \geq 0\,. \qquad (7.3.1.9)$$

Based on the assumption that mechanical and thermal dissipations are decoupled and that energy dissipations due to plastic flow and damage processes are independent, dissipation rate can be separated into two parts:

$$\sigma^p : \dot{\varepsilon}^p + \sigma' : \dot{\alpha}' + \sigma'' : \dot{\alpha}'' \geq 0 \quad (7.3.1.10)$$

$$Y : \dot{D} + Y' : \dot{\beta}' + Y'' : \dot{\beta}'' \geq 0 \quad (7.3.1.11)$$

Above equations show that one can assume that there exist a plastic dissipative potential and damage dissipative potential, i.e.

$$F_p(\sigma^p, D, \sigma', \sigma'') = 0 \quad (7.3.1.12)$$

$$F_d(Y, Y', Y'') = 0 . \quad (7.3.1.13)$$

7.3.2. Effective stress, effective strain and damage effect tensor M(D)

The basic hypothesis in most isotropic and anisotropic models of continuum damage mechanics is that, neglecting the details of microscopic damage growth, damage can be viewed as a macroscopic state variable which affects the average microscopic damage growth in the sense of "effective stress".

Based on the concepts of the continuum damage mechanics, metals deteriorate at different stages of loading. The deterioration, is postulated to be attributed to the formation and realignment of dislocations, micro-cracks, voids and other types of material defects and flaws. A damage variable, which provides a measure of the change of an element surface area S to $\overline{S}$ due to loading, is defined as:

$$D = \frac{S - \overline{S}}{S} \quad (7.3.2.1)$$

The corresponding effective Cauchy stress tensor $\overline{\sigma}$ is postulated to be:

$$\overline{\sigma} = \sigma \frac{S}{\overline{S}} = \frac{\sigma}{1 - D} \quad (7.3.2.2)$$

This basic hypothesis of effective stress can be formulated as [130]: there exists a "damage effect tensor" M(D) applied to the stress tensor σ which defines the effective stress tensor $\overline{\sigma}$, which may be expressed in a generalized form of anisotropic damage as:

$$\overline{\sigma} = M(D) : \sigma \quad (7.3.2.3)$$

where the damage effect tensor $M(D)$ is a second –order tensor or fourth – order tensor depending on the damage tensor D. In this approach four fundamental variables of continuum damage mechanics have been identified as: damage tensor D, the damage effect tensor M(D), the effective stress tensor $\overline{\sigma}$ and effective strain tensor $\overline{\varepsilon}$.

Damage induced material anisotropy may be characterized by a symmetric second order tensor D. Because of its mathematical simplicity D has been used extensively to study various aspect of damage problems including elasticity,

elastoplacity, and elasto-visco-plasticity. Perhaps the most attractive property of symmetric tensor D is that it always possesses three orthogonal principal directions and the corresponding principal values.

There is no uniquely defined mathematical formulation of M(D) and various formulations have been proposed. One of the simplest forms is to introduce material damage in stress tensor principal direction only:

$$\begin{bmatrix}\overline{\sigma}_1 & \overline{\sigma}_2 & \overline{\sigma}_2\end{bmatrix}^T = M\begin{bmatrix}\sigma_1 & \sigma_2 & \sigma_3\end{bmatrix}^T \tag{7.3.2.4}$$

with second-order of damage effect tensor:

$$M(D) = \begin{bmatrix} \dfrac{1}{1-D_1} & 0 & 0 \\ 0 & \dfrac{1}{1-D_2} & 0 \\ 0 & 0 & \dfrac{1}{1-D_3} \end{bmatrix} \tag{7.3.2.5}$$

where D_1, D_2 and D_3 are damage variables in their principal axes. The damage in the material is represented by internal variables D_i, corresponding to a material degradation in each orthotropic principal direction i, $0 \le D_i \le 1$, where $D_i = 0$ corresponds to a virgin element while $D_i = 1$ corresponds to fully damaged element. However, if stress tensor is defined in an arbitrary coordinate system, the damage effect tensor must be suitably modified. One obvious criterion for developing such a generalized form of the damage effect tensor is that it should reduce to scalar for isotropic damage. This reduction should be made possible not only in principal coordinate system but also in any coordinate system.

One formulation, which satisfies the above criterion, was proposed in the principal coordinate system of damage as [113]:

$$\begin{bmatrix}\overline{\sigma}_{11} & \overline{\sigma}_{22} & \overline{\sigma}_{33} & \overline{\sigma}_{23} & \overline{\sigma}_{31} & \overline{\sigma}_{12}\end{bmatrix}^T = M\begin{bmatrix}\sigma_{11} & \sigma_{22} & \sigma_{33} & \sigma_{23} & \sigma_{31} & \sigma_{12}\end{bmatrix}^T \tag{7.3.2.6}$$

with the symmetric tensor:

$$M = diag \begin{bmatrix} \dfrac{1}{1-D_1} & \dfrac{1}{1-D_2} & \dfrac{1}{1-D_3} & \dfrac{1}{\sqrt{(1-D_2)(1-D_3)}} & \dfrac{1}{\sqrt{(1-D_3)(1-D_1)}} & \dfrac{1}{\sqrt{(1-D_1)(1-D_2)}} \end{bmatrix} \tag{7.3.2.7}$$

It can be seen that first formulation is particular case of second generalized formulation which can be readily reduced to a scalar for isotropic damage when $D_1 = D_2 = D_3 = D$. Because of its simplicity the generalized effect tensor M(D) will be used to derive the constitutive equations of the proposed anisotropic damage model.

The stress-space variables associated with the plastic hardening are assumed to be mapped into effective-stress space by the same operator:

$$\overline{\sigma}' = M(D) : \sigma' \qquad (7.3.2.8) \qquad \overline{\sigma}'' = M(D) : \sigma''. \qquad (7.3.2.9)$$

The mapping of the stress to the effective stress is required for later derivation, and was assumed for purely conceptual reason.

Assuming that the inverse of the effective-stress operator, $\boldsymbol{M^{-1}}$, exist, then the dissipation rate, equation (7.3.1.8), can be rewritten using the effective-stress operator as:

$$\begin{aligned}\gamma = {} & \sigma^p : (M^T : M^{-T}) : \dot{\varepsilon}^p + \sigma' : (M^T : M^{-T}) : \dot{\alpha}' + \sigma'' : (M^T : M^{-T}) : \dot{\alpha}'' \\ & + Y : (M^T : M^{-T}) : \dot{D} + Y' : (M^T : M^{-T}) : \dot{\beta}' + Y'' : (M^T : M^{-T}) : \dot{\beta}''\end{aligned} \qquad (7.3.2.10)$$

Motivated by this form of the dissipation rate, the rate forms of the plasticity variables based in strain space are assumed to be mapped into an effective space by the inverse of the effective-stress operator, that is:

$$\dot{\bar{\varepsilon}}^p \equiv M^{-T}(D) : \dot{\varepsilon}^p, \ \dot{\bar{\boldsymbol{\alpha}}}' \equiv \boldsymbol{M^{-T}}(\boldsymbol{D}) : \dot{\boldsymbol{\alpha}}', \ \dot{\bar{\boldsymbol{\alpha}}}'' \equiv \boldsymbol{M^{-T}}(\boldsymbol{D}) : \dot{\bar{\boldsymbol{\alpha}}}'' \qquad (7.3.2.11)$$

and then the dissipation rate (Eq. 7.3.1.9) could be written in the following form:

$$\gamma = \overline{\sigma}^p : \dot{\bar{\varepsilon}}^p + \overline{\sigma}' : \dot{\bar{\alpha}}' + \overline{\sigma}'' : \dot{\bar{\alpha}}'' + Y : \dot{D} + Y' : \dot{\beta}' + Y'' : \dot{\beta}'' \geq 0 \qquad (7.3.2.12)$$

7.3.3. Hypothesis of energy equivalence

Instead of the conventional postulate of strain or stress equivalence, which has rather limited use in the derivation of constitutive equations including progressive deterioration of mechanical properties due to anisotropic damage, Cordebois and Sidoroff [131] proposed a hypothesis of energy equivalence. This hypothesis states that the complementary elastic energy for a damaged material has same form as that of a fictitious undamaged material except that the stress is replaced by the effective stress in the energy formulation, or mathematically,

$$W_e(\sigma, D) = W_e(\overline{\sigma}, \overline{D}) \qquad (7.3.3.1)$$

or

$$\frac{1}{2}\overline{\sigma}^T : C_e^{-1} : \overline{\sigma} = \frac{1}{2}\sigma^T : \overline{C}_e^{-1} : \sigma \qquad (7.3.3.2)$$

where C_e and $\overline{C}_e$ are the virgin and damaged elastic material stiffness tensor respectively. By recalling expression for effective stress tensor:

$$\overline{\sigma} = M(D) : \sigma \qquad (7.3.3.3)$$

it can be proved that:

$$\overline{C}_e^{-1} = M(D) : C_e^{-1} : M(D) \tag{7.3.3.4}$$

and according to the hypothesis of energy equivalence the effective elastic strain vector is:

$$\overline{\varepsilon}_e = M^{-1} : \varepsilon_e \tag{7.3.3.5}$$

where:

$$M^{-1} = diag \left[1-D_1 \quad 1-D_2 \quad 1-D_3 \quad \sqrt{(1-D_2)(1-D_3)} \quad \sqrt{(1-D_3)(1-D_1)} \quad \sqrt{(1-D_1)(1-D_2)}\right] \tag{7.3.3.6}$$

7.4. Anisotropic elasticity and damage

When material is damaged, the constitutive relation is:

$$\sigma = \overline{C}_e : \varepsilon_e \tag{7.4.1}$$

Using the following equation:

$$\overline{C}_e^{-1} = M(D) : C_e^{-1} : M(D) \tag{7.4.2}$$

equation (7.4.1) yields:

$$\overline{C}_e = M^{-1} : C_e : M^{-1} \tag{7.4.3}$$

Since the elastic tensor C_e is symmetric, $\overline{C}_e$ is symmetric too. The elastic tensor C_e may be represented by 6x6 matrix, which for orthotropic materials is:

$$C_e^{-1} = \begin{bmatrix} \frac{1}{E_1} & \frac{-\upsilon_{21}}{E_2} & \frac{-\upsilon_{31}}{E_3} & 0 & 0 & 0 \\ \frac{-\upsilon_{12}}{E_1} & \frac{1}{E_2} & \frac{-\upsilon_{32}}{E_3} & 0 & 0 & 0 \\ \frac{-\upsilon_{13}}{E_1} & \frac{-\upsilon_{23}}{E_2} & \frac{1}{E_3} & 0 & 0 & 0 \\ 0 & 0 & 0 & \frac{1}{G_{23}} & 0 & 0 \\ 0 & 0 & 0 & 0 & \frac{1}{G_{31}} & 0 \\ 0 & 0 & 0 & 0 & 0 & \frac{1}{G_{12}} \end{bmatrix} \tag{7.4.4}$$

The symmetry of C_e imposes the following constrains on the material parameters:

$$\frac{\upsilon_{12}}{E_1}=\frac{\upsilon_{21}}{E_2},\ \frac{\upsilon_{31}}{E3}=\frac{\upsilon_{13}}{E_1},\ \frac{\upsilon_{32}}{E_3}=\frac{\upsilon_{23}}{E_2} \tag{7.4.5}$$

thus C_e is defined as:

$$C_e=\begin{bmatrix} \frac{E_1(1-\upsilon_{32}\upsilon_{23})}{\Delta_c} & \frac{E_2(\upsilon_{12}+\upsilon_{13}\upsilon_{32})}{\Delta_c} & \frac{E_3(\upsilon_{13}+\upsilon_{12}\upsilon_{23})}{\Delta_c} & 0 & 0 & 0 \\ \frac{E_1(\upsilon_{21}+\upsilon_{23}\upsilon_{31})}{\Delta_c} & \frac{E_2(1-\upsilon_{13}\upsilon_{31})}{\Delta_c} & \frac{E_3(\upsilon_{23}+\upsilon_{21}\upsilon_{13})}{\Delta_c} & 0 & 0 & 0 \\ \frac{E_1(\upsilon_{31}+\upsilon_{21}\upsilon_{32})}{\Delta_c} & \frac{E_2(\upsilon_{32}+\upsilon_{32}\upsilon_{23})}{\Delta_c} & \frac{E_3(1-\upsilon_{21}\upsilon_{12})}{\Delta_c} & 0 & 0 & 0 \\ 0 & 0 & 0 & G_{23} & 0 & 0 \\ 0 & 0 & 0 & 0 & G_{31} & 0 \\ 0 & 0 & 0 & 0 & 0 & G_{12} \end{bmatrix} \tag{7.4.6}$$

where:

$$\Delta_c=1-\upsilon_{21}\upsilon_{12}-\upsilon_{31}\upsilon_{13}-\upsilon_{32}\upsilon_{23}-\upsilon_{12}\upsilon_{23}\upsilon_{31}-\upsilon_{21}\upsilon_{13}\upsilon_{32} \tag{7.4.7}$$

The symmetry properties, can be additionally expressed by the following relations:

$$\begin{aligned} &E_1(\upsilon_{21}+\upsilon_{23}\upsilon_{31})=E_2(\upsilon_{12}+\upsilon_{13}\upsilon_{32}) \\ &E_1(\upsilon_{31}+\upsilon_{21}\upsilon_{32})=E_3(\upsilon_{13}+\upsilon_{12}\upsilon_{23}) \\ &E_2(\upsilon_{32}+\upsilon_{12}\upsilon_{31})=E_3(\upsilon_{23}+\upsilon_{21}\upsilon_{13}) \end{aligned} \tag{7.4.8}$$

In order to assure the positive definiteness of $\overline{C}_e$, the following conditions should be satisfied:

$$\begin{aligned} &0<\Delta_c\le 1,\ 0<1-\upsilon_{ij}\upsilon_{ji}\le 1,\ 0\le D_i<1 \\ &G_{23}>0,\ G_{31}>0,\ G_{12}>0 \\ &E_1>0,\ E_2>0,\ E_3>0 \end{aligned} \tag{7.4.9}$$

7.5. Effective-stress space yield function and damage function

A generalized yield function, F_p, that separates the elastic and elasto-plastic domains in effective-stress space is assumed to be of the form:

$$F_p(\bar{\sigma},\bar{\sigma}',\bar{\sigma}'') = F_{p1}(\bar{\sigma}-\bar{\sigma}'') - [F_{p2}(\bar{\sigma}') + \sigma_Y] \le 0 \qquad (7.5.1)$$

where σ_Y is a positive scalar material parameter used to describe the onset of plastic behaviour (an initial yield stress), and scalar-value tensor functions F_{p1} and F_{p2} are required to be homogeneous of degree one.

If we assume that only isotropic hardening is sufficient to describe material behaviour, than above equation degenerates into following form:

$$F_p(\bar{\sigma},\bar{\sigma}') = F_{p1}(\bar{\sigma}) - [F_{p2}(\bar{\sigma}') + \sigma_Y] \le 0 \qquad (7.5.2)$$

and this equation in case of Hill's anisotropic plasticity model with isotropic hardening becomes:

$$F_p(\bar{\sigma},R) = \bar{\sigma}_F - [R(\alpha') + R_0] = 0 \qquad (7.5.3)$$

where $\bar{\sigma}_F$ is effective equivalent plastic stress, R_0 is initial strain hardening threshold – initial yield stress, and $R(\alpha')$ is isotropic constitutive relationship which describe isotropic change in the yield surface or hardening. For sake of brevity in further text we will use following equality $\boldsymbol{\alpha} = \boldsymbol{\alpha}'$.

In a similar manner, we can consider a damage criterion that takes the following form:

$$F_d(Y,Y',Y'') = F_{d1}(Y-Y'') - [F_{d2}(Y') + \omega_0] \le 0 \qquad (7.5.4)$$

where ω_0 is a positive scalar material parameter used to describe the onset of damage behaviour (a damage energy threshold). The scalar-valued tensor functions, F_{d1} and F_{d2}, are likewise required to be homogeneous of degree one. The use of tensor, Y', equal in tensor order to the damage variable is required for a general anisotropic description of the damage surface. Many anisotropic damage theories have been proposed that employ only a scalar variable to describe the shape of the damage surface. A scalar can only describe an isotropic surface or equal damage evolution in all directions, which is inadequate for description of anisotropic damage in materials.

In the case where damage is represented only with a damage variable that describes the shape and size of damage surface, according to the analogy with anisotropic plasticity, damage criterion takes following form:

$$F_d = Y_{eq} - [B(\beta') + B_0] \qquad (7.5.5)$$

where Y_{eq} is the equivalent damage energy release rate, B_0 initial damage threshold, and $B(\beta')$ is increment of damage depending on the β', damage variable that describes the shape and size of the damage surface. In further text β' will be referred as $\boldsymbol{\beta}$ for brevity.

7.5.1. Anisotropic plastic yield surface

As previously stated, in the damage characterization of materials undergoing large plastic deformations, Hill's yield criterion [76] in stress space is expressed in the following form:

$$\boldsymbol{F_p}(\overline{\boldsymbol{\sigma}}, \boldsymbol{R}) = \overline{\boldsymbol{\sigma}}_{\boldsymbol{F}} - [\boldsymbol{R}(\boldsymbol{\alpha}) + \boldsymbol{R}_0] = 0 \tag{7.5.1.1}$$

where R_0 is the initial strain hardening threshold.

The effective equivalent stress $\overline{\sigma}_F$ is:

$$\overline{\boldsymbol{\sigma}}_{\boldsymbol{F}} = \left[\frac{1}{2}\overline{\boldsymbol{\sigma}}^{\boldsymbol{T}} : \mathrm{H} : \overline{\boldsymbol{\sigma}}\right]^{1/2} = \left[\frac{1}{2}\boldsymbol{\sigma}^{\boldsymbol{T}} : \overline{\mathrm{H}} : \boldsymbol{\sigma}\right]^{1/2} \tag{7.5.1.2}$$

The effective plastic characteristic tensor $\overline{H}$ is given by:

$$\overline{\mathrm{H}} = \boldsymbol{M}(\boldsymbol{D}) : \mathrm{H} : \boldsymbol{M}(\boldsymbol{D}) \tag{7.5.1.3}$$

The positive definite tensor $\boldsymbol{H}$ [76] for orthotropic materials is represented by 6x6 matrix as in the material principal coordinate system:

$$\mathrm{H} = \begin{bmatrix} \boldsymbol{G}+\boldsymbol{H} & -\boldsymbol{H} & -\boldsymbol{G} & 0 & 0 & 0 \\ -\boldsymbol{H} & \boldsymbol{H}+\boldsymbol{F} & -\boldsymbol{F} & 0 & 0 & 0 \\ -\boldsymbol{G} & -\boldsymbol{F} & \boldsymbol{F}+\boldsymbol{G} & 0 & 0 & 0 \\ 0 & 0 & 0 & 2\boldsymbol{N} & 0 & 0 \\ 0 & 0 & 0 & 0 & 2\boldsymbol{L} & 0 \\ 0 & 0 & 0 & 0 & 0 & 2\boldsymbol{M} \end{bmatrix} \tag{7.5.1.4}$$

where F, G, H, L, M, N are parameters characterizing the current state of plastic anisotropy. For a strain-hardening material, the uniaxial yield stress varies with increasing plastic deformation, and therefore the anisotropic parameters should also vary, since they are functions of the current yield stress. The consistency between the general thermodynamic framework and treatment of anisotropic hardening require tensor H to be a state variable. Since we work with weak degree of anisotropy, tensor H in plastic flow rule could be treated as constant tensor.

By assuming an associated flow rule, the rate-independent damage plastic response is characterized as follows:

Plastic flow rule:

$$\dot{\boldsymbol{\varepsilon}}_{\boldsymbol{p}} = \dot{\boldsymbol{\lambda}}_{\boldsymbol{p}} \frac{\partial \boldsymbol{F}_{\boldsymbol{p}}}{\partial \boldsymbol{\sigma}} = \frac{\boldsymbol{M} : \mathrm{H} : \boldsymbol{M} : \boldsymbol{\sigma}}{2\overline{\boldsymbol{\sigma}}_{\boldsymbol{F}}} \dot{\boldsymbol{\lambda}}_{\boldsymbol{p}} \tag{7.5.1.5}$$

Isotropic hardening rule:

$$\dot{R} = \dot{\lambda}_p \frac{dR}{d\alpha} \tag{7.5.1.6}$$

Plastic loading/unloading rule:

$$F_p \le 0\,,\ \dot{\lambda}_p \ge 0\,,\ \dot{\lambda}_p F_p = 0 \tag{7.5.1.7}$$

7.5.2. Damage evolution surface

Similarly to the plastic dissipative potential, it can be assumed that there exists a surface, $\boldsymbol{F_d} = 0$, which separates the damaged from undamaged state of material [111]. A damage criterion in a quadratic homogeneous function of the damage energy release rate can be expressed in the following form:

$$\boldsymbol{F_d} = \boldsymbol{Y_{eq}} - [\boldsymbol{B}(\boldsymbol{\beta}) + \boldsymbol{B}_0] \tag{7.5.2.1}$$

where Y_{eq} is the equivalent damage energy release rate is defined by:

$$Y_{eq} = \left[\frac{1}{2} Y^T : J : Y\right]^{1/2} \tag{7.5.2.2}$$

in which J is damage characteristic tensor.

Normally the damage characteristic tensor J seems to be a fourth order tensor similarly to the plastic characteristic tensor H. However, since we work in the principal coordinate system of damage as $Y_{12} = Y_{23} = Y_{31} = 0$, it can be treated like a second order tensor, and this tensor can be assumed to be symmetric, the operator in its general form has six independent components.

The purpose of introducing a damage characteristic tensor J, like the introduction of plastic characteristic tensor H in the theory of plasticity, is to take account of the anisotropic nature of damage growth.

There are several existing formulations of J, which have been proposed by different authors. The damage characteristic tensor J in the Cordebois-Sidoroff [131] model was expressed as:

$$J = \begin{bmatrix} 1 & 0 & 0 \\ 0 & \mu & 0 \\ 0 & 0 & \mu \end{bmatrix},\ 0 \le \mu \le 1 \tag{7.5.2.3}$$

where μ is a material constant. It reduces to a scalar equation, only if $\mu = 1$.

Following form of J, has also been proposed in literature [111]:

$$J = \begin{bmatrix} 1 & \mu & \mu \\ \mu & 1 & \mu \\ \mu & \mu & 1 \end{bmatrix} \tag{7.5.2.4}$$

to describe anisotropic damage evolution. However, their assumption that μ is a material constant is not realistic.
Recently, Chow and Lu [115], proposed the following generalized expression for J:

$$J = \begin{bmatrix} 1 & J_{12} & J_{12} \\ J_{12} & 1 & J_{12} \\ J_{12} & J_{12} & 1 \end{bmatrix} \tag{7.5.2.5}$$

and this formulation has only one unknown parameter to be determined from a standard tensile test:

$$J_{12} = \left.\frac{dD_1}{dD_2}\right|_{d\sigma_2=0} = \left.\frac{dD_2}{dD_1}\right|_{d\sigma_1=0} \tag{7.5.2.6}$$

However, it is only suited for the case when the virgin material properties are isotropic. A new damage characteristic tensor J, similar to the plastic characteristic tensor H in the theory of the plasticity, with more general properties and more rational physical significance then the previous formulation has been proposed on the basis of the damage energy equivalence by Zhu and Cescotto [111] as:

$$J = 2\begin{bmatrix} J_1 & \sqrt{J_2} & \sqrt{J_3} \\ \sqrt{J_2} & J_2 & \sqrt{J_2 J_3} \\ \sqrt{J_3} & \sqrt{J_2 J_3} & J_3 \end{bmatrix} \tag{7.5.2.7}$$

In the case of damage hardening materials, the equivalent damage energy release rate increases with increasing total damage growth, and hence, the anisotropic parameters in definition of the damage characteristic tensor should also vary.

In much the same way as the definition of plastic flow, the evolution of anisotropic damage is characterized as:

Damage evolution rule:

$$\dot{D} = -\dot{\lambda}_d \frac{\partial F_d}{\partial Y} = -\frac{J : Y}{2Y_{eq}} \lambda_d \tag{7.5.2.8}$$

Damage hardening rule:

$$\dot{\beta} = -\dot{\lambda}_d \frac{\partial F_d}{\partial B} = \dot{\lambda}_d \tag{7.5.2.9}$$

$$\dot{B} = \frac{dB}{d\beta}\dot{\beta} = \frac{dB}{d\beta}\dot{\lambda}_d \tag{7.5.2.10}$$

Damage loading/unloading rule:

$$F_d \le 0,\ \dot{\lambda}_d \ge 0,\ \dot{\lambda}_d F_d = 0 \tag{7.5.2.11}$$

7.6. Calibration of the damage model

The change in the equivalent energy release rate in any principal direction depends on the total amount of damage work done in that direction. For an equivalent variation, the damage work done in each component should be the same [110]. For the case of a linear damage hardening, the damage work in component 1 is (Fig. 7.6.1.):

$$W_{d1} = \frac{1}{2}D_1(Y_{10} + Y_1) = \frac{1}{2}\frac{(Y_1 - Y_{10})}{D_{t1}}(Y_{10} + Y_1) = \frac{1}{2D_{t1}}(Y_1^2 - Y_{10}^2) \tag{7.6.1.}$$

Similarly the damage work done in terms of equivalent damage energy release rate Y_{eq} is:

$$W_{d1} = \frac{1}{2D_t}(Y_{eq}^2 - Y_0^2) \tag{7.6.2.}$$

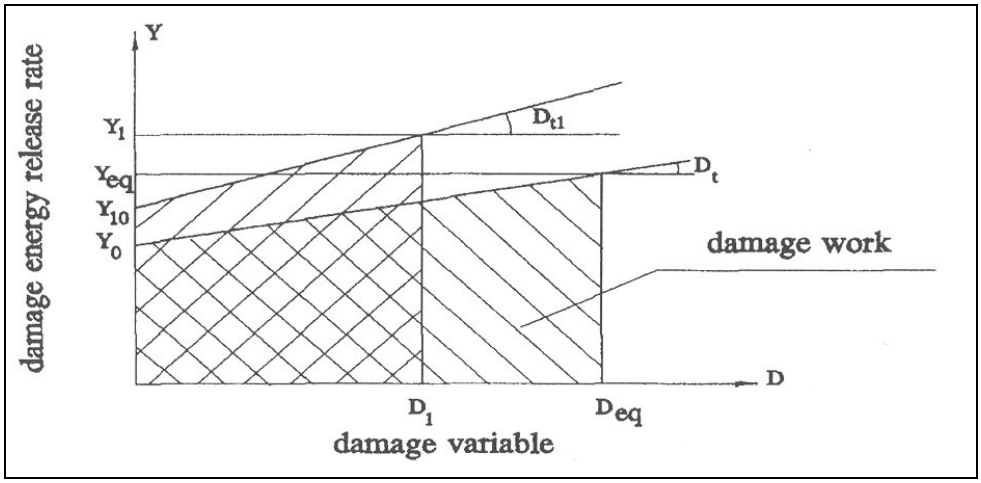

Fig. 7.6.1. Equating damage work

By equating above equations, we have:

$$J_1 = \left(\frac{Y_{eq}}{Y_1}\right)^2 = \frac{Y_{eq}^2}{(D_{t1}/D_t)(Y_{eq}^2 - Y_0^2) + Y_{10}^2} \tag{7.6.3.}$$

Similarly, we have:

$$J_2 = \left(\frac{Y_{eq}}{Y_2}\right)^2 = \frac{Y_{eq}^2}{(D_{t2}/D_t)(Y_{eq}^2 - Y_0^2) + Y_{20}^2} \tag{7.6.4.}$$

$$J_3 = \left(\frac{Y_{eq}}{Y_1}\right)^2 = \frac{Y_{eq}^2}{(D_{t3}/D_t)(Y_{eq}^2 - Y_0^2) + Y_{30}^2} \tag{7.6.5.}$$

Obviously, if component 1 coincides with the reference component, then

$$B_0 = Y_{10},\ B(\beta) = Y_1 - Y_{10}, \tag{7.6.6.}$$

and we can write:

$$J_1 = 1$$

$$J_2 = \frac{Y_1^2}{(D_{t2}/D_{t1})(Y_1^2 - Y_{10}^2) + Y_{20}^2} \tag{7.6.7.}$$

$$J_3 = \frac{Y_1^2}{(D_{t3}/D_{t1})(Y_1^2 - Y_{10}^2) + Y_{30}^2}$$

In the above equations, the damage hardening rates D_{ti} are the slopes of $Y_i - D_i$ curves with component i; Y_i the current equivalent damage energy release rate corresponding to component i; Y_{i0} the initial equivalent damage energy release rate corresponding to component i.

The damage characteristic tensor J may be handled as a constant tensor H, in order to avoid complex derivation, and comparisons between simulation and experiment show that this assumption gives interesting results.

The required curves for determination of members of damage characteristic tensor J, are the damage energy released rate-damage ones: $Y_i D_i$. From definition for damage energy release rate:

$$Y = -\rho\frac{\partial \psi}{\partial D} = -\frac{\partial W_e(\sigma, D)}{\partial D} = -\sigma^T : M : C_e^{-1} : \frac{\partial M}{\partial D} : \sigma \tag{7.6.8.}$$

when vector notation instead of a second order symmetric tensor is adopted, the three principal components of Y can be expressed as:

$$-Y_i = \frac{\sigma_i}{1 - D_i}\frac{C_{ij}^{-1}}{(1 - D_i)(1 - D_j)}\sigma_j \tag{7.6.9.}$$

Applied on a tensile test in a direction i, we can get:

$$-Y_i = \frac{\sigma^2{}_{ii}}{E_i(1-D_i)^3} \tag{7.6.10.}$$

Traditionally using loading-unloading cycles, the evolution of the effective Young modulus $\overline{E}_i(\varepsilon_{ii})$ has been measured. In this approach damage component evolution $D_i(\varepsilon_{ii})$ is expressed as:

$$D_i(\varepsilon_{ii}) = 1 - \sqrt{\frac{\overline{E}(\varepsilon_{ii})}{E_i}} \tag{7.6.11.}$$

where E_i is the initial value of the Young modulus.

In this work another approach has been proposed. Using cumulative damage criterion, which was proposed by Dremin and Molodets, modified Klepaczko's cumulative failure criterion in the integral form can be written as follows:

$$\int_0^{t_c} \left(\frac{\sigma(t)/\mu(T)}{\sigma_0/\mu_0} \right)^{\left(\frac{\mu(T)b^3u_0}{kT}\right)} dt = t_{c0} \tag{7.6.12.}$$

For determining the parameters t_{c0}, σ_0 and u_0 of proposed model, after integrating modified Klepaczko's failure criterion, it is possible to write a fitting equation in the following form:

$$\frac{\sigma}{\mu(T)} = \frac{\sigma_0}{\mu_0}\left[\left(\frac{u_0 b^3 \mu(T)}{kT} + 1 \right) \frac{t_{c0}}{t_c} \right]^{\left(\frac{kT}{u_0 b^3 \mu(T)}\right)} \tag{7.6.13.}$$

Using plate impact test data, and plotting normalized spall stress data $\boldsymbol{\sigma/\mu(T)}$ in function of critical time of loading $\boldsymbol{t_c}$ and applying above fitting equation, parameters t_{c0}, σ_0 and u_0 can be easily found.

Damage component evolution $D_i(\varepsilon_{ii})$ using above proposed criterion can be expressed as:

$$D_i(\varepsilon_{ii}) = \frac{\left[\int_0^{t_c} \left(\frac{\sigma_i(t)/\mu(T)}{\sigma_0/\mu_0} \right)^{\left(\frac{\mu(T)b^3u_0}{kT}\right)} dt \right]}{t_{c0}} \tag{7.6.14.}$$

or in following form, which is more appropriate for interpretation of tensile test data:

$$D_i(\varepsilon_{ii}) = \frac{t_c}{t_{c0}} \frac{1}{\left(\left(\frac{\mu(T)b^3u_0}{kT}\right)+1\right)} \left(\frac{\sigma_i(t) \big/ \mu(T)}{\sigma_0 \big/ \mu_0} \right)^{\left(\frac{\mu(T)b^3u_0}{kT}\right)} \qquad (7.6.15.)$$

where the strain rate and strain can be correlated to the characteristic time concept as follows:

$$\boldsymbol{t_c} = \frac{\boldsymbol{\varepsilon_c}}{\dot{\boldsymbol{\varepsilon}}} \qquad (7.6.16.)$$

where $\boldsymbol{\varepsilon_c}$ is critical strain.

So if $\sigma_{ii}(\varepsilon_{ii})$ curves are known by measurement and if $D_i(\varepsilon_{ii})$ is defined by damage criterion, using equation for damage energy released rate – damage, we can easily produce $Y_i D_i$ curves.

In a case when it is not possible to perform tensile test in the other directions and such a direct approach cannot be applied, we can take advantage of the measurement of the strains in the width and thickness direction of the specimen.

Values D_i, where $i = 2,3$, can be directly deduced using a direct algebraic transformation of constitutive equation:

$$\varepsilon_e = \overline{C}_e^{-1} : \sigma \qquad (7.6.17.)$$

Substituting classical Hook's elastic tensor for orthotropic materials into above constitutive equation Eq. 7.6.17., and combining with equation:

$$\overline{C}_e^{-1} = M(D) : C_e^{-1} : M(D) \qquad (7.6.18.)$$

one can obtain following expression:

$$D_i(\varepsilon_{11}) = 1 + \frac{\upsilon_{i1}\sigma_{11}}{(1 - D_1(\varepsilon_{11}))E_i\varepsilon_{ii}} = 1 + \frac{\nu_{i1}}{\overline{\nu}_{i1}}(1 - D_1(\varepsilon_{11})) \;;\; i = 2,3 \qquad (7.6.19.)$$

Thus the curves $Y_i(D_i)$, $(i = 2,3)$ can be computed thanks to the damage work equivalence principle. Using relation for damage energy released rate – damage, with stress values for σ_{ii}, $(i = 2,3)$ produced by the Hill model and $D_{ii}(\varepsilon_{ii})$, $(i = 2,3)$ curves we can reach the final $(\overline{\sigma}_{ii}\overline{\varepsilon}_{ii})$ behaviour for $i = 2,3$.

7.7. Results and conclusions

A novel procedure for calibration of damage model has been developed in this research. The calibration procedure has been applied on the aluminium alloy AA7010 and results are presented on the following graphs.

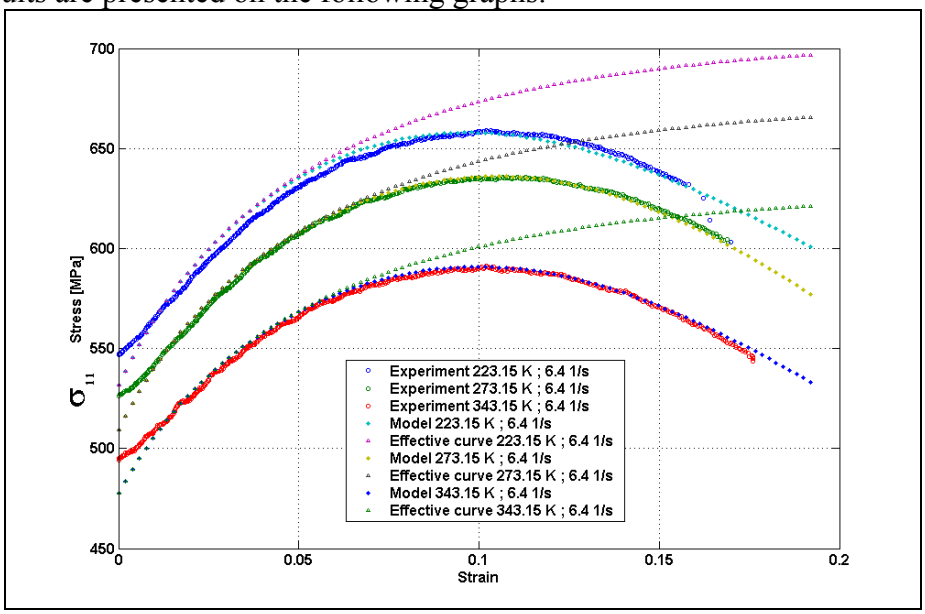

Fig. 7.7.1. $(\sigma_{11}\varepsilon_{11})$ Stress-strain and effective strain curves of AA7010 at $\dot{\varepsilon} = 6.4x10^{0}s^{1}$

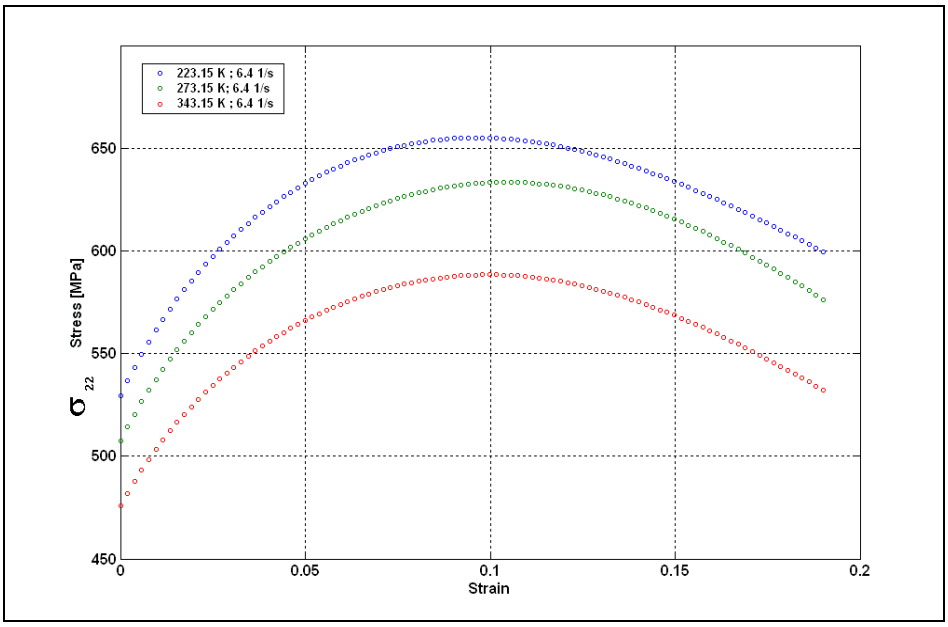

Fig. 7.7.2. $(\sigma_{11}\varepsilon_{11})$ Stress-strain curves of AA7010 at $\dot{\varepsilon} = 6.4x10^{0}s^{1}$

The figure Fig. 7.7.1. and Fig. 7.7.3. compare the experimental curves form tensile test at different temperatures and strain rates to the simulation results. We can observe that the simulated test, rather near the experimental one, presents a decrease of the stress after a certain amount of strain, corresponding to a high damage growth. Comparison between σ_{11} stress-strain and effective stress-strain curves at different temperatures and strain rates is also presented.

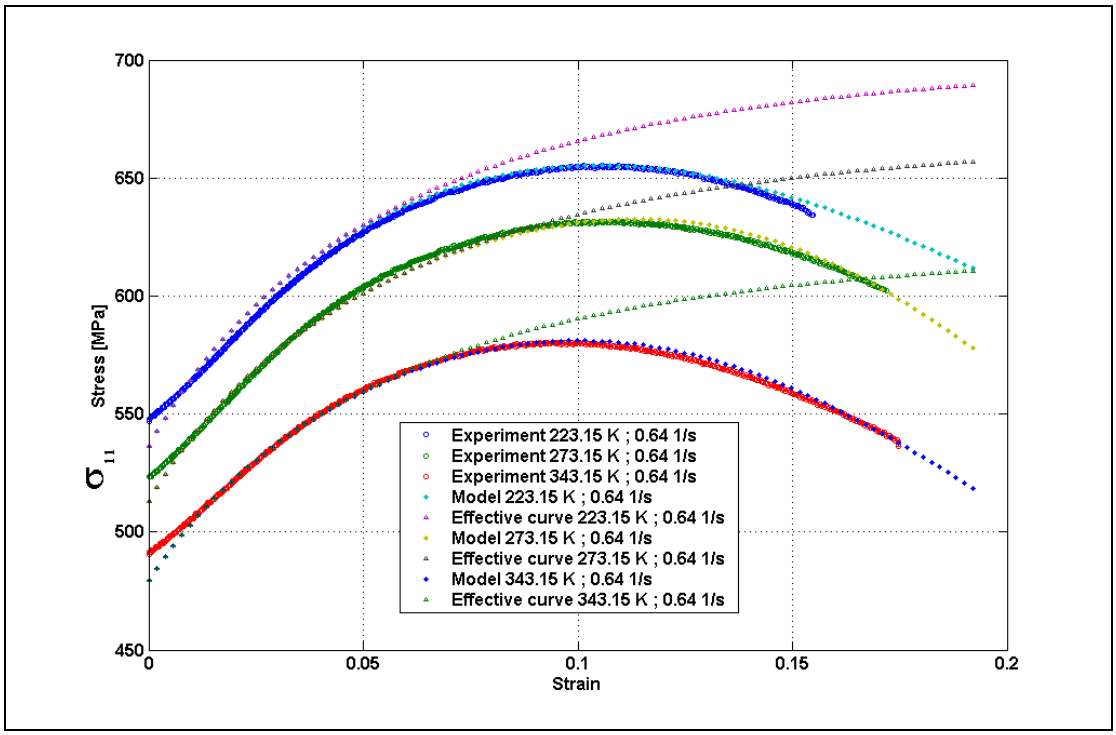

Fig. 7.7.3. $(\sigma_{11}\varepsilon_{11})$ Stress-strain and effective strain curve of AA7010 at $\dot{\varepsilon} = 6.4x10^{-1}s^{1}$

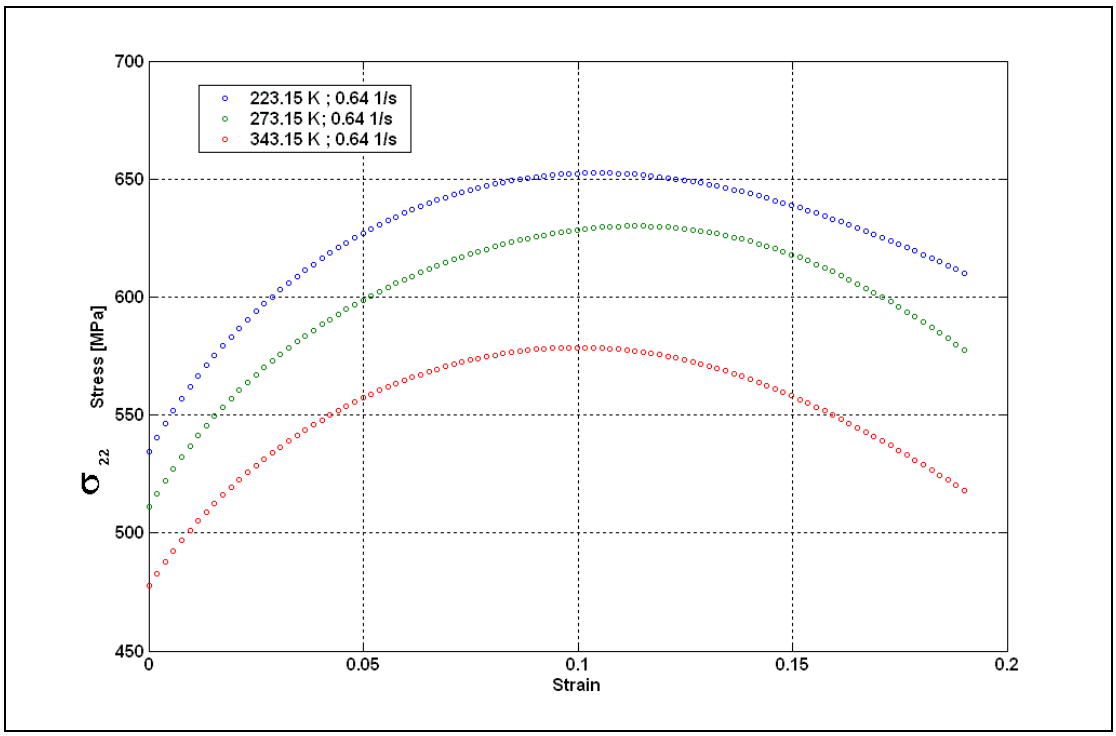

Fig. 7.7.4. $(\sigma_{11}\varepsilon_{11})$ Stress-strain curves of AA7010 at $\dot{\varepsilon} = 6.4x10^{-1}s^{1}$

From the general Hill criterion and the knowledge of the set parameters F, G, H, N σ_{22} stress-strain curves are produced and presented in Fig. 7.7.2. and Fig. 7.7.4. for different temperature and strain rate levels.

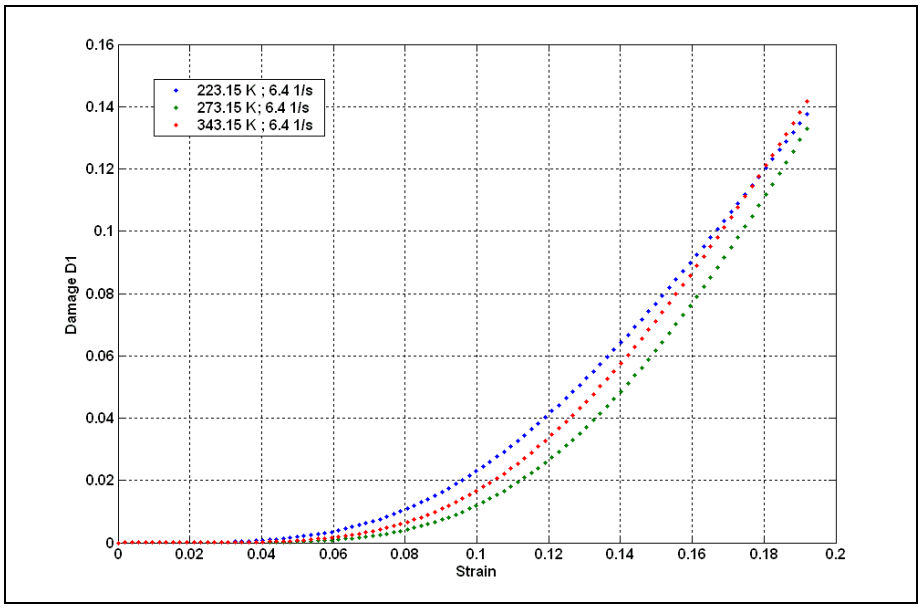

Fig. 7.7.5. Damage variable D_1 vs strain under simple tension

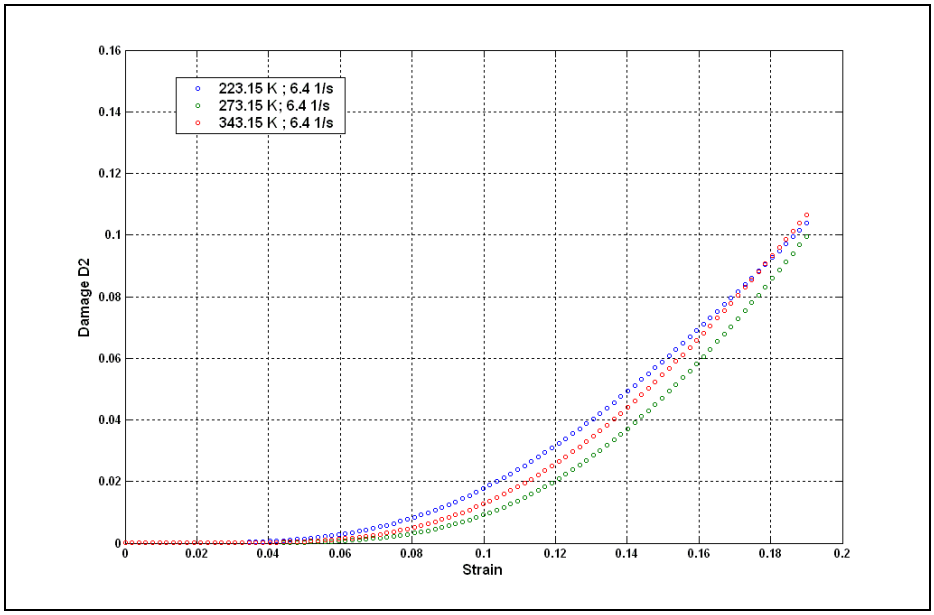

Fig. 7.7.6. Damage variable D_2 vs strain under simple tension

The damage evolutions, D_1 and D_2 against true strain are reproduced and shown in Fig. 7.7.5. and Fig. 7.7.6. respectively. From the damage-strain curves for AA7010 through simple tension test, it is readily seen that D_1 in the direction of maximum principal tensile stress grows much more rapidly then D_2 does, i.e. $\dot{D}_1 > \dot{D}_2$ and at the moment D_1 reaches its critical value which also signifies the fracture of the specimen, the corresponding value of D_2 is significantly smaller.

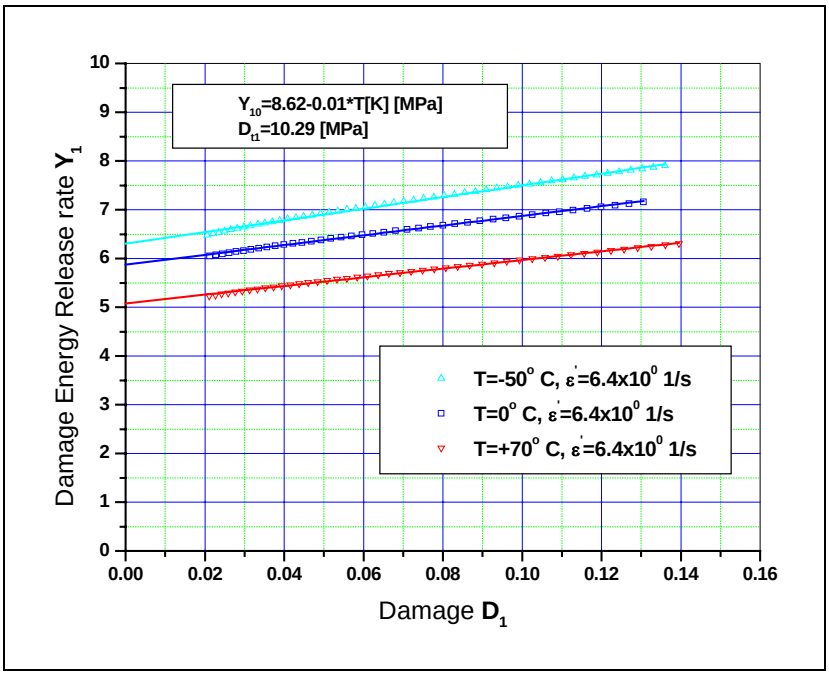

Fig. 7.7.7. Linear description of the damage energy released rate for AA7010 at $\dot{\varepsilon} = 6.4x10^0 s^1$

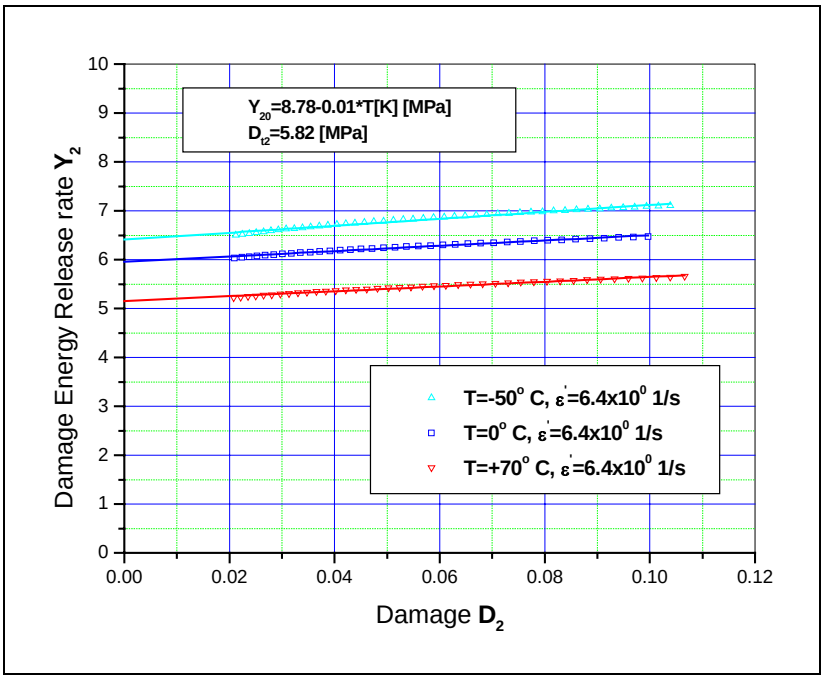

Fig. 7.7.8. Linear description of the damage energy released rate for AA7010 at $\dot{\varepsilon} = 6.4x10^0 s^1$

So as $\sigma_{ii}(\varepsilon_{ii})$ is known by measurement and $D_i(\varepsilon_{ii})$ is defined by damage criterion, using equation for damage energy released rate – damage, we can produce $Y_i D_i$ curves easily for i equal 1 and 2. In this development linear model is fitted, and results are presented in figures Fig. 7.7.7. and Fig. 7.7.8..

Table Tab. 7.7.1.a. and Tab. 7.7.1.b. give final set of the parameters for a fitting using tensile tests in large strains of AA7010. As no information on $(\sigma_{33}\varepsilon_{33})$ curves are available, parameters in the principal direction 3 are assumed to be equal to parameters in referent direction.

Tab. 7.7.1.a. Material parameters – Elastic modulus

Parameter	Description	Nominal value
E_1	Initial elastic modulus	71,1 GPa
E_2	Initial elastic modulus	70,3 GPa
E_3	Initial elastic modulus	71,1 GPa

Tab. 7.7.1.b. Damage curve parameters

Parameter	Description	Nominal value
Y_{10}	Initial damage energy release rate	$8.62 - 0.01T$ MPa
D_{t1}	Damage hardening	10.29 MPa
Y_{20}	Initial damage energy release rate	$8.78 - 0.01T$ MPa
D_{t2}	Damage hardening	5.82 MPa
Y_{30}	Initial damage energy release rate	$8.62 - 0.01T$ MPa
D_{t3}	Damage hardening	10.29 MPa

8. NUMERICAL IMPLEMENTATION

8.1. Introduction

Because one of the main objectives of this research was to offer the improvement of the existing simulation tools used for analysis of metals and structures, purpose of this chapter is to demonstrate that proposed anisotropic elastoplastic damage model is suitable for large-scale computations. Developed model of anisotropic damage growth together with proposed elastic predictor/plastic return corrector/damage return mapping, integration algorithm can be easily implemented in existing finite elements programs to solve practical engineering problems. LLNL-DYNA3D has been chosen as a numerical test bed for implementation and validation of developed model.

General anisotropic material model has been chosen as a starting point for the new material model development. This model is implemented as material model 33 [14] into an explicit finite element code, Cranfield University's version of LLNL-DYNA3D.

This model is a general anisotropic elastic-plastic material model, which was originally developed at Lawrence Livermore National Laboratories. It combines the orhotropic elastic model (material type 2 in LLNL-DYNA3D), with the Hill orthotropic yield criterion. This model uses the normal return algorithm for the update of the plastic stress, and important drawback of this stress update algorithm is that the solution may drift away from the yield surface. The algorithm involves the calculation of a new elastic-plastic stiffness matrix in a each time step. In this model associated plasticity is employed and elliptic shape of the yield surface is assumed.

Following DYNA3D routines are associated with implemented General Anisotropic material model:

- ***solde*** – subroutine processes all the solid elements, and other subroutines are called from this subroutine for executing different tasks such as packing and unpacking the data for the material model (hvpac1 and hvpac2), loading element stress tensor (hvpac1), storing new stress tensor (hvpac2) ,calculation of the rotated stress tensor (rstrss), calculation the critical time step and bulk viscosity (bulkg), calculation of the kinetic energy for every element (engbrk).

- ***matin*** –subroutine reads in the material data from the input file

- ***initlz*** – subroutine contains calls to subroutines that initialise values that are required during the solution phase but they re not separately defined in the input file

- ***f3dm33*** – subroutine is the main subroutine which calculates the new stress tensor

- ***sets33*** – subroutine which is called from subroutine matin and reads in all the material specific data for material model 33

- ***inse33*** – subroutine initialise the values related to the q matrix, which is the transformation matrix from element to material matrix

The implementation required changes to several routines in the code, not just the main f3dm3 subroutine for the general anisotropic model, and the implemented model requires more input parameters. In summary the additions to general anisotropic elastoplastic material model 33 are:

- Coupling of anisotropic elastoplasticity and damage through utilisation of the damage tensor $\boldsymbol{D}$, the damage effect tensor $\boldsymbol{M}(\boldsymbol{D})$, the damage characteristic tensor $\boldsymbol{J}$, the effective plastic characteristic tensor $\overline{\mathrm{H}}$, and the effective elastic stiffness tensor $\overline{\boldsymbol{C}_{\boldsymbol{e}}}$.

- Strain rate and temperature dependent isotropic strain hardening.

- Linear damage hardening with temperature dependant initial damage threshold.

- Implementation of elastic predictor/plastic return corrector/damage return mapping, integration algorithm.

Constitutive equations of anisotropic elastoplastic-damage model, neccesery for numerical implementation of the proposed model, and numerical algorithm are presented in the following sections.

8.2. Coupled anisotropic elastoplastic-damage formulation

8.2.1. Isotropic strain hardening

Restricting our consideration to relatively simple loading histories, in this development we employed isotropic hardening yield surface. According to the yield criterion, and taking time derivatives we can get following expression:

$$\dot{\boldsymbol{R}} = \dot{\bar{\boldsymbol{\sigma}}}_{\boldsymbol{F}} \tag{8.2.1.1.}$$

The stress is related to plastic strain by the hardening modulus Π. Expressed in rate form this is:

$$\dot{\boldsymbol{\sigma}} = \Pi \dot{\boldsymbol{\varepsilon}}_{\boldsymbol{p}} \tag{8.2.1.2.}$$

The same expression holds for the relation between the equivalent stress and the equivalent or accumulated plastic strain:

$$\dot{\bar{\boldsymbol{\sigma}}}_{\boldsymbol{F}} = \Pi \dot{\hat{\boldsymbol{\varepsilon}}}_{\boldsymbol{p}} = \Pi \dot{\boldsymbol{\alpha}} \tag{8.2.1.3.}$$

Combining this with equation Eq. 8.2.1.1., the rate of expansion of yield surface radius becomes:

$$\dot{\boldsymbol{R}} = \Pi \dot{\boldsymbol{\alpha}} \tag{8.2.1.4.}$$

Now we can write isotropic hardening rule as:

$$\dot{\boldsymbol{R}} = \frac{\boldsymbol{dR}}{\boldsymbol{d\alpha}} \frac{\boldsymbol{d\alpha}}{\boldsymbol{dt}} = \Pi \dot{\boldsymbol{\alpha}} = \Pi \dot{\boldsymbol{\lambda}}_{\boldsymbol{p}} \tag{8.2.1.5.}$$

and hence

$$\frac{\boldsymbol{dR}}{\boldsymbol{d\alpha}} = \Pi \tag{8.2.1.6.}$$

Increment of strain hardening in this development is represented by mechanical threshold stress model:

$$\boldsymbol{R}(\boldsymbol{\alpha}) = \boldsymbol{R}(\hat{\boldsymbol{\varepsilon}}_{\boldsymbol{p}}) = \frac{\boldsymbol{\mu}(\boldsymbol{T})}{\boldsymbol{\mu}_0} \left(1 - \left[\frac{\boldsymbol{kT} \ln\left(\dot{\hat{\boldsymbol{\varepsilon}}}_{\boldsymbol{p}0} / \dot{\hat{\boldsymbol{\varepsilon}}}_{\boldsymbol{p}} \right)}{\boldsymbol{\mu}(\boldsymbol{T}) \boldsymbol{b}^3 \boldsymbol{g}_0} \right]^{1/q} \right)^{1/p} \int \boldsymbol{\theta} \left(\frac{\tanh\left[\boldsymbol{\alpha} \dfrac{\hat{\boldsymbol{\sigma}}_{\boldsymbol{\varepsilon}}}{\hat{\boldsymbol{\sigma}}_{\boldsymbol{as}}(\dot{\boldsymbol{\varepsilon}}, \boldsymbol{T})} \right]}{\tanh(\boldsymbol{\alpha})} \right) \boldsymbol{d\hat{\varepsilon}}_{\boldsymbol{p}} \tag{8.2.1.7.}$$

which has been discussed in details in Chapter 4, and initial yield stress $\boldsymbol{R}_0$ corresponds to the athermal component of MTS flow model:

$$\boldsymbol{R}_0 = \boldsymbol{\sigma}_{\boldsymbol{a}} \tag{8.2.1.8.}$$

8.2.2. Plastic flow rule

Recalling the expression for the effective equivalent stress[Eq. 7.5.1.2.]:

$$\bar{\sigma}_F = \left[\frac{1}{2}\boldsymbol{\sigma}^T \overline{\mathrm{H}}\,\boldsymbol{\sigma}\right]^{1/2} \tag{8.2.2.1.}$$

we can determine the relation for $\frac{\partial \boldsymbol{F}_p}{\partial \boldsymbol{\sigma}}$ as:

$$\frac{\partial \boldsymbol{F}_p}{\partial \boldsymbol{\sigma}} = \frac{\overline{\mathrm{H}}\,\boldsymbol{\sigma}}{2\bar{\sigma}_F} = \frac{\boldsymbol{M}\mathrm{H}\boldsymbol{M}\boldsymbol{\sigma}}{2\bar{\sigma}_F}. \tag{8.2.2.2.}$$

Therefore the plastic flow rule can be determined as follows:

$$\dot{\boldsymbol{\varepsilon}}_p = \dot{\lambda}_p \frac{\partial \boldsymbol{F}_p}{\partial \boldsymbol{\sigma}} = \frac{\boldsymbol{M}\mathrm{H}\boldsymbol{M}\boldsymbol{\sigma}}{2\bar{\sigma}_F}\dot{\lambda}_p \tag{8.2.2.3.}$$

8.2.3. Linear damage hardening

It has been showed that damage evolution in the aluminium alloys, which have been considered in this investigation, could be described with linear damage hardening. Hence linear damage evolution law was utilized in this material model development in the following form:

$$\dot{\boldsymbol{B}} = \frac{d\boldsymbol{B}}{d\boldsymbol{\beta}}\dot{\boldsymbol{\beta}} = \frac{d\boldsymbol{B}}{d\boldsymbol{\beta}}\dot{\lambda}_p \tag{8.2.3.1.}$$

Increment in damage hardening is defined as:

$$\boldsymbol{B}(\boldsymbol{\beta}) = \boldsymbol{B}(\hat{\boldsymbol{D}}) = \mathcal{D}\ \hat{\boldsymbol{D}} \tag{8.2.3.2.}$$

and because $\dot{\boldsymbol{\beta}} = \dot{\lambda}_d$ damage hardening modulus is defined as:

$$\frac{d\boldsymbol{B}}{d\boldsymbol{\beta}} = \mathcal{D} \tag{8.2.3.3.}$$

where $\boldsymbol{\beta}$ is equivalent or accumulated overall damage $\hat{\boldsymbol{D}}$, represented with modified Klapezcko's damage evolution criteria:

$$\hat{\boldsymbol{D}}(\hat{\boldsymbol{\varepsilon}}_p) = \frac{\hat{\boldsymbol{\varepsilon}}_{pc}}{\hat{\boldsymbol{\varepsilon}}_{pc0}} \frac{1}{\left(\left(\frac{\boldsymbol{\mu}(\boldsymbol{T})\boldsymbol{b}^3\boldsymbol{u}_0}{\boldsymbol{kT}}\right)+1\right)} \left(\frac{\boldsymbol{\sigma}_m / \boldsymbol{\mu}(\boldsymbol{T})}{\boldsymbol{\sigma}_0 / \boldsymbol{\mu}_0}\right)^{\left(\frac{\boldsymbol{\mu}(\boldsymbol{T})\boldsymbol{b}^3\boldsymbol{u}_0}{\boldsymbol{kT}}\right)} \tag{8.2.3.4.}$$

It has been found that initial damage threshold $\boldsymbol{B}_0$ is in function of temperature, and that dependence could be expressed with following relationship:

$$\boldsymbol{B}_0 = \boldsymbol{B}_{01} - \boldsymbol{B}_{02}\boldsymbol{T} \tag{8.2.3.5.}$$

where $\boldsymbol{B}_{01}$ and $\boldsymbol{B}_{02}$ are material dependant constants and T is temperature.

8.2.4. Damage evolution rule

Noting that equivalent damage energy release rate is defined by:

$$\boldsymbol{Y}_{eq} = \left[\frac{1}{2}\boldsymbol{Y}^{T}\boldsymbol{J}\boldsymbol{Y}\right]^{1/2} \tag{8.2.4.1.}$$

relation for $\frac{\partial \boldsymbol{F}_d}{\partial \boldsymbol{Y}}$ could be found as:

$$\frac{\partial \boldsymbol{F}_d}{\partial \boldsymbol{Y}} = \frac{\boldsymbol{J}\boldsymbol{Y}}{2\boldsymbol{Y}_{eq}} \tag{8.2.4.2.}$$

Hence the damage evolution rule can be determined as:

$$\dot{\boldsymbol{D}} = -\dot{\boldsymbol{\lambda}}_d \frac{\partial \boldsymbol{F}_d}{\partial \boldsymbol{Y}} = -\frac{\boldsymbol{J}\boldsymbol{Y}}{2\boldsymbol{Y}_{eq}}\dot{\boldsymbol{\lambda}}_d \tag{8.2.4.3.}$$

8.2.5. Determination of plasticity multiplier $\dot{\lambda}_p$

Starting from the definition of plastic potential:

$$\boldsymbol{F}_p(\overline{\boldsymbol{\sigma}}, \boldsymbol{R}) = \overline{\boldsymbol{\sigma}}_F - [\boldsymbol{R}(\boldsymbol{\alpha}) + \boldsymbol{R}_0] = 0 \tag{8.2.5.1.}$$

and using so-called plasticity consistency condition $\dot{\boldsymbol{F}}_p = 0$, parameter $\dot{\boldsymbol{\lambda}}_p$ could be determined. Hence during plastic loading one has [116]:

$$\dot{\boldsymbol{F}}_p = \frac{\partial \boldsymbol{F}_p}{\partial \boldsymbol{\sigma}}\dot{\boldsymbol{\sigma}} + \frac{\partial \boldsymbol{F}_p}{\partial \boldsymbol{R}}\dot{\boldsymbol{R}} = 0\,. \tag{8.2.5.2.}$$

Because of the fact that:

$$\frac{\partial \boldsymbol{F}_p}{\partial \boldsymbol{R}} = -1 \tag{8.2.5.3.}$$

the consistency condition could be rewritten as:

$$\dot{\boldsymbol{F}}_p = \frac{\partial \boldsymbol{F}_p}{\partial \boldsymbol{\sigma}}\dot{\boldsymbol{\sigma}} - \dot{\boldsymbol{R}} = 0\,. \tag{8.2.5.4.}$$

Recalling the constitutive equation for the damaged material [Eq. 7.4.1.]:

$$\boldsymbol{\sigma} = \overline{\boldsymbol{C}}_{\boldsymbol{e}} \boldsymbol{\varepsilon}_{\boldsymbol{e}} \tag{8.2.5.5.}$$

and noting relation for the strain decomposition:

$$\boldsymbol{\varepsilon} = \boldsymbol{\varepsilon}_{\boldsymbol{e}} + \boldsymbol{\varepsilon}_{\boldsymbol{p}} \tag{8.2.5.6.}$$

we can write:

$$\dot{\boldsymbol{\sigma}} = \overline{\boldsymbol{C}}_{\boldsymbol{e}} (\dot{\boldsymbol{\varepsilon}} - \dot{\boldsymbol{\varepsilon}}_{\boldsymbol{p}}) \tag{8.2.5.7.}$$

Now consistency condition could be expressed as follows:

$$\dot{\boldsymbol{F}}_{\boldsymbol{p}} = \frac{\partial \boldsymbol{F}_{\boldsymbol{p}}}{\partial \boldsymbol{\sigma}} \overline{\boldsymbol{C}}_{\boldsymbol{e}} \dot{\boldsymbol{\varepsilon}} - \frac{\partial \boldsymbol{F}_{\boldsymbol{p}}}{\partial \boldsymbol{\sigma}} \overline{\boldsymbol{C}}_{\boldsymbol{e}} \dot{\boldsymbol{\varepsilon}}_{\boldsymbol{p}} - \frac{\boldsymbol{dR}}{\boldsymbol{d\alpha}} \frac{\boldsymbol{d\alpha}}{\boldsymbol{dt}} = 0 \tag{8.2.5.8.}$$

Using formulation for isotropic hardening rule, which is defined as:

$$\dot{\boldsymbol{R}} = \dot{\boldsymbol{\lambda}}_{\boldsymbol{p}} \frac{\boldsymbol{dR}}{\boldsymbol{d\alpha}} \tag{8.2.5.9.}$$

where

$$\dot{\boldsymbol{\alpha}} = \dot{\boldsymbol{\lambda}}_{\boldsymbol{p}} \tag{8.2.5.10.}$$

and the plastic flow rule:

$$\dot{\boldsymbol{\varepsilon}}_{\boldsymbol{p}} = \dot{\boldsymbol{\lambda}}_{\boldsymbol{p}} \frac{\partial \boldsymbol{F}_{\boldsymbol{p}}}{\partial \boldsymbol{\sigma}} \tag{8.2.5.11.}$$

the plasticity consistency equation now can be rewritten as:

$$\dot{\boldsymbol{F}}_{\boldsymbol{p}} = \frac{\partial \boldsymbol{F}_{\boldsymbol{p}}}{\partial \boldsymbol{\sigma}} \overline{\boldsymbol{C}}_{\boldsymbol{e}} \dot{\boldsymbol{\varepsilon}} - \frac{\partial \boldsymbol{F}_{\boldsymbol{p}}}{\partial \boldsymbol{\sigma}} \overline{\boldsymbol{C}}_{\boldsymbol{e}} \dot{\boldsymbol{\lambda}}_{\boldsymbol{p}} \frac{\partial \boldsymbol{F}_{\boldsymbol{p}}}{\partial \boldsymbol{\sigma}} - \dot{\boldsymbol{\lambda}}_{\boldsymbol{p}} \frac{\boldsymbol{dR}}{\boldsymbol{d\alpha}} = 0 \tag{8.2.5.12.}$$

This expression now can be solved for $\dot{\boldsymbol{\lambda}}_{\boldsymbol{p}}$ to obtain following expression:

$$\dot{\boldsymbol{\lambda}}_{\boldsymbol{p}} = \frac{\dfrac{\partial \boldsymbol{F}_{\boldsymbol{p}}}{\partial \boldsymbol{\sigma}} \overline{\boldsymbol{C}}_{\boldsymbol{e}} \dot{\boldsymbol{\varepsilon}}}{\dfrac{\partial \boldsymbol{F}_{\boldsymbol{p}}}{\partial \boldsymbol{\sigma}} \overline{\boldsymbol{C}}_{\boldsymbol{e}} \dfrac{\partial \boldsymbol{F}_{\boldsymbol{p}}}{\partial \boldsymbol{\sigma}} - \dfrac{\boldsymbol{dR}}{\boldsymbol{d\alpha}}} \tag{8.2.5.13.}$$

where the elastic tensor for damaged material is defined as:

$$\overline{\boldsymbol{C}}_{\boldsymbol{e}} = \boldsymbol{M}^{-1}(\boldsymbol{D}) \boldsymbol{C}_{\boldsymbol{e}} \boldsymbol{M}^{-1}(\boldsymbol{D}) . \tag{8.2.5.14.}$$

8.2.6. Effective elastoplastic-damage constitutive matrix

Assuming associative plasticity elastoplastic tangent moduli [117] could be represented as:

$$\overline{\boldsymbol{C}}_{ep} = \overline{\boldsymbol{C}}_e - \overline{\boldsymbol{C}}_e \frac{\partial \boldsymbol{F}_p}{\partial \boldsymbol{\sigma}} \{\boldsymbol{C}_\lambda\}^T \tag{8.2.6.1.}$$

where $\{\boldsymbol{C}_\lambda\}^T$ is defined by the relation of the plastic multiplier $\boldsymbol{d\lambda}$ to the strain increment:

$$\boldsymbol{d\lambda} = \{\boldsymbol{C}_\lambda\}^T \boldsymbol{d\varepsilon} \tag{8.2.6.2.}$$

Comparing with general expression for $\boldsymbol{d\lambda}$

$$\boldsymbol{d\lambda}_p = \frac{\frac{\partial \boldsymbol{F}_p}{\partial \boldsymbol{\sigma}} \overline{\boldsymbol{C}}_e \boldsymbol{d\varepsilon}}{\frac{\partial \boldsymbol{F}_p}{\partial \boldsymbol{\sigma}} \overline{\boldsymbol{C}}_e \frac{\partial \boldsymbol{F}_p}{\partial \boldsymbol{\sigma}} - \frac{\boldsymbol{dR}}{\boldsymbol{d\alpha}}} \tag{8.2.6.3.}$$

it is clear that $\{\boldsymbol{C}_\lambda\}^T$ can be expressed by:

$$\{\boldsymbol{C}_\lambda\}^T = \frac{\frac{\partial \boldsymbol{F}_p}{\partial \boldsymbol{\sigma}} \overline{\boldsymbol{C}}_e}{\frac{\partial \boldsymbol{F}_p}{\partial \boldsymbol{\sigma}} \overline{\boldsymbol{C}}_e \frac{\partial \boldsymbol{F}_p}{\partial \boldsymbol{\sigma}} - \frac{\boldsymbol{dR}}{\boldsymbol{d\alpha}}} \tag{8.2.6.4.}$$

one obtains the following expression for the elasto-plastic-damage constitutive matrix:

$$\overline{\boldsymbol{C}}_{ep} = \overline{\boldsymbol{C}}_e - \overline{\boldsymbol{C}}_e \frac{\partial \boldsymbol{F}_p}{\partial \boldsymbol{\sigma}} \frac{\frac{\partial \boldsymbol{F}_p}{\partial \boldsymbol{\sigma}} \overline{\boldsymbol{C}}_e}{\frac{\partial \boldsymbol{F}_p}{\partial \boldsymbol{\sigma}} \overline{\boldsymbol{C}}_e \frac{\partial \boldsymbol{F}_p}{\partial \boldsymbol{\sigma}} - \frac{\boldsymbol{dR}}{\boldsymbol{d\alpha}}} . \tag{8.2.6.5.}$$

8.2.7. Determination of damage multiplier $\dot{\lambda}_d$

Damage multiplier could be derived from damage consistency condition [119]:

$$\dot{\boldsymbol{F}}_d = \frac{\partial \boldsymbol{F}_d}{\partial \boldsymbol{Y}} \dot{\boldsymbol{Y}} + \frac{\partial \boldsymbol{F}_d}{\partial \boldsymbol{B}} \dot{\boldsymbol{B}} = 0 \tag{8.2.7.1.}$$

where damage potential is defined as:

$$\boldsymbol{F}_d = \boldsymbol{Y}_{eq} - [\boldsymbol{B}(\boldsymbol{\beta}) + \boldsymbol{B}_0] . \tag{8.2.7.2.}$$

Because of the fact that:

$$\frac{\partial \boldsymbol{F_d}}{\partial \boldsymbol{B}} = -1 \tag{8.2.7.3.}$$

the consistency condition can be rewritten as:

$$\dot{\boldsymbol{F}}_{\boldsymbol{d}} = \frac{\partial \boldsymbol{F_d}}{\partial \boldsymbol{Y}} \dot{\boldsymbol{Y}} - \dot{\boldsymbol{B}} = 0\,. \tag{8.2.7.4.}$$

Using formulation for damage hardening rule, which is defined as:

$$\dot{\boldsymbol{B}} = \frac{\boldsymbol{dB}}{\boldsymbol{d\beta}} \frac{\boldsymbol{d\beta}}{\boldsymbol{dt}} = \frac{\boldsymbol{dB}}{\boldsymbol{d\beta}} \dot{\boldsymbol{\lambda}}_{\boldsymbol{d}} \tag{8.2.7.5.}$$

where

$$\dot{\boldsymbol{\beta}} = \dot{\boldsymbol{\lambda}}_{\boldsymbol{d}} \tag{8.2.7.6.}$$

the damage consistency equation now can be rewritten as:

$$\dot{\boldsymbol{F}}_{\boldsymbol{d}} = \frac{\partial \boldsymbol{F_d}}{\partial \boldsymbol{Y}} \dot{\boldsymbol{Y}} - \dot{\boldsymbol{\lambda}}_{\boldsymbol{d}} \frac{\boldsymbol{dB}}{\boldsymbol{d\beta}} = 0\,. \tag{8.2.7.7.}$$

This expression now can be solved for $\dot{\boldsymbol{\lambda}}_{\boldsymbol{d}}$ to obtain following expression:

$$\dot{\boldsymbol{\lambda}}_{\boldsymbol{d}} = \frac{\dfrac{\partial \boldsymbol{F_d}}{\partial \boldsymbol{Y}} \dot{\boldsymbol{Y}}}{\dfrac{\boldsymbol{dB}}{\boldsymbol{d\beta}}}\,. \tag{8.2.7.8.}$$

8.2.8. Constitutive relations for anisotropic elastoplastic-damage

According constitutive equation for the damaged material:

$$\boldsymbol{\sigma} = \overline{\boldsymbol{C}}_{\boldsymbol{e}} \boldsymbol{\varepsilon}_{\boldsymbol{e}} \tag{8.2.8.1.}$$

and noting relation for the strain decomposition:

$$\boldsymbol{\varepsilon} = \boldsymbol{\varepsilon}_{\boldsymbol{e}} + \boldsymbol{\varepsilon}_{\boldsymbol{p}} \tag{8.2.8.2.}$$

objective rate form [117] of above equation could be written as:

$$\dot{\boldsymbol{\sigma}} = \overline{\boldsymbol{C}}_{\boldsymbol{e}} (\dot{\boldsymbol{\varepsilon}} - \dot{\boldsymbol{\lambda}}_{\boldsymbol{p}} \frac{\partial \boldsymbol{F_p}}{\partial \boldsymbol{\sigma}}) \tag{8.2.8.3.}$$

or

$$\dot{\boldsymbol{\sigma}} = \overline{\boldsymbol{C}}_{\boldsymbol{e}}(\dot{\boldsymbol{\varepsilon}} - \dot{\boldsymbol{\lambda}}_{\boldsymbol{p}} \frac{\boldsymbol{M}\mathrm{H}\boldsymbol{M}\boldsymbol{\sigma}}{2\overline{\boldsymbol{\sigma}}_{\boldsymbol{F}}}) \tag{8.2.8.4.}$$

From definition for damage energy release rate:

$$Y \equiv -\rho \frac{\partial \psi}{\partial D} \tag{8.2.8.5.}$$

and from degenerated form of the Helmholtz free energy:

$$\boldsymbol{\rho\psi}(\boldsymbol{\sigma}, \boldsymbol{D}, \boldsymbol{\alpha}, \boldsymbol{\beta}) = \boldsymbol{W}(\boldsymbol{\sigma}_{\boldsymbol{e}}, \boldsymbol{D}) + \boldsymbol{H}_{\boldsymbol{p}}(\boldsymbol{\alpha}) + \boldsymbol{H}_{\boldsymbol{d}}(\boldsymbol{\beta}) \tag{8.2.8.6.}$$

where according to the energy equivalence hypothesis, the complementary elastic energy $W_e(\sigma, D)$ is evaluated as:

$$\boldsymbol{W}_{\boldsymbol{e}}(\boldsymbol{\sigma}, \boldsymbol{D}) = \frac{1}{2}\overline{\boldsymbol{\sigma}}^{\boldsymbol{T}}\boldsymbol{C}_{\boldsymbol{e}}^{-1}\overline{\boldsymbol{\sigma}} = \frac{1}{2}\boldsymbol{\sigma}^{\boldsymbol{T}}\boldsymbol{M}\boldsymbol{C}_{\boldsymbol{e}}^{-1}\boldsymbol{M}\boldsymbol{\sigma} \tag{8.2.8.7.}$$

we can write:

$$\boldsymbol{Y} = -\frac{\partial \boldsymbol{W}_{\boldsymbol{e}}(\boldsymbol{\sigma}, \boldsymbol{D})}{\partial \boldsymbol{D}} = -\boldsymbol{\sigma}^{\boldsymbol{T}}\boldsymbol{M}\boldsymbol{C}_{\boldsymbol{e}}^{-1}\frac{\partial \boldsymbol{M}}{\partial \boldsymbol{D}}\boldsymbol{\sigma}\,. \tag{8.2.8.8.}$$

Now, the coupled elastoplastic-damage constitutive equations are summarized as below:

$$\dot{\varepsilon} = \dot{\varepsilon}_e + \dot{\varepsilon}_p \tag{8.2.8.9.}$$

$$\dot{\boldsymbol{\sigma}} = \overline{\boldsymbol{C}}_{\boldsymbol{e}}(\dot{\boldsymbol{\varepsilon}} - \dot{\boldsymbol{\lambda}}_{\boldsymbol{p}} \frac{\boldsymbol{M}\mathrm{H}\boldsymbol{M}\boldsymbol{\sigma}}{2\overline{\boldsymbol{\sigma}}_{\boldsymbol{F}}}) \tag{8.2.8.10.}$$

$$\dot{\boldsymbol{\varepsilon}}_{\boldsymbol{p}} = \frac{\boldsymbol{M}\mathrm{H}\boldsymbol{M}\boldsymbol{\sigma}}{2\overline{\boldsymbol{\sigma}}_{\boldsymbol{F}}}\dot{\boldsymbol{\lambda}}_{\boldsymbol{p}} \tag{8.2.8.11.}$$

$$\dot{\alpha} = \dot{\lambda}_p \tag{8.2.8.12.}$$

$$\dot{R} = \dot{\lambda}_p \frac{dR}{d\alpha} \tag{8.2.8.13.}$$

$$-\boldsymbol{Y} = \boldsymbol{\sigma}^{\boldsymbol{T}}\boldsymbol{M}\boldsymbol{C}_{\boldsymbol{e}}^{-1}\frac{\partial \boldsymbol{M}}{\partial \boldsymbol{D}}\boldsymbol{\sigma} \tag{8.2.8.14.}$$

$$\dot{\boldsymbol{D}} = -\frac{\boldsymbol{JY}}{2\boldsymbol{Y_{eq}}}\dot{\boldsymbol{\lambda}}_{\boldsymbol{d}} \tag{8.2.8.15.}$$

$$\dot{\beta} = \dot{\lambda}_d \tag{8.2.8.16.}$$

$$\dot{B} = \frac{dB}{d\beta}\dot{\lambda}_d \tag{8.2.8.17.}$$

$$\boldsymbol{F_p} = \left[\frac{1}{2}\boldsymbol{\sigma^T M}\mathrm{H}\boldsymbol{M\sigma}\right]^{1/2} - \boldsymbol{R}_0 - \boldsymbol{R}(\boldsymbol{\alpha}) \tag{8.2.8.18.}$$

$$\boldsymbol{F_d} = \left[\frac{1}{2}\boldsymbol{Y^T JY}\right]^{1/2} - \boldsymbol{B}_0 - \boldsymbol{B}(\boldsymbol{\beta}) \tag{8.2.8.19.}$$

8.3. Algorithmic treatment for anisotropic damage model

The first part of the implemented numerical routine is concerned with the reading and initialisation of all material properties. In a nonlinear finite element analysis, the constitutive equations of the material have to be integrated locally at each time step. If stresses, state variables, etc. are expressed in global coordinates, at the beginning of each new step, they should be firstly transferred to the principal axes of anisotropy using classical rules of coordinates transformations. Then, the constitutive relations developed above could be used directly. Hence, the rotation of the stress and strain rate tensors from global to material coordinates has been utilised. The next step is to calculate the strains from the strain-rates by multiplying with time steps.

The elastic constitutive matrix $\boldsymbol{C_e}$ is initialised, and damaged elastic constitutive matrix $\overline{\boldsymbol{C}}_{\boldsymbol{e}}$ is calculated as:

$$\overline{\boldsymbol{C}}_{\boldsymbol{e}} = \boldsymbol{M}(\boldsymbol{D})^{-1}\boldsymbol{C_e}\boldsymbol{M}(\boldsymbol{D})^{-1} \tag{8.3.1.}$$

where:

$$M^{-1} = diag \left[1-D_1 \quad 1-D_2 \quad 1-D_3 \quad \sqrt{(1-D_2)(1-D_3)} \quad \sqrt{(1-D_3)(1-D_1)} \quad \sqrt{(1-D_1)(1-D_2)}\right] \tag{8.3.2.}$$

therefore damaged elastic constitutive matrix could be calculated as:

$$\overline{C_e} = \begin{bmatrix} \frac{Ce_{11}}{(1-D_1)^{-2}} & \frac{Ce_{12}}{(1-D_1)^{-1}(1-D_2)^{-1}} & \frac{Ce_{13}}{(1-D_1)^{-1}(1-D_3)^{-1}} & 0 & 0 & 0 \\ \frac{Ce_{21}}{(1-D_1)^{-1}(1-D_2)^{-1}} & \frac{Ce_{22}}{(1-D_2)^{-2}} & \frac{Ce_{23}}{(1-D_2)(1-D_3)} & 0 & 0 & 0 \\ \frac{Ce_{31}}{(1-D_1)^{-1}(1-D_3)^{-1}} & \frac{Ce_{32}}{(1-D_2)^{-1}(1-D_3)^{-1}} & \frac{Ce_{33}}{(1-D_3)^{-2}} & 0 & 0 & 0 \\ 0 & 0 & 0 & \frac{Ce_{44}}{(1-D_2)^{-1}(1-D_3)^{-1}} & 0 & 0 \\ 0 & 0 & 0 & 0 & \frac{Ce_{55}}{(1-D_3)^{-1}(1-D_1)^{-1}} & 0 \\ 0 & 0 & 0 & 0 & 0 & \frac{Ce_{66}}{(1-D_1)^{-1}(1-D_2)^{-1}} \end{bmatrix} \quad (8.3.3.)$$

Next step is initialisation of H matrix, where matrix constituents F, G, H, L, M, N are calculate from anisotropy parameters R, P, Q_{ab}, Q_{bc}, Q_{ca}. This is followed with determination of effective plastic characteristic tensor $\overline{\mathrm{H}}$, which is defined as:

$$\overline{\mathrm{H}} = \boldsymbol{M}(\boldsymbol{D})\mathrm{H}\boldsymbol{M}(\boldsymbol{D}) \quad (8.3.4.)$$

where damage effect tensor is calculated as:

$$M = diag\left[\frac{1}{1-D_1} \quad \frac{1}{1-D_2} \quad \frac{1}{1-D_3} \quad \frac{1}{\sqrt{(1-D_2)(1-D_3)}} \quad \frac{1}{\sqrt{(1-D_3)(1-D_1)}} \quad \frac{1}{\sqrt{(1-D_1)(1-D_2)}}\right] \quad (8.3.5.)$$

and hence the effective plastic characteristic tensor $\overline{\mathrm{H}}$ can be determined as:

$$\overline{\mathrm{H}} = \begin{bmatrix} \frac{G+H}{(1-D_1)^2} & \frac{-H}{(1-D_1)(1-D_2)} & \frac{-G}{(1-D_1)(1-D_3)} & 0 & 0 & 0 \\ \frac{-H}{(1-D_1)(1-D_2)} & \frac{H+F}{(1-D_2)^2} & \frac{-F}{(1-D_2)(1-D_3)} & 0 & 0 & 0 \\ \frac{-G}{(1-D_1)(1-D_3)} & \frac{-F}{(1-D_2)(1-D_3)} & \frac{F+G}{(1-D_3)^2} & 0 & 0 & 0 \\ 0 & 0 & 0 & \frac{2N}{(1-D_2)(1-D_3)} & 0 & 0 \\ 0 & 0 & 0 & 0 & \frac{2L}{(1-D_3)(1-D_1)} & 0 \\ 0 & 0 & 0 & 0 & 0 & \frac{2M}{(1-D_1)(1-D_2)} \end{bmatrix} \quad (8.3.6.)$$

The yield stress is updated using mechanical threshold stress model:

$$\sigma_Y = R(\hat{\varepsilon}_p) = \frac{\mu(T)}{\mu_0}\left(\left(1-\left[\frac{kT\ln\left(\dot{\hat{\varepsilon}}_{p0}/\dot{\hat{\varepsilon}}_p\right)}{\mu(T)b^3 g_0}\right]^{1/q}\right)^{1/p}\int\theta\left(\frac{\tanh\left[\alpha\frac{\hat{\sigma}_\varepsilon}{\hat{\sigma}_{es}(\dot{\varepsilon},T)}\right]}{\tanh(\alpha)}\right)d\hat{\varepsilon}_p\right) \quad (8.3.7.)$$

where $\hat{\varepsilon}_p$ is equivalent plastic strain, which was calculated during previous time step at the end of the routine.

The final step in initialisation phase of the subroutine consists of passing the stress and strain tensor to new variables.

Using the stress tensor components from the previous time step the old equivalent stress is calculated as:

$$\bar{\sigma}_F = \left[\frac{1}{2} \boldsymbol{\sigma}^T \bar{\mathrm{H}} \boldsymbol{\sigma} \right]^{1/2} \tag{8.3.8.}$$

Two obtained values for the flow stress and equivalent stress are compared and the largest value is stored to be used further in the routine.

The next section in the routine consists of the calculation of the stress and plastic strain increments together with the calculation of the history variables that have to be known in the next time step.

Firstly an elastic trail stress is calculated as follows:

$$\boldsymbol{\sigma}^{trail} = \boldsymbol{\sigma}^{tn} + \bar{\boldsymbol{C}}_e \Delta \boldsymbol{\varepsilon} \tag{8.3.9.}$$

The equivalent trial stress is then calculated and the elastic fraction of the stress increment is calculated. If the new equivalent stress, based on the old constitutive matrix $\bar{\boldsymbol{C}}_e$, is less then the current yield stress, then this means that increment was completely elastic and hence that constitutive matrix that was used was correct. In this case algorithm moves straight to the later part of the routine in which the new strains and equivalent plastic strain are calculated. If the equivalent stress is larger then the current yield stress however then a correction is necessary because the stress increment was not completely inside of yield surface. Corrections to the constitutive matrix will be necessary. The first step in this process is to determine which part of the stress increment was elastic. The elastic part of the trial stress is calculated as a fraction of the trail stress:

$$\boldsymbol{m} = \frac{\boldsymbol{\sigma}_Y - \bar{\boldsymbol{\sigma}}_F^{t_n}}{\bar{\boldsymbol{\sigma}}_F^{trail} - \bar{\boldsymbol{\sigma}}_F^{t_n}} \tag{8.3.10.}$$

if $\boldsymbol{\sigma}_Y = \bar{\boldsymbol{\sigma}}_F^{t_n}$ then the stress increment is fully plastic, and using *m* ratio, the stress is updated with elastic part as:

$$\boldsymbol{\sigma}^{t_{n+1},TEMP} = \boldsymbol{\sigma}^{t_n} + \boldsymbol{m} \bar{\boldsymbol{C}}_e \Delta \boldsymbol{\varepsilon} \tag{8.3.11.}$$

If the value obtained for m does not lie between 0 and 1 then *m* is set 0 or 1 respectively. The plastic part fraction of the stress increment is simply 1-*m*.

The following step is calculation of the plastic stress increment with the correct constitutive matrix. In order to do this elastoplastic constitutive matrix has to be calculated:

$$\overline{\boldsymbol{C}}_{ep} = \overline{\boldsymbol{C}}_e - \overline{\boldsymbol{C}}_e \frac{\partial \boldsymbol{F}_p}{\partial \boldsymbol{\sigma}} \{\boldsymbol{C}_{\lambda}\}^T \tag{8.3.12.}$$

or

$$\overline{\boldsymbol{C}}_{ep} = \overline{\boldsymbol{C}}_e - \overline{\boldsymbol{C}}_e \frac{\partial \boldsymbol{F}_p}{\partial \boldsymbol{\sigma}} \frac{\dfrac{\partial \boldsymbol{F}_p}{\partial \boldsymbol{\sigma}} \overline{\boldsymbol{C}}_e}{\dfrac{\partial \boldsymbol{F}_p}{\partial \boldsymbol{\sigma}} \overline{\boldsymbol{C}}_e \dfrac{\partial \boldsymbol{F}_p}{\partial \boldsymbol{\sigma}} - \dfrac{\boldsymbol{dR}}{\boldsymbol{d\alpha}}} \tag{8.3.13.}$$

Using above values for the elastoplastic constitutive matrix, the new stress can be calculated as:

$$\boldsymbol{\sigma}^{t_{n+1}} = \boldsymbol{\sigma}^{t_n} + \boldsymbol{m}\boldsymbol{C}_e \Delta\boldsymbol{\varepsilon} + (1-\boldsymbol{m})\boldsymbol{C}_{ep} \Delta\boldsymbol{\varepsilon} \tag{8.3.14.}$$

or

$$\boldsymbol{\sigma}^{t_{n+1}} = \boldsymbol{\sigma}^{t_{n+1},TEMP} + (1-\boldsymbol{m})\left(\overline{\boldsymbol{C}}_e - \overline{\boldsymbol{C}}_e \frac{\partial \boldsymbol{F}_p}{\partial \boldsymbol{\sigma}} \{\boldsymbol{C}_{\lambda}\}^T \right) \Delta\boldsymbol{\varepsilon} \tag{8.3.15.}$$

This expression is used when points make elastic-to-plastic transition and do not necessarily lie on the yield surface. For the purely plastic loading step (m=0) it is obtained:

$$\boldsymbol{\sigma}^{t_{n+1}} = \boldsymbol{\sigma}^{t_n} + \left(\boldsymbol{C}_e - \boldsymbol{C}_e \frac{\partial \boldsymbol{F}_p}{\partial \boldsymbol{\sigma}} \{\boldsymbol{C}_{\lambda}\}^t \right) \Delta\boldsymbol{\varepsilon} = \boldsymbol{\sigma}^{t_n} + \boldsymbol{C}_{ep} \Delta\boldsymbol{\varepsilon} \tag{8.3.16.}$$

Next step is the calculation of the plastic strains and the equivalent plastic strain, where plastic strain is calculated as follows:

$$\boldsymbol{d\varepsilon}_p = \frac{\overline{\mathrm{H}}\boldsymbol{\sigma}}{2\overline{\boldsymbol{\sigma}}_F} \boldsymbol{d\lambda}_p = \frac{\overline{\mathrm{H}}\boldsymbol{\sigma}}{2\overline{\boldsymbol{\sigma}}_F} \boldsymbol{d\hat{\varepsilon}}_p \tag{8.3.17.}$$

because

$$\boldsymbol{d\hat{\varepsilon}}_p = \frac{\overline{\boldsymbol{\sigma}}_F - \boldsymbol{\sigma}_Y}{\Pi} \tag{8.3.18.}$$

one can write:

$$\boldsymbol{d\varepsilon}_p = \frac{\overline{\mathrm{H}}\boldsymbol{\sigma}}{2\overline{\boldsymbol{\sigma}}_F} \frac{\overline{\boldsymbol{\sigma}}_F - \boldsymbol{\sigma}_Y}{\Pi} \tag{8.3.19.}$$

The effective plastic strain is updated by using the plastic stress increment and plastic modulus:

$$\hat{\boldsymbol{\varepsilon}}_p^{t_{n+1}} = \hat{\boldsymbol{\varepsilon}}_p^{t_n} + \frac{\overline{\boldsymbol{\sigma}}_F - \boldsymbol{\sigma}_Y}{\Pi} \tag{8.3.20.}$$

Numerical procedure presented so far could be categorized as elastic predictor/plastic return corrector. Once the plastic consistency condition is enforced the state variables at the end of the plastic corrector phase become:

$$\left\{ \boldsymbol{\sigma}^{t_{n+1}}, \boldsymbol{\varepsilon}^{t_{n+1}}, \boldsymbol{D}^{t_n}, \boldsymbol{R}^{t_{n+1}} \right\} \tag{8.3.21.}$$

To complete the algorithm, it remains to develop an process consistent with damage evolution that operates on initial conditions (Eq. 8.3.21.) to produce final state:

$$\left\{ \boldsymbol{\sigma}^{t_{n+1}}, \boldsymbol{\varepsilon}^{t_{n+1}}, \boldsymbol{D}^{t_{n+1}}, \boldsymbol{R}^{t_{n+1}} \right\} \tag{8.3.22.}$$

Although plasticity and damage are coupled in rate equations, the algorithmic treatment uncouples plasticity and damage, because as soon as the plasticity is corrected, all the damage variables are fixed. Hence proposed numerical procedure proceeds along two following steps [118].

Checking of damage loading consists of determination of damage energy release rate:

$$\boldsymbol{Y} = -\boldsymbol{\sigma}^{T} \boldsymbol{M} \boldsymbol{C}_{e}^{-1} \frac{\partial \boldsymbol{M}}{\partial \boldsymbol{D}} \boldsymbol{\sigma} \tag{8.3.23.}$$

which is used for calculation of equivalent damage energy release rate:

$$\boldsymbol{Y}_{eq} = \left[\frac{1}{2} \boldsymbol{Y}^{T} \boldsymbol{J} \boldsymbol{Y} \right]^{1/2} \tag{8.3.24.}$$

and increment in damage hardening is determined utilizing linear damage hardening rule:

$$\boldsymbol{B}(\boldsymbol{\beta}) = \boldsymbol{B}(\hat{\boldsymbol{D}}) = \mathcal{D}\ \hat{\boldsymbol{D}} \tag{8.3.25.}$$

where equivalent or accumulated overall damage $\hat{\boldsymbol{D}}$ is represented as:

$$\hat{\boldsymbol{D}}(\hat{\boldsymbol{\varepsilon}}_{p}) = \frac{\hat{\boldsymbol{\varepsilon}}_{pc}}{\hat{\boldsymbol{\varepsilon}}_{pc0}} \frac{1}{\left(\left(\dfrac{\boldsymbol{\mu}(\boldsymbol{T}) \boldsymbol{b}^{3} \boldsymbol{u}_{0}}{\boldsymbol{kT}} \right) + 1 \right)} \left(\frac{\boldsymbol{\sigma}_{m} / \boldsymbol{\mu}(\boldsymbol{T})}{\boldsymbol{\sigma}_{0} / \boldsymbol{\mu}_{0}} \right)^{\left(\frac{\boldsymbol{\mu}(\boldsymbol{T}) \boldsymbol{b}^{3} \boldsymbol{u}_{0}}{\boldsymbol{kT}} \right)} \tag{8.3.26.}$$

At the end of this step damage loading condition is checked:

$$\boldsymbol{Y}_{eq} \leq [\boldsymbol{B}(\boldsymbol{\beta}) + \boldsymbol{B}_{0}] \tag{8.3.27.}$$

In case that above condition is satisfied algorithm moves straight to the end of the routine. If, on another hand, damage loading condition is violated then damage loading is taking place and correction is necessary and algorithm moves to the next step. Hence damage return mapping is applied leading to calculation of damage multiplier $\dot{\lambda}_d$:

$$\dot{\lambda}_d = \frac{\partial \boldsymbol{F}_d}{\partial \boldsymbol{Y}} \dot{\boldsymbol{Y}} / \mathcal{D} \tag{8.3.28.}$$

which is used for update of damage:

$$\dot{\boldsymbol{D}} = -\frac{\boldsymbol{J}\boldsymbol{Y}}{2\boldsymbol{Y}_{eq}} \dot{\lambda}_d \tag{8.3.29.}$$

This concludes elastic predictor/plastic return corrector/damage return mapping algorithm and finally at the end of routine, the rotation of the stresses and strains back to the global axes is applied.

8.4. Numerical results and conclusions

A novel constitutive anisotropic elastoplastic-damage model was developed within the general framework of continuum thermodynamics for irreversible processes by identifying a proper set of internal variables together with their conjugate generalized forces.

The proposed framework is capable of accommodating: general nonlinear elastoplastic response, coupling of damage and plasticity, temperature and strain rate dependant isotropic strain hardening, and linear damage hardening with temperature dependant initial damage threshold. Anisotropic damage evolution law was developed by adopting the damage surface concept. The material anisotropy is considered for elastic, plastic and damage response. In the elastic regime anisotropy was introduced by the appropriate elastic constants in the elastic compliance matrix. Anisotropic plasticity was achieved by utilising Hill's yield function, and in the damage regime, by introducing a damage characteristic tensor $\boldsymbol{J}$ in the damage evolution law, which can be conveniently determined by equivalence of damage work. Plastic evolution law and damage evolution law were derived by utilisation of the damage tensor $\boldsymbol{D}$, the damage effect tensor $\boldsymbol{M}(\boldsymbol{D})$, the damage characteristic tensor $\boldsymbol{J}$, and the effective plastic characteristic tensor $\overline{\mathrm{H}}$.

The new material model has been implemented in DYNA3D, using for this purpose developed elastic predictor/plastic corrector/damage mapping, integration algorithm. Numerical simulations of Taylor impact cylinder test for AA7010, have been carried out to validate implemented model and simulation results are given to illustrate the potential applicability of the proposed model (Fig. 8.4.1. and Fig. 8.4.2.). Good agreement with experimental results was obtained. Comparison of numerical results for purely isotropic models like as Johnson-Cook (Chapter 4), Mechanical Threshold Stress (Chapter 4) and anisotropic elastoplastic model (Chapter 5), with

proposed anisotropic elastoplastic-damage model illustrates significant differences in material response. It could be concluded following: proposed model is capable to capture more accurately major and minor distributions of plastic strains, and furthermore, developed model can describe evolution of damage adequately.

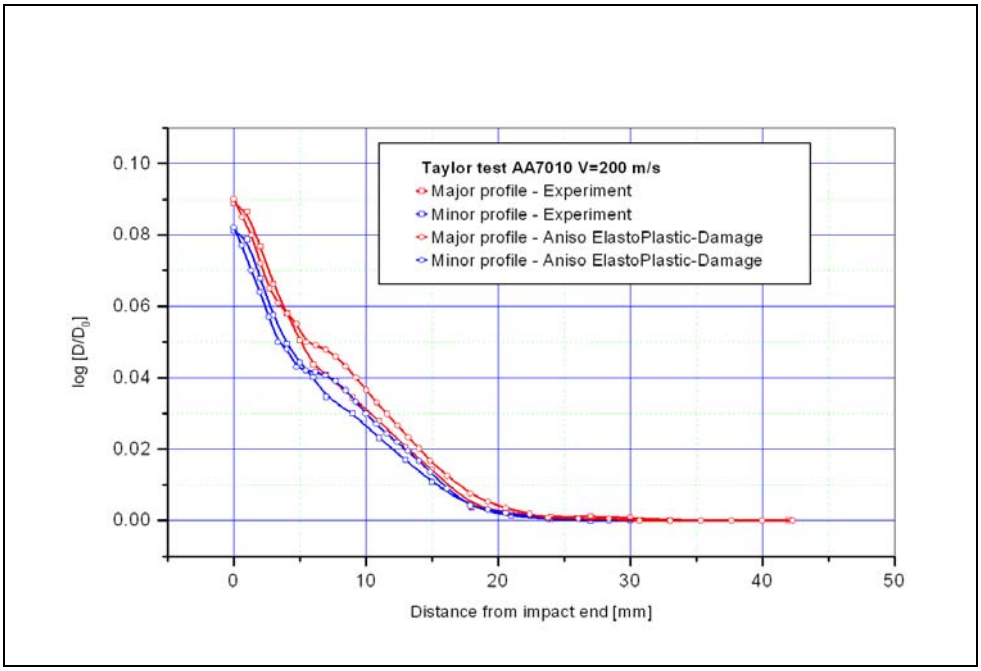

Fig. 8.4.1. Comparison of experimental and simulation results for major and minor distributions of plastic strains of Taylor cylinder test impacted at 200 m/s

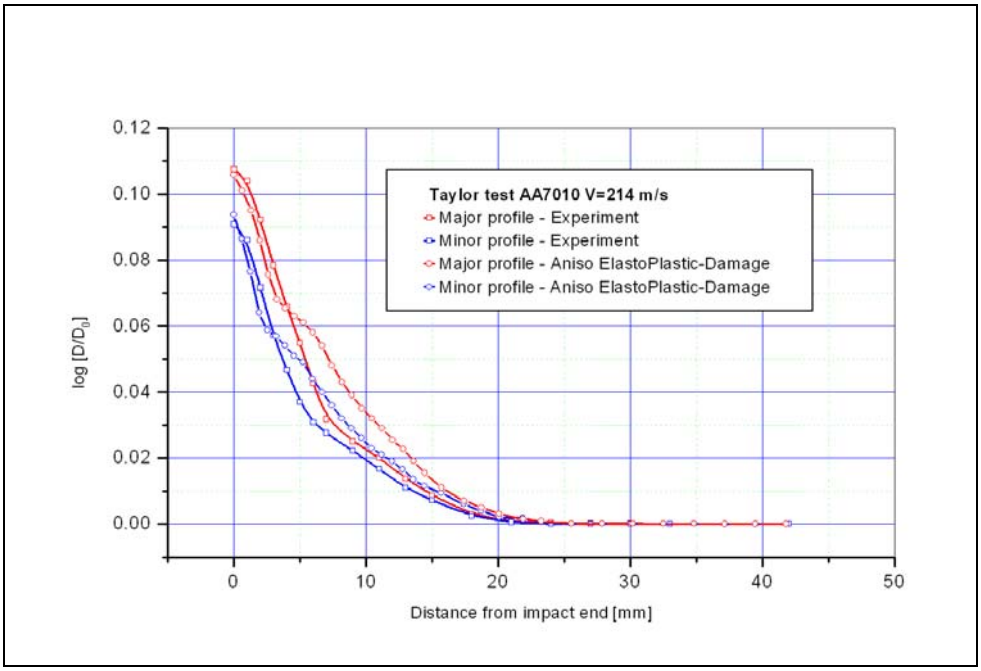

Fig. 8.4.2. Comparison of experimental and simulation results for major and minor distributions of plastic strains of Taylor cylinder test impacted at 214 m/s

9. CONCLUSIONS

The main objective of this thesis was development of tools for modelling of strain rate and temperature dependant behaviour of aluminium alloys, typical for aerospace structures with pronounced orthotropic properties, and the implementation of the tools in computer codes. A constitutive model with an orthotropic yield criterion, damage growth and failure mechanism has been developed and implemented into DYNA3D. Another important aspect of this work was development of relatively simple experimental methods for characterization of engineering materials, and the extensive experimental work that has been undertaken.

The principal work and conclusions of the thesis are:

An iterative material model development approach has been applied. Initially the new material model has been designed as a temperature and strain rate dependant strength model in a simple isotopic form, and subsequently the complexity of the model has been increased through further iterations, applying coupling of isotropic stain hardening model with orthotropic yield criterion, then including damage evolution and failure criteria.

Several Taylor impact cylinder tests at different impact velocities have been carried out for AA7010 aluminium alloy using gas gun. Geometric profile data for deformed specimens were measured using a 3D scanning machine. Following data have been generated: digitised side profiles for minor and major direction, and digitised footprints that give cross-sectional area at the impact interface.

Tensile tests were used for the characterisation of two aluminium alloys AA2024 and AA7010, at five different levels of the strain rates in the intermediate regime up to $10x10^0$ 1/s, at five different temperatures, and for three different orientations of materials. Due to the limitations of measurement equipment, measurements of only longitudinal strains have been taken.

Another set of tensile tests has been carried out, at higher strain rate regime $10x10^2$ 1/s, and at ambient temperature. Contact-less optical strain rate measurement technique allowed simultaneous measurement of both longitudinal and transverse strain during tensile tests.

Procedures for derivation of parameters for temperature and strain rate dependant strength models: Johnson-Cook (JC), Zerrili-Armstrong (ZA) and Mechanical Threshold Model (MTS), were developed and parameters for JC and MTS constitutive relations were derived on the basis of uniaxial tensile tests at intermediate strain rate. In order to validate derived parameters for constitutive relations for JC and MTS Taylor impact test simulation has been done, and compared with experimental results in terms of cylinder footprints at the impact interface.

As an alternative to the standard tensile specimen geometry, in this work a non-standard specimen geometry was proposed, because one of the requirements for tensile test was achieving of intermediate strain rate conditions, using standard servo hydraulic fatigue machine.

Based on the hypothesis that strain rate and temperature are interchangeable, low temperature tensile tests at intermediate strain rate regime, have been carried out. Those tensile test results have been used for calibration of MTS constitutive relation. Afterwards the MTS constitutive model has been used to predict the stress-strain response of material at high strain of rate, and good agreement has been observed. In that way hypothesis of interchangeability of strain rate and temperature has been validated.

A method for calibration of orthotropic yield criterion has been developed and parameters have been identified for the Hill's orthotropic model under the associated flow rule assumption. Tensile tests at intermediate strain rate regime, in three different material directions, have been used for model calibration, together with cylinder impact tests, which was used for derivation of Lankford coefficient.

Simultaneous measurement of longitudinal and transverse strain of tensile specimen during tensile tests at higher strain rate regime, allowed direct measurement of Lankford coefficient, and hence validation of proposed calibration method of orthotropic model.

It has been shown that the anisotropic behaviour of the aluminium alloy AA7010 can be correctly described by Hill criteria in combination with a sound parameter estimation procedure. Numerical simulations of Taylor test experiments have been done, and results from the simulations of the cylinder impact test: major and minor side profiles, and impact-interface footprints have been compared with test data. Simple assumption of isotropic hardening has been proven to be sufficient to obtain good agreement between experimental and numerical simulation data.

To account for the physical mechanisms of failure, the concept of thermal activation of damage and failure has been adopted as a basis for this material model development. This basic assumption makes the proposed approach compatible with the Mechanical Threshold Stress model, which was used as the strength part of the proposed constitutive model in this development iteration. A method for calibration of damage model has been proposed based on the plate impact tests. In order to validate the model, a series of FE simulations of plate impact experiments were performed for OFHC Cu and microscopic observations of the softly recovered spalled specimen have been carried out. It has been proven that the proposed model is able to reproduce typical longitudinal stress reloading observed in plate impact tests, which is caused by the creation of the internal free surface. Plate impact tests used for model validation were performed on a single-stage gas gun, and longitudinal stresses were measured with stress gauges.

Another validation, using cylinder impact test for AA7010, of the proposed criterion for tensile failure was performed, were damage fields generated in Taylor specimen have been simulated and analysed.

In the final phase, the complexity of the model has been further increased through coupling of hardening model with orthotropic yield criterion including damage evolution and failure criteria. The constitutive model was developed within the general framework of continuum thermodynamics for irreversible processes. Method

for derivation of damage parameters have been developed utilizing simple uniaxial tensile test, and good correlation with parameters, which have been determined using plate impact tests, has been found.

Developed model has been implemented in DYNA3D, using proposed elastic predictor/plastic corrector/damage mapping, integration algorithm. Numerical simulations of Taylor impact cylinder, have been carried out to validate implemented model and good agreement with experimental results was obtained.

Further work can improve capability of developed material model in several areas:

Further implementation of developed model into DYNA3D, could extend usability of material model to the other elements, like as shells and beams, and in that way it could enable applicability of the simulation toll to analyse complex engineering structures, which are dynamically loaded and subjected to the different levels of temperatures and strain rates.

A modification of the Hill's yield criterion, which allows combined isotropic-kinematic strain hardening, could be integrated into proposed material model, using demonstrated framework of continuum thermodynamics for irreversible processes. This would allow applicability of the material model to other engineering materials that exhibit kinematic strain hardening behaviour.

Similarly a kinematic type damage hardening could be introduced into material model, and instead of linear damage evolution law, nonlinear damage hardening could be considered, in order to extend applicability of anisotropic elastoplastic-damage material model to other class of engineering materials.

Accuracy of the stress update algorithm could be improved by implementing fully coupled integration scheme, i.e. elastic predictor / coupled plastic-damage corrector integration algorithm.

Coupling between plasticity and damage could be improved by using separate plasticity and damage surfaces with separate non-associated flow rules in such way that both plasticity and damage flow rules are dependent on both the plastic and damage potentials.

10. REFERENCES

[**1**] V. Panov, “1.0.1. Progress Report on Orthotropic Material Model Development”, Cranfield University, Cranfield, 2003.
[**2**] V. Panov, “1.0.2. Progress Report on Orthotropic Material Model Development”, Cranfield University, Cranfield, 2004.
[**3**] V. Panov, “1.0.3. Progress Report on Orthotropic Material Model Development”, Cranfield University, Cranfield, 2004.
[**4**] V. Panov, “1.0.4. Progress Report on Orthotropic Material Model Development”, Cranfield University, Cranfield, 2004.
[**5**] V. Panov, “2.1.0. Progress Report on Orthotropic Material Model Development”, Cranfield University, Cranfield, 2005.
[**6**] V. Panov, “2.2.0. Progress Report on Orthotropic Material Model Development”, Cranfield University, Cranfield, 2005.
[**7**] V. Panov, “3.1.0. Progress Report on Orthotropic Material Model Development”, Cranfield University, Cranfield, 2006.
[**8**] V. Panov, R. Vignjevic, N. Bourne, J. Millet, “Material failure modelling in Metals at High Strain Rates”, AIP Conference Proceedings SCCM05, 2006, Vol. 845, pp. 646-649.
[**9**] H. E. Davis, G. E. Troxell. G. F. W. Hauck, “The testing of engineering materials”, New York, McGraw-Hill, 1982.
[**10**] V. John, “Testing of materials”, Houndmills, Macmillan Education LTD, 1992.
[**11**] R. D. Lohr, M. Steen, “Ultra high temperature mechanical testing”, Cambridge: Woodhead Publishing, 1995.
[**12**] J. E. Field, S. M. Walley, N. K. Bourne and J. M. Huntley, “Experimental methods at high rates of strain”, Journal de Physique IV, Colloque C8 supplement au Journal de Physique III, Vol. 4, 1994, C8 3 – 22.
[**13**] G. T. Gray III, “High-Strain-Rate of Materials: The Split-Hopkinson Pressure Bar”, in Methods in Materials Research, eds., John Wiley Press, 2000.
[**14**] Lin J. I., “DYNA3D User Manual”, Methods Development Group Mechanical Engineering, 1998.
[**15**] A. M. S. Hamouda and M. S. J. Hashmi, “Modelling the impact and penetration events of modern engineering materials: Characteristics of computer codes and material models”, Journal of Materials Processing Technology, Vol. 56, 1996, pp. 847-862.
[**16**] MIL-HDBK-5H, “Metallic Materials and Elements for Aerospace Vehicle Structures” , Department of Defense Handbook, U.K., 1998.
[**17**] M. S. Binning and P. G. Partridge, “Subzero tensile properties of 7010 aluminium alloy and Ti-6A1-4V and IMI550 titanium alloys in sheet form”, Cryogenics, Vol. 24, No. 2, 1984, pp. 97-105.
[**18**] D. R. Kumar amd K. Swaminathan, “Tensile deformation behaviour of two aluminium alloys at elevated temperatures”, Materials at High Temperatures, Vol. 16, No. 4, 1999, pp. 161-172.
[19] D. Liu, H. V. Atkinson, P. Kapranos, W. Jirattiticharoean, H. Jones, “Microstructural evolution and tensile mechanical properties of thixoformed high performance aluminium alloys”, Material Science and Engineering A361, 2003, pp. 213-224.
[**20**] G. H. Strijbos, W. H. Kool, “Superplastic behaviour of rapidly solidified 7475 aluminium alloy”, Materials Science and Engineering, Vol. A194, 1995, pp. 129-136.

[**21**] J. H. Kim, S. L. Semiatin, C. S. Lee, "Constitutive analysis of the high-temperature deformation of Ti-6Al-4V with a transformed microstructure", Acta Materialia, Vol. 51, 2003, pp. 5616-5626.
[**22**] K. A. Lee, C. S. Lee, "The effect of strain rate on the anomalous peak of yield stress in β-CuZn alloy", Scripta Materialia, Vol. 39, No. 9, 1998, pp. 1289-1294.
[**23**] F. D. Torre, H. V. Swygenhoven, M. Victoria, "Nanocrystalline electrodeposited Ni: microstruture and tensile properties", Acta Materialia, Vol. 50, 2001, pp. 3957-3970.
[**24**] P. J. Maudlin, J. F. Bingert, J. W. House, S. R. Chen, "On the modelling of the Taylor cylinder impact test for orthotropic textured materials, experiments and simulations", International Journal of Plasticity, Vol. 15, 1999, pp. 139-166.
[**25**] P. J. Maudlin, J. F. Bingert, G. T. Gray III, "Low-symmetry plastic deformation in BCC tantalum: experimental observation, modelling and simulations", International Journal of Plasticity, Vol. 19, 2003, pp. 483-515.
[**26**] P. J. Maudlin, J. C. Foster, JR, S. E. Jones, "A continuum mechanics code analysis of steady plastic wave propagation in the Taylor test", Int. J. Impact Engng., Vol. 19, No. 3, 1997, pp. 231-256.
[**27**] W. K. Rule, "A numerical scheme for extracting strength model coefficients from Taylor test data", Int. J. Impact Engng., Vol. 19, Nos. 9-10, 1997, pp. 797-810.
[**28**] V. R. Ikkurthi, S. Chaturvedi, "Use of different damage models for simulating impact-driven spallation in metals", International Journal of Impact Engineering, Article in Press.
[**29**] A. M. Rajendran, "Critical measurements for validation of constitutive equations under shock and impact loading conditions", Optics and Laser in Engineering, Vol 40, 2003, pp. 249-262.
[**30**] I. Rohr, H. Nahme, K. Thoma, "Material characterization and constitutive modelling of ductile high strength steel for a wide range of strain rates", International Journal of Impact Engineering Vol. 31, 2005, pp. 401-433.
[**31**] L. Kruger, L.W. Meyeer, S. V. Razorenov, G. I. Kanel, "Investigation of dynamic flow and strength properties of Ti-6-22-22S at normal and elevated temperatures", International Journal of Impact Engineering, Vol. 28, 2003, pp. 877-890.
[**32**] J. Zheng, Z. P. Wang, "Spall damage in aluminium alloy", Int. J. Solids Structures, Vol. 32, No. 8/9, 1995, pp. 1135-1148.
[**33**] J. N. Johnson, G. T. Gray III, N. K. Bourne, "Effect of pulse duration and strain rate on incipient spall fracture in coper", Journal of Applied Physics, Vol. 86, No. 9, 1999, pp. 4892 – 4901.
[**34**] R. Vignjevic, N. K. Bourne, J. C. F. Millett, T. De Vuyst, "Effects of orientation on the strength of the aluminium alloy 7010-T6 during shock loading: Experiment and simulation", Journal of Applied Physics, Vol. 92, No. 8, 2002, pp. 4342-4348.
[**35**] Jonas A. Zukas, "Impact Dynamics", New York: Wiely-Interscience, 1982.
[**36**] Jonas A. Zukas, "High Velocity Impact Dynamics", New York: Wiely-Interscience, 1990.
[**37**] Marc A. Meyers, "Dynamic Behavior of Materials", New York: Wiely-Interscience, 1994.
[**38**] M. A. Meyers, R. W. Armstrong, H. O. K. Kirchner, "Mechanics and Materials", New York: Wiely-Interscience, 1999.
[**39**] T. Z. Blazynski, "Materials at High Strain Rates", New York: Elsevier Applied Science, 1987.

[**40**] L. E. Malvern, "Introduction to the Mechanics of a Continuous Medium", Prentice-Hall Inc., 1969.
[**41**] G.R. Johnson, J.M. Hoegfeldt, U.S. Lindholm, and A. Nagy, "Response of various metals to large torsional strains over a large range of strain rates – Part1: Ductile metals", ASME J. Eng. Mater. Tech., Vol. 105 , 1983. pp. 42-47.
[**42**] G.R. Johnson, J.M. Hoegfeldt, U.S. Lindholm, and A. Nagy, "Response of various metals to large torsional strains over a large range of strain rates – Part2: Less ductile metals", ASME J. Eng. Mater. Tech., Vol. 105, 1983. pp. 48-53.
[**43**] G.R. Johnson and W.H. Cook, "A constitutive model and data for metals subjected to large strains, high strain rates and high temperatures", Proceedings of the seventh international symposium on ballistic, The Hague, The Netherlands, 1983, pp. 541-547.
[**44**] T.J. Holmquist, G.R. Johnson, "Determination of constants and comparison of results for various constitutive models", Journal de Physique IV, Colloque C3, suppl. au Journal de Physique III, Vol. 1, 1991, pp. C3-853 - C3-860.
[**45**] D. R. Lesuer, "Experimental investigations of material models for Ti-6Al-4V titanium and 2024-T3 aluminium", LLNL report No. DOT/FAA/AR-00/25, 2000.
[**46**] G. R. Johnson, W. H. Cook, "Fracture characteristics of three metals subjected to various strains, strain rates, temperatures and pressures", Engineering Fracture Mechanics, Vol. 21, No. 1, 1985, pp. 31-48.
[**47**] G. R.Johnson, T. J. Holmquist, "Evaluation of cylinder-impact test data for constitutive model constants", J. Appl. Phys., Vol. 64, No. 8, 1988, pp. 3901-3910.
[**48**] F.J. Zerilli, and R.W. Armstrong, "Dislocation-mechanics-based constitutive relations for material dynamics calculations", J. Appl. Phys., Vol. 61, N0.5, 1987, pp. 1816-1825.
[**49**] B.D. Goldthorpe, "Constitutive equations for annealed and explosively shocked iron for application to high strain rates and large strains", Journal de Physique IV, Colloque C3, suppl. au Journal de Physique III, Vol. 1, 1991, pp. C3-829 - C3-835.
[**50**] D. A. S. Macdougall, J. Harding, "A constitutive relation and failure criterion for Ti6Al4V alloy at impact rates of strain", Journal of the Mechanics and Physics of Solids, Vol 47, 1999, pp. 1157-1185.
[**51**] J. P. Noble and J. Harding, "An evalution of constitutive relations for high-rate material behaviour using the tensile Hopkinson-bar", Journal De Physique, Colloque C8, supplement au Journal de Physique II, Vol. 4, 1994, pp. C8 477-482.
[**52**] J. Harding, "The development of constitutive relationships for material behaviour at high rates of strain", Inst. Phys. Conf., Ser. No. 102, Session 5, 1989, pp. 189 – 203.
[**53**] A. S. Khan, R. Liang, "Behaviors of three BCC metal over a wide range of strain rates and temperatures: experiments and modelling", International Journal of Plasticity, Vol. 15, 1999, pp. 1089-1109.
[**54**] R. Liang, A. S. Khan, "A critical review of experimental results and constitutive models for BCC and FCC metals over a wide range of strain rates and temperatures", International Journal of Plasticity, Vol. 15, 1999, pp. 963-980.
[**55**] U.F. Kocks, A.S. Argon, and M.F. Ashby, "Thermodynamics and Kinetics of Slip", Prog. Mater. Sci., Vol. 19, Pergamon Press, New York, 1975.
[**56**] Y.P. Varshni, "Temperature Dependence of the Elastic Constants", Phys. Rev. B, Vol. 2, 1970, pp. 3952-3958.
[**57**] W. H. Gourdin, D.H. Lassila, "Flow stress of OFE copper at strain rates from 10^{-3} to $10^{4}\,s^{-1}$: Grain-size effects and comparison to the mechanical threshold stress model", Acta Metallurgica et Materialia, Vol. 39, 1991, pp. 2337-2348.

[**58**] C.W.MacGregor and J.C.Fisher, "A velocity-modified temperature for the plastic flow of metals", J.Appl. Mech., Vol. 68, 1946, pp. A11-A16.
[**59**] P.S. Follansbee, U.F. Kocks, "A constitutive description of the deformation of copper based on the use of the mechanical threshold stress as internal state variable", Acta Metallurgica, Vol. 36, 1988, pp. 81-93.
[**60**] U.F.Kocks, "Laws for Work-Hardening and Low-Temperature Creep", J. Eng. Mater. Tech., Trans. ASME, Vol. 98, 1976, pp. 76-85.
[**61**] P.S. Follansbee, U.F. Kocks and G. Regazzoni, "The mechanical threshold of dynamically deformed copper and nitronic 40", Journal-de-physique-colloque, Vol. 46, No. c-5, 1985, pp. 25-34.
[**62**] P. S. Follansbee, "High-Strain-Rate Deformation of FCC Metals amd Alloys", Conference Proceedings "Metallurgical Applications of Shok-wave and High-Strain-Rate Phenomena", edited by Murr, Staudhammer, Meyers, 1986, pp. 451-477.
[**63**] G. Regazzoni, U. F. Kocks and P.S. Follansbee, "Dislocation kinetics at high strain rates", Acta metal, Vol. 35, No. 12, 1987, pp. 2865-2875.
[**64**] P. S. follamsbee, G. Regazzoni and U. F. Kocks, "The transition to drag-controlled deformation in copper at high strain rates", Inst. Phys. Conf., Ser. No. 70, 1984, pp. 71-80.
[**65**] K. Raznjevc, "Handbook of thermodynamics table and chart", New York: McGraw-Hill, 1975.
[**66**] S.R. Chen and G.T. Gray, III, "Constitutive Behaviour of Tantalum and Tantalum-Tungsten Alloys", Metallurgical and Materials Transactions A, 27A, 1996, pp. 2994-3006.
[**67**] S. R. Chen, G. T. Gray III, "Constitutive Behaviour of Tungsten and Tantalum: Experiments and Modelling", 2nd Intenational Conference on Tungsten and Refractory Metals, 1995, pp. 489-498.
[**68**] D.M. Goto, J. Bingert, S.R. Chen, G.T. Gray, III and R.K. Garrett, Jr., "The Mechanical Threshold Stress Constitutive Strength Model Description of HY-100 Steel", Metallurgical and Materials Transactions A, 31(#8), 2000, pp. 1985-1996.
[**69**] S.R. Chen, P.J. Maudlin and G.T. Gray, III, "Mechanical properties and constitutive relations for molybdenum under high rate deformation", Molybdenum and Molybdenum Alloys, 1998, pp. 155-172, edited by A. Crowson, E.S. Chen, J.A. Shields and P.R. Subramanian (The Minerals, Metals and Materials Society, Warrenddale, PA).
[**70**] G.T. Gray, III, S.R. Chen and K.S. Vecchio, "Influence of grain size on the constitutive response and substructure evolution of monel 400", Metallurgical and Materials Transactions A, Vol. 30A, 1999, pp. 1235-1247.
[**71**] S. R. Chen, P. J. Maudlin, G. T. Gray III, "Constitutive Behavior of Model FCC, BCC, and HCP Metals: Experiments, Modeling and Validation", Constutive and Damage Modelling of Inelastic Deformation and Phase Transformation, 1998, edited by A.S. Khan, Neat Press, Maryland, USA, pp. 623-626.
[**72**] N. Tsuchida, Y. Tomota, H. Moriya, O. Umezawa and K. Nagai, "Application of the Kocks-Mecking model to tensile daformation of an austentic 25Cr-19Ni stell", Acta mater, 49, 2001, pp. 3029-3038.
[**73**] D. M. Goto, J.F. Bingert, W. R. Reed and R. K. Garrett Jr., "Anisotrop-corected MTS constitutive strength modelling in HY-100 steel", Script mater., 42, 2000, pp. 1125-1131.
[**74**] L. Daridon, O. Oussouaddi, S. Ahzi, "Influence of the material constitutive models on the adiabatic shear band spacing: MTS, power law and Johnson-Cook models", International Journal ofSolids and Structures, 41, 2001, pp. 3109-3124.

[**75**] D. J. Steinberg, “Equation of state and strength properties of selected materials”, Lawrence Livermore National Laboratory, UCRL-MA-106439, 1991.
[**76**] Hill R., “The mathematical Theory of Plasticity”, Oxford University Press, 1950.
[**77**] W. Johnson, P. B. Mellor, “Engineering Plasticity”, Ellis Horwood Limited, 1983
[**78**] A. S. Khan, S. Huang, “Continuum Theory of Plasticity”, John Wiley & Sons, 1995.
[**79**] L. J. Klingler, G. Sachs, “Plastic Flow Characteristics of Aluminium-Alloy Plate”, Journal of the Aeronautical Sciences, 15, 1948, pp. 599-604.
[**80**] W. Szczepinski, J. Miastkowski, “An Experimental study of the effect of the prestraining history on the yield surfaces of an aluminium alloy”, J. Mech. Phys. Solids, 16, 1968, pp. 153 - 162.
[**81**] T. Naka, Y. Nakayama, T. Uemori, R. Hino, F. Yoshida, “Effects of temperature on yield locus for 5083 aluminium alloy sheet”, Journal of Materials Processing Technology, 140, 2003, pp. 494-499.
[**82**] Han-Chin Wu, “Anisotropic plasticity for sheet metals using the concept of combined isotropic-kinematic hardening”, International Journal of Plasticity 18, 2002, pp. 1661-1682.
[**83**] D. Banabic, T. Kuwabara, T. Balan, D. S. Comsa, D. Julean, “Non-quadratic yield criterion for orthotropic sheet metals under plane-stress conditions”, Intenational Journal of Mechanical Sciences, 45, 2003, pp. 797-811.
[**84**] O. Cazacu, F. Barlat, “Application of the theory of representation to describe yielding of anisptropic aluminium alloys”, International Journal of Engineering Science, 41, 2003, pp. 1367-1385.
[**85**] A. Khalfallah, H. B. Hadj Salah, A. Dogui, “Anisotropic parameter identification using inhomogeneous tensile test”, European Journal of Mechanics A/Solids, 21, 2002, pp. 927-942.
[**86**] K. A. Malo, O. S. Hopperstad, O. G. Lademo, “Calibration of anisotropic yield criteria using uniaxial tension tests and bending tests”, Journal of Materials Processing Technology, 80-81, 1998, pp. 538-544.
[**87**] O. G. Lademo, O. S. Hopperstad, M. Langseth, “An evaluation of yield criteria and flow rules for aluminium alloys”, International Journal of Plasticity, 15, 1999, pp. 191-208.
[**88**] D. E. Green, K. W. Neale, S.R. MacEwen, A. Makinde, R. Perrin, “Experimental investigation of the biaxial behaviour of an aluminium sheet”, International Journal of Plasticity, 20, 2004, pp. 1677-1706.
[**89**] K. R. Gilmour, A.G. Leacock, M.T. J. Ashbridge, “The influence of plastic strain ratios on the numerical modelling of stretch forming”, Journal of Materials Processing Technology, 152, 2004, pp. 116-125.
[**90**] R. W. Logan, W. F. Hosford, “Upper-Bound Anisotropic Yield Locus Calculations Assuming <111>-Pencil Glide”, Int. J. Mech. Sci., Vol. 22, 1980, pp. 419-430.
[**91**] M. Jansson, L. Nilsson, K. Simonsson, “On constutive modelling of aluminium alloys for tube hydroforming applications”, International Journal of Plasticity, Article in press.
[**92**] I. Ragai, D. Lazim, J. A. Nemes, “Anisotropy of springback in draw-bending of stainless steel 410: experimental and numerical study”, Journal of Materials Processing Technology, Article in press.
[**93**] A. S. Krausz and H. Eyring, “Deformation kinetics”, John Wiley & Sons, 1975.
[**94**] D. Krajcinovic, “Damage mechanics”, Elsevier Science, 1996.

[**95**] G. Maugin, "The Thermomechanics of Plasticity and Fracture", Cambridge Uneversity Press, 1992.
[**96**] F.R. Tuler, B.M. Butcher, "A criterion the time dependence of dynamic fracture", The international Journal of Fracture Mechanics, Vol. 4, No. 4, 1968, pp. 431-437.
[**97**] J.J. Gilman, F.R. Tuler, "Dynamic Fracture by Spallation in Metals", International Journal of Fracture Mechanics, Vol. 6, No. 2, 1970, pp. 169-182.
[**98**] S.N. Zhurkov, "Kinetic concept of the strength of solids", International Journal of Fracture Vol. 1, 1965, pp. 311-323.
[**99**] F. Kozin and J. L. Bogdanoff, "Cumulative damage model for mean fatigue crack growth based on the kinetic theory of thermally activated fracture", Engineering Fracture Mechanics, Vol. 37, No. 5, 1990, pp. 995-1010.
[**100**] A. N. Dremin, A. M. Molodets, "On the spall strength of metals", Proceedings of the international symposium on intense dynamic loading and its effects, Beijing, 1986, pp. 13-22.
[**101**] J.R. Klepaczko, "Dynamic crack initiation, some experimental methods and modelling", In: J.R. Klepaczko, editor, "Crack dynamics in metallic materials", Vienna: Springer-Verlag, 1990, pp. 428 – 445.
[**102**] P. Chevrier, J.R. Klepaczko, "Spall fracture: Mechanical and microstructural aspects", Engineering Fracture Mechanics, 63, 1999, pp. 273-294.
[**103**] P. F. Chevrier, J. R. Klepaczko, "Spalling of aluminium alloy 7020-T6, experimental and theoretical analyses", Proceed. 11th Biennial Eoropean Conference on Fracture, Mechanisms and Mechanics of Damage and Failure, Vol. 1, 1996, pp. 693-698.
[**104**] S. Hanim, J.R. Klapaczko, "Numerical study of spalling in an aluminium alloy 7020-T6", International Journal of Impact Engineering, 22, 1999, pp 649-673.
[**105**] S. Hanim, S. Ahzzi, "A unified approach for pressure and temperature effects in dynamic failure criteria", International Journal of Plasticity, 17, 2001, pp. 1215-1244.
[**106**] S. Bouzid, A. Nyoungue, Z. Azari, N. Bouaoudja, G. Pluvinage, "Fracture criterion for glass under impact loading", International Journal of Impact Engineering, 25, 2001, pp. 831 –845.
[**107**] D.R. Curran, L. Seaman and D. A. Shockey, "Dynamic failure of solids", Physics reports, Vol 147, Nos. 5 & 6, 1987, pp. 253-388.
[**108**] S. Cocchran, D. Banner, "Spall studies in uranium", Journal of Applied Physics, Vol. 48, 1977, pp. 2729-2737.
[**109**] N. R. Hansen, H. L. Schreyer, "A thermodynamically consistent framework for theories of elastoplasticity coupled with damage", Int. J. Solids Structures, Vol. 31, No. 3, 1994, pp. 359 – 389.
[**110**] A. M. Habraken, J. F. Charles, S. Secotto, "Calibration and validation of an anisotropic elasto-plastic damage model for sheet metal forming", Damage Mechancs in Engineering Materials, Editors G. Z. Voyiadjis, J. W. W. Ju and J. L. Chaboche, Elsevier Science, 1998, pp. 401- 420.
[**111**] Y. Y. Zhu, S. Cescotto, "A fully coupled elasto-visco-plastic damage theory for anisotropic materials", Int. J. Solids Structures, Vol. 32, No. 11, 1995, pp. 1607-1641.
[**112**] T. J. Lu, C. L. Chow, "On constitutive equations of inelastic solids with anisotropic damage", Theoretical and Applied Fracture Mechanics, Vol. 14, 1990, pp. 187 – 218.
[**113**] C. L. Chow, J. Wang, "An anisotropic theory of elasticity for continuum damage mechanics", International Journal of Fracture, Vol. 33, 1987, pp. 3 – 16.

[**114**] C. L. Chow, J. Wang, "An anisotropic theory of continuum damage mechanics for ductile fracture", Engineering Fracture Mechanics, Vol. 27, No. 5, 1987, pp. 547 – 558.
[**115**] C. L. Chow, T. J. Lu, "On evolution laws of anisotropic damage", Engineering Fracture Mechanics, Vol. 34, No. 3, 1989, pp. 679 – 701.
[**116**] J. W. Ju, ""On energy-based coupled elastoplastic damage theories: constitutive modelling and computational aspects", Int. J. Solids Structures, Vol. 25, No. 7, 1989, pp. 803 – 833.
[**117**] J. C. Simo, J. W. Ju, "Strain and stress based continuum damage models – I. Formulation", Int. J. Solids Structures, Vol. 23, No. 7. 1987, pp. 821 – 840.
[**118**] J. C. Simo, J. W. Ju, "Strain and stress based continuum damage models – II. Computational aspects", Int. J. Solids Structures, Vol. 23, No. 7, 1987, pp. 841 – 869.
[**119**] K. Hayakawwa, S. Murakamai, Y. Liu, "An irreversible thermodynamics theory for elastic-plastic-damage materials", European Journal of Mechanics, A/Solids, Vol. 17, No, 1, 1998, pp. 13 – 32.
[**120**] R. K. Abu Al-Rub, G. Z. Voyiadjis, "On the coupling of anisotropic damage and plasticity models for ductile materials", Inernational Journal of Solids and Structures, Vol. 40, 2003, pp. 2611 – 2643.
[**121**] P. Isaksson, R. Hagglund, P. Gradin, "Continuum damage mechanics applied to paper", International Journal of Solids and Structures, Vol. 41, 2004, pp. 4731 – 4755.
[**122**] J. Lemaitre, "A continuous damage mechanics model for ductile fracture", Journal of Engineering Materials and Technology, Vol. 107, 1985, pp. 83 – 89.
[**123**] Steinberg D. J, Cochran S. G., Guinan M. W., "A constitutive model for metals applicable at high-strain rate", Journal of Applied Physics, Vol. 51(3), 1988, pp. 1498-1504.

[**124**] Steinberg D. J., Lund C. M., "A constitutive model for strain rates from 10^{-4} to 10^{6} s^{-1}", Journal of Applied Physics, Vol. 65(4), 1988, 1528-1533.

[**125**] Bodner S. R., Symonds P. S., "Experimental and Theoretical Investigation if the Plastic Deformation of Cantelever Beams Subjected to Impulsive Loading", Journal of Applied Mechanics, ASME, 1962, pp. 719-728.

[**126**] Campbell J. D., Cooper R. H., Proc. Conf. On the Physical basis of Yield and Fracture (London: Inst. Of Phys. And Physical Soc.), 1966, pp. 77-87.

[**127**] Gurson, A.L., "Continum theory of ductile rupture by void nucleation and growth. Part I: Yield criteria and flow rules for porous ductile madia", Journal of Engineering Materials and Technology, 1977, Vol. 99, pp. 2-15.

[**128**] Tvergaard V., "Material failure by void coalescence in localized shear bands", International Journal of Solids and Structures, 1982, Vol. 18, pp.659-672.

[**129**] Tvergaard V., Needleman A., "Analysis of cup-cone fracture in a round tensile bar", Acta Mettallurgica, 1984, 32, 57-169.

[**130**] Chaboche J. L., "Continuous damage mechanics – a tool to describe phenomena before crack initiation", Nucl. Engng. Des., 1981, 64, 233-247.

[**131**] Cordebois J. P., Sidoroff F., "Damage induced elastic anisotropy", Euromech 115, Villars de Lans, 1979, pp.761-774.

APPENDIX A – Cranfield University Tensile Tests

Following tables (Tab. A.1. and Tab. A.2.) represent matrices for tensile tests conducted at Cranfield University for two aluminium alloys with maximal practical achievable ranges for temperature and crosshead speed.

Temperature / Crosshead Speed	-50°C	0°C	+70°C	+140°C	+199°C[**1**] +197°C [**2**,**3**]	α
0.008 mm/s	7L8M3M51 7L8M3M52 7L8M3M53	7L8M3001 7L8M3002 7L8M3003	7L8M3P71 7L8M3P72 7L8M3P73	7L8M3141 7L8M3142 7L8M3143	7L8M320**1** 7L8M320**2** 7L8M320**3**	0°
	7T8M3M51 7T8M3M52 7T8M3M53	7T8M3001 7T8M3002 7T8M3003	7T8M3P71 7T8M3P72 7T8M3P73	7T8M3141 7T8M3142 7T8M3143	7T8M320**1** 7T8M320**2** 7T8M320**3**	90°
			7D8M3P71 7D8M3P72 7D8M3P73			45°
0.08 mm/s	7L8M2M51 7L8M2M52 7L8M2M53	7L8M2001 7L8M2002 7L8M2003	7L8M2P71 7L8M2P72 7L8M2P73	7L8M2141 7L8M2142 7L8M2143	7L8M220**1** 7L8M220**2** 7L8M220**3**	0°
	7T8M2M51 7T8M2M52 7T8M2M53	7T8M2001 7T8M2002 7T8M2003	7T8M2P71 7T8M2P72 7T8M2P73	7T8M2141 7T8M2142 7T8M2143	7T8M220**1** 7T8M220**2** 7T8M220**3**	90°
			7D8M2P71 7D8M2P72 7D8M2P73			45°
0.8 mm/s	7L8M1M51 7L8M1M52 7L8M1M53	7L8M1001 7L8M1002 7L8M1003	7L8M1P71 7L8M1P72 7L8M1P73	7L8M1141 7L8M1142 7L8M1143	7L8M120**1** 7L8M120**2** 7L8M120**3**	0°
	7T8M1M51 7T8M1M52 7T8M1M53	7T8M1001 7T8M1002 7T8M1003	7T8M1P71 7T8M1P72 7T8M1P73	7T8M1141 7T8M1142 7T8M1143	7T8M120**1** 7T8M120**2** 7T8M120**3**	90°
			7D8M1P71 7D8M1P72 7D8M1P73			45°
8 mm/s	7L8P0M51 7L8P0M52 7L8P0M53	7L8P0001 7L8P0002 7L8P0003	7L8P0P71 7L8P0P72 7L8P0P73	7L8P0141 7L8P0142 7L8P0143	7L8P020**1** 7L8P020**2** 7L8P020**3**	0°
	7T8P0M51 7T8P0M52 7T8P0M53	7T8P0001 7T8P0002 7T8P0003	7T8P0P71 7T8P0P72 7T8P0P73	7T8P0141 7T8P0142 7T8P0143	7T8P020**1** 7T8P020**2** 7T8P020**3**	90°
			7D8P0P71 7D8P0P72 7D8P0P73			45°
80 mm/s	7L8P1M51 7L8P1M52 7L8P1M53	7L8P1001 7L8P1002 7L8P1003	7L8P1P71 7L8P1P72 7L8P1P73	7L8P1141 7L8P1142 7L8P1143	7L8P120**1** 7L8P120**2** 7L8P120**3**	0°
	7T8P1M51 7T8P1M52 7T8P1M53	7T8P1001 7T8P1002 7T8P1003	7T8P1P71 7T8P1P72 7T8P1P73	7T8P1141 7T8P1142 7T8P1143	7T8P120**1** 7T8P120**2** 7T8P120**3**	90°
			7D8P1P71 7D8P1P72 7D8P1P73			45°

Tab. A.1. Tensile test matrix for AA7010

Temperature / Crosshead Speed	-50°C	0°C	+70°C	+140°C	+199°C[**1**]	α
0.008 mm/s	2L8M3M51	2L8M3001	2L8M3P71 2L8M3P72 2L8M3P73	2L8M3141	2L8M320**1**	0°
	2T8M3M51	2T8M3001	2T8M3P71 2T8M3P72 2T8M3P73	2T8M3141	2T8M320**1**	90°
			2D8M3P71 2D8M3P72 2D8M3P73			45°
0.08 mm/s	2L8M2M51	2L8M2001	2L8M2P71 2L8M2P72 2L8M2P73	2L8M2141	2L8M220**1**	0°
	2T8M2M51	2T8M2001	2T8M2P71 2T8M2P72 2T8M2P73	2T8M2141	2T8M220**1**	90°
			2D8M2P71 2D8M2P72 2D8M2P73			45°
0.8 mm/s	2L8M1M51	2L8M1001	2L8M1P71 2L8M1P72 2L8M1P73	2L8M1141	2L8M120**1**	0°
	2T8M1M51	2T8M1001	2T8M1P71 2T8M1P72 2T8M1P73	2T8M1141	2T8M120**1**	90°
			2D8M1P71 2D8M1P72 2D8M1P73			45°
8 mm/s	2L8P0M51	2L8P0001	2L8P0P71 2L8P0P72 2L8P0P73	2L8P0141	2L8P020**1**	0°
	2T8P0M51	2T8P0001	2T8P0P71 2T8P0P72 2T8P0P73	2T8P0141	2T8P020**1**	90°
			2D8P0P71 2D8P0P72 2T8P0P73			45°
80 mm/s	2L8P1M51	2L8P1001	2L8P1P71 2L8P1P72 2L8P1P73	2L8P1141	2L8P120**1**	0°
	2T8P1M51	2T8P1001	2T8P1P71 2T8P1P72 2T8P1P73	2T8P1141	2T8P120**1**	90°
			2D8P1P71 2D8P1P72 2D8P1P73			45°

Tab. A.2. Tensile test matrix for AA2024

Yield strength values listed in tables Tab. A.3. and Tab. A.4., are determined from CU tensile tests for AA7010 and AA2024. Tests have been conducted for five different strain rates and temperatures, and for three different orientations for each material.

$\dot{\varepsilon}[1/s]$	T [C]	$\sigma_y[0^o]$ [MPa]	$\sigma_y[90^o]$ [MPa]	$\sigma_y[45^o]$ [MPa]
6.4x 10^{0}	-50	547.0	545.8	-
6.4x 10^{0}	0	527.3	525.6	-
6.4x 10^{0}	+70	496.7	493.5	467.4
6.4x 10^{0}	+140	467.2	465.1	-
6.4x 10^{0}	+200	392.7	387.4	-

$\dot{\varepsilon}[1/s]$	T [C]	$\sigma_y[0^o]$ [MPa]	$\sigma_y[90^o]$ [MPa]	$\sigma_y[45^o]$ [MPa]
6.4x 10^{-1}	-50	545.9	543.6	-
6.4x 10^{-1}	0	521.1	520.6	-
6.4x 10^{-1}	+70	493.9	488.4	465.3
6.4x 10^{-1}	+140	459.7	457.6	-
6.4x 10^{-1}	+200	378.0	374.4	-

$\dot{\varepsilon}[1/s]$	T [C]	$\sigma_y[0^o]$ [MPa]	$\sigma_y[90^o]$ [MPa]	$\sigma_y[45^o]$ [MPa]
6.4x 10^{-2}	-50	540.3	535.3	-
6.4x 10^{-2}	0	516.8	515.1	-
6.4x 10^{-2}	+70	491.1	485.5	463.8
6.4x 10^{-2}	+140	443.9	441.7	-
6.4x 10^{-2}	+200	352.1	346.7	-

$\dot{\varepsilon}[1/s]$	T [C]	$\sigma_y[0^o]$ [MPa]	$\sigma_y[90^o]$ [MPa]	$\sigma_y[45^o]$ [MPa]
6.4x 10^{-3}	-50	536.2	530.1	-
6.4x 10^{-3}	0	511.9	510.6	-
6.4x 10^{-3}	+70	485.1	482.6	461.6
6.4x 10^{-3}	+140	429.5	427.8	-
6.4x 10^{-3}	+200	320.2	318.8	-

$\dot{\varepsilon}[1/s]$	T [C]	$\sigma_y[0^o]$ [MPa]	$\sigma_y[90^o]$ [MPa]	$\sigma_y[45^o]$ [MPa]
6.4x 10^{-4}	-50	530.3	527.6	-
6.4x 10^{-4}	0	509.2	507.9	-
6.4x 10^{-4}	+70	483.1	480.1	457.4
6.4x 10^{-4}	+140	414.0	409.8	-
6.4x 10^{-4}	+200	295.7	289.6	-

Tab. A.3. Yield stresses for AA7010

$\dot{\varepsilon}[1/s]$	T [C]	$\sigma_y[0^o]$ [MPa]	$\sigma_y[90^o]$ [MPa]	$\sigma_y[45^o]$ [MPa]
6.4x 10^{0}	-50	365.32	311.27	-
6.4x 10^{0}	0	352.98	304.26	-
6.4x 10^{0}	+70	343.20	299.85	296.74
6.4x 10^{0}	+140	333.08	289.59	-
6.4x 10^{0}	+200	318.78	280.66	-

$\dot{\varepsilon}[1/s]$	T [C]	$\sigma_y[0^o]$ [MPa]	$\sigma_y[90^o]$ [MPa]	$\sigma_y[45^o]$ [MPa]
6.4x 10^{-1}	-50	361.13	309.73	-
6.4x 10^{-1}	0	350.49	302.01	-
6.4x 10^{-1}	+70	339.22	296.84	294.85
6.4x 10^{-1}	+140	317.47	274.14	-
6.4x 10^{-1}	+200	312.50	275.75	-

$\dot{\varepsilon}[1/s]$	T [C]	$\sigma_y[0^o]$ [MPa]	$\sigma_y[90^o]$ [MPa]	$\sigma_y[45^o]$ [MPa]
6.4x 10^{-2}	-50	356.53	307.90	-
6.4x 10^{-2}	0	348.36	300.58	-
6.4x 10^{-2}	+70	330.84	294.42	292.35
6.4x 10^{-2}	+140	310.13	272.56	-
6.4x 10^{-2}	+200	294.97	270.29	-

$\dot{\varepsilon}[1/s]$	T [C]	$\sigma_y[0^o]$ [MPa]	$\sigma_y[90^o]$ [MPa]	$\sigma_y[45^o]$ [MPa]
6.4x 10^{-3}	-50	352.72	305.15	-
6.4x 10^{-3}	0	346.61	298.43	-
6.4x 10^{-3}	+70	325.92	292.07	290.46
6.4x 10^{-3}	+140	305.96	269.09	-
6.4x 10^{-3}	+200	284.10	262.65	-

$\dot{\varepsilon}[1/s]$	T [C]	$\sigma_y[0^o]$ [MPa]	$\sigma_y[90^o]$ [MPa]	$\sigma_y[45^o]$ [MPa]
6.4x 10^{-4}	-50	347.90	303.01	-
6.4x 10^{-4}	0	344.46	296.15	-
6.4x 10^{-4}	+70	310.67	291.04	289.85
6.4x 10^{-4}	+140	298.52	261.45	-
6.4x 10^{-4}	+200	271.75	252.21	-

Tab. A.4. Yield stresses for AA2024

Typical stress-strain plots for aluminium alloy AA2024 from tensile tests performed at $+70^{o}C$ in the strain rate range from $\dot{\varepsilon} = 6.4x10^{-4}s^{-1}$ to $\dot{\varepsilon} = 6.4x10^{0}s^{-1}$ for three different specimen orientations at 0^{o}, 45^{o} and 90^{o}, are presented in Fig. A.1. – Fig. A.5.

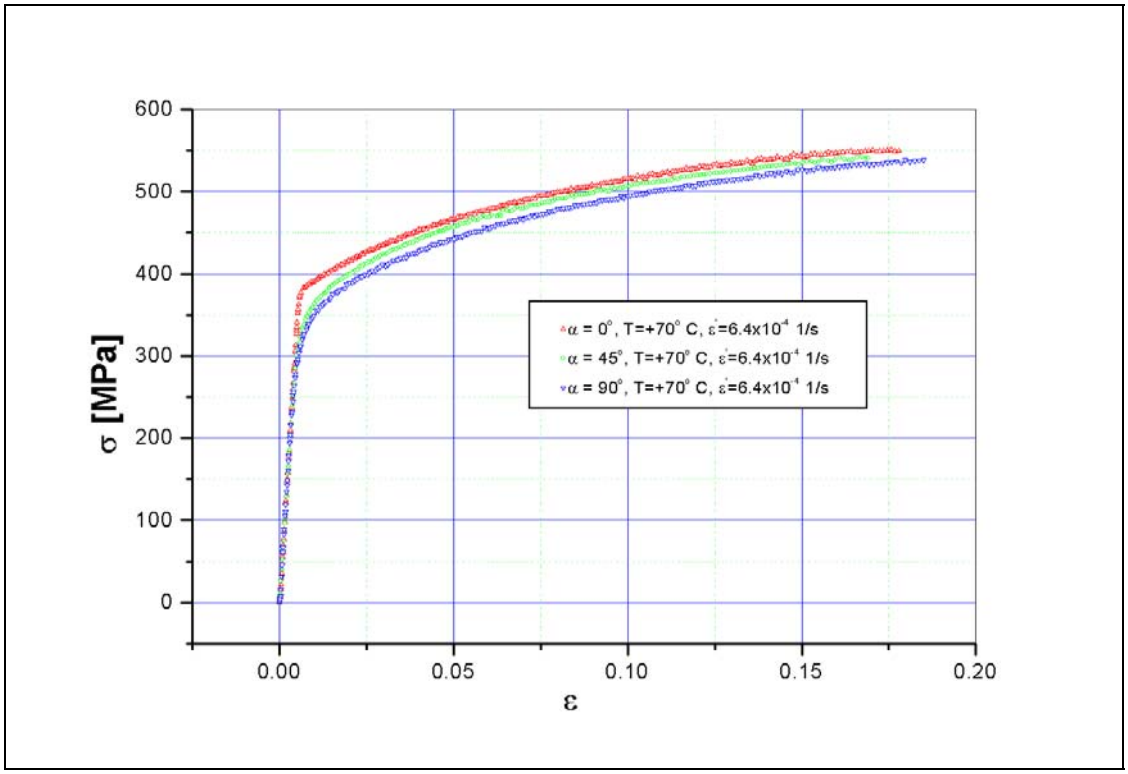

Fig. A.1. Stress-strain response for AA2024 at $+70^{0}$ C and $\dot{\varepsilon} = 6.4x10^{-4}s^{-1}$

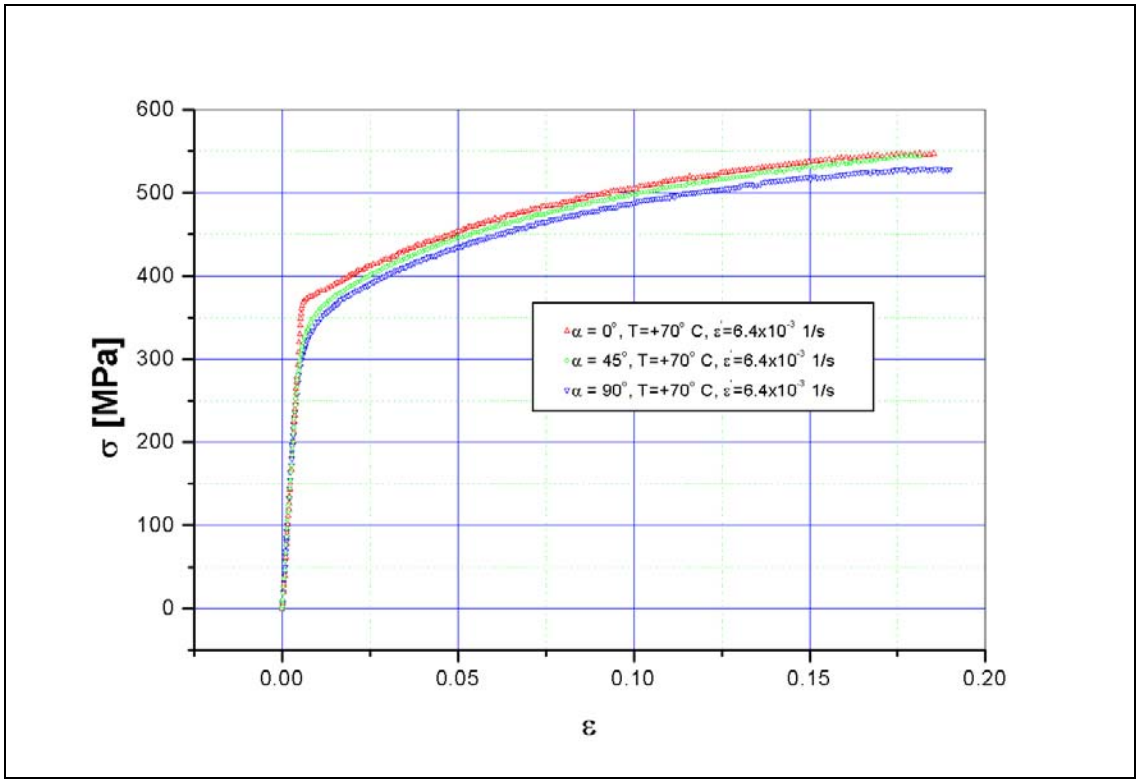

Fig. A.2. Stress-strain response for AA2024 at $+70^{0}$ C and $\dot{\varepsilon} = 6.4x10^{-3}s^{-1}$

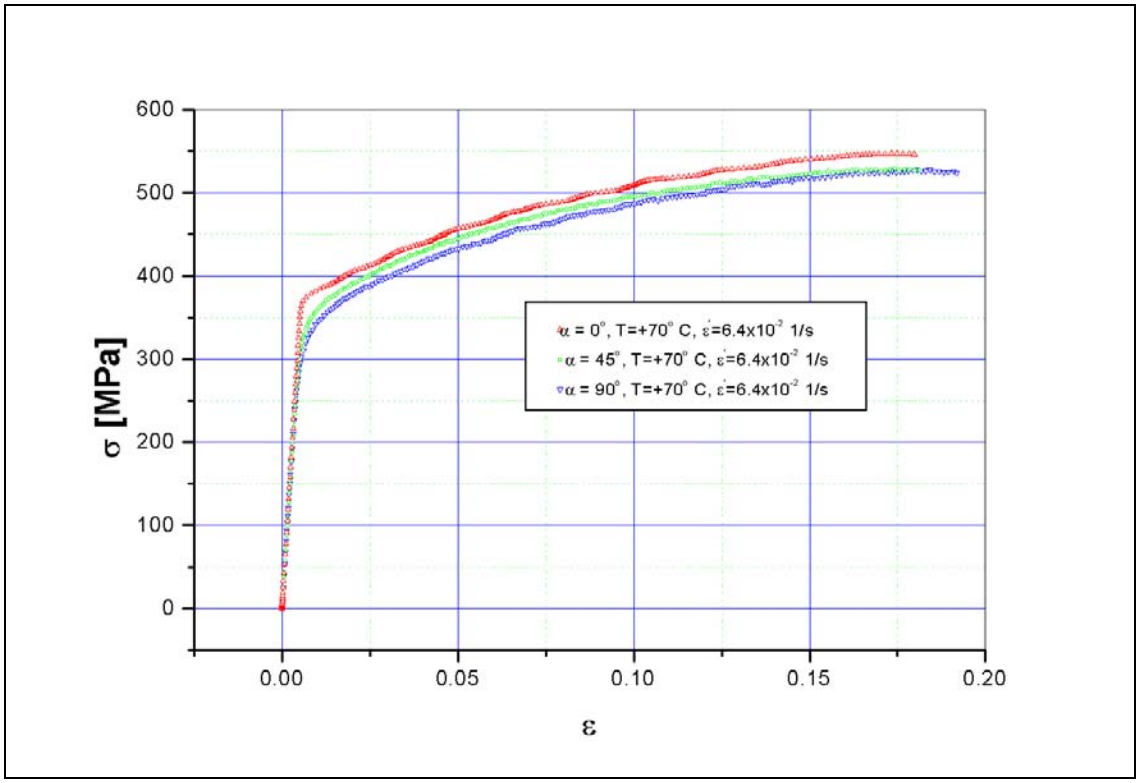

Fig. A.3. Stress-strain response for AA2024 at $+70^0$ C and $\dot{\varepsilon} = 6.4x10^{-2}s^{-1}$

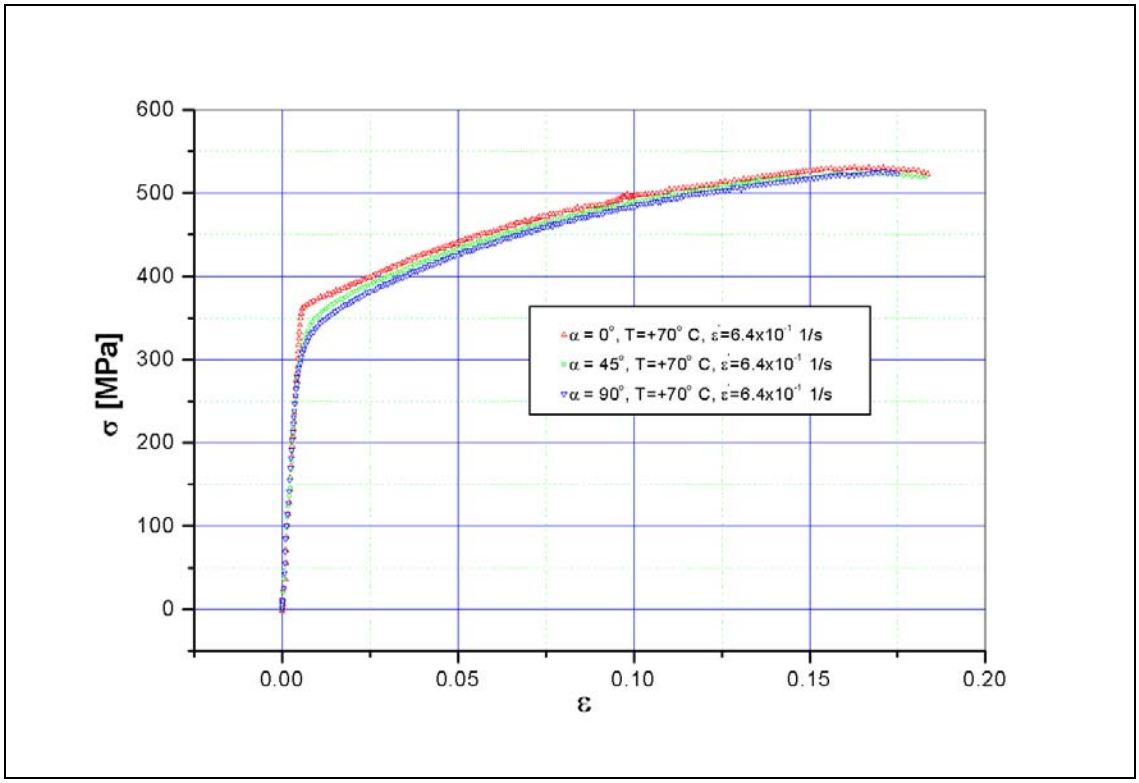

Fig. A.4. Stress-strain response for AA2024 at $+70^0$ C and $\dot{\varepsilon} = 6.4x10^{-1}s^{-1}$

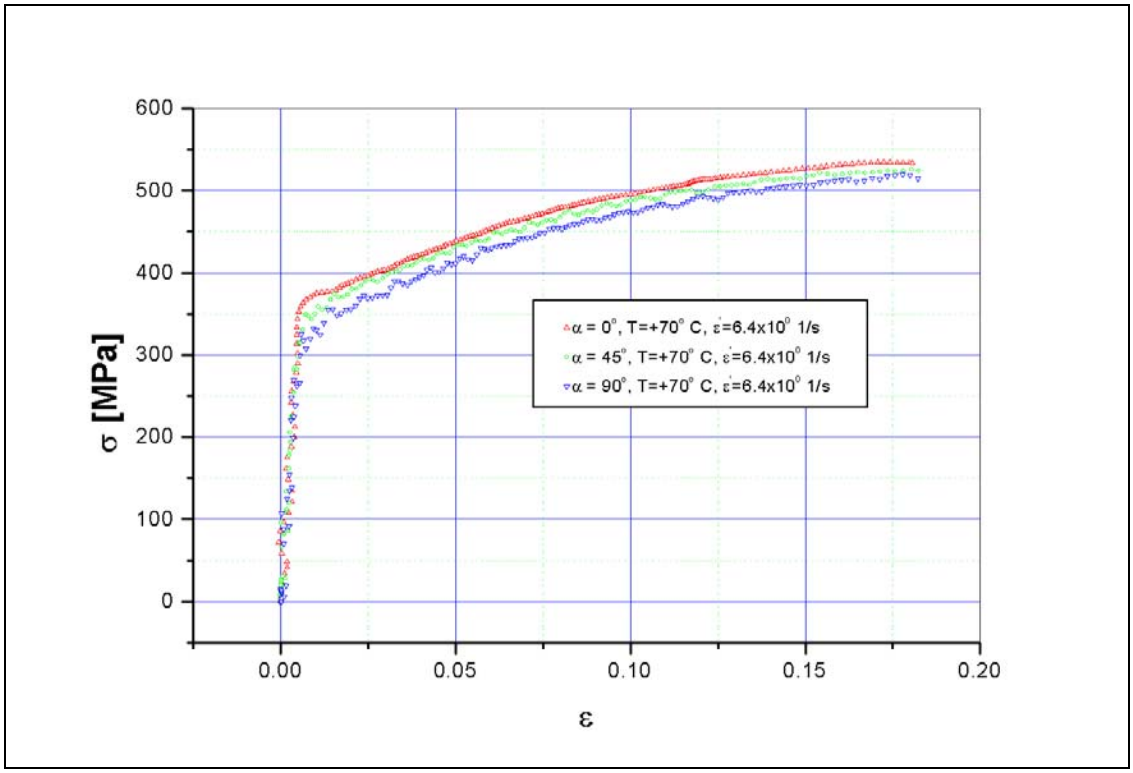

Fig. A.5. Stress-strain response for AA2024 at +70^0 C and $\dot{\varepsilon} = 6.4x10^0 s^{-1}$

Another set of the stress-strain plots for aluminium alloy AA7010 from tensile tests performed at $+70^o C$ in the strain rate range from $\dot{\varepsilon} = 6.4x10^{-4} s^{-1}$ to $\dot{\varepsilon} = 6.4x10^0 s^{-1}$ for three different specimen orientations at 0^o, 45^o and 90^o, are presented in Fig. A.6. – Fig. A.10

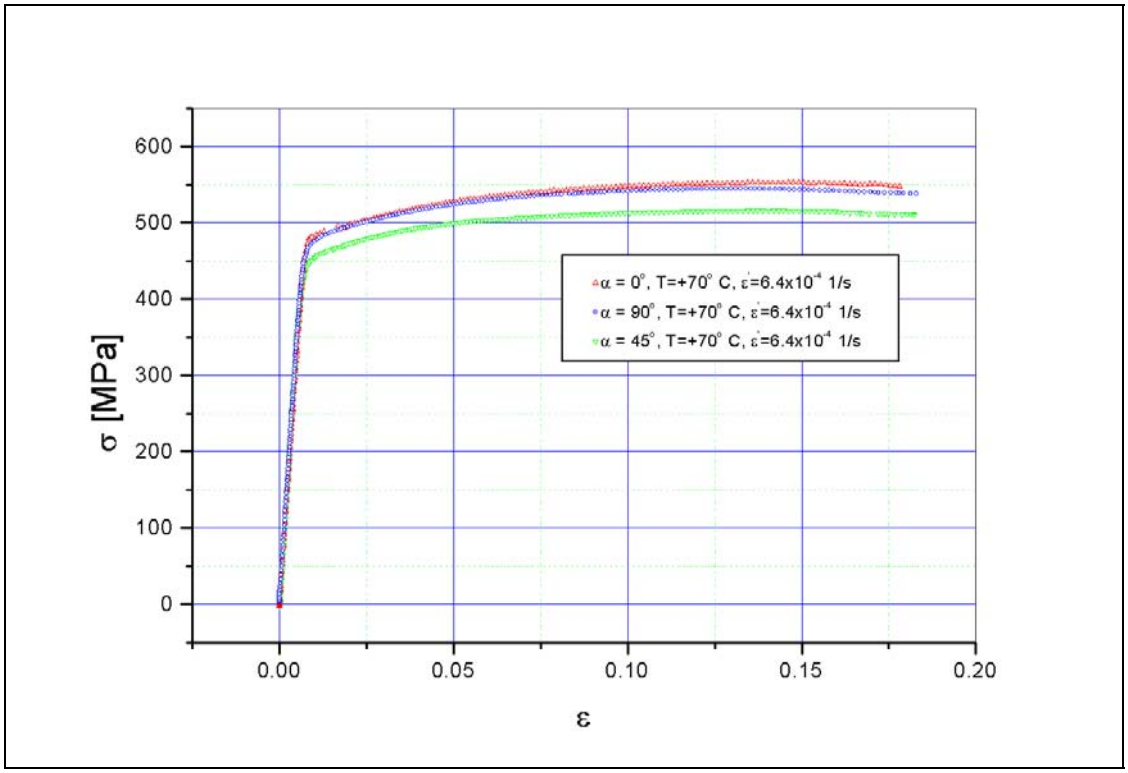

Fig. A.6. Stress-strain response for AA7010 at +70^0 C and $\dot{\varepsilon} = 6.4x10^{-4} s^{-1}$

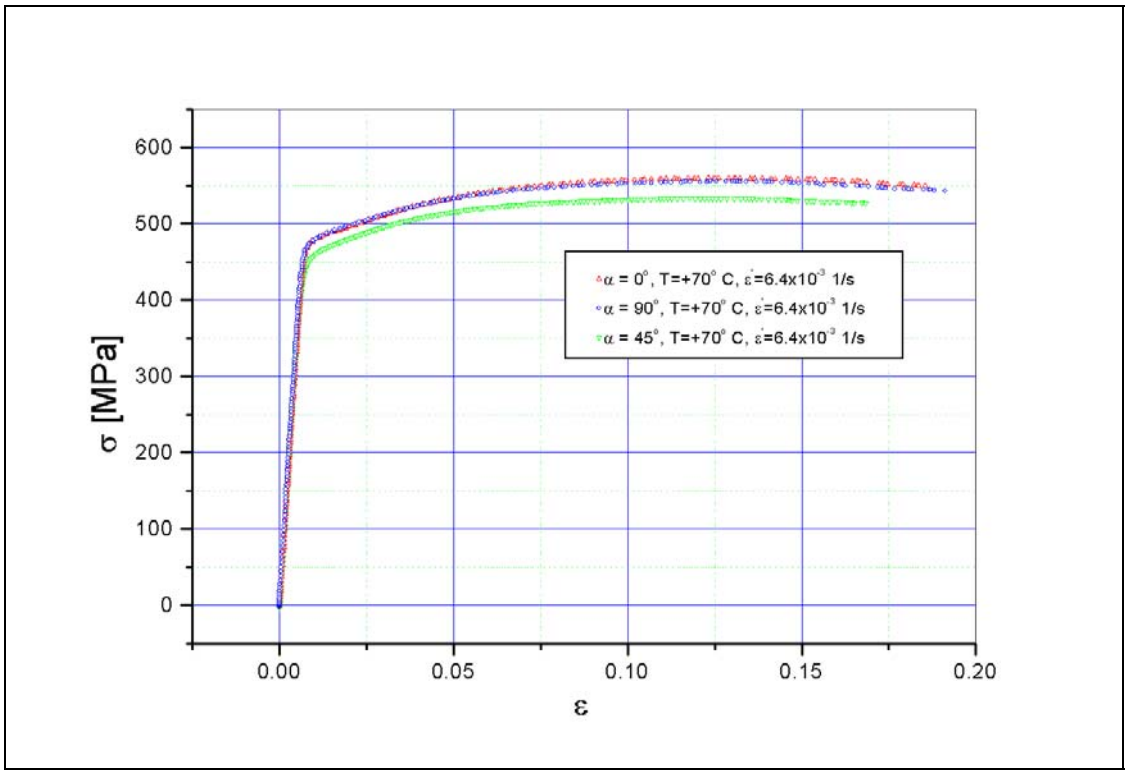

Fig. A.7. Stress-strain response for AA7010 at $+70^0$ C and $\dot{\varepsilon} = 6.4x10^{-3}s^{-1}$

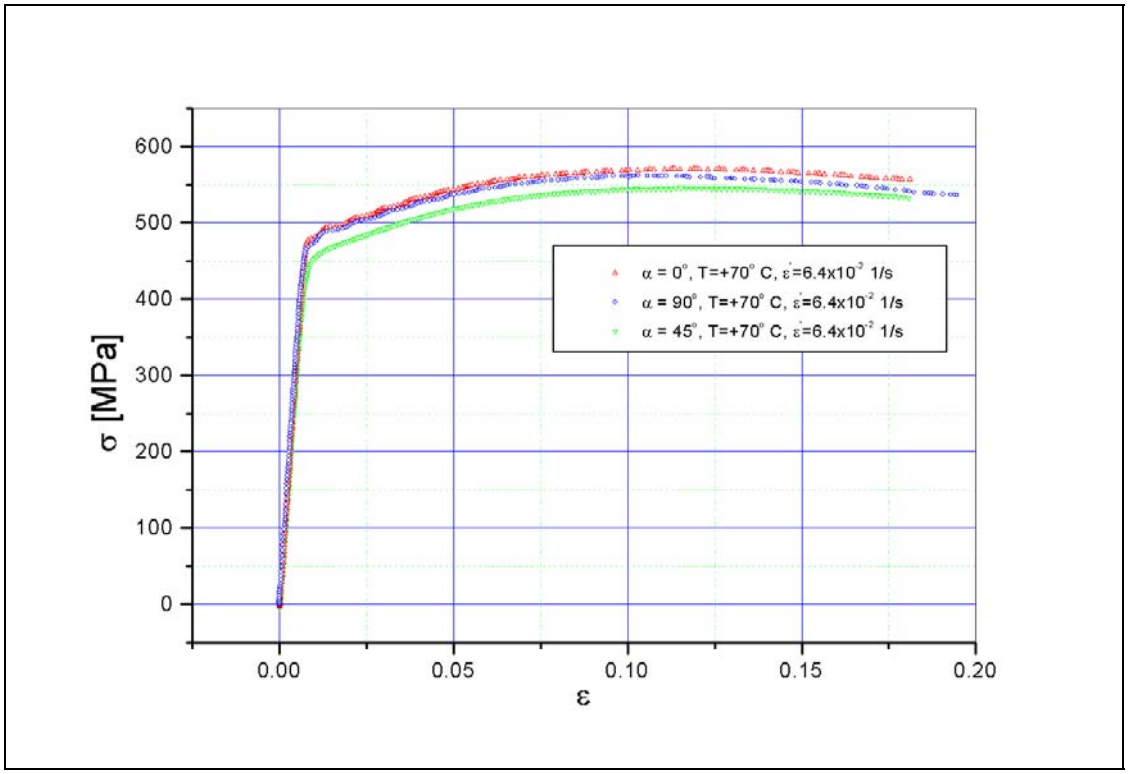

Fig. A.8. Stress-strain response for AA7010 at $+70^0$ C and $\dot{\varepsilon} = 6.4x10^{-2}s^{-1}$

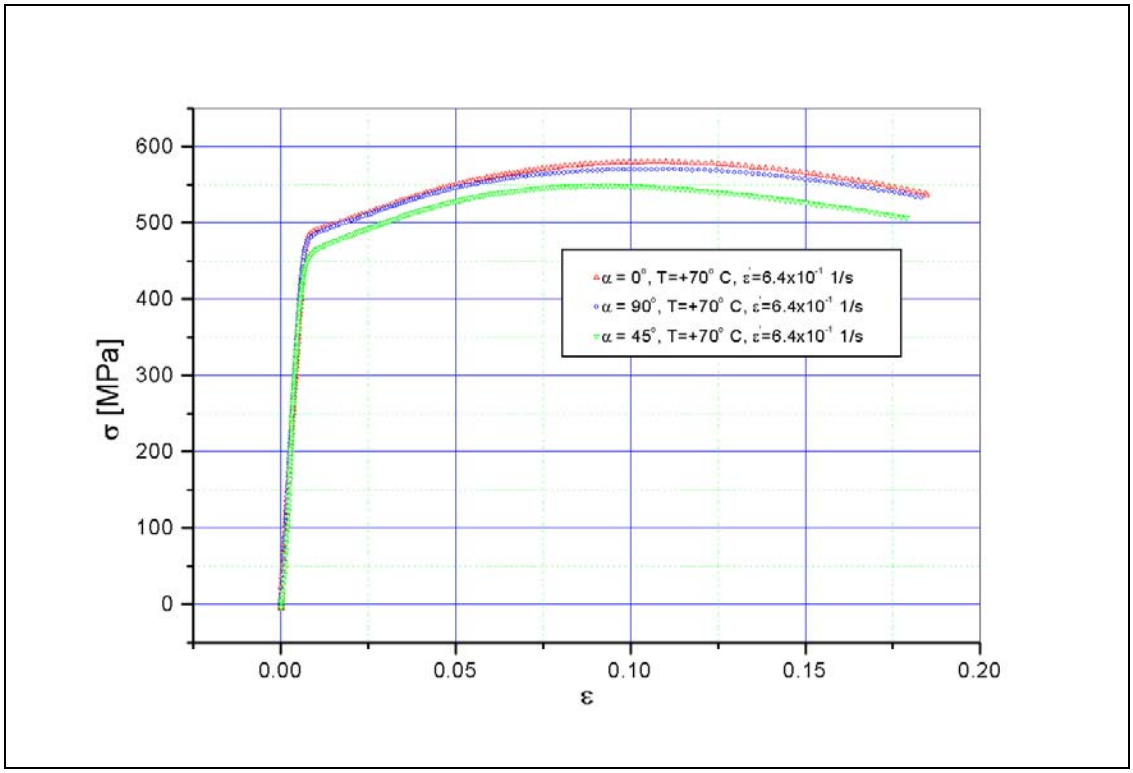

Fig. A.9. Stress-strain response for AA7010 at $+70^0$ C and $\dot{\varepsilon} = 6.4x10^{-1}s^{-1}$

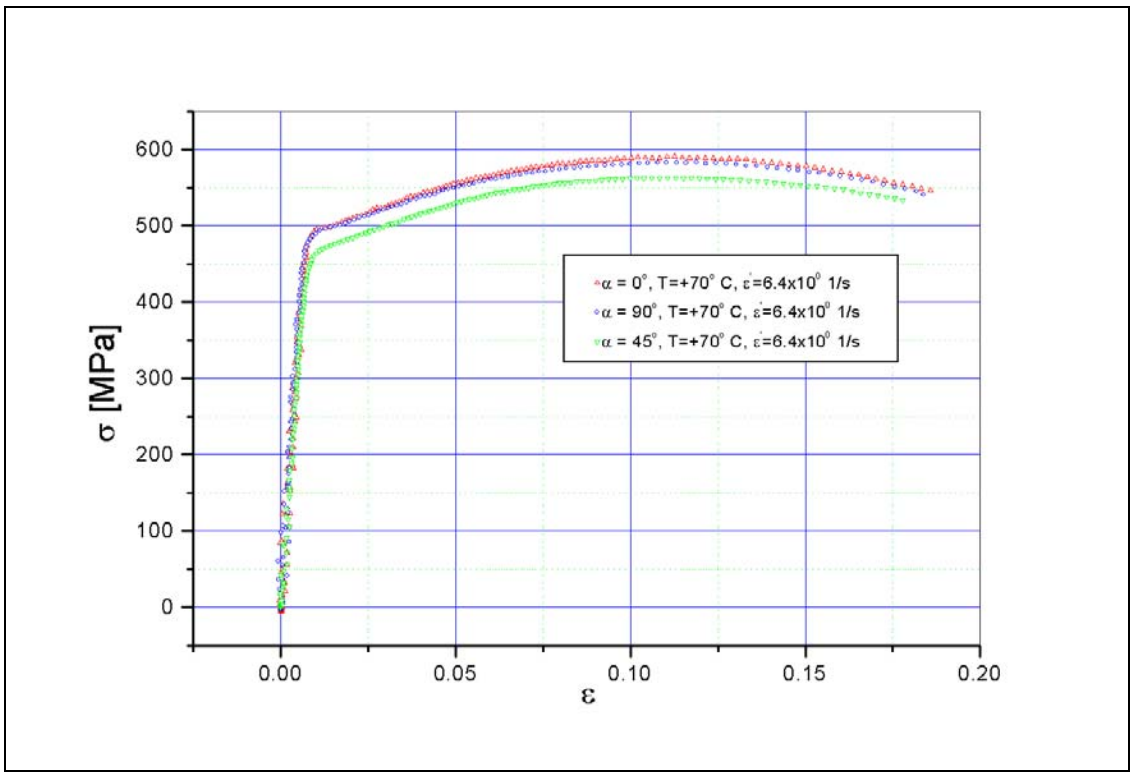

Fig. A.10 Stress-strain response for AA7010 at $+70^0$ C and $\dot{\varepsilon} = 6.4x10^{0}s^{-1}$

Values of yield stresses in 0^o, 45^o, 90^o, directions and Lankford coefficients R, listed in Tab. A.5. and Tab. A.6., were used to calculate parameters included in Hill's orthotropic criterion for AA7010 and AA2024.

Tab. A.5. Hill's model constants for AA7010 (R=0.836)

F	G	H	N
$\frac{1}{\sigma_{90}^{\ 2}} - \frac{R_0}{\sigma_{90}^{\ 2}(1+R_0)}$	$\frac{1}{\sigma_0^{\ 2}(1+R_0)}$	$\frac{R_0}{\sigma_0^{\ 2}(1+R_0)}$	$\frac{1}{2}\left(\frac{4}{\sigma^2_{45}} - \frac{1}{\sigma^2_{90}} + \frac{R_0-1}{\sigma_0^{\ 2}(1+R_0)}\right)$
0.5524	0.5447	0.4553	1.6870

Tab. A.6. Hill's model constants for AA2024 (R= 0.772)

F	G	H	N
$\frac{1}{\sigma_{90}^{\ 2}} - \frac{R_0}{\sigma_{90}^{\ 2}(1+R_0)}$	$\frac{1}{\sigma_0^{\ 2}(1+R_0)}$	$\frac{R_0}{\sigma_0^{\ 2}(1+R_0)}$	$\frac{1}{2}\left(\frac{4}{\sigma^2_{45}} - \frac{1}{\sigma^2_{90}} + \frac{R_0-1}{\sigma_0^{\ 2}(1+R_0)}\right)$
0.7048	0.5643	0.4357	1.8457

Yield surfaces which were computed with identified anisotropic coefficients of Hill's yield function for the AA7010 and AA2024, where rolling direction, $\alpha = 0^o$, was chosen as the reference direction, are presented in Fig. A.11.

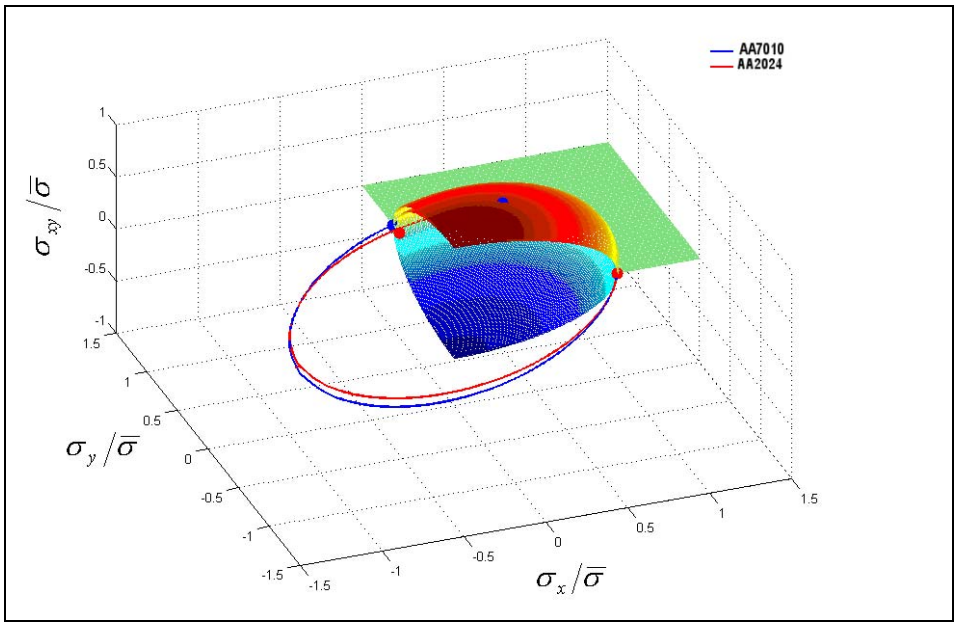

Fig. A.11. Predicted initial yield surfaces for AA7010 and AA2024

Sets of data for adopted reference direction, $\alpha = 0^o$, presented in tables Tab. A.1. and Tab. A.2. have been used for derivation of parameters for two temperature and strain rate dependent strength material models, JC and MTS. Calculated parameters for two aluminium alloys AA7010 and AA2024 are summarized in the following tables (Tab. A.7. – Tab. A.9.).

Tab. A.7. JC model constants for AA7010

Parameter	Description	Nominal value
G	Shear modulus	26.0 GPa
A	Yield stress constant	547.03 MPa
B	Strain hardening coefficient	601.58 Mpa
n	Strain hardening exponent	0.65
C	Strain rate dependence coefficient	0.0022
m	Temperature dependence coefficient	1.30
T_m	Melt temperature	893.15 K
T_r	Reference temperature	293.15 K
$\dot{\varepsilon}_0$	Reference strain rate	$10^1 1/\boldsymbol{s}$
C_p	Specific heat	896 J/kgK
$p_{cut}(\sigma_m)$	Pressure cutoff (Failure stress)	1.30 GPa

Tab. A.8. MTS model constants for AA7010

Parameter	Description	Nominal value
σ_a	Athermal rate independent threshold stress	10.0 MPa
σ_0	Initial threshold stress at zero plastic strain	600.0 MPa
$g_{0\varepsilon}$	Normalized activation energy	1.606
$\dot{\varepsilon}_{0\varepsilon}$	Reference strain rate	$1x10^7$ s^{-1}
B	Magnitude of Burgers vector	$0.286x10^{-9}$m
K	Boltzmann's constant	$1.38x10^{-23}$ J/K
p_ε	Free energy equation exponent	1
q_ε	Free energy equation exponent	1
A	Saturation stress equation material constant	5.542
$\hat{\sigma}_{s0}$	Saturation stress at zero degrees K	801.01 MPa
$\dot{\varepsilon}_{s0}$	Saturation stress reference strain rate	$1x10^7$ s^{-1}
a_0	Hardening function constant	67604.6 MPa
a_1	Hardening function constant	1816.9 MPa
a_2	Hardening function constant	202.3 MPa
b_0	Shear modulus at zero degrees K	28.83 GPa
b_1	Shear modulus constant	4.45 GPa
b_2	Shear modulus constant	248.5 K
T_r	Reference temperature	293.15 K
ρ	Density	2810 kg/m^3
C_p	Heat capacity	896 J/kgK

Tab. A.9. JC model constants for AA2024

Parameter	Description	Nominal value
G	Shear modulus	28.6 GPa
A	Yield stress constant	369.0 MPa
B	Strain hardening coefficient	684.0 Mpa
n	Strain hardening exponent	0.73
C	Strain rate dependence coefficient	0.0083
m	Temperature dependence coefficient	1.7
T_m	Melt temperature	775.15 K
T_r	Reference temperature	293.15 K
$\dot{\varepsilon}_0$	Reference strain rate	$10^1 1/\boldsymbol{s}$
C_p	Specific heat	875 J/kgK
$p_{cut}(\sigma_m)$	Pressure cutoff (Failure stress)	1.67 GPa

APPENDIX B - Ernst-Mach-Institute Tensile Tests

Matrix of tensile tests conducted at Ernst-Mach-Institute (Germany), is presented on table Tab. B.1. Tests have been conducted using servo-hydraulic test machine with maximal withdrawal velocity of 20 m/s at ambient temperature and crosshead speed of 8 m/s for two orientation of the AA7010.

Tab. B.1. AA7010 Tensile matrix

Temperature / Crosshead Speed	15°C	α
8000 mm/s	7L8P3151 7L8P3152 7L8P3153	0°
	7T8P3151 7T8P3152 7T8P3153	90°

Compared Cranfield University (CU) and Ernst-Mach-Institute (EMI), tensile test results are presented on figures Fig. B.1. and Fig. B.2.

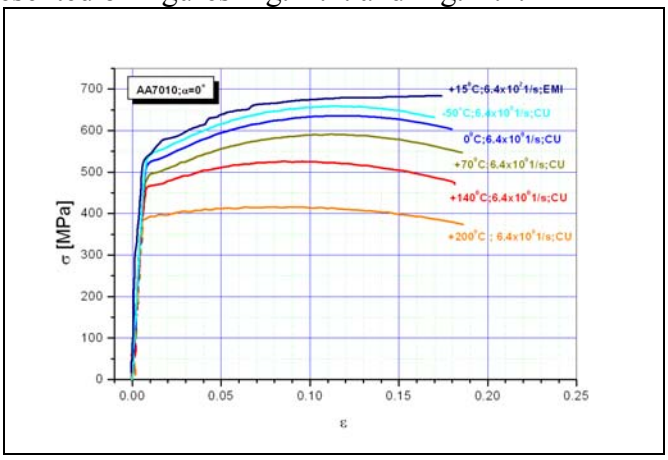

Fig. B.1. AA7010 stress-strain responses for $\alpha = 0^0$ orientation obtained from CU and EMI tests

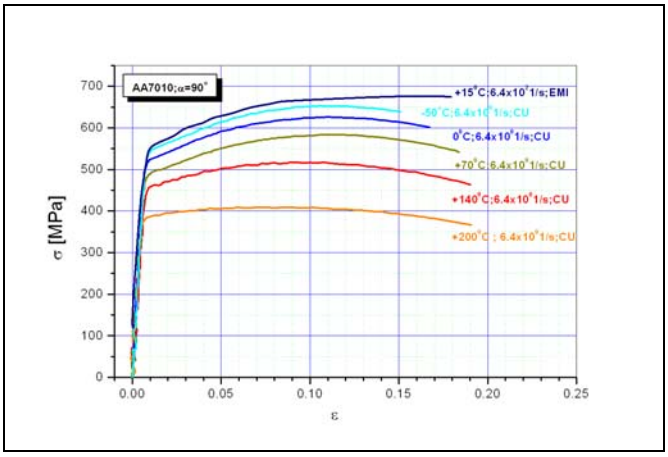

Fig. B.2. AA7010 stress-strain responses for $\alpha = 90^0$ orientation obtained from CU and EMI tests

Contact-less optical strain measurement technique has been applied (Fig. B.3.), which allowed simultaneous measurement of both longitudinal and transverse strain for the determination of R-value (Lankford coefficient).

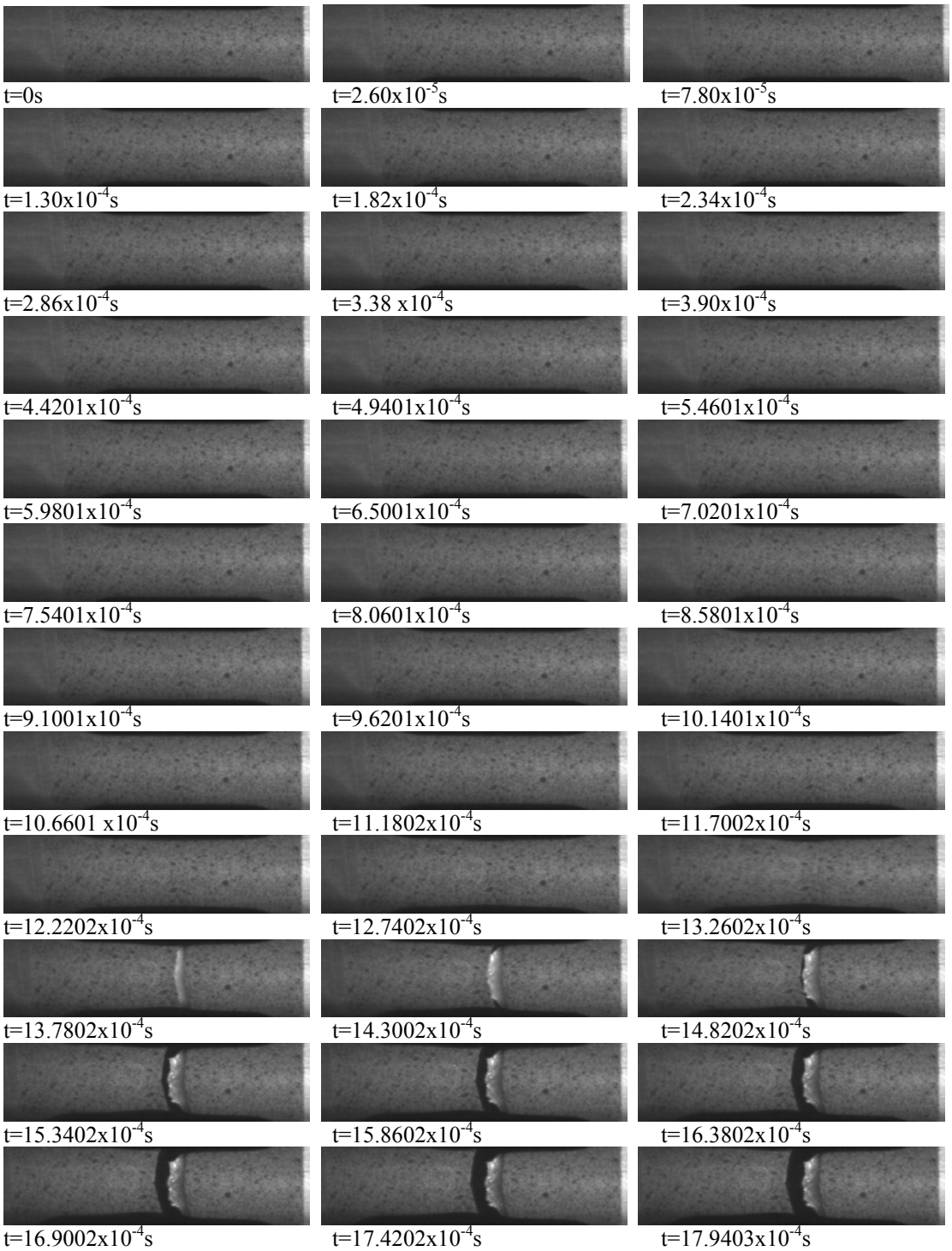

Fig. B.3. Tensile test time sequence obtained using contact-less optical strain measurement technique for the test 7L8P3153.

Lankford coefficient has been determined from the plastic strain using longitudinal and strain in width direction:

$$R = \frac{-\varepsilon_w^p}{\varepsilon_l^p + \varepsilon_w^p} \qquad \text{(B.1.)}$$

It can be seen from figure Fig. B.4., that the R values vary with plastic straining. Initial region of the curve was singular and was therefore omitted from this plot. The R-values exhibit a slight increase at the onset of elastic yielding, which was proceeded by an initial sharp reduction from the singular value (not shown on the graph). Any detailed analysis of the R-values obtained at this low strain is only speculative at best and should be avoided due to the considerable scatter in this region. It can be seen that value of $R = 0.836$ for Lankford coefficient deduced using Taylor impact test corresponds to the maximal value of Lankford coefficient in Fig. B.4.

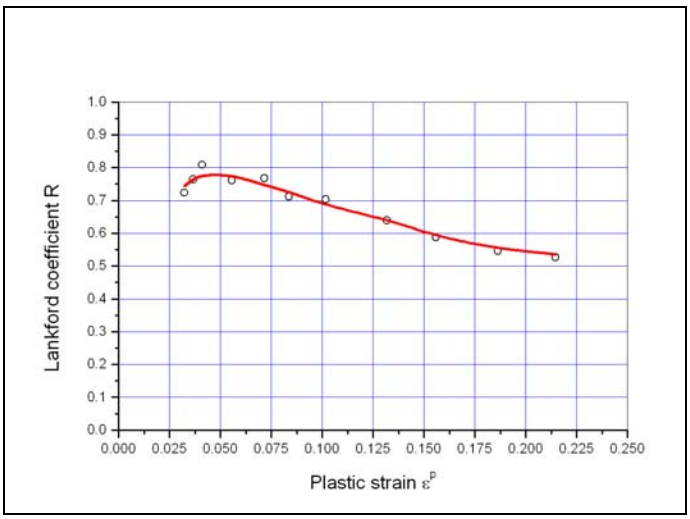

Fig. B.4. R value variation with plastic straining

In order to validate the hypothesis that strain rate and temperature dependence of material are interchangeable, parameters for MTS model, which have been fitted using AA7010 stress-strain data up to $6.4x10^0 s^{-1}$ strain rate and temperature of $-50^o C$, have been used to predict stress-strain response of material at $6.4x10^2$ strain rate. Comparison of the prediction of the MTS model with experimental data is presented in Fig. B.5., and good agreement has been observed.

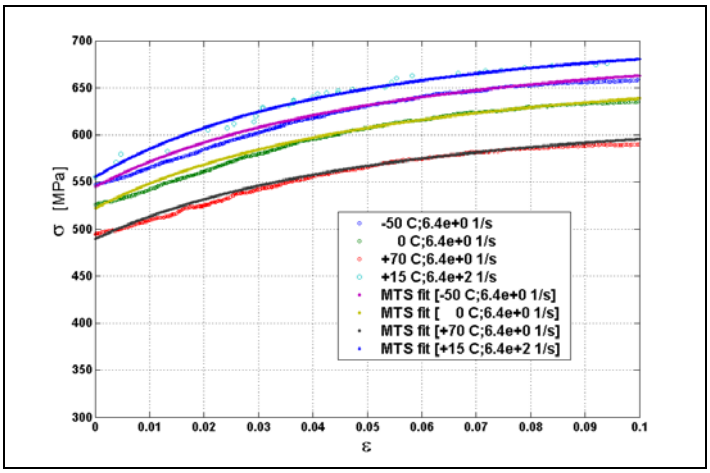

Fig. B.5. MTS model fit stress-strain response of AA7010

APPENDIX C - Grunisen Equation of State

The three-dimensional stress state of material is normally modelled by decomposing the stress into hydrostatic components (pressure term) and deviatoric components (plasticity term). At low strain rates pressure is calculated as a mean stress. In material characterisation of high strain rates pressure is calculated from equation of state. Since high strain rate deformations involves the generation of high temperatures under shock wave conditions, temperature or energy must also be considered in the formulation.

The mathematical formulation that describes the behaviour of hydrostatic components of stress and strain is called the equation of state and can be expressed in the general form as:

$$P = f(E,V) \tag{C.1.}$$

where P is pressure, E is internal energy and V is relative volume.

One of the most commonly used equation s to model material behaviour under impact conditions is the Gruneisen equation of state. It defines the pressure for compressed materials ($\mu > 0$) as:

$$P(\mu,E) = \frac{\rho_0 C^2 \mu\left[1+\left(1-\frac{\gamma_0}{2}\right)\mu - \frac{a}{2}\mu^2\right]}{\left[1-(S_1-1)\mu - S_2\frac{\mu^2}{\mu+1} - S_3\frac{\mu^3}{(\mu+1)^2}\right]} + (\gamma_0 + a\mu)E \tag{C.2.}$$

and for expanded materials ($\mu < 0$) as;

$$P(\mu,E) = \rho_0 C^2 \mu + (\gamma_0 + a\mu)E \tag{C.3.}$$

Were μ is compression coefficient, which is defined as:

$$\mu = \frac{\rho}{\rho_0} - 1 \tag{C.4.}$$

and C_0 is intercept of the shock velocity vs. article velocity $(v_s - v_p)$ curve, S_1, S_2, S_3 are coefficients of the slope of the $(v_s - v_p)$ curve, and γ_0 is Gruneisen gamma.

The Gruneisen equation of state is available in DYNA3D and was used in numerical simulations. The advantage of this equation of state is that it is derived from laboratory experiments and covers a wide range of conditions.

Values of Gruneisen EoS parameters, for aluminium alloys AA7010 and AA2024 are summarized in following tables Tab. C.1. amd Tab. C.2.

Table C.1. Grunisen EOS constants for AA7010 [75]

Parameter	Description	Nominal value
C_0	Bulk sound speed	0.52 $cm/\mu s$
S_1	First Hugoniot slope coefficient	1.36
S_2	Second Hugoniot slope coefficient	0
S_3	Third Hugoniot slope coefficient	0
γ_0	Gruneisen coefficient	2.20
B	First order volume correction coefficient	0.48

Table C.2. Grunisen EOS constants for AA2024 [75]

Parameter	Description	Nominal value
C_0	Bulk sound speed	0.5328 $cm/\mu s$
S_1	First Hugoniot slope coefficient	1.338
S_2	Second Hugoniot slope coefficient	0
S_3	Third Hugoniot slope coefficient	0
γ_0	Gruneisen coefficient	2.00
B	First order volume correction coefficient	0.48

APPENDIX D – Mesh sensitivity analysis of the plate impact FE simulation model

The mesh sensitivity study for the plate impact test numerical simulation has been performed. Numerical simulations using the three different meshes were performed, and those meshes are presented in the following figures Fig. D.1, Fig D.2. and Fig. D.3.

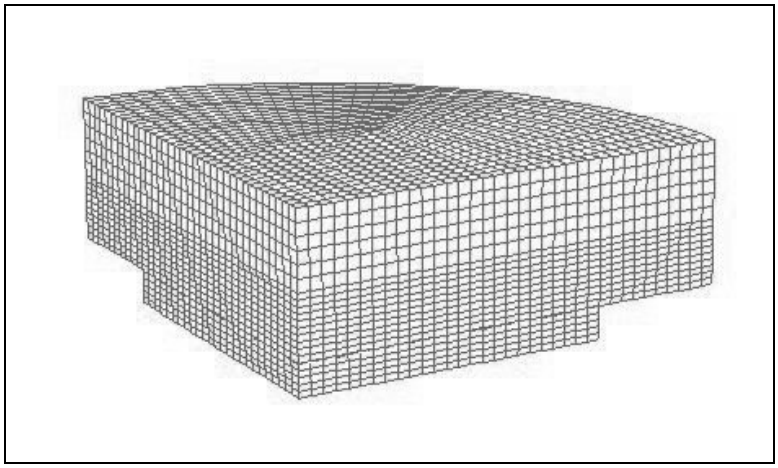

Fig. D.1. Mesh 1

Mesh 1 (Fig. D.1.) has been used to assess influence of the mesh size of the supporting plate. Mesh density, through the thickness direction, of the supporting plate was twice as coarse then mesh density of the target and flyer. Mesh 2 (Fig. D.2.) has been used as a reference mesh, and this mesh has identical mesh density through thickness for all three parts, namely: flyer, target and supporting plate.

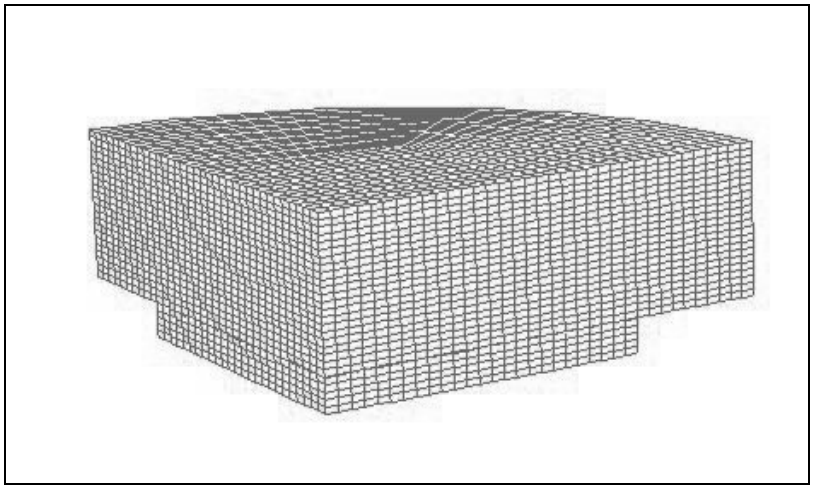

Fig. D.2. Mesh 2

Influence of the mesh size of the flyer and target plate has been assessed using Mesh 3 (Fig. D.3.). In this mesh configuration, mesh density in the radial direction of the flyer and target was twice as fine then in reference mesh configuration - Mesh 2.

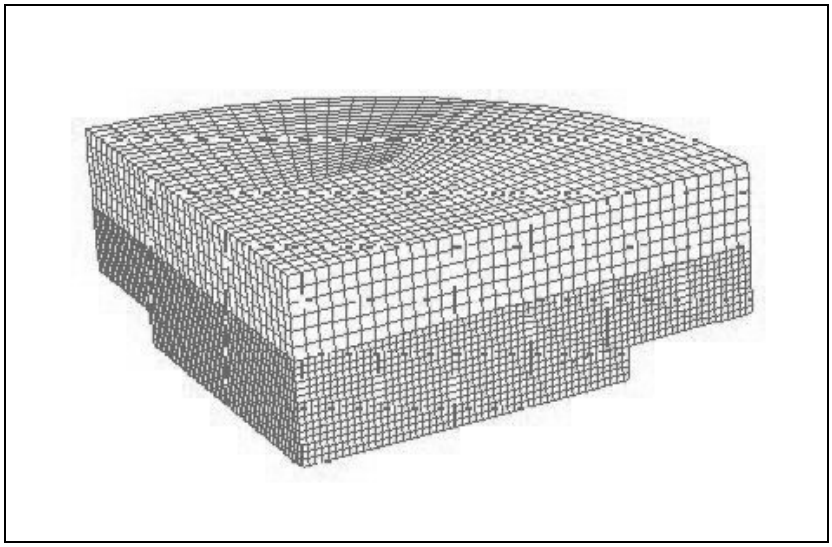

Fig. D.3. Mesh 3

In order to analyse mesh sensitivity of the FE model for the numerical simulation of the plate impact test, Langrangian time-distance diagrams were used, and results from numerical simulations were compared.

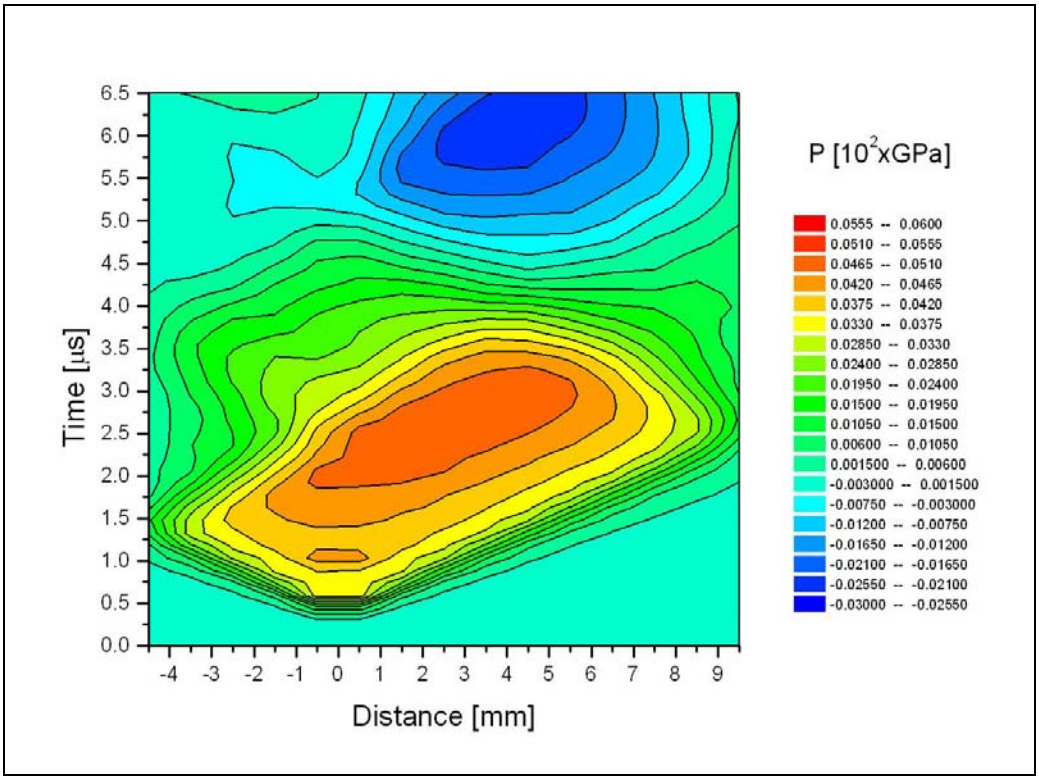

Fig. D.4. Time distance diagram for OFHC Cu plate impact test numerical simulation with Mesh 1

Diagrams were created for the sets of the elements through thickness of the flyer and the target, which are positioned on the axis of the symmetry. The time-distance diagrams were constructed from pressure-time data for the three different mesh configurations (Fig. D.4. – Fig. D.6.) and for 6.5 μs response time.

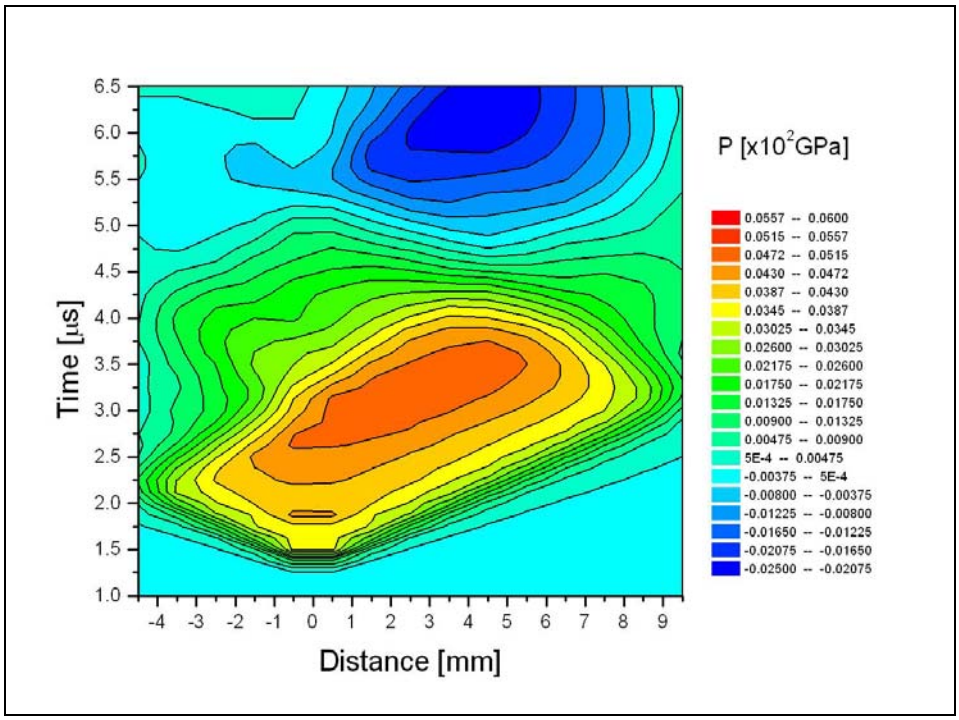

Fig. D.5. Time distance diagram for OFHC Cu plate impact test numerical simulation with Mesh 2

Numerical simulations were performed using DYNA3D. All three plates, namely flyer, target and support plate, were modelled with Isotropic-Elastic-Plastic-Hydrodynamics material model in combination with Mie-Grunisen equation of state.

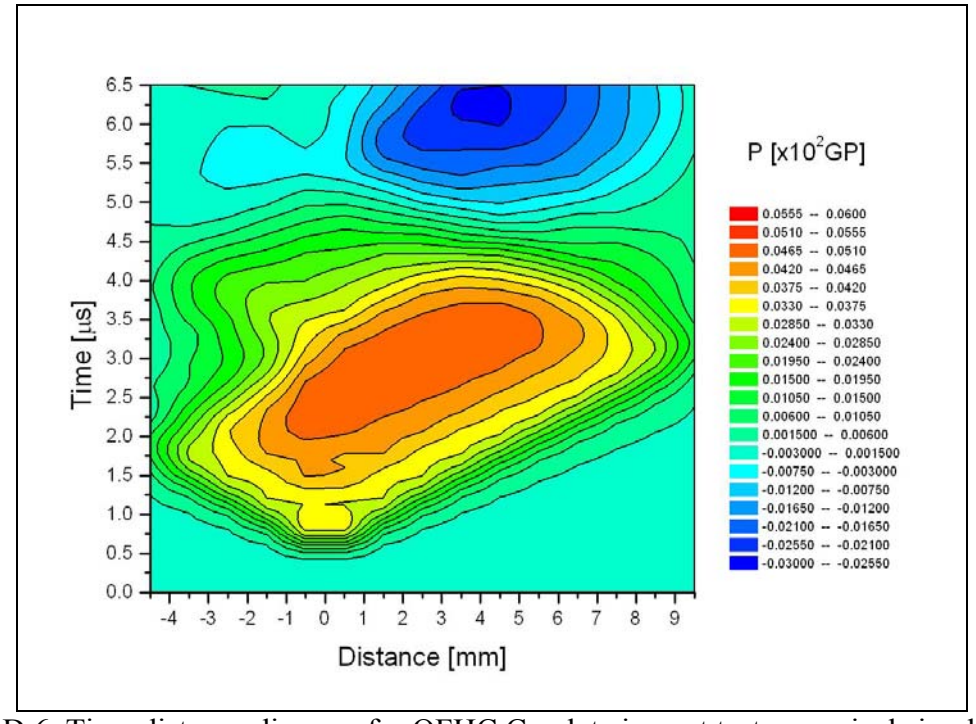

Fig. D.6. Time distance diagram for OFHC Cu plate impact test numerical simulation with Mesh 3

Pressure time histories for the elements in interior of the target and for three different mesh configurations are compared and presented in the figure Fig. D.7. Elements in all three configurations were positioned on the axis of the symmetry and half way through thickness of the target plate.

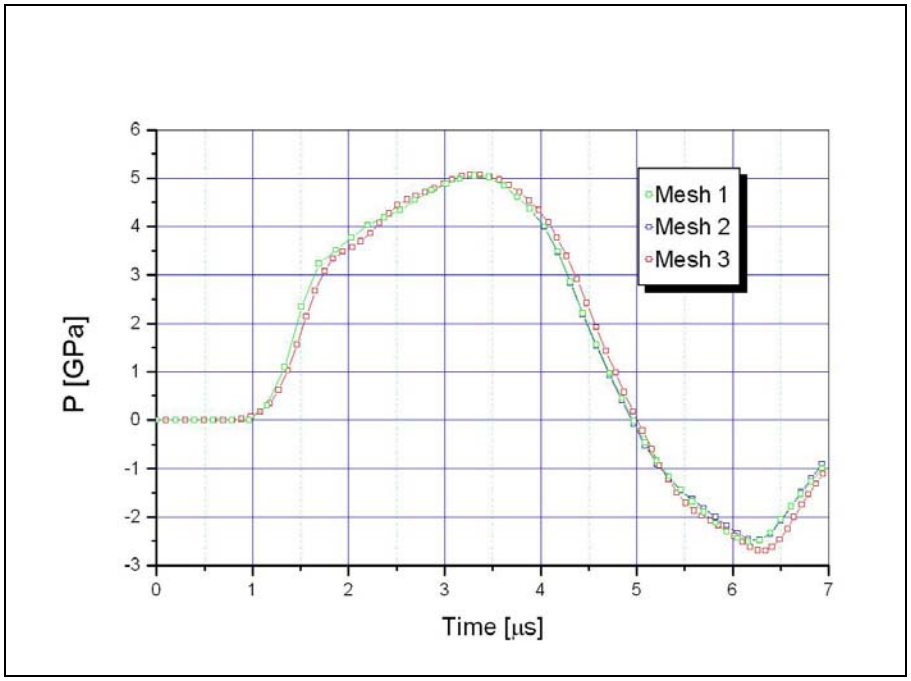

Fig. D.7. Pressure time histories for the elements in interior of the target plate for three different mesh configurations

The effect of mesh size on the loading behaviour of target specimen has been investigated and very limited effect was observed. Evaluating the CPU time spent in simulations, it is possible to conclude that Mesh 1 conducts to the best compromise present between accuracy and CPU time.